

Modeling Primary Hemostasis

Inaugural-Dissertation
zur
Erlangung des Doktorgrades

der Mathematisch-Naturwissenschaftlichen Fakultät
der Universität zu Köln

vorgelegt von
Masoud Hoore
aus Zanzan, Iran

Jülich 2018

Berichterstatter:
(Gutachter)

Prof. Dr. Gerhard Gompper
Prof. Dr. Joachim Krug

Tag der mündlichen Prüfung:

9 May 2018

Dedicated to my wife, Mahsa . . .

Acknowledgements

My gratitude goes to all people who helped me along my whole life so far, without whose help and support I may not have been able to pursue my education to this point. I start from my parents who provided me with a peaceful atmosphere that I could have studied well.

I am thankful to my country, where I was born and grew up, whose sources I have used, until I became erudite enough to do research independently. I owe a lot to Allameh Helli high school in Tehran, belonging to the National Organization for Development of Exceptional Talents at that time during the years 2003 to 2007. My university, Sharif University of Technology, provided me with all that I needed for increasing my knowledge and expertise. I thank all of my instructors, supervisors, and classmates there. Especially, I express my gratitude to Prof. Saman Moghimi-Araghi. He mentored me for my thesis work in the department of physics. He taught me a precious thing, how to conduct independent research, from the way of thinking, to implementing the ideas and expressing the results.

I thank Dr. Dmitry Fedosov for his support during my PhD. I learned a lot from him. He was a very nice and calm person; I can say he was more like a friend than a supervisor. I would like to express my deep acknowledgements to Prof. Dr. Gerhard Gompper. He, as my second supervisor, and my official *Doktorvater*, provided me with all the facilities and opportunities to learn and perform my best. He also showed me the power of theory! I thank both Dmitry and Gerhard again for providing me a peaceful environment to implement my ideas in our research. I hope we will keep in touch and probably collaborate further after I leave their group. I also thank my office-mates, my colleagues, and other supervisors in our department who were always open to help.

I have a full support of all kinds during my PhD from my beloved wife, Ms. Mahsa Sayadmanesh. I owe my whole PhD to her. My deep gratitude to you, Mahsa!

The last but not least, a financial support from the DFG Research Unit FOR 1543 SHENC - "Shear Flow Regulation in Hemostasis" is gratefully acknowledged. I thank also a CPU time grant by the Jülich Supercomputing Center.

Abstract

The physical properties of blood cells and blood flow are important for various biological functions of blood and for biomedical issues, ranging from blood diseases such as malaria to blood-related applications such as drug delivery. The main objective of this thesis is to study the very early stages of hemostasis, the process which stops bleeding after injury. The plasma protein von Willebrand factor (VWF) is a necessary component in primary hemostasis, especially at high shear rates, when platelets are not able to firmly adhere to an injured vessel wall on their own. A realistic model for this process is developed, in order to better understand how hemostasis occurs in the microvasculature.

An important role in primary hemostasis is played by VWF concatemers with lengths of a few to tens of microns. Such large lengths make their size comparable to blood cells, *i.e.* they interact with blood cells as mesoscale objects in a different manner than the simple plasma. The dynamics of VWFs is studied here by mesoscale hydrodynamic simulations in simple shear and capillary flows, with and without blood cells.

VWFs remain collapsed at low shear rates, due to intra-molecular attractions, while they stretch at shear rates beyond a critical value. The shielding of adhesive ligands of VWFs in the collapsed state makes these proteins shear-sensitive, so that VWFs adhere to vessel walls or platelets only when they are stretched. Thus, at high enough shear rates, VWFs and platelets form aggregates triggered by the shear sensitivity of VWFs for adhesion. Such aggregates are reversible and disappear at low shear rates.

In blood flow, VWFs migrate toward the vessel walls through a process called margination. VWF margination is mediated by red blood cells since they migrate toward the center of the vessels and push VWFs to the walls. The presence of platelets and stretched VWFs near the vessel walls leads to their spontaneous aggregation. These aggregates are highly porous and deformable and eventually migrate to the center of a blood vessel due to a strong hydrodynamic lift force. Low shear rates at the center of a vessel lead to aggregate dissociation. This is a completely mechanical process which regulates the aggregation and restricts the formation of free-flowing large thrombi.

In addition to the mechanical regulation of undesired aggregates, the concentration of large VWFs is controlled by the protease enzyme, ADAMTS13, which cleaves stretched VWFs. Modeling of this process shows that VWF polymers get cleaved gradually from their extruded ends, providing enough time for the hemostatic activity. The size distribution of VWFs obeys a power law according to the model predictions.

The new model presented here for VWF and its aggregation with platelets captures detailed realistic behavior of VWFs and aggregates in flow. It allows the simulation of blood flow and coagulation on the cellular level for the first time, in order to interpret the causes of several VWF-related diseases, and find the possible treatment strategies. Also, the proposed models can be employed in more complex cases, like the blood vessel bifurcations, and blood discharge from the capillaries.

Kurzzusammenfassung

Die physikalischen Eigenschaften von Blutzellen und Blutströmungen sind wichtig für verschiedene biologische Funktionen des Bluts und für biomedizinische Fragestellungen, die von Blutkrankheiten wie Malaria bis zu blutbezogenen Anwendungen wie der Arzneimittellabgabe reichen. Das Hauptziel dieser Arbeit ist die Untersuchung der sehr frühen Stadien der Hämostase, des Prozesses, der die Blutung nach einer Verletzung stoppt. Das Plasmaprotein von Willebrand-Faktor (VWF) ist eine notwendige Komponente in der primären Hämostase, insbesondere bei hohen Scherraten, wenn Blutplättchen nicht in der Lage sind, alleine fest an einer verletzten Gefäßwand zu haften. Ein realistisches Modell für diesen Prozess wird entwickelt, um besser zu verstehen, wie Hämostase in der Mikrovaskulatur funktioniert.

Eine wichtige Rolle bei der primären Hämostase spielen VWF-Konkatemere mit Längen von wenigen bis einigen zehn Mikrometern. Diese Längenskalen machen ihre Größe vergleichbar mit der von Blutzellen. VWF interagiert deshalb mit Blutzellen als mesoskalige Objekte auf andere Weise als das einfache Plasma. Die Dynamik des VWF wird hier durch mesoskalige hydrodynamische Simulationen in einfachen Scher- und Kapillarströmungen mit und ohne Blutzellen untersucht.

VWF haben eine kompakte, kugelförmige Konformation aufgrund von intramolekularen Anziehungen bei niedrigen Scherraten, während sie sich bei Scherraten über einem kritischen Wert strecken. Die Abschirmung von Liganden des VWF im kollabierten Zustand macht die Adhäsion dieses Proteins scherempfindlich, so dass der VWF nur an Gefäßwänden oder Thrombozyten haften kann, wenn er stark gestreckt wird. Somit bilden VWF und Plättchen bei ausreichend hohen Scherraten Aggregate, die durch die Scherempfindlichkeit des VWF für die Adhäsion ausgelöst werden. Solche Aggregate sind reversibel und lösen sich bei niedrigen Scherraten wieder auf.

In der Blutströmung wandern die VWF-Proteine zu den Gefäßwänden, getrieben durch einen Prozess der als Margination bezeichnet wird. Die VWF-Margination wird durch rote Blutkörperchen vermittelt, da sie in Richtung der Mitte der Gefäße wandern und dadurch die VWF an die Wände drücken. Das Vorhandensein von Plättchen und gestreckten VWF in der Nähe der Gefäßwände führt zur spontanen Aggregation. Die Aggregate sind hochporös und

verformbar, und wandern deshalb aufgrund einer starken hydrodynamischen Auftriebskraft in das Zentrum des Blutgefäßes. Niedrige Scherraten in der Mitte eines Gefäßes führen zu der Aggregatdissoziation. Dies ist ein vollständig mechanischer Prozess, der die Aggregation reguliert, und damit die Bildung freifließender großer Thromben einschränkt.

Neben der mechanischen Regulation unerwünschter Aggregate wird die Konzentration großer VWF Proteine durch das Protease-Enzym ADAMTS13 gesteuert, das gestreckten VWF spaltet. Die Modellierung dieses Prozesses zeigt, dass VWF-Polymere allmählich von ihren extrudierten Enden her gespalten werden, was ausreichend Zeit für die hämostatische Aktivität lässt. Die Größenverteilung der VWF folgt einem Potenzgesetz gemäß Modellvorhersagen.

Das hier vorgestellte neue Modell für VWF und seine Aggregation mit Thrombozyten erlaubt ein detailliertes Verständnis des Verhaltens von VWF und ihrer Aggregate im Blutfluss. Es ermöglicht erstmals die Simulation von Blutfluss und Koagulation auf zellulärer Ebene, und ermöglicht so die Interpretation der Ursachen mehrerer VWF-bedingter Erkrankungen und die Entwicklung mögliche Behandlungsstrategien. Auch können die vorgeschlagenen Modelle in komplexeren Fällen, wie Blutgefäßverzweigungen und Blutabfluss aus den Kapillaren, eingesetzt werden.

Table of contents

List of figures	xvii
List of tables	xxi
Nomenclature	xxiii
1 Introduction	1
1.1 Blood	1
1.2 Primary hemostasis	2
1.3 von Willebrand factor	3
1.4 Hydrodynamics	5
1.5 Red Blood Cell	8
1.6 Margination	11
1.7 What has been done so far.	13
1.8 Outline	15
2 Models and Methods	17
2.1 Membranes	17
2.2 Fluid model for hydrodynamic interactions	20
2.3 Polymer model	22
2.4 Polymer activity	23
2.5 Adhesive bonds	24
2.6 Coupling and boundary conditions	24
2.7 2D simulations	26
I Margination in Blood flow	29
3 Margination of von Willebrand factor in the blood stream	31

3.1	Introduction	31
3.2	Setup	33
3.3	VWF model	34
3.4	Experiments	35
3.5	Simulation and experimental measurements	37
3.6	VWF margination and stretching in blood flow	39
3.7	VWF adhesion	45
3.8	Summary	48
4	Reverse Fåhræus effect for drug carriers in blood stream	51
4.1	Introduction	51
4.2	Theory	52
4.3	Results	55
4.4	Summary	57
II	von Willebrand factor adhesion	59
5	Flow-induced adhesion of shear-activated polymers to a substrate	61
5.1	Introduction	62
5.2	Shear-activated polymer model	64
5.3	Adhesive bonds	66
5.4	Setup	68
5.5	Initial adhesion	69
5.6	Adhesion states	71
5.7	Reversible shear-dependent polymer adhesion	75
5.8	Comparison with the adhesion of a conformation-independent polymer . . .	76
5.9	Summary	79
6	Critical reversible aggregation of platelets and von Willebrand factor	81
6.1	Introduction	81
6.2	Adhesive bonds	82
6.3	Polymer avidity	83
6.4	Setup	85
6.5	Criteria for healthy behavior	86
6.6	Criticality of VWF-platelet adhesion	87
6.7	Reversibility of aggregate formation	91
6.8	Effect of shear rate and polymer cohesion	95

6.9	Summary	97
III	Aggregates in blood flow	99
7	Platelet-VWF aggregation in blood flow	101
7.1	Introduction	101
7.2	Setup	102
7.3	Results	103
7.4	Discussion	109
7.5	Summary	110
8	Aggregate Dynamics in Blood Flow and primary hemostasis	115
8.1	Introduction	115
8.2	Setup	116
8.3	Process of hemostasis	117
8.4	Free aggregate dynamics	120
8.5	Aggregation on the wall	126
8.6	Summary	127
IV	Regulation of von Willebrand factor by cleavage	129
9	Cleavage of von Willebrand factor by ADAMTS13 protease in flow	131
9.1	Introduction	132
9.2	VWF cleavage model	133
9.3	Setup	135
9.4	Stretching of VWF in shear flow	136
9.5	Susceptibility of VWF to cleavage	139
9.6	Cleavage pattern	142
9.7	Cleavage dynamics	144
9.8	Margination of VWFs in blood flow	145
9.9	Cleavage Statistics in blood	146
9.10	Summary	149
10	Size distribution of degrading polymers	151
10.1	Introduction	151
10.2	Results	152

10.3 Summary	156
V Red blood cell aggregates	159
11 Mapping the erythrocyte doublet forms	161
11.1 Introduction	161
11.2 Membrane model	162
11.3 Adhesion model	165
11.4 Experiment	166
11.5 Doublet shapes	167
11.6 Comparison with experiments	173
11.7 Summary	176
12 Conclusion & future perspective	179
Bibliography	183
References	183

List of figures

1.1	Schematic of primary hemostasis.	2
1.2	VWF molecular structure.	4
1.3	Schematic of the derivation of the Navier-Stokes equations.	6
1.4	Schematic of the curvature of a surface.	9
1.5	RBC membrane structure.	10
1.6	Schematic of lift force.	12
2.1	Schematics of the models used in the 2D and 3D simulations.	18
3.1	Calibration of the 3D VWF model against experiments.	34
3.2	Simulation and experimental measurements.	36
3.3	Relation between the wall-shear rate and the average shear rate.	38
3.4	Simulated margination and stretching of VWF and a repulsive polymer. . .	41
3.5	Phase diagrams of VWF polymer location and stretching.	42
3.6	Margination of VWF in microfluidics and simulations.	43
3.7	Comparison of margination and stretching of VWFs with a different number of monomers.	44
3.8	VWF extension within a channel cross-section.	45
3.9	Potential-adhesion probability of VWF and a repulsive polymer.	46
3.10	VWF adhesion in experiments.	47
4.1	Margination in blood flow.	53
4.2	Ratio of tube and discharge volume fractions for RBCs and marginated particles, platelets and large polymers.	55
4.3	The RBC-FL thickness for different pressure gradients and tube hematocrits. .	56
4.4	Margination of blood components for different pressure gradients and tube hematocrits.	56
5.1	Schematic of an attractive polymer with $N = 30$ beads in shear flow. . . .	64

5.2	VWF extension and avidity calibrated with the experimental results.	65
5.3	Bond lifetime of the two-pathway model.	68
5.4	Schematic illustration of polymer adhesion to a substrate.	70
5.5	Extension of an adhered polymer followed in time.	71
5.6	Adhesion state diagrams of a shear-activated polymer	73
5.7	At flow stasis, the adhesion of the polymers to the substrate is characterized by various properties in time.	74
5.8	Typical CI- and CD-polymer conformation in shear flow and when the flow is stopped.	76
5.9	Effect of conformation-dependent activation on the reversibility of polymer adhesion.	78
6.1	VWF total avidity, ψN_{beads} , as a function of threshold criteria, R_{thres} and θ_{thres} , and VWF polymer size, L_{VWF}	85
6.2	Schematic view of VWF stretching and its aggregation with platelets for different shear rates.	86
6.4	Adhesion of platelets to immobilized VWFs.	88
6.5	VWF-platelet adhesion and VWF avidity with respect to time and shear rate.	89
6.3	Adhesion of platelets to fibrinogen substrates.	90
6.6	Effect of affinity and avidity on the adhesion of platelets to immobilized VWF substrate.	91
6.7	Reversible shear-dependent platelet-VWF aggregation in simple shear flow without interactive substrate.	92
6.8	Reversible shear-dependent platelet-VWF aggregation in simple shear flow with interactive substrate.	93
6.9	Aggregate dissociation in time for two different affinities.	94
6.10	Aggregation in 2D simulations.	96
6.11	Density profile and margination parameter.	96
6.12	Polymer stretching and avidity with respect to shear rate and cohesive potential.	97
7.1	Simulation setup and models.	103
7.2	Schematic view on the possibility of VWF-platelet aggregates.	105
7.3	Reversible aggregation of platelets and VWFs in simulations and experiments.	106
7.4	Margination to and aggregation in the RBC-FL.	107
7.5	Continual margination, aggregation, demargination, dissociation, and re-margination.	108
7.6	Migration to the center of the vessel (Demargination.)	109

7.7	Density profile comparison.	110
7.8	Migration to the center of the vessel (demargination) for blood in a simple shear flow.	111
7.9	Summary of platelet-polymer aggregation in blood flow.	112
8.1	Stretching phase of polymers in blood flow in absence and presence of adhesive wall.	119
8.2	VWF density profile and number of bonds in time.	120
8.3	2D simulations of blood flow and aggregation.	121
8.4	The aggregation process for different pressure drops and hematocrits. . . .	123
8.5	Density profile of blood components in 2D simulations.	123
8.6	Margination parameter for different hematocrits and pressure drops in normal flow and aggregated flow case.	124
8.7	RBC-FL thickness, δ_{CFL} , normalized by the channel width, W (a), and margination probability for platelets and VWF polymers (b) in normal and aggregation condition.	125
8.8	Aggregation as a function of the association and dissociation rates.	126
8.9	Aggregation of platelets and VWF polymers at the presence of a bulge. . .	128
9.1	Schematic of a VWF with $N = 40$ in shear flow.	134
9.2	Stretching of VWF.	137
9.3	Probability distribution $p(R_s)$ of VWF extension.	138
9.4	Geometrical model for the susceptibility of VWF to cleavage.	139
9.5	Tension model for the relative susceptibility of VWF to cleavage.	140
9.6	Cleavage period as a function of shear rate.	141
9.7	Illustration of cleavage events.	142
9.8	Cleavage pattern of VWF using the geometrical model.	143
9.9	Cleavage pattern of VWF using the tension force model.	143
9.10	Temporal evolution of VWF distribution under cleavage.	144
9.11	Susceptibility to cleavage and lifetime of VWF.	145
9.12	Distribution of polymer extension.	146
9.13	Cleavage probability in the blood flow during simulation period.	147
9.14	Cleavage pattern of VWF in pressure driven blood flow and in simple shear flow.	148
9.15	Effective cleavage rate and VWF extension in flow direction of blood stream with respect to blood pressure and hematocrit, for 2D simulations.	149

10.1	Size distribution of polymers is dependent on the physical condition of the system.	153
10.2	Frequency vs. size.	154
10.3	Size distribution in experiments and the model.	155
10.4	The monomer frequency as a function of power-law exponent $-\beta$ and α_0 . .	157
11.1	Schematic of the two discretization models for the bending energy.	163
11.2	Result of bending model discretization scheme	164
11.3	Analysis of the contact area and the approximation of effective adhesion energy.	165
11.4	The ratio of the reduced adhesion energy to the reduced pairwise energy. . .	166
11.5	RBC doublet configurations as a function of $v_1 = v_2 = v$ and γ with aligned and offset first point of contacts.	169
11.6	RBC doublet configurations as a function of v_1 and v_2 at a constant adhesion strength $\gamma = 8$	170
11.7	RBC doublet configurations as a function of spectrin network's shear modulus. .	171
11.8	Stress-free shape of RBC affects the doublet phases at low adhesion strengths and low reduced volumes	173
11.9	RBC doublet shapes.	174
11.10	Various rouleau phases in experiments and simulations.	175

List of tables

2.1	Membrane properties.	20
2.2	SDPD fluid properties.	21
2.3	Polymer properties.	22
2.4	Adhesive bond properties for the two-pathway model.	23
2.5	LJ interaction properties.	25
2.6	2D simulation parameters compared to their 3D counterparts.	26
8.1	Setup for 3D simulations.	117
11.1	Membrane properties in simulations and related references.	164

Nomenclature

Selected symbols

E_{adh}	Adhesion energy
Φ_i^j	Adhesion parameter between i and j entities
Γ	Adhesion strength
k_{on}	Association rate (on-rate)
Ψ	Average relative avidity of polymers
κ_{b}	Bending constant
$E_{\text{b}}, U_{\text{b}}$	Bending energy
ε_{b}	Bending energy surface density
κ_{c}	Bending rigidity
\mathbf{f}_{body}	Body force density
k_{B}	Boltzmann constant
ζ	Bulk viscosity
k_{c}	Catch dissociation rate (catch off-rate)
W	Channel width
k_{c}	Cleavage rate
A_{c}	Contact area
$\dot{\gamma}_{\text{c}}^{\text{a}}$	Critical shear rate of platelet-polymer aggregation

$\dot{\gamma}_c$	Critical shear rate of polymer stretching
$\mathbf{a} \times \mathbf{b}$	Cross product of vectors \mathbf{a} and \mathbf{b}
\mathbf{c}	Curvature matrix
r_c	Cutoff radius
$r_{\text{cut}}^{\text{on}}$	Cutoff range for bond association
ρ	Density
$p(y)$	Density profile
d_{pol}	Diameter of polymer beads
H_d	Discharge hematocrit
J_d	Discharge volume fraction of margined particles
$U_{\text{KN}}, U_{\text{GK}}$	Discretized bending energies
k_{off}	Dissociation rate (off-rate)
\tilde{E}_b	Effective bending energy
D_{eff}	Effective diameter
$\tilde{\epsilon}$	Effective pairwise adhesion energy
$\tilde{\gamma}$	Effective reduced adhesion energy
A_0, A	Equilibrium surface area of membrane
V_0, V	Equilibrium volume of membrane
R_s	Extension of polymer along flow direction
f_n	Frequency/population of a polymer with size n
κ_g	Gaussian bending modulus
K	Gaussian curvature
k_a	Global area rigidity
k_v	Global volume rigidity

$\mathbf{a} \cdot \mathbf{b}$	Inner (dot) product of \mathbf{a} and \mathbf{b}
∇^2	Laplacian operator, $\equiv \nabla \cdot \nabla$
L	Length of vessel or channel
L_{VWF}	Length of VWF polymer
ϵ_{LJ}	Lennard Jones potential energy unit
T_l	Lifetime
k_l	Local area rigidity
H	Local hematocrit
J	Local volume fraction of marginated particles
M	Margination parameter
P	Margination probability
m	Mass
λ	Material constant
D/Dt	Material derivative
H	Mean curvature
∇	Nabla, differential operator, $\equiv (\partial_x, \partial_y, \partial_z)$
$\dot{\gamma}^*$	Non-dimensional pseudo-shear rate
$\dot{\gamma}_w^*$	Non-dimensional wall shear rate
\mathbf{n}	Normal unit vector
\mathbf{n}_{ijk}	Normal vector on discretized triangular lattice
n	Number density
N_b	Number of bonds (inter-molecular)
N_{bonds}	Number of bonds (intra-molecular)
N_v	Number of membrane vertices

N	Number of polymer beads
$\tilde{\epsilon}$	Pairwise adhesion energy, $\equiv \epsilon_{\text{LJ}}$
∂_t	Partial derivative, $\equiv \frac{\partial}{\partial t}$
p	Pressure
c_1, c_2	Principal curvatures
$p(i, n)$	Probability of cleavage at site i of a polymer with size n
$P(n)$	Probability of cleavage of a polymer with size n
$\bar{\gamma}$	Pseudo-shear rate
$g(r)$	Radial distribution (pair correlation) function
g_n	Rate of generation of a polymer with size n
δ_{CFL}	Red blood cell free layer thickness
γ	Reduced adhesion energy
$\tilde{\epsilon}_b$	Reduced effective bending energy
v	Reduced volume
ψ	Relative avidity of a polymer
χ_c	Relative cleavage site
ψ	Relative susceptibility of VWF to cleavage, also $\psi_\theta, \psi_R, \psi_{\text{R}}, \psi_f$
Re	Reynolds number
s_n	Secretion rate of a polymer with size n
μ_o	Shear modulus of membrane
k_s	Slip dissociation rate (slip off-rate)
c_0	Spontaneous curvature
\mathbf{E}	Strain rate tensor
\mathbf{S}	Stress tensor

T	Temperature
$k_B T$	Thermal energy unit at 27°C
θ_{thres}	Threshold angle for conformation-dependent active polymer model
R_{thres}	Threshold radius for conformation-dependent active polymer model
t	Time
τ	Time scale
$\text{tr}(\mathbf{A})$	Trace of matrix \mathbf{A}
H_t, H_c	Tube/channel Hematocrit (volume fraction of red blood cells)
J_t	Tube volume fraction of margined particles
$\mathbb{1}$	Unitary tensor
\mathbf{u}	Velocity field
η	Viscosity
$\dot{\gamma}_w$	Wall shear rate

Acronyms / Abbreviations

2D	Two-dimension(al)
3D	Three-dimension(al)
BC	Boundary condition
CD	Conformation-dependent
CI	Conformation-independent
COM	Center of mass
DPD	Dissipative particle dynamics
F-B	Flat-Biconcave
F-C	Flat-Concave
FENE	Finite extensible nonlinear elastic

FPM	Fluid particle model
LBM	Lattice Boltzmann method
LJ	Lennard-Jones
M-F	Male-Female
MPC	Multi-particle collision dynamics
N-S	Navier-Stokes
PBS	Phosphate Buffered Saline
RBC-FL	Red blood cell free layer
RBC	Red blood cell
S-B	Sigmoid-Biconcave
SDPD	Smoothed dissipative particle dynamics
SD	Standard deviation
SPH	Smoothed particle hydrodynamics
TTP	Thrombotic thrombocytopenic purpura
UL-VWF	Ultra-large von Willebrand Factor
VWD	Von Willebrand disease
VWF	Von Willebrand factor
WLC	Worm-like chain
WPB	Weibel–Palade body

Chapter 1

Introduction

1.1 Blood

Blood is one of the basic tissues in animals. From the beginning of evolution, the main task of blood is to flow around tissues and transport nutrients. A heart has also evolved to pump the blood through the organisms of the animals. As animals evolved to be larger, the circulation of essential gases for the metabolism became necessary, since they could not sustain gas exchange without a gas exchange organ (lung or gill) and a closed circulation system. The blood has evolved to mediate this task for all vertebrates and a few invertebrates. Consequently, red blood cells (RBCs) have evolved to transport Oxygen (O_2) from the environment to the tissues, and Carbon dioxide (CO_2) from the tissues to the environment. RBCs are produced in the bone marrow, lack nucleus and their cytoplasm contains a high concentration of hemoglobin, a protein which binds Oxygen and Carbon dioxide.

Blood does not only accomplish the transport of gases and nutrients, but also regulates body temperature. For this purpose, the blood vessels can change their diameter to control the flow rate of the blood to the boundaries of the body (close to skin), in order to control heat exchange between the body and the environment.

The circulation system must remain closed. In case of an injury, the system has an internal procedure to restore its integrity. Platelets have evolved to perform this task. Platelets are disc-like cells, which bud out of megakaryocytes¹⁷⁸, one of the largest bone marrow cells. Similar to RBCs, they lack nucleus. Platelets bind to an injured blood vessel and plug the wound in order to keep the blood tissue inside the vasculature. Granules of platelet's cytoplasm contain von Willebrand factor (VWF), a protein necessary for blood clotting.

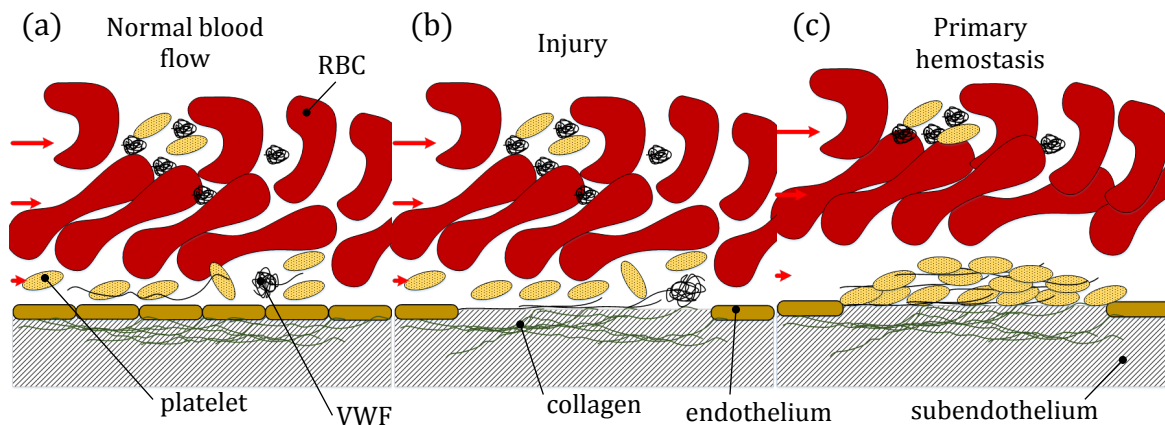


Fig. 1.1 Schematic of primary hemostasis. (a) VWFs and platelets flow with RBCs in the blood vessels. (a) At high shear rates, VWFs stretch and adhere to the injured surface. By stretching, they become adhesive to platelets and tether them at the injured site. (c) The adhesion of VWFs and platelets to the injured site continues until the whole opening gets covered by their aggregate. This process is called primary hemostasis. After this stage, platelets become activated and fill the voids in the aggregate. They also induce polymerization of fibrins, which cover the aggregate firmly and make it more stable.

1.2 Primary hemostasis

The word hemostasis consists of two parts *hemo* and *stasis*, *hemo* meaning blood, and *stasis* meaning stoppage of the flow. Platelets are the main contributors to the hemostasis, such that blood discharge from an injured vessel does not stop without them. Although platelets adhesion to the injured site is firm at low shear rates ($600\text{--}900\text{ s}^{-1}$)¹⁸⁸, the strength of adhesive bonds between platelets and the injured substrate is too weak to keep them at the surface if shear rate is high. In such cases, long multimeric protein VWF plays a vital role, of course along with the synergy of many other factors that come after the primary adhesion^{95,187}. In arteries, arterioles, and capillaries, the wall shear rate can be high causing platelet detachment. VWFs stretch at high shear rates and become adhesive both to platelets and the injured surface. The bonding of platelets to VWFs is firm enough to keep them at the site of injury. The initial blood clotting process before platelets get activated is called primary hemostasis. When platelets get activated, they protrude their membranes to fill any void in their aggregate. They also signal polymerization of fibrins from fibrinogens. Figure 1.1 shows a time-line of primary hemostasis. The blood components flow normally until they reach the injured site. VWFs stretch and adhere to the site, and tether platelets. The adhesion of VWFs to injured site, and to the adhered platelets takes place until the whole opening is covered by platelet aggregates.

For primary hemostasis to happen, a sufficiently large number of platelets and VWFs must flow close to the injured wall. A process known as margination increases the probability of adhesion by increasing the concentration of platelets and VWFs close to the walls.

1.3 von Willebrand factor

The VWF protein is named after a Finnish medical doctor, Erik von Willebrand, who first discovered a hereditary disease of increased bleeding in 1926 and distinguished it from other diseases such as hemophilia^{239,240}. Since the disorder had many similarities to hemophilia, the term pseudohemophilia proposed by him was used in literature for this disease^{47,160,204} until it was found that it is related to a plasma factor^{4,115,171} different from hemophilia's clotting factors. The symptoms of the disease vanished even by adding the plasma of patients with hemophilia^{150,151}. This provided another clue that pseudohemophilia is related to a plasma protein¹⁸³. The disease name was therefore gradually changed to von Willebrand disease (VWD) and the protein was called von Willebrand factor.

VWF is the largest protein in blood plasma³³. It is a linear polymer of dimeric VWF units linked to each other end-to-end⁷¹. In order to differentiate between linear and branched multimers, the term concatemer is referred to the chain of VWF²¹². The molecular structure of VWF is shown in Figure 1.2. The VWF dimers make stiff tweezer-like structure at low pH (see Figure 1.2-a), in the storage granules of endothelial cells, Weibel–Palade bodies (WPBs)²³⁵. WPBs are cylindrical granules in the cytoplasm of endothelial cells, tightly packing the helical-tubular structures of VWF dimers^{91,242}. Large VWF polymers are secreted into the blood stream from WPBs of the endothelial cells. In blood plasma, the protein finds a quite random configuration, but mostly remains globular, shielding its adhesive sites to platelet receptors or collagen²¹³ (see Figure 1.2-b). Under tensile force, the polymer chain stretches and exposes its adhesive sites (see Figure 1.2-c). In this state, each VWF dimer can stretch to 100 nm²¹³ while it is 60 nm in WPBs⁷¹. Several configurations of two VWF dimers are shown in Figure 1.2-d. The contour length of VWF multimers can reach several to several tens of micrometers^{33,42,71,176}. The structure of VWF dimer is essential in defining the polymer activity.

In addition to the adhesive domains for binding to platelet receptors and collagen from an injured subendothelial tissue, there is a domain in each monomer of VWF, which is susceptible to cleavage by VWF protease ADAMTS13^{212,213}. The lack or gain of function in any of these crucial domains causes a specific type of disease. For instance, some mutations can increase the affinity of VWF to platelet receptors causing von Willebrand disease (VWD) type 2B¹⁸⁵. Also other mutations may on one hand increase the susceptibility

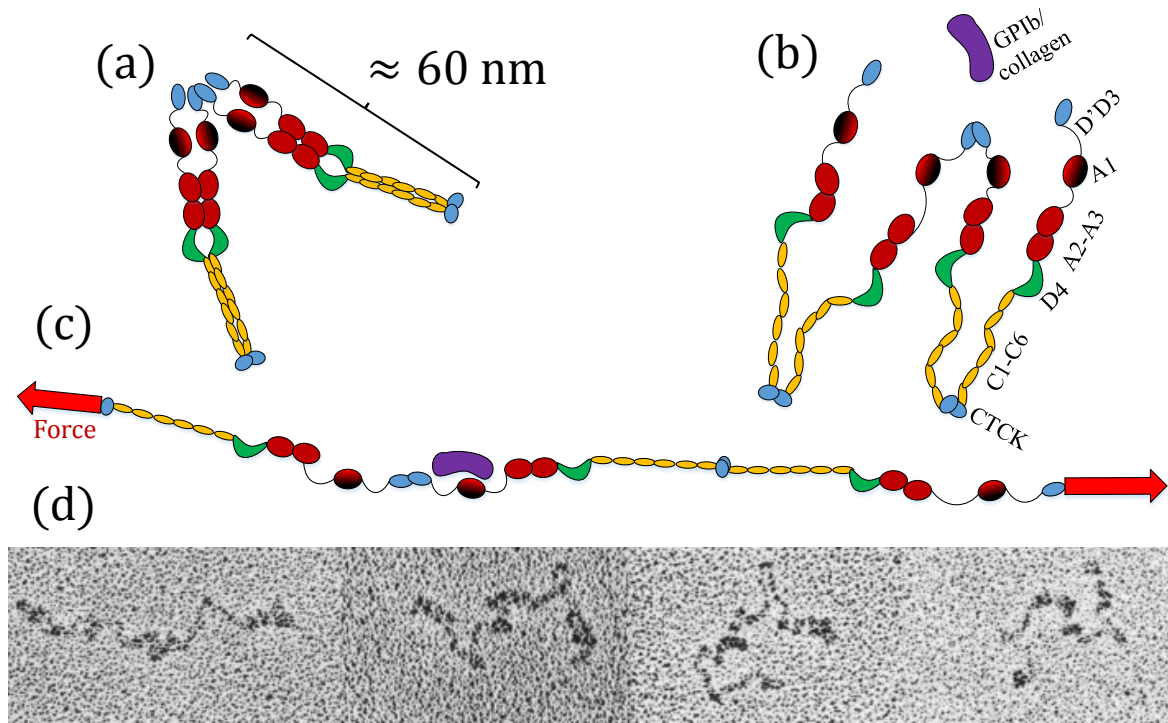


Fig. 1.2 VWF molecular structure. (a) VWF dimers acquire strong self-association at low pH; they have a stiff tweezer-like structure two-by-two, and arrange in a helix-tubular structure. The whole tubule among other VWF tubules is tightly wrapped by a lipid bilayer, composing a granule unique to endothelial cells, called Weibel-Palade-Body (WPB). (b) Configuration of VWF dimers in blood plasma. In this case, the VWF dimer is flexible and at the same time collapses into a globule, shielding its adhesive domains from platelet receptors and collagen. All VWF domains are shown, including the adhesive domain A1 and A3, and cleavage domain A2. (c) VWF dimers stretch if the polymer is under shear, or tensile force. In this state, the adhesive domains are able to bind receptors and the cleavage domain is prone to the cleaving VWF protease, ADAMTS13. (d) Several VWF configurations in blood plasma, reprinted from Fowler et al. 1985⁷¹.

of VWF to cleavage by ADAMTS13, resulting in the bleeding disease type 2A¹⁸⁵, or on the other hand decrease its susceptibility and cause the life threatening disease Thrombotic Thrombocytopenic Purpura (TTP)^{29,186,192}, where spontaneous platelet-VWF aggregates form even at normal shear rates.

Two mechanisms for the efficacy of VWF in blood clotting (or hemostasis) are known to be most important: VWF affinity to platelet receptors and collagen, and VWF avidity which is the number of activated VWF ligands able to form bonds with those receptors²¹³. Although the avidity of VWF does not seem to be as important as VWF domain affinities, both characteristics are required for a healthy action of VWF. The VWF avidity is directly

proportional to its size and defines the efficiency of primary hemostasis^{36,176,183}, that over-short VWFs in VWD type 2A are unable to stop bleeding in an appropriate time.

What defines the adhesive behavior of VWF at high shear rates rather than low shear rates is the shielding of its interactive domains when polymer is under low tension^{11,75,128}. In theory, a self-attractive polymer, such as VWF, coils at low shear rates and stretches critically at high shear rates^{6,8}. At high shear rates, the tensile forces dominate the cohesion of the polymer and facilitate its stretching. It then demonstrates a coil-stretch dynamics since it rotates at the same time as it stretches^{34,191,210}. Recently, it has been found that the VWF ligand A1 domain adheres to the platelet receptor Glycoprotein Ib α if the shear rate is beyond a threshold¹⁰³ which occurs after the polymer chain unwraps and unshields the ligand⁷⁵. Interestingly, the critical force on the polymer chain, beyond which the VWF ligand gets activated⁷⁵ (more than 10 pN), is close to the critical force beyond which the VWF chain gets cleaved by its protease ADAMTS13²⁵², and is equal to around 20 pN. This is not a coincidence since the cleavage site of the polymer, A2 domain, is very close to the adhesive ligand A1 domain and may be shielded simultaneously with it by a VWF structure²³¹ or by binding a receptor¹³⁰.

1.4 Hydrodynamics

Blood plasma can be considered as a homogeneous viscous fluid. The dynamics of a fluid is derived from the classic Newton's laws. The equations of motion for a differential volume of fluid are

$$\frac{D}{Dt}\rho + \rho \nabla \cdot \mathbf{u} = 0, \text{ and} \quad (1.1)$$

$$\rho \frac{D}{Dt}\mathbf{u} = \mathbf{f}_{\text{body}} + \nabla \cdot \mathbf{S}. \quad (1.2)$$

Equation (1.1) is the continuity equation which determines the density of a differential volume element based on the fluxes of mass. It satisfies the conservation of mass for the system. If there is no source or sink of mass, the change in mass of a volume element must be equal to the influx/outflux of matter to/from the element. Equation (1.2) is the conservation of momentum for a differential volume element. It is Newton's second law, relating the change in momentum of a volume element to the stresses applied at the boundaries of the element and body forces exerted on it. Figure 1.3 illustrates the free diagram of a differential volume of fluid, which results in the momentum equation (1.2).

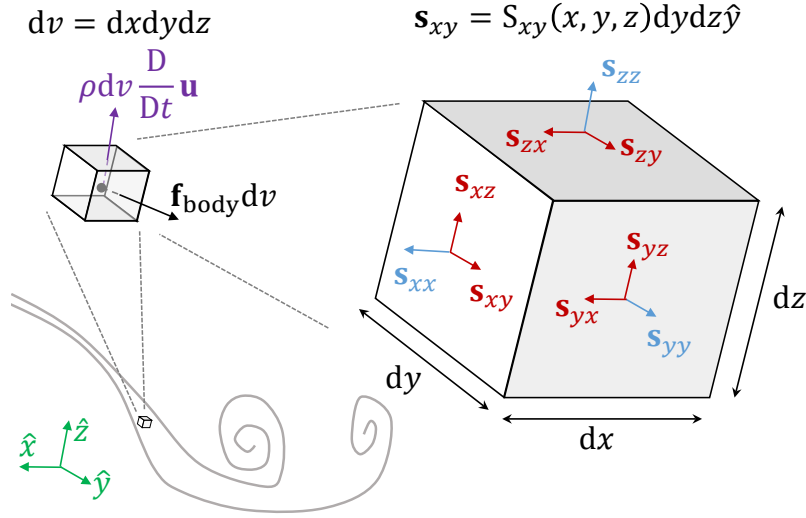


Fig. 1.3 Schematic of the derivation of the Navier-Stokes equations. The conservation of momentum can be written for a differential volume of the fluid. The resultant forces on the differential volume must equal its change of momentum. The stress forces on three faces are shown. The divergence of the stress tensor is derived by summing up stress forces on all faces.

D/Dt is called the material derivative and is defined as

$$\frac{D}{Dt} \equiv \frac{\partial}{\partial t} + \mathbf{u} \cdot \nabla, \quad (1.3)$$

and ∇ , t , ρ , \mathbf{u} , \mathbf{S} , and \mathbf{f}_{body} are spatial derivative or gradient, time, density, velocity, stress tensor, and body force density, respectively. The stress tensor \mathbf{S} in continuum mechanics is given by the constitutive equation¹¹³

$$\mathbf{S} = -p\mathbf{1} + \lambda \nabla \cdot \mathbf{u} \mathbf{1} + 2\eta \mathbf{E}, \quad (1.4)$$

for Newtonian (or linearly viscous) fluids, where $\mathbf{E} = (\nabla \mathbf{u} + \nabla \mathbf{u}^T)/2$ is the rate of strain (or deformation) tensor. Here, p is pressure, and λ and η are material constants. η is the dynamic viscosity of the fluid, while λ is related to the coefficient of bulk viscosity, which is the ratio of the viscous mean normal stress to the rate of change of volume,

$$\zeta = \frac{p - \bar{p}}{\nabla \cdot \mathbf{u}} = \frac{p + \frac{1}{3}\text{tr}(\mathbf{S})}{\nabla \cdot \mathbf{u}} = \lambda + \frac{2}{3}\eta, \quad (1.5)$$

where $\bar{p} = -\text{tr}(\mathbf{S})/3$ is the mechanical pressure, and p is the thermodynamic pressure. These two pressures are equal if the fluid is incompressible

Substituting Equation (1.4) and (1.1) into (1.2) yields

$$\rho \left(\frac{\partial \mathbf{u}}{\partial t} + \mathbf{u} \cdot \nabla \mathbf{u} \right) = \mathbf{f}_{\text{body}} - \nabla p + \eta \nabla^2 \mathbf{u} + \left(\zeta + \frac{1}{3} \eta \right) \nabla (\nabla \cdot \mathbf{u}), \quad (1.6)$$

where $\nabla^2 \equiv \nabla \cdot \nabla$ is the Laplacian operator. Equation (1.6) is the Navier-Stokes (N-S) equation of a general isotropic fluid. By mapping the parameters to non-dimensional units, the N-S equation reads

$$\text{Re} (\partial_t \mathbf{u} + \mathbf{u} \cdot \nabla \mathbf{u}) = \chi (\mathbf{f}_{\text{body}} - \nabla p) + \nabla^2 \mathbf{u} + \left(\frac{\zeta}{\eta} + \frac{1}{3} \right) \nabla (\nabla \cdot \mathbf{u}), \quad (1.7)$$

with mappings $\mathbf{u} \rightarrow \mathbf{u}/U$, $\nabla \rightarrow L\nabla$, $t \rightarrow Ut/L$, $p \rightarrow p/P_0$, and $f \rightarrow Lf/P_0$ so that all quantities in Equation (1.7) are dimensionless. U and L are characteristic velocity and length scale of a system. $\text{Re} = \rho UL/\eta$ is the ratio of inertial forces to viscous forces, known as the Reynolds number. χ in Equation (1.7) is

$$\chi = \begin{cases} \text{Re} & , \text{ if } P_0 \equiv \rho U^2 \text{ (inertial reference)} \\ 1 & , \text{ if } P_0 \equiv \frac{\eta U}{L} \text{ (viscous reference)} \end{cases}. \quad (1.8)$$

Generally, the reference pressure is defined in inertial terms when Re is high, and in viscous terms when Re is low. Equation (1.7) is interpreted as follows; the resultant of inertial forces of the fluid, the body forces, the pressure forces, the viscous forces, and the bulk viscous forces due to the compressibility of the fluid is zero.

Blood plasma under physiological conditions is assumed to be incompressible, *i.e.* $\nabla \cdot \mathbf{u} \sim 0$, and the viscosity dominates for all physiological blood pressures. Therefore, the N-S equation (1.7) simplifies to

$$\mathbf{f}_{\text{body}} - \nabla p + \nabla^2 \mathbf{u} = 0, \quad (1.9)$$

the so-called Stokes equation. In Stokes flow regime, mass is hindered by viscosity, and the velocity profile of the system is only related to pressure gradient and body forces. Note that the Stokes flow regime is only applicable for blood flow in microvasculature, where Re is small enough.

Stokes equation expresses how cells affect and get affected by their fluid environment. Although the material properties of the environment are fixed when we go to smaller scales, the dynamical regime of the system is very different from what we intuitively expect through our ordinary life experiences. It is worth to compare the flow experience of a red blood cell in blood flow under normal physiological conditions with a human swimming in a pool of water. Defining the Reynolds number based on the average shear rate around an object and

its effective diameter, we obtain

$$\text{Re} = \begin{cases} \frac{\rho \bar{\gamma} D_{\text{eff}}^2}{\eta} \sim \frac{10^3 \frac{\text{kg}}{\text{m}^3} \times 10^2 \frac{1}{\text{s}} \times 10^{-10} \text{m}^2}{10^{-3} \text{Pa.s}} \sim 10^{-2} & \text{for red blood cell} \\ \frac{\rho \bar{\gamma} D_{\text{eff}}^2}{\eta} \sim \frac{10^3 \frac{\text{kg}}{\text{m}^3} \times 1 \frac{1}{\text{s}} \times 1 \text{m}^2}{10^{-3} \text{Pa.s}} \sim 10^6 & \text{for human swimming in water} \end{cases}$$

where $\bar{\gamma}$ is average shear rate over the body. These numbers suggest that man must increase the viscosity of the fluid by a factor of 10^8 to feel the fluid flow a red blood cell experiences in normal blood flow. Such viscosity is ten thousand times higher than the viscosity of honey; if a person swims in a pool of a viscous fluid which is as more viscous to honey as honey is more viscous to water, she will feel roughly the same conditions as a RBC in blood flow feels!

Fluid modeling can be performed by several approaches, depending which characteristics of the fluid are the most important. The fluid models include continuum based finite volume²³⁸ and finite element methods^{15,93}, such as immersed boundary¹⁶¹ and boundary integral¹⁶⁶ methods, and particle-based methods such as smoothed particle hydrodynamics (SPH)^{138,139}, multi-particle collision dynamics (MPC)^{10,79,129}, lattice Boltzmann²⁷, etc. In this work, dissipative particle dynamics (DPD)^{84,88} and smoothed dissipative particle dynamics (SDPD)^{45,141} are used.

1.5 Red Blood Cell

Red blood cells (RBCs) comprise around 30 to 50% volume of the whole blood depending on the gender, genetics, geographical conditions, etc. These cells are formed from stem cells in the bone marrow. Step-by-step in their formation process, they acquire a high concentration of hemoglobin, become denucleated, and attain a biconcave shape. RBCs are highly deformable because they lack nucleus. Their biconcave shape also helps them flow in microvessels easily and exchange gases efficiently.

The dynamics of RBCs in blood flow is determined mostly by their membrane properties and the viscosity of their cytoplasm. RBC membrane is made of a fluid bilayer, membrane proteins and carbohydrates, and a network of cytoskeletons right beneath the membrane, formed by spectrin proteins connected to transmembrane proteins. This mesh of cytoskeleton beneath the fluid bilayer provides the membrane with shear elasticity. The shear elasticity helps RBCs maintain their integrity and keep their high deformability.

In the 1970s, the mechanics of RBC membrane was investigated by three independent groups^{22,48,85}. A more clear analysis among them was given by Wolfgang Helfrich in 1973. He derived a model for the bending of a lipid bilayer from the continuum-mechanical

approach⁸⁵. As Helfrich stated, the mechanics of lipid bilayers is obtained from the thin elastic shell theory¹⁴³ with zero shear elasticity because of membrane fluidity⁸⁵. Although such model explains the mechanics of lipid bilayers very well, it is not always a sufficient model for RBC membrane because it omits shear elasticity.

Below, the Helfrich bending model is explained briefly. If a membrane is defined by the height function $z = f(x, y)$, the normal unit vector of the surface is defined as $\mathbf{n} = \nabla f / |\nabla f| = (n_x, n_y, n_z)$, where $n_z = \sqrt{1 - n_x^2 - n_y^2}$. Thus, $\nabla \times \mathbf{n} = 0$. The curvature of the surface is given by the Hessian matrix $\mathbf{c} = \nabla \mathbf{n}$. The principal curvatures at each point are given by the eigenvalues of \mathbf{c} , and are equal to the inverse of the radius of the two circles tangent to the surface at that point, as shown in Figure 1.4.

The curvature-elastic energy (or simply the bending energy) for the membrane is assumed to be a quadratic function of the derivatives of the normal vector⁸⁵. For small deflections, this assumption is valid since every potential at its extrema can be fitted by a quadratic function for a small range.

The fluidity of the membrane implies that the energy must be invariant under rotation of axes x and y . This rules out many terms, leaving only⁸⁵

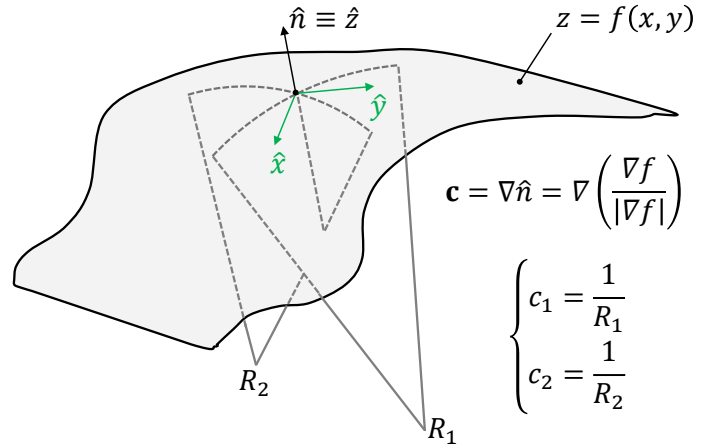


Fig. 1.4 Schematic of the curvature of a surface. The two tangent circles to the surface with radii R_1 and R_2 , and the principal curvatures are shown.

$$\begin{aligned} & \frac{\partial n_x}{\partial x} + \frac{\partial n_y}{\partial y}, \\ & \left(\frac{\partial n_x}{\partial x} + \frac{\partial n_y}{\partial y} \right)^2, \text{ and} \\ & \frac{\partial n_x}{\partial x} \frac{\partial n_y}{\partial y} + \frac{\partial n_x}{\partial y} \frac{\partial n_y}{\partial x}. \end{aligned} \quad (1.10)$$

Therefore, the bending energy per area ε_b must have a form of

$$\varepsilon_b = k_1 \left(\frac{\partial n_x}{\partial x} + \frac{\partial n_y}{\partial y} \right) + k_2 \left(\frac{\partial n_x}{\partial x} + \frac{\partial n_y}{\partial y} \right)^2 + k_3 \left(\frac{\partial n_x}{\partial x} \frac{\partial n_y}{\partial y} + \frac{\partial n_x}{\partial y} \frac{\partial n_y}{\partial x} \right), \quad (1.11)$$

where k_i are material constants. The constitutive equation (1.11) determines the fluid membrane shape and dynamics, and is similar to the constitutive equations for Newtonian fluid, as has already been explained (see Equation 1.4). The standard form of the Helfrich bending energy is written in terms of the mean and Gaussian curvatures, for the whole membrane in integral form

$$E_b = \frac{1}{2} \kappa_c \oint_{\partial V} da (2H - c_0)^2 + \kappa_g \oint_{\partial V} da K, \quad (1.12)$$

where $2H = c_1 + c_2$ is the mean curvature and $K = c_1 c_2$ is the Gaussian curvature. c_0 , κ_c , and κ_g are the spontaneous curvature, bending rigidity, and Gaussian bending modulus, respectively, and are related to coefficients k_i in Equation (1.11). Here, the integrals are taken over the whole membrane encapsulating the volume V . ∂V refers to the boundary of volume V , which is essentially the membrane surface area. The Helfrich bending energy can be simplified if the topology of the membrane is fixed; the Gaussian bending energy is invariant due to the Gauss-Bonnet theorem for a fixed topology^{80,81}, and can be ignored in the bending energy. Similar bending energies have been derived from other continuum-mechanical-based approaches around the same date^{22,48}, but the Helfrich approach is more detailed and is widely accepted by the scientific community. The bending energy κ_c is a material constant, which depends on the membrane thickness and its elastic properties^{22,48}.

The Helfrich bending energy describes the behavior of fluid membranes very well. However, RBC membranes possess significant shear elasticity due to their spectrin network. The spectrin network is made of protein assemblies connected to the fluid membrane by actin assemblies, as illustrated in Figure 1.5. Spectrin assemblies are long filamentous structures which are resistant to stretching and ten-

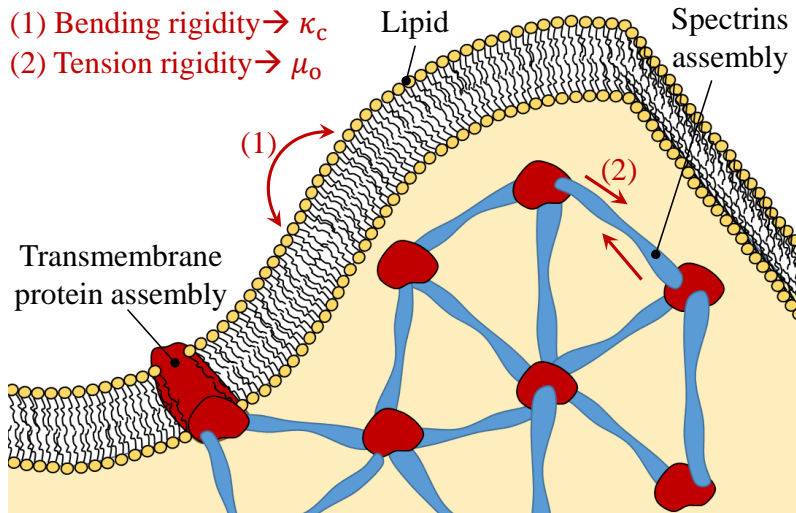


Fig. 1.5 RBC membrane structure. The schematic of a spectrin network connected to a fluid lipid bilayer is shown. The elasticity of the lipid bilayer results in a bending rigidity of the membrane, while the elasticity of spectrins results in their tension rigidity and a shear elasticity of the membrane.

sion, similar to ropes. The actin assemblies, are made of actins and other transmembrane proteins which diffuse in the bilayer and are connected to the spectrin. The spectrin network

does not withstand bending torques, but tolerates shear tension. On the other hand, the lipid bilayer is fluid and compliant to shear tension, while it has bending elasticity as discussed above. In effect, the RBC membrane can be modeled as a solid rather than a fluid membrane.

Since the spectrins might make a roughly homogeneous triangular network, they can be modeled by homogeneous bonds and vertices. The lipid bilayer, can also be modeled by tiling the surface with triangles. The bending energy must be discretized over the triangular network. The shear elasticity can be added to or removed from the system by respectively adding bond stiffness to or removing the bond potential from the bonds of the network.

1.6 Margination

VWF polymers are present in blood plasma. They flow together with RBCs and platelets through blood vessels. For hemostasis to happen, they must be close enough to the vessel walls in order to adhere to an injured surface; otherwise, they would not see the wound and would flow away not being used for hemostatic process. Large VWFs, which are necessary for blood clotting, and platelets flow close to the blood vessel walls because of a phenomenon called margination. The margination is mediated by RBCs. Since RBCs are highly deformable and soft membranes, they deform and tank-tread in flow within the blood vessel, and experience a hydrodynamic lift force which pushes them away from the vessel walls.

Dynamics of RBC membrane in flow such as tank-treading and tumbling, and the deformation of the membrane lead to a lift force. The tank-treading motion is the rotation of the membrane around its center of mass such as the tread of a tank. The tumbling motion is a rigid-body-like rotation of the membrane around its center of mass. The two dynamics have been observed for RBCs, vesicles, and even bubbles in experiments^{1,14,64,65}, simulations^{110,153,154,250}, and theory^{101,136,155,156,207}.

A very intuitive explanation for the lift force on flowing RBCs due to their tank-treading motion is achieved by supposing that the RBC membrane is like a tank-tread with several dents (or feet). In a fluid, when the membrane tank treads, it is like it is walking in the fluid. The tank-treading of the membrane in flow produces a high pressure at the locations close to the wall, which is higher than the fluid pressure. It is like that the membrane is pushing fluid to the wall and moving away from it. Then, high viscosity will help the membrane to move away from the wall by tank-treading. At low viscosity, tank-treading of the membrane does not produce a lift force. On the contrary, at high Reynolds numbers, it induces higher flow velocities close to the walls, and lower pressure thereafter which pushes the membrane to the wall than lifting it away from it. However, tank-treading may not occur at low Reynolds

numbers since it is shear-tension driven and shear tension is related to Reynolds number. Tumbling with deformation of the membrane, produces a lift force with a similar mechanism, where the whole membrane pushes fluid to the wall.

The pressure difference due to tank-treading and tumbling of membranes also depends on the shape of the membrane. If the membrane acquires more surface at the high pressure zone, the lift force would become larger. This idea is illustrated in Figure 1.6. It shows that RBC shape is advantageous for having a higher pressure close to the wall as well. Then, the lift force on RBCs is stronger than the lift force on vesicles or other cells in the blood. In consequence, RBCs in blood flow migrate to the center of the vessel and move away from the vessel walls.

While RBCs are lifted away from the wall, a RBC free layer (RBC-FL) is formed close to the wall. Within this layer, there is usually no RBC. The thickness of the RBC-FL depends mainly on the flow rate or pressure gradient¹⁰⁰, volume fraction of RBCs (hematocrit)^{56,223}, the size of the vessel⁵⁶, and the deformability of RBCs²⁵¹, as investigated in simulations^{56,100,251}, and both *in vivo*^{223,248} and *in vitro* experiments^{104,106}.

A result of the RBC migration is the change of blood viscosity by flowing through capillaries. It has been discovered by Fåhræus and Lindqvist⁵², and is called Fåhræus-Lindqvist effect. The Fåhræus-Lindqvist effect explains the shear-thinning of the blood by flowing through microvessels.

The migration of RBCs to the center of the vessels has another important effect on the microparticle distribution over the cross-section of blood vessels. The migration of RBCs to the center of the vessel leads to their collision with other blood components. By filling the majority of space at the center of the vessel, RBCs push the other blood components such as platelets, large VWFs, and even white blood cells to the walls. Consequently, the microparticles end up flowing in the RBC-FL where they do not collide with RBCs. This

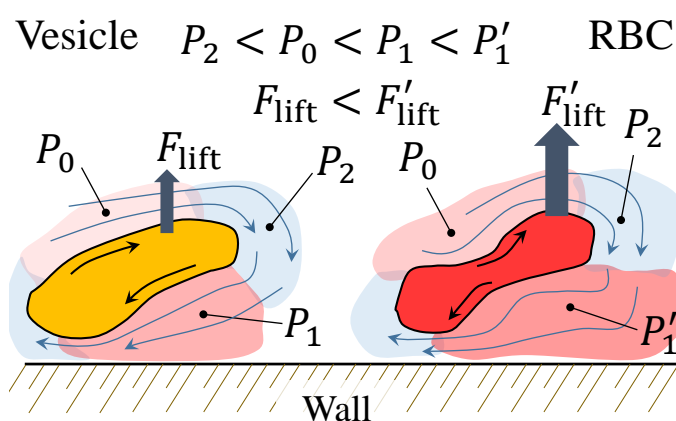


Fig. 1.6 Schematic of lift force. The illustration is inspired by Meßlinger et al. 2009¹³⁵. RBC shape and elasticity help them deform substantially and tank-tread in the flow. It will result in a high pressure close to the wall. Similarly for other cells and vesicles, the pressure difference lifts them away from the wall, however, their pressure difference and lift force are smaller than for RBCs.

process is called margination. Many simulation studies have been performed to understand the margination process and quantify it for particles with different sizes and shapes^{100,142,254,255}. It has been found that nanoparticles marginate much worse than microparticles^{140,144,227}. The margination of microparticles results from their collision with RBCs. Even large cells, like white blood cells marginate^{57,58,73,78,145}, but they cannot fit into the RBC-FL. Smaller particles, however, find enough space among RBCs so that they do not effectively marginate. Their distribution in the vessel is similar to the plasma distribution, filling the whole vessel homogeneously. Although most emphasis about margination has been on platelets and spherical micro-scale drug carriers so far, we have recently found that margination occurs for any microparticle, even for large VWF polymers¹⁷².

1.7 What has been done so far.

While there are very few studies of primary hemostasis *in silico*, plenty of simulations have been conducted regarding the prerequisite processes, such as margination, polymer dynamics, and adhesion in shear flow. In the following, a brief review about this research is provided.

The margination process came to the attention of scientific society after the Fåhræus effect⁵¹ had been discovered in 1929. Fåhræus found that RBCs migrate toward the center of a capillary tube when flowing through it, leaving a thin layer close to the walls, which is called RBC free layer (RBC-FL). Afterwards, related macroscopic aspects, such as a change of viscosity of blood stream through capillaries⁵² and the RBC-FL thickness¹⁶⁸, were studied and suggested to be the consequences of this effect. Another example of the Fåhræus effect was observed in the cross-sectional distribution of particles in capillaries. Margination of leukocytes^{12,62,152} and platelets^{221,222} had been observed in experiments. Soon after, the margination of platelets in arterioles and venules was distinguished in experiments²⁴³, and was related to the flow properties such as shear rate and hematocrit.

The margination process has also been investigated using various simulation techniques, such as immersed boundary method²³⁴, boundary integral method^{111,255}, dissipative particle dynamics^{140,172}, smoothed dissipative particle dynamics^{100,142}, Lattice-Boltzmann method^{133,175}, etc. Recently, predictive theories have been derived for the margination of micro-particles^{37,170}. Such migration behavior occurs not only for RBCs and other deformable cells or vesicles^{1,2,23}, but also for rigid elliptical particles^{96,99} that a margination (or sometimes segregation) takes place for rigid spheres with different sizes²⁵. Nevertheless, the biconcave shape and high deformability of RBCs is the main reason that other components, regardless of their size compared with RBCs, are pushed to the vessel wall. For example, leukocytes which are generally larger than RBCs, marginate^{57,73,78} as well

as small platelets. However, investigations show that nano-particles marginate worse than micro-particles^{117,140,227}.

Besides margination, polymer dynamics in shear flow is another important aspect of primary hemostasis, since only large VWFs have been found to provide the most efficient hemostatic activity^{36,176,183}. As discussed before, the activity of VWF depends on the extent of stretching in shear flow²¹³. Polymer dynamics in shear flow has been a subject to intensive investigations for quite a while, and valuable theories have been derived for the motion and dynamics of polymers in shear flow^{34,35}. Polymers behave differently under different flow conditions, such as shear^{116,210} and elongational^{159,211} flows, both of which are relevant for the blood flow and the behavior of VWF proteins. Experiments on VWF behavior in shear flow have shown that these polymers are collapsed to a globule at low shear rates, while strong enough shear forces lead to their stretching^{75,191}. A simple self-attractive polymer model⁶⁻⁸ has been shown to mimic the behavior of VWF polymers in shear flow very well¹⁹¹. Although, another more sophisticated model, a self-associating polymer^{5,199,200}, may represent more realistic characteristics of VWFs, both models reproduce the shear-sensitive stretching of the polymer in shear flow^{5,6,8,200}.

The adhesion of VWF polymers to substrates have been modeled, using the existing VWF polymer models⁸. The adhesion to the substrate has been modeled by a homogeneous attractive potential between polymer beads and an adhesive surface¹⁷³ or by specific bond interactions between polymer beads and adhesive sites on a surface^{174,203}. These models do not represent a realistic adhesive behavior for VWF, which must be triggered by shear stresses and its adhesion should be reversible. Recently, we proposed a shear-responsive polymer model which considers realistic activity of VWF, making a polymer adhesive in the stretched state and non-adhesive in the collapsed state⁸⁹. Such model successfully reproduces the adhesive behavior of VWF polymers⁸⁹. Similar to the adhesion of a single VWF polymer to an adhesive surface, the adhesion of platelets to VWFs is shear-dependent and reversible^{40,92,182,188}. An *in vivo* experiment on primary hemostasis shows that platelet aggregation takes place at high shear rates, like in stenosis, and the aggregates desorb reversibly when the flow conditions turn back to normal¹⁴⁶. Although the reversibility of VWF-platelet aggregation is achieved even without shear-sensitive activity²⁶, more details must be considered for polymer activity in order to properly mimic a firm adhesion at high shear rates and reversible desorption at low shear rates.

Many studies attempted to model the aggregation of platelets in the process of primary hemostasis, as reviewed by Fogelson and Neeves 2015⁷⁰ and Hosseinzadegan and Tafti 2017⁹⁰. A continuum-based immersed boundary method has been proposed for modeling aggregation of platelets to an adhesive wall under shear flow conditions^{68,69}, omitting the

presence of VWF polymers and RBCs. It predicts how the aggregates form on an adhesive surface at large scales of hundreds of micrometers. Another model, which assumes a homogeneous distribution of particles representing platelets, has been introduced and platelet aggregation on an adhesive surface has been studied¹⁶³. The particles in such model are under a force field¹³¹ similar to sedimenting particles. The aggregation takes place based on three different states considered for platelets: passive, triggered, and activated. Similarly, several other models and theories have been proposed^{132,245,246,249}, many of which omit the margination process, by ignoring RBCs or assuming unrealistic RBC models, and neglect an explicit model for the shear-sensitive VWF polymers. Consequently, there is a lack of multi-component models which include a realistic behavior of RBCs and shear-activated VWF polymers.

1.8 Outline

The contents of all chapters in this thesis are independent of each other. Because the models, simulation setup, and preliminary biological informations are different for each chapter, the introduction section of each chapter provides all necessary information independently.

The chapters are categorized into five parts based on their theme. [Part I](#) concerns the margination process in blood flow. The margination of VWFs, in addition to the well-known margination of platelets is studied. Also, a novel idea is proposed which is correlated to the Fåhræus effect, but reverse it, and is always valid even for larger diameters of blood vessels in contrast to the Fåhræus effect. [Part II](#) includes two chapters regarding the adhesion of VWF polymers. The adhesion of a single VWF polymer to an adhesive substrate, in the presence of flow and in absence of it is studied. The adhesive behavior of VWF is calibrated with the results of the experiments on single VWF polymers. It is shown that the aggregation of platelets to VWFs occurs at high shear rates, when VWFs are stretched. Such aggregates dissolve at low shear rates because VWF ligands get shielded when VWF chains collapse into globules. Two important characteristics of VWF polymers are introduced, affinity - the likelihood of adhesion for single ligand-receptors, and avidity - the number of active ligands in a VWF chain. In [Part III](#), the aggregation of platelets and VWFs in blood flow is studied. A very important question is answered; while VWFs marginate and stretch in the RBC-FL, they become active and can initiate thrombosis even in absence of injury. Moreover, some thrombi or a part of them may detach from the injured site and get into the blood flow. It is explained that once aggregates get into the flow, they demarginate - migrate to the center of the vessel, and dissolve at lower shear rates there. Then, the dissociated platelets and VWFs remarginate back into the RBC-FL. In addition, a systematic study on aggregate dynamics

in blood flow and primary hemostasis is performed. [Part IV](#) studies VWF cleavage by its protease, ADAMTS13, as a regulation of VWF sizes and aggregate formation. A model for VWF cleavage is proposed. The size distribution of degrading polymers, such as VWFs, is analyzed by a theoretical model. The last part of the thesis, [Part V](#), concerns the aggregation of RBCs which occurs at low shear rates. RBC doublet phases, as a function of the adhesion strength and membrane elasticity are investigated. The thesis concludes with suggestions and ideas for future works.

Chapter 2

Models and Methods

Many mesoscale simulations in this thesis employ our in-house version of the highly parallel molecular dynamics simulation package, LAMMPS¹⁶⁴ (<http://lammps.sandia.gov>). The simulations include membrane models for RBCs and platelets, fluid models for hydrodynamic interactions, and a polymer model for VWFs.

Figure 2.1 illustrates the schematics of the membrane, polymer, and fluid models used for 2D and 3D simulations.

2.1 Membranes

Membranes are modeled by a triangulated mesh with visco-elasticity, bending rigidity, area and volume conservation^{54,55,120,244}. The elasticity of the membrane is represented by the worm-like chain (WLC) bonds between membrane vertices and a repulsive potential to impose a nonzero equilibrium bond length⁵⁵. The WLC potential is given by

$$U_{\text{WLC}}(x) = \frac{k_{\text{B}} T l_{\text{max}}}{4\xi_{\text{p}}} \frac{3x^2 - 2x^3}{1 - x}, \quad (2.1)$$

where l_{max} and ξ_{p} are respectively the maximum length and persistence length, and $x = l/l_{\text{max}}$ where l is the current bond length. The WLC model is an appropriate representation of polymer chains¹⁶² such as spectrins underneath the lipid bilayer.

A repulsive potential is imposed to the vertices to set a non-zero equilibrium length of the bonds and compensate for purely attractive WLC potential. The repulsive potential is

$$U_{\text{POW}}(l) = \frac{-k_{\text{p}}}{1 - \alpha} l^{(1-\alpha)}, \quad (2.2)$$

where α is a positive number ($\alpha \neq 1$) and k_p is the repulsive force coefficient⁵³. The resultant force from this potential would be $F = k_p l^{-\alpha}$. The shear modulus, μ_o , is derived from these potentials⁵³.

The bending rigidity of membranes is modeled by the bending potential

$$U_b(\theta) = \kappa_b (1 - \cos(\theta - \theta_0)), \quad (2.3)$$

in which κ_b is the bending constant. θ is the instantaneous angle between the normals of two adjacent triangles sharing a bond, and θ_0 is the spontaneous angle. κ_b determines the bending rigidity of the membrane. For a spherical membrane, the bending energy for all pairs of triangles is nearly the same so that the whole bending energy of the sphere can be computed as a product of the number of adjacent triangle pairs (equal to the number of bonds) and the energy of a single pair. Providing that the bending energy of a sphere is known from the Helfrich model of membrane bending, to be $8\pi\kappa_c$, the bending rigidity of the membrane κ_c is related to the bending constant κ_b via $\kappa_c = \kappa_b \sqrt{3}/2$ ^{19,55,80,121}. Note that Equation (2.3) is not a very reliable discretization of Helfrich's bending energy; however, it is a sufficient model for the RBCs with large shear elasticity. More details about the bending models are provided in [chapter 11](#).

For area conservation, a harmonic potential is assigned for global and local area changes as

$$U_{\text{area}} = \frac{1}{2} k_a \frac{(A - A_0)^2}{A_0} + \sum_{\text{triangles}} \frac{1}{2} k_d \frac{(A^{\text{loc}} - A_0^{\text{loc}})^2}{A_0^{\text{loc}}}, \quad (2.4)$$

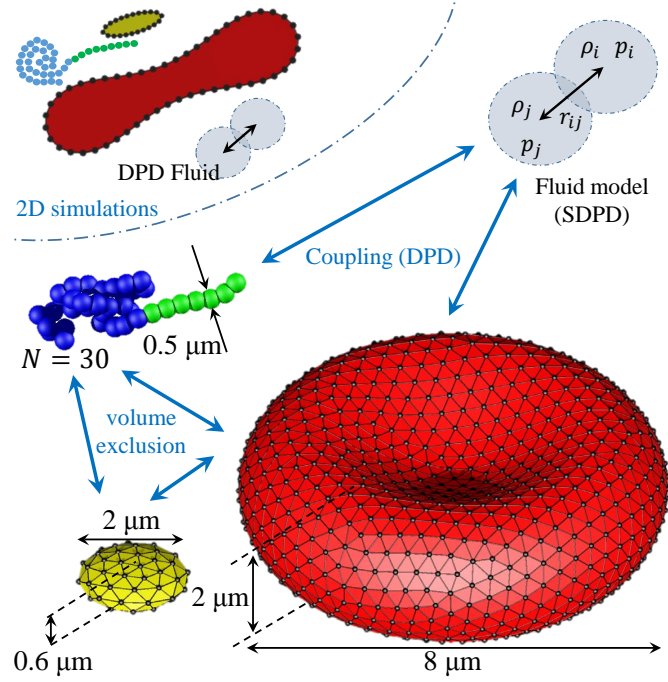


Fig. 2.1 Schematics of the models used in the 2D and 3D simulations. The membrane vertices are shown with smaller beads than their actual size for more clarity. The 2D membranes have similar dimensions with their 3D counterparts.

where A is the total area of the membrane and A^{loc} is the area of each triangle. Similarly for volume conservation, we have

$$U_{\text{volume}} = \frac{1}{2} k_v \frac{(V - V_0)^2}{V_0}, \quad (2.5)$$

in which the subscript 0 refers to the equilibrium value.

The membrane viscosity is modeled by a pair of dissipative and random forces applied on the vertices sharing a bond⁵⁸,

$$\mathbf{F}_{ij}^D = -\gamma^T \mathbf{v}_{ij} - \gamma^C (\mathbf{v}_{ij} \cdot \mathbf{e}_{ij}) \mathbf{e}_{ij}, \quad (2.6)$$

$$\tilde{\mathbf{F}}_{ij} = \sqrt{2k_B T} \Delta t^{-1} \left(\sqrt{2\gamma^T} d\mathbf{W}_{ij}^S + \frac{1}{3} \sqrt{3\gamma^C - \gamma^T \text{tr}[d\mathbf{W}]} \mathbb{1} \right) \cdot \mathbf{e}_{ij}, \quad (2.7)$$

where γ^T and γ^C are the translational and central dissipative coefficients, $\mathbf{v}_{ij} = \mathbf{v}_i - \mathbf{v}_j$ is the relative velocity between bound vertices and $\mathbf{e}_{ij} = \mathbf{r}_{ij}/r_{ij}$ is the unit vector in the direction of the bond. $d\mathbf{W}$ is a matrix with the independent Wiener process increments, $d\mathbf{W}_{ij}$, and $d\mathbf{W}^S$ is the traceless symmetric part of the Wiener process matrix. $\mathbb{1}$ is the unitary tensor.

Setting the spontaneous angle to zero (flat membrane as an equilibrium state) and defining the reduced volume to be $v = \frac{6\sqrt{\pi}V}{A^{3/2}} = 0.64$, a biconcave discocyte shape becomes the rest shape of RBCs in equilibrium. For platelets, the spontaneous curvature is set equal to the local curvature of a predefined oblate sphere with one micron radius and aspect ratio $\lambda = 0.3$, so that it keeps its shape. The membrane properties are tabulated in Table 2.1.

For volume exclusion between membranes of different RBCs in case they collide, their vertices interact via Lennard-Jones potential

$$U_{\text{LJ}}(r) = 4\epsilon_{\text{LJ}} \left[\left(\frac{\sigma_{\text{LJ}}}{r} \right)^{12} - \left(\frac{\sigma_{\text{LJ}}}{r} \right)^6 \right], \quad (2.8)$$

where ϵ_{LJ} and σ_{LJ} are the energy and characteristic length of the LJ interaction. Setting the cutoff radius of the potential at the minimum energy, i.e. $r_{\text{cut}} = \sqrt[6]{2}\sigma_{\text{LJ}}$, only the repulsive part of the potential is taken into account. The discontinuity of the repulsive LJ energy can be solved by shifting the potential with ϵ_{LJ} value to get zero energy at the cutoff radius. The LJ interaction is applied to all particle types in order to avoid overlapping. The used values for the LJ parameters are tabulated in Table 2.5, as will be explained shortly.

Table 2.1 Membrane properties. τ is the RBC relaxation time $\tau = \eta D_{\text{eff}}^3 \kappa_c^{-1}$, η being the viscosity of the fluid and D_{eff} being the effective diameter of RBCs. The subscript RBC refers to the quantities belonging to RBCs.

Type	RBC	platelet	Description
N_v	500	60	number of vertices
A_0 (μm^2)	132.8	6.86	equilibrium surface area
V_0 (μm^3)	92.5	1.12	equilibrium volume
D_{eff} (μm)	6.5	1.48	effective diameter $D_{\text{eff}}^2 = \frac{A_0}{\pi}$
$\kappa_c / k_B T$	70	7,000	bending rigidity
$\mu_o (D_{\text{eff}}^3 / \kappa_c)_{\text{RBC}}$	4,160	41,600	shear modulus
$k_a (D_{\text{eff}}^2 \kappa_c^{-1})_{\text{RBC}}$	29,600	296,000	global area rigidity
$k_d (D_{\text{eff}}^2 \kappa_c^{-1})_{\text{RBC}}$	604	6,040	local area rigidity
$k_v (D_{\text{eff}}^3 \kappa_c^{-1})_{\text{RBC}}$	196,200	1,962,000	global volume rigidity
$\gamma^T (D_{\text{eff}} \tau^{-1} \kappa_c^{-1})_{\text{RBC}}$	5.25×10^{-2}	5.25×10^{-2}	translational mem. viscosity
$\gamma_c (D_{\text{eff}} \tau^{-1} \kappa_c^{-1})_{\text{RBC}}$	1.58×10^{-1}	1.58×10^{-1}	central mem. viscosity

2.2 Fluid model for hydrodynamic interactions

There are a number of mesoscopic methods for modeling fluid flow, such as the lattice Boltzmann method (LBM)²¹⁷, multi-particle collision dynamics (MPC)^{79,129}, dissipative particle dynamics (DPD)^{46,88}, and the smoothed DPD (SDPD)^{45,141} method. We employ the SDPD method^{45,141}, which is derived from the smoothed particle hydrodynamics (SPH)^{127,139} and DPD^{46,88} methods and combines their main advantages, such as direct connection to Navier-Stokes equations and consistent thermal fluctuations^{44,237}. In SDPD, a simulated system consists of a collection of fluid particles which represent small fluid volumes. Particles interact locally through three forces (conservative, dissipative, and random), which vanish beyond a cutoff radius r_c . The dynamics of SDPD particles is governed by Newton's second law of motion. The SDPD method parameters used in simulations are given in Table 2.2. In the SDPD method, the equation of state can be prescribed, allowing the control of fluid compressibility. In particular, this affects the flow Mach number defined as $M = \dot{\gamma} l / c$, where $\dot{\gamma}$ is the shear rate, l is the length scale, and c is the speed of sound ($c^2 = \partial p / \partial \rho$). For the parameters in Table 2.2, the Mach number in our simulations is smaller than 0.16, remaining within the incompressible flow regime. Another important parameter characterizing the flow is Reynolds number defined as $\text{Re} = \rho \dot{\gamma} l^2 / \eta$, where ρ is the fluid density and η is the dynamic viscosity. For this physical system $\text{Re} \sim 3 \times 10^{-3}$ at the shear rate of $\dot{\gamma} \sim 10^4 \text{ s}^{-1}$. In simulations, the Re number is chosen to be about ten times larger for computational efficiency; however, we have verified that it is still small enough to remain within the Stokes regime.

In contrast to the DPD method, SDPD directly satisfies Navier-Stokes equations so that the fluid properties such as viscosity, density, and pressure can be directly set in a simulation, while the fluctuation-dissipation theorem is satisfied via the random force term similar to DPD⁴⁴.

Full descriptions of the DPD method have been provided by Hoogerbrugge and Koelman 1992⁸⁸, Español and Warren 1995⁴⁶, and Groot and Warren 1997⁸⁴, and the SDPD method is described by Español and Revenga 2003⁴⁵, Müller et al. 2015¹⁴¹, and Ellero and Español 2018⁴⁴ in more detail. Here, a brief description of the SDPD method is provided.

A volume, mass, density, and pressure are assigned to each SDPD particle. The density of each particle depends on its overlapping neighbors with mass m_j as

$$\rho_i = \sum_j m_j W(r_{ij}), \quad (2.9)$$

where $W(r_{ij})$ is a kernel function which determines how the particle interaction is distributed in space. The kernel function is normalized to unity by integrating over the whole space, $\int_0^\infty W(r)dr = 1$. For computational convenience, the kernel function $W(r)$ is cut off at $r = r_c$. A positive function $F_{ij} \geq 0$ is introduced such that $\nabla_{\mathbf{r}_{ij}} W(r_{ij}) = -\mathbf{r}_{ij} F_{ij}$ ⁴⁵, where $\mathbf{r}_{ij} = \mathbf{r}_i - \mathbf{r}_j$. The kernel is supposed to be the Lucy function¹²⁷ in standard SDPD method proposed by Español and Revenga⁴⁵.

The SDPD force on each fluid particle is split into a conservative force,

$$\mathbf{F}_{ij}^C = \left(\frac{p_i}{\rho_i^2} + \frac{p_j}{\rho_j^2} \right) F_{ij} \mathbf{r}_{ij}, \quad (2.10)$$

a translational dissipative force as in Equation (2.6), a rotational dissipative force,

$$\mathbf{F}_{ij}^R = -\frac{\gamma^T}{2} \mathbf{r}_{ij} \times (\boldsymbol{\omega}_i + \boldsymbol{\omega}_j), \quad (2.11)$$

Table 2.2 SDPD fluid properties. The unit length l and unit mass m are taken as unity and $k_B T = 0.4$ in the simulations. The conversion to physical units must be done using length $l = 1 \mu\text{m}$, temperature $k_B T = 1.38 \times 10^{-23} \times 300 \text{ J}$, and an appropriate time scale in the simulation which is chosen here as the relaxation time of RBCs, $\tau = \eta D_{\text{eff}}^3 \kappa_c^{-1}$. The time scale τ is 0.95 s in physiological conditions and 3923 in simulations. More details on SDPD equations are provided by Español and Revenga 2003⁴⁵ and Müller et al. 2015¹⁴¹.

Type	Value	Description
ρ_0	$3 \frac{m}{l^3}$	ref. density
p_0	$250 \frac{k_B T}{l^3}$	ref. pressure
$\beta = 7, b = -p_0$	$p = p_0 \left(\frac{\rho}{\rho_0} \right)^\beta + b$	Eq. of state
η	$125 \sqrt{m k_B T} / l^2$	viscosity
r_c	$1.5l$	cutoff

and a random force exactly similar to Equation (2.7). The dissipative coefficients are assumed to be

$$\gamma^T = \gamma^C = \frac{20\eta}{7} \frac{F_{ij}}{\rho_i \rho_j}. \quad (2.12)$$

The SDPD fluid parameters are tabulated in Table 2.2.

2.3 Polymer model

VWF polymers which are efficient in hemostasis are long around tens of micrometers²¹³. One long chain of VWF comprises several VWF dimers linked to each other end-to-end. As only large micro-scale VWFs actively play role in aggregation and hemostasis¹⁷⁶, and as only large VWFs marginate to the RBC-FL^{140,172}, the large VWFs with lengths of several microns are considered for the simulations, omitting short VWF chains.

VWF polymers are represented by N beads bound to their adjacent neighbors with finite extensible nonlinear elastic (FENE) potential¹⁰⁹,

$$U_{\text{FENE}}(r) = -\frac{k_{\text{FENE}} r_{\text{max}}^2}{2} \ln \left[1 - \left(\frac{r}{r_{\text{max}}} \right)^2 \right], \quad (2.13)$$

where r , k_{FENE} , and r_{max} are respectively the distance between two bound beads, the FENE bond stiffness, and the maximum extension of the bond. The FENE potential is relatively stiff and prohibits polymer extensions beyond the contour length. For volume exclusion, the LJ potential in Equation (2.8) is applied to all pairwise interactions among the beads of the same polymer. The repulsive part of LJ potential provides volume-exclusion, while its attractive part draws the polymer chain into a globule. The polymer then remains globular at low shear rates and stretches at high shear rates. Such model first proposed by Alexander-Katz and Netz^{6,8,9} is extensively used for studying VWF dynamics in shear flow^{94,125,174,198} and is experimentally verified¹⁹¹. Nevertheless, another model has been proposed for specific self-association of polymer which leads to a similar stretching behavior^{5,199,200}. Table 2.3

Table 2.3 Polymer properties.

Type	Value	Description
N_{bead}	30	number of beads
ϵ_{LJ}	$4 k_B T$	LJ energy unit
σ_{LJ}	$0.5 l$	LJ length unit
r_c^{LJ}	$2.5 \sigma_{\text{LJ}}$	intra-molecular LJ cutoff
r_c^{LJ}	$\sqrt[6]{2} \sigma_{\text{LJ}}$	inter-molecular LJ cutoff
k_{FENE}	$25000 k_B T / l^2$	FENE bond stiffness
r_{max}	$2 \sigma_{\text{LJ}}$	max. FENE bond extension
L_{VWF}	$14.5 \mu\text{m}$	length, $(N_{\text{bead}} - 1) \sigma_{\text{LJ}}$

outlines the properties for the polymer model calibrated with experiments^{89,94} (see also Table 2.5).

2.4 Polymer activity

The adhesive ligands of VWF polymers are shielded in the collapsed conformation preventing their adhesion to platelet receptors or collagen^{11,75,128,130,213,231}. In the coarse-grained model of VWF polymer, each polymer bead represents many VWF dimers which contain several adhesive domains. In order to have an appropriate model for adhesive behavior of each bead, two geometrical criteria are considered⁸⁹. Accordingly, the bead whose bonds make an angle larger than a threshold angle, and which is not surrounded by other beads inside a threshold radius is considered to be active. Imposing these criteria for polymer activity, provides a VWF model with a similar adhesive behavior as observed in experiments⁸⁹. The two criteria are formulated as

$$\text{i'th bead active} \begin{cases} \theta_{(i-1)i(i+1)} \geq \theta_{\text{thres}} & 1 < i < N_{\text{beads}} \\ r_{ij} \geq R_{\text{thres}} & j \neq i, i \pm 1 \end{cases}. \quad (2.14)$$

The threshold radius R_{thres} is set to $1.2\sigma_{\text{LJ}}$ ($1.1\sigma_{\text{LJ}}$ in 2D) and the threshold angle θ_{thres} is set to 150° . The polymer activity in this model closely agrees with experiments^{75,89} (see also chapter 6).

Table 2.4 Adhesive bond properties for the two-pathway model.

Type	Value	Description
k_{on}	$10^3 \tau^{-1}$	on-rate
r_{c}^{on}	$1.1 \sigma_{\text{LJ}}$	cutoff for association
k_{c}^{o}	$10^{-1} \tau^{-1}$	catch-bond off-rate
k_{s}^{o}	$10^{-4} \tau^{-1}$	slip-bond off-rate
x_{c}	$0.625 \sigma_{\text{LJ}}$	catch-bond charac. length
x_{s}	$1.075 \sigma_{\text{LJ}}$	slip-bond charac. length
l_{eq}	σ_{LJ}	equilibrium bond length
$f(x)$	$-k_{\text{eff}}(x - l_{\text{eq}})$	adhesive bond force
k_{eff}^*	$2500 k_{\text{B}} T l^{-2}$	effec. adhes. bond stiffness
*: The actual bond stiffness is calibrated with the experiments as $40k_{\text{eff}}$ for VWFs and $10k_{\text{eff}}$ for platelets while only slip-bond term is considered for platelet interaction with the adhesive ligands on the wall (see chapter 6).		

2.5 Adhesive bonds

The adhesive bonding between platelet vertices, considered as a set of receptors, and VWF beads obeys a standard reaction formulated as



where k_{on} and k_{off} are association rate (on-rate) and dissociation rate (off-rate). The on-rate generally depends on how close the ligand and receptors are and on the properties of the medium such as pH, temperature, pressure, etc. It is usually assumed to be constant. The more sophisticated parameter is the off-rate which depends on the ligand and receptor molecular structure. Intuitively, the lifetime of the bond decreases as the dissociating force on the bond increases. However, it has been discovered recently that many biological bonds behave differently^{108,225}. Such behavior was first suggested by Dembo et al. 1988³⁸ and named as a catch-bond in contrast to the slip bond. Since every bond must finally detach by increasing the force, pure catch bonds do not exist. Therefore, catch bonds change to slip bonds at some point as force increases and therefore, catch-slip bond is an appropriate name for such bonds.

The interaction between VWF ligand and platelet receptor is found to be of catch-bond kind^{40,103,247}. The two-pathway model^{157,158} for catch-slip bonds represents such behavior well. The two-pathway model is similar to the well-known Bell model¹⁸, but contains two parts, as formulated below¹⁶⁷.

$$k_{\text{off}} = k_{\text{c}}^{\text{o}} \exp\left(\frac{f(x_{\text{c}} - l_{\text{eq}})}{k_{\text{B}}T}\right) + k_{\text{s}}^{\text{o}} \exp\left(\frac{f(x_{\text{s}} - l_{\text{eq}})}{k_{\text{B}}T}\right) \quad (2.16)$$

Table 2.4 provides the parameters used for the catch-slip bond model for VWF-platelet and VWF-surface interactions. The adhesive bond model is thoroughly explained in [chapter 5](#).

2.6 Coupling and boundary conditions

The coupling of SDPD fluid to membranes and polymer beads is accomplished by simple DPD interaction without the conservative force. The strength of this DPD interaction depends on the surface number density of the membrane vertices (linear number density of beads for the polymer) n_{m} , the fluid number density n , the fluid viscosity η , the pair correlation function of fluid particles $g(r)$, and the weight function (kernel) of DPD dissipative force w_{D} ⁸⁴. Assuming a flat surface of membrane immersed in the fluid, the theoretical shear force

on it is $A\dot{\gamma}\eta$ where A is the area of the membrane. This theoretical force must be equal to the resultant dissipative force from the fluid formulated as $N \iiint_{V_h} ng(r)F_D^{\parallel} dv$, where V_h is the volume of the hemisphere above the membrane with the origin at each vertex⁵⁴. Here, N denotes the number of vertices on the membrane (or beads of the polymer), and F_D^{\parallel} is the parallel-projection of the pairwise DPD dissipative force. It is supposed that $g(r) \approx 1$ since the conservative force is turned off for the coupling. Finally, this calculation results in the coupling DPD strength as

$$\gamma_D = \frac{4\eta}{\pi n_m n Q}, \quad (2.17)$$

where $Q = \int_0^{r_c} w_D r^3 dr$. Similarly for polymers, the strength of DPD interaction can be calculated.

In this work, no distinction between the inner and outer fluid surrounding the membranes is made. The membranes are thus transparent to the fluid. Such assumption omits the fact that inner fluid has different viscosity than the outer fluid because of the cytoplasm, but the collective dynamics of RBCs in blood flow remains similar. In consequence, the transparent model is chosen as a much faster simulation scheme.

Table 2.5 LJ interaction properties.

Pairwise interaction	σ_{LJ}	ϵ_{LJ}	r_{cut}
pol.-pol. (intra-mol)	$0.5 \, l$	$4 \, k_B T$	$1.5 \, l$
pol.-pol. (inter-mol)	$0.5 \, l$	$4 \, k_B T$	$0.5612 \, l$
pol.-mem. vert.	$0.4 \, l$	$2.5 \, k_B T$	$0.4490 \, l$
mem. vert.-mem. vert.	$0.3 \, l$	$2.5 \, k_B T$	$0.3367 \, l$

The pairwise LJ interaction is not applied to the particles which share a bond if the volume exclusion is already applied in the bond potential. The surface area of the membranes and their number of vertices define the size of vertices, $\sigma_{LJ} = (2A/\sqrt{3}(N_v - 2))^{1/2}$.

In addition to friction forces, the membranes and polymers must not overlap. To this end, the repulsive part of the LJ potential is set between all vertices and beads. The LJ characteristic length σ_{LJ} is set depending on the particle sizes. The size of the polymer beads, and membrane vertices is defined by their equilibrium bond length. Table 2.5 gives a summary on the LJ interactions used in simulations.

The periodic boundary condition is assigned for the boundaries in the flow direction (x -direction), and in the vorticity direction (z -direction). The velocity gradient direction is bound by solid walls. The solid walls contain frozen particles from the same SDPD fluid in equilibrium, possessing the same radial distribution function, and density. The wall particles interact with SDPD fluid particles, but they are fixed. For pressure-driven Poiseuille flow, the fluid particles in the channel are under a constant force in the axial direction. For simple shear flow, wall particles are moved in opposite directions, inducing shear stress on the system.

The particles hitting the wall are bounced back, and an adaptive shear force is added to the SDPD particles to maintain no-slip boundary conditions at the walls^{59,119}.

2.7 2D simulations

A systematic investigation of all the parameters for blood flow in 3D is very expensive computationally, regarding that each 3D simulation of blood flow is a very large parallel simulation by itself. 2D simulations come useful in such cases. Omitting one dimension decreases the complexity of the problem by at least one order of magnitude, so that a systematic study of all parameters of the system becomes affordable.

In contrast to triangulated membranes in 3D, the RBCs and platelets are represented by closed chains of polymer beads. κ_c , as the bending rigidity of a polymer chain in 2D, is implemented to a pair of adjacent bonds through an angle potential. The volume conservation is changed to area conservation, while the area conservation is changed to circumference conservation. The polymer model remains the same. The fluid model is changed to simple DPD with a larger density to increase fluid incompressibility. Table 2.6 summarizes the 2D simulation parameters.

The fluid model in 2D corresponds to the simple DPD⁸⁴, with a dissipative coefficient γ^T resulting in the macroscopic viscosity η . The parameters not presented in Table 2.6 have the same value as in 3D. The coupling in Equation (2.17) changes to $\gamma_D^{2D} = 3\eta(2nn_m Q^{2D})^{-1}$,

Table 2.6 2D simulation parameters compared to their 3D counterparts. All other parameters are equal to their 3D counterparts.

Type	Model	Properties	
Fluid	DPD	thermal energy $k_B T$	1.0
		viscosity η	$144.4 \sqrt{mk_B T} / l$
		dissip. coef. γ^T	$20.0 \sqrt{mk_B T} / l$
		number density n	$5.0 l^{-2}$
		conserv. force const. a	$40.0 k_B T / l$
		cutoff r_c	$1.5 l$
Membrane/polymer	closed/open pol.	LJ energy $\varepsilon / k_B T$	1.0
		N_{bead} (RBC/pl./VWF)	50/22/40
		length (RBC/pl./VWF)	19.2/4.3/15.6 l
		area (RBC/pl.)	13.6/0.92 l
		σ_{LJ} (RBC/VWF)	0.4 l
		σ_{LJ} (pl.)	0.2 l
		σ_{LJ} (pl. with RBC/VWF)	0.3 l
		$\kappa_c / k_B T$ (RBC/pl.)	20/2000
		$k_v D_{\text{eff}}^2 \kappa_c^{-1}$ (RBC/pl.)	1,900/9.4
		$k_a D_{\text{eff}} \kappa_c^{-1}$ (RBC/pl.)	306/6.84
		$\mu_0 D_{\text{eff}}^2 \kappa_c^{-1}$ (RBC/pl.)	2800/13.9

where $Q^{2D} = \int_0^{r_c} w_D r^2 dr$. The time scale in 2D is $\tau = \eta D_{\text{eff}}^2 \kappa_c^{-1}$, where $D_{\text{eff}} = L/\pi$. For 2D simulations, k_v and k_a are area and circumference conservation strengths, respectively.

Part I

Margination in Blood flow

Chapter 3

Margination of von Willebrand factor in the blood stream

The protein von Willebrand factor (VWF) is essential in primary hemostasis, as it mediates platelet adhesion to vessel walls. VWF retains its compact (globule-like) shape in equilibrium due to internal molecular associations, but is able to stretch when a high enough shear stress is applied. Even though the shear-flow sensitivity of VWF conformation is well accepted, the behavior of VWF under realistic blood flow conditions remains poorly understood. We perform mesoscopic numerical simulations together with microfluidic experiments in order to characterize VWF behavior in blood flow for a wide range of flow-rate and hematocrit conditions. In particular, our results demonstrate that the compact shape of VWF is important for its migration (or margination) toward vessel walls and that VWF stretches primarily in a near-wall region in blood flow making its adhesion possible. Our results show that VWF is a highly optimized protein in terms of its size and internal associations which are necessary to achieve its vital function. A better understanding of the relevant mechanisms for VWF behavior in microcirculation provides a further step toward the elucidation of the role of mutations in various VWF-related diseases.

3.1 Introduction

The blood Glycoprotein von Willebrand factor (VWF) is involved in hemostasis, as it mediates platelet adhesion at vessel walls in case of an injury^{134,213}. VWF can bind flowing platelets and withstand very high shear forces¹⁷⁷, an essential aid at high shear rates where platelets cannot bind autonomously^{188,190}. Multimeric VWF is the largest protein in blood, with a contour length reaching up to 250 μm ^{41,213}. VWF is stored at and released from

endothelial cells and is present freely floating (called plasmatic VWF) in blood. The release of stored VWF can be triggered by the signals of a vascular damage or in certain blood diseases¹⁷⁶. Stored VWF is often much longer than plasmatic VWF, since the length of plasmatic VWF is controlled by the ADAMTS13 protease, which is able to cut a VWF-chain if a cleavage site is exposed^{42,184,253}. Various VWF dysfunctions can lead to uncontrolled bleeding as in the von Willebrand disease (VWD)^{76,186,192} or to spontaneous thrombotic events¹⁹². In addition to the pivotal role of VWF in hemostasis, there is a growing evidence that VWF plays an important role in cancer^{16,72}.

Several experimental studies^{13,137,181} have focused on adhesion of platelets to VWF, suggesting that the adhesion depends strongly on the shear rate and the length of VWF. These studies also indicate that with increasing shear rate, a conformational change of VWF occurs both at a dimeric level (opening-up of the dimer structure)^{103,213} and multimeric level (stretching of VWF from a compact globule-like form to an extended chain form)¹⁹¹, and is accompanied by an increased platelet adhesion. Recent experiments¹⁹¹ and simulations⁸ for a single VWF in shear flow have shown that the extension of VWF is shear-rate dependent and that VWF stretches above a critical shear rate of several thousand s^{-1} ¹⁹¹. A mixture of VWF and platelets has been found to exhibit the formation of reversible aggregates at high shear rates, which disappear when the shear rate is decreased^{26,92}. However, there is still no comprehensive picture of VWF behavior in the microcirculation, where various flow rates and hematocrit values H_t (the volume fraction of red blood cells (RBC)) are encountered.

The distribution and stretching of VWF under realistic blood-flow conditions are important for understanding its behavior in the microvasculature. Several experimental^{3,215} and numerical^{102,233} studies have shown that flexible polymers in a dilute suspension are subject to cross-stream migration in Couette and Poiseuille flow. Furthermore, platelets²²¹ and micro-particles^{117,140} are known to marginate (i.e., migrate toward vessel walls) in blood flow. Margination of spherical micron-size particles is mediated by RBCs, which migrate to the center of a vessel due to both hydrodynamic interactions with the walls (also called lift force)^{1,23,135} and asymmetric collisions of non-spherical and deformable objects under flow¹¹² leading to a RBC-free layer (RBC-FL) near the walls⁵⁶ and expelling the particles into the RBC-FL. Particle deformation generally results in less margination in blood flow¹⁴². Thus, a detailed understanding of the margination and extension properties of large VWF multimers under realistic microcirculatory conditions is required for the interpretation of their adhesive behavior.

In this chapter, we study margination and stretching of large multimeric VWFs for a wide range of flow rates and H_t values using mesoscopic hydrodynamic simulations, and consistently link the obtained picture of VWF behavior in blood flow to our microfluidic

experiments on VWF margination and adhesion. We find that large multimeric VWFs mainly retain their compact shape within the blood-flow core populated primarily by RBCs, and that this compact configuration facilitates their efficient margination into the RBC-FL. After margination, VWF stretches in the RBC-FL near a wall, thereby facilitating the adhesion to the vessel wall. VWF margination and extension have a non-trivial dependence on flow rate, H_t , and the contour length of VWF. The proposed dynamics of VWF in blood flow obtained from simulations is consistent with our experimental observations and provides an excellent explanation for VWF adhesion with respect to various investigated conditions. Our findings are also relevant for VWF-pertinent blood diseases resulting from various VWF mutations.

3.2 Setup

The simulation setup consists of a single channel of a cylindrical shape in 3D with a diameter $W = 20 \mu\text{m}$ and a length $L = 12.3 D_{\text{eff}}$. In 2D, we use slit geometry with a width $W = 20 \mu\text{m}$ and a length $L = 28.6 D_{\text{eff}}$. The channel is filled with fluid particles and with suspended VWFs and RBCs. The number of RBCs is determined by the selected hematocrit, which corresponds to the volume fraction of RBCs in 3D and to the area fraction of RBCs in 2D. For both 3D and 2D simulations the number of VWFs is $N_{\text{VWF}} = 6$. The volume fraction of VWFs remains very small in all simulations such that the effect of concentration on its behavior can be neglected.

In the flow direction, periodic boundary conditions (BCs) were imposed, while in the other directions the suspension was confined by walls. The walls are modeled by frozen fluid particles with the same structure as the fluid. Thus, the interactions of fluid particles with wall particles are the same as fluid-fluid interactions, and the interactions of structures with the wall are identical to those with a suspending fluid. To prevent wall penetration, fluid particles as well as vertices of RBCs and beads of VWFs are subject to reflection at the fluid-solid interface. We employed bounce-back reflections, because they provide a better approximation for the no-slip boundary conditions than specular reflection of particles. To ensure that no-slip BCs are strictly satisfied on the walls, we also add a tangential adaptive shear force¹⁴¹ which acts on the fluid particles in a near-wall layer.

3.3 VWF model

As proposed by Alexander-Katz et al. 2006⁸ and Alexander-Katz and Netz 2008⁶, the VWF is modeled as a self-avoiding bead-spring chain with intramolecular attractive interactions and a monomer radius a_m . The resultant potential for polymer beads is the superposition of a harmonic bond potential, with stiffness k_s and equilibrium bond length $l_b = 2a_m$, and an attractive Lennard-Jones (LJ) pairwise potential with $\sigma = l_b$ and $\varepsilon = 4k_B T$; this value is a result of the calibration of a critical shear rate for polymer stretching in 3D against experimental data reported by Schneider et al. 2007¹⁹¹ shown in Figure 3.1. In 2D, the depth of the LJ potential is kept the same. The VWF model includes the attractive part of LJ interaction while the repulsive polymer model (e.g., self-avoiding polymer) excludes the attractive part. The equilibrium bond length is set to $0.6 \mu\text{m}$ in 2D and $0.5 \mu\text{m}$ in 3D simulations. The harmonic bond stiffness is $k_s = 400k_B T a_m^{-2}$ in 2D and $k_s = 3125k_B T a_m^{-2}$ in 3D in all presented simulations. In order to prevent overlap between RBCs and VWFs, we also employ the LJ potential only with its repulsive part.

In order to estimate the potential-adhesion probability Ψ of VWF, we employ two conditions: (i) a chain monomer has to be close enough to the channel wall and (ii) this monomer has to be activated for adhesion which is characterized by the degree of local stretching of the polymer chain. The adhesive distance to the wall is assumed to be $\delta_{\text{adhes}} = 1 \mu\text{m}$, and VWF polymer bead activity depends on how the polymer is stretched locally. In particular, a VWF polymer bead is considered to be active if it sees no more than its neighbor bound beads inside a threshold radius R_{thres} and if its bonds make up an angle more than a threshold angle θ_{thres} (this condition is not considered for the end beads). Consequently, the locally stretched VWF portion can become active while the collapsed portion remains inactive. The threshold criteria are chosen as $R_{\text{thres}} = 1.2l_b$ and $\theta_{\text{thres}} = 130^\circ$ which provide satisfactory

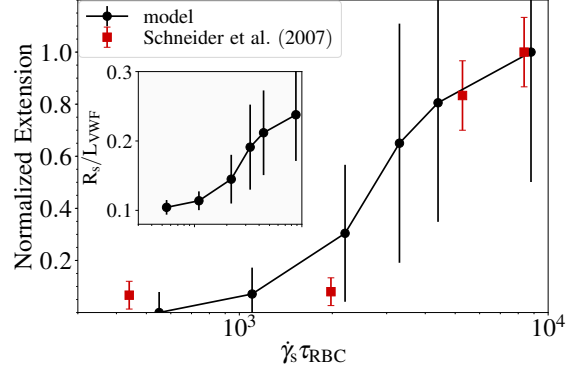


Fig. 3.1 Calibration of the 3D VWF model against experiments. Comparison of simulated VWF stretching in simple shear flow with experiments¹⁹¹, where the critical shear rate for polymer stretching in the model is adjusted by changing the attractive strength of LJ potential. The model employs the LJ potential with $\sigma = l_b$ and $\varepsilon = 4k_B T$. The maximum extension point is normalized to unity for both simulation and experimental data. γ_s is the shear rate, which is normalized by the characteristic relaxation time of a RBC τ_{RBC} ($\tau_{\text{RBC}} \approx 1.1 \text{ s}$) in order to properly relate the time scale of VWF stretching and τ_{RBC} . Inset shows the simulated extension normalized by VWF's contour length L_{VWF} .

activity based on VWF configuration. As a result, $\Psi = \left(\sum_i^{N_{time}} N_{act}^i \right) / (N_{tot} N_{time})$, where N_{act}^i is the number of active beads within a layer δ_{adhes} , N_{time} is the total number of time instances considered, and N_{tot} is the total number of VWF beads in the simulation domain.

3.4 Experiments

For microfluidic experiments, we use a pneumatically driven channel system (BioFlux, San Francisco, CA, USA), see Figure 3.2(b). Its pressure interface connects a high precision electropneumatic pump to the well plates to initiate a controlled flow rate with a nominal shear rate precision of 36 s^{-1} . The channels with a size of $350 \times 75 \text{ }\mu\text{m}$ are coated with collagen type I (C7661, Sigma Aldrich, St. Louis, MO, USA) in a concentration of 0.01% for one hour at 37° C . The microfluidic channel system is mounted onto an inverted microscope (Zeiss Axio Observer Z.1, Zeiss AG, Oberkochen, Germany). Image acquisition is performed using a CCD camera (AxioCam MrM) and ZEN software (both Zeiss AG, Jena, Germany).

For microfluidic measurements, perfusion media with different hematocrit levels containing EGFP-marked VWF are perfused through the collagen-coated channels at distinct wall shear rates. After five minutes of continuous perfusion, margination of VWF is measured through the intensity of fluorescent-labeled VWF near the channel bottom (I_x) in an area free of adhered VWF particles, and is normalized by the wall autofluorescence intensity I_w , which remained constant throughout all performed experiments. To analyze the impact of hematocrit on adhesion of marginated VWF to the collagen-coated channel bottom, the fluorescence intensity of adhered VWF particles is quantified. Under distinct shear rates of 100 s^{-1} , 250 s^{-1} , 500 s^{-1} , and $1,000 \text{ s}^{-1}$, the surface coverage of adhered VWF particles per observation area is monitored in time. For image analysis, we use ZEN software (Zeiss AG, Jena, Germany) and the open-source software ImageJ (V. 1.46r, National Institute of Health, Bethesda, MD, USA). Mean data from experiments are given with standard deviation (SD).

For recombinant VWF expression, we use HEK293 cells. Cells are cultured in Dulbecco Modified Eagle Medium (DMEM, Invitrogen, Karlsruhe, Germany) with 10% fetal bovine serum and 1% penicillin/streptavidin at 37° C . Then, cells are transfected with Lipofectamine LTX (Invitrogen, Karlsruhe, Germany). Recombinant expression of VWF is performed as follows. In brief, HEK293 cells transiently expressing VWF are treated with 160 nmol/L PMA. Samples of the supernatant are taken, centrifuged (5 min at $13,000 \text{ g}$, 4° C) and VWF concentration is determined by VWF:Ag-ELISA. VWF is fluorescently marked by EGFP via a His-tag; EGFP-VWF has been provided by the group of R. Schneppenheim (University Medical Center Eppendorf, Hamburg, Germany) and added to the perfusion media in a concentration of $20 \text{ }\mu\text{g/ml}$. Blood has been collected into citrated vacuum tubes

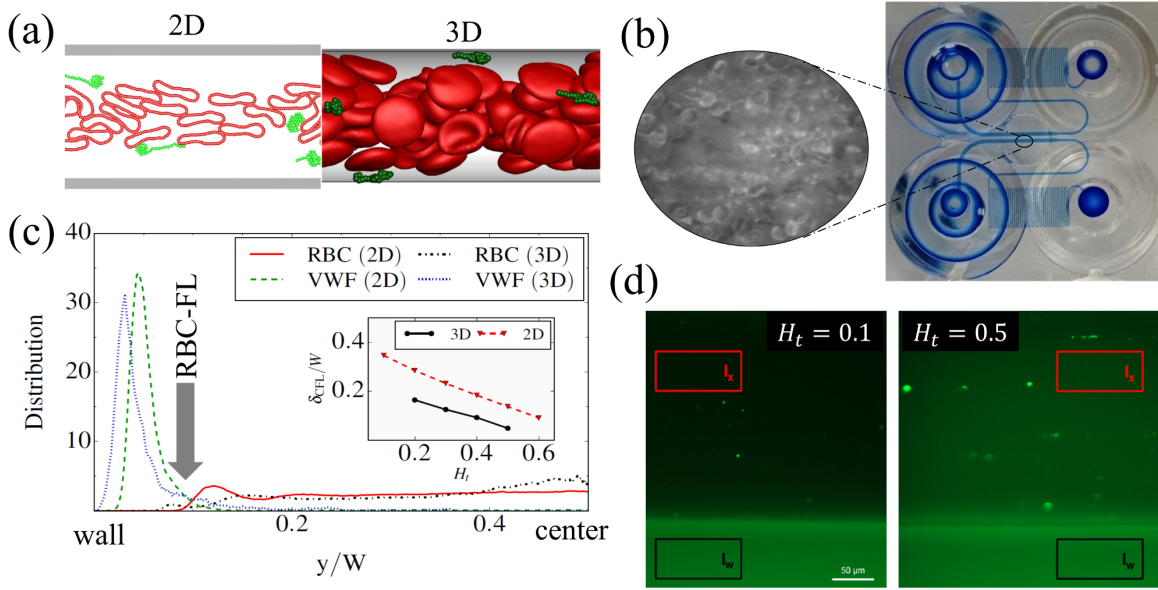


Fig. 3.2 Simulation and experimental measurements. (a) Snapshots from 2D and 3D simulations with RBCs colored in red and VWFs in green. The simulation setup corresponds to a cylindrical microvessel in 3D with the diameter $W = 20 \mu\text{m}$ or to a channel in 2D with the width $W = 20 \mu\text{m}$. (b) Experimental setup consists of a microfluidic system with multiple identical channels (two channels are shown). At the pre-processing step, channel walls are coated with collagen. Blood with different H_t levels is perfused through the device (from an inlet on the right to an outlet on the left) using a pneumatic pump. Optical microscopy is performed in the middle of the wide-channel section marked by the small oval area, where we can observe RBCs but not VWF because it needs to be detected by fluorescence microscopy. (c) Simulation measurements supply distributions of different components in blood flow. The plot shows a comparison of center-of-mass (COM) distributions of RBCs and VWFs obtained from a 2D simulation with $H_t = 0.6$ and a 3D simulation with $H_t = 0.4$ for a nearly same thickness of RBC-FL and a pseudo-shear rate of $\dot{\gamma}^* \approx 60$ ($\dot{\gamma} \approx 62 \text{ s}^{-1}$). The distributions from 2D and 3D simulations compare well for a fixed thickness of the RBC-FL, indicating that hematocrit values in 2D correspond to lower hematocrits in 3D. The inset presents the RBC-FL thicknesses δ_{CFL} for different H_t and demonstrates that a negative shift by about 0.15-0.2 is required to relate H_t in 2D to that in 3D. (d) Experimental measurements provide fluorescence intensity of labeled VWFs near the channel bottom. The isotropic background level of measured intensity (I_x) characterizes the amount of flowing VWF near the wall (or VWF margination), while the bright spots correspond to adhered VWF molecules or aggregates. The intensity in the right plot for $H_t = 0.5$ is clearly stronger than on the left for $H_t = 0.1$ indicating that VWF margination is more pronounced at $H_t = 0.5$. All measured intensities are normalized by the wall autofluorescence intensity I_w (the black marked area), which remains constant throughout all performed experiments. Scale bars correspond to $50 \mu\text{m}$.

from healthy volunteers after informed consent. To reach the indicated levels of hematocrit, RBCs are isolated from blood samples, washed and supplemented with HEPES buffered Ringer solution (HBRS) containing (in mmol/L): 140 NaCl, 5 KCl, 1 MgCl, 1 CaCl₂, 5 glucose, 10 HEPES (N-2-hydroxyethylpiperazin-N0-2-ethanesulfonic acid) adjusted to pH 7.4. This study has been conducted in conformity with the Declaration of Helsinki and with the International Conference on Harmonisation of Technical Requirements for Registration of Pharmaceuticals for Human Use (ICH) Guidelines available at <http://www.ich.org>. It has been approved by the Ethics Committee II of the Heidelberg University (Mannheim, Germany).

3.5 Simulation and experimental measurements

Blood is modeled as a suspension of RBCs⁶⁰ and a few macromolecules (e.g., flexible polymers, VWFs), which flow in a cylindrical microvessel in 3D with diameter W , or in a channel in 2D with width W , see Figure 3.2(a) and *Methods* for technical details. A VWF model has to incorporate internal associations within a molecule, which give rise to its compact shape in the absence of flow, and reproduce the stretching of VWF in shear flow above a critical shear rate¹⁹¹. The internal associations can be modeled explicitly by intra-molecular dynamic bonds, as in a self-associating polymer model^{5,199,200}, or implicitly by imposing pairwise attractive interactions between the monomeric units of a polymer^{6–8}. We have selected the VWF model with inter-bead attractive interactions^{6–8} for our simulations, since it is able to reproduce quantitatively the experimentally observed stretching of VWF in shear flow¹⁹¹. The resultant potential between polymer units is the superposition of a harmonic bond potential and an attractive Lennard-Jones (LJ) pairwise potential. The VWF model includes the attractive part of LJ interaction while the repulsive polymer model (e.g., self-avoiding polymer) excludes the attractive part of the LJ potential. The repulsive polymer model is employed for comparison with the VWF model in order to demonstrate the importance of VWF self-associations and/or the significance of VWF critical stretching for its behavior in blood flow. Calibration of the attractive LJ interactions for the VWF model against the experimental data of VWF stretching in simple shear flow¹⁹¹ is displayed in Figure 3.1.

The flow strength is characterized by a non-dimensional shear rate defined as $\dot{\gamma}^* = \bar{\gamma}\tau_{\text{RBC}} = \bar{\gamma}\eta D_{\text{eff}}^3/\kappa_c$, where $\bar{\gamma} = \bar{v}/W$ is the average shear rate (or pseudo shear rate) with average flow velocity \bar{v} computed from the velocity profile, and τ_{RBC} is the characteristic RBC relaxation time defined through the fluid viscosity η , effective RBC diameter D_{eff} , and the membrane bending rigidity κ_c . Here, $D_{\text{eff}} = \sqrt{A_o/\pi}$ in 3D and $D_{\text{eff}} = L_o/\pi$ in 2D, with

A_0 being the RBC surface area in 3D and L_0 the cell circumference in 2D. The characteristic relaxation time is $\tau_{\text{RBC}} \approx 1.1$ s for healthy RBCs under physiological conditions^{58,140}, and therefore, the pseudo-shear rate $\bar{\gamma}$ is roughly equivalent in magnitude to $\dot{\gamma}^*$ in inverse seconds.

The experimental setup corresponds to a microfluidic system with multiple identical channels of a rectangular cross-section, see Figure 3.2(b) and *Methods* for details. The walls of the channel are functionalized with collagen to facilitate the adhesion of VWF, while the flow in the channel is controlled by an electro-pneumatic pump. Controlled parameter in experiments is the wall shear rate $\dot{\gamma}_w$, which can be related to the pseudo shear rate $\bar{\gamma}$ as $\dot{\gamma}_w \geq 8\bar{\gamma}$ for a tube flow in 3D ($\dot{\gamma}_w \geq 6\bar{\gamma}$ for a channel in 2D), where the equal sign holds only for a parabolic flow with a Newtonian fluid (e.g., only blood plasma). The presence of RBCs can make the ratio $\dot{\gamma}_w/\bar{\gamma}$ significantly larger than 8 in 3D (or 6 in 2D), especially for high hematocrits ($H_t \geq 0.3$), as illustrated in Figure 3.3.

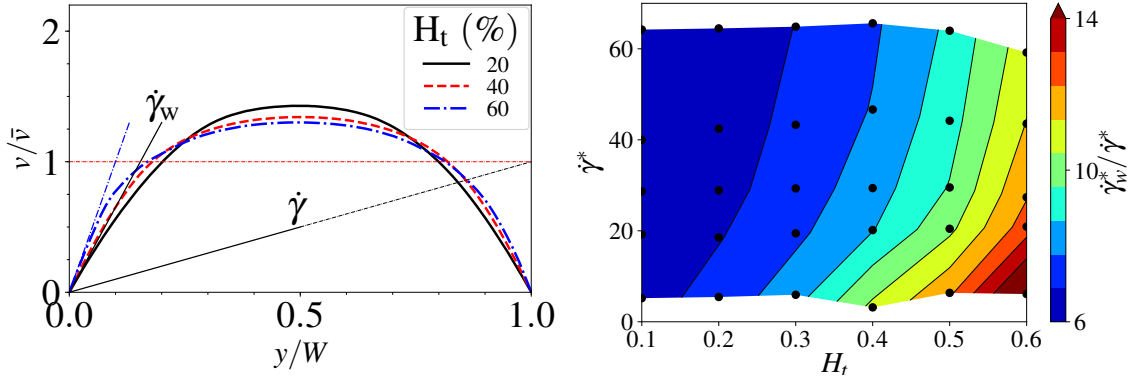


Fig. 3.3 Relation between the wall-shear rate and the average shear rate. **(left)** Flow velocity profiles for different hematocrit values at $\dot{\gamma}^* = 30$. Wall shear rates $\dot{\gamma}_w$ for different H_t are indicated by tangent lines to the velocity profiles near the wall. The average shear rate $\dot{\gamma}$ is indicated by the solid line. **(right)** Diagram showing the ratio between the wall-shear rate and the average shear rate in 2D for various H_t values and flow conditions. The black dots indicate the values of H_t and $\dot{\gamma}^*$ for which simulations have been performed.

Simulations constitute the typical distributions of blood components for RBCs and VWF, as shown in Figure 3.2(c) in 2D with $H_t = 0.6$ and in 3D with $H_t = 0.4$ for a nearly same thickness of the RBC-FL and a pseudo-shear rate of $\dot{\gamma}^* \approx 60$ ($\bar{\gamma} \approx 62 \text{ s}^{-1}$). The distributions of VWF clearly show a peak near the channel wall indicating strong margination of the VWF polymers, while RBCs mainly populate the center of the channel. The thickness of the RBC-FL is calculated based on the edge of RBC core of the flow, analogously to the measurements of RBC-FL performed by Kim et al. 2007¹⁰⁵ and Fedosov et al. 2010c⁵⁶. It is important to note that the 2D and 3D simulations are compared at different H_t values but for a nearly same thickness of RBC-FL, since margination of particles in blood flow

is strongly correlated with the RBC-FL thickness^{87,142}. The good correspondence of the distributions for a fixed RBC-FL thickness demonstrates that H_t value in 2D has a different meaning than in 3D. The inset in Figure 3.2(c) presents the RBC-FL thicknesses δ_{CFL} for different H_t values, indicating that a negative shift by about 0.15-0.2 is required to relate H_t in 2D to that in 3D.

Throughout the chapter, we will mainly employ 2D simulations to enable a systematic investigation of the behavior of VWF in blood flow for a wide range of conditions (e.g., hematocrit, flow rate, VWF size), which would be computationally intractable in 3D. However, the 2D model qualitatively reproduces the relevant physical effects in blood flow in comparison to 3D, as demonstrated in Figure 3.2(c). Furthermore, we have verified that 2D and 3D simulations agree well at several selected H_t values. The similarity between 2D and 3D simulations has also been shown for the margination of micro- and nano-carriers in blood flow¹⁴⁰.

In experiments, blood samples with different hematocrits are perfused through the channel in order to monitor margination and adhesion of fluorescent-labeled VWF. VWF margination is measured through isotropic background level of the fluorescence intensity I_x near the bottom wall of the channel, as shown in Figure 3.2(d). I_x is normalized by the autofluorescence intensity I_w of the lateral channel wall, which remains constant throughout all performed experiments. VWF adhesion is quantified by the intensity and area of the immobile bright spots illustrated in Figure 3.2(d), which correspond to adhered VWF molecules or their aggregates. A detailed measurement of VWF distribution along the channel cross-section, as it is done in simulations, is not possible experimentally since individual VWF chains cannot be observed and tracked. For the same reason, it is not feasible to identify the composition of immobile aggregates adhered at the channel wall. Finally, the distribution of VWF lengths in experiments corresponds to an average physiological distribution in blood, which is clearly polydisperse, while simulations are performed for a fixed length of VWF. Therefore, a direct comparison between simulations and experiments is not intended; however, we consistently integrate our numerical and experimental observations in order to understand better VWF behavior in blood flow.

3.6 VWF margination and stretching in blood flow

Margination properties of large VWFs in blood flow are very important for their efficient adhesion, since margination is a necessary precondition for adhesion. In order to quantify VWF margination properties, we define margination probability P as a probability of the polymer's center of mass (COM) to be within a certain distance δ away from the wall.

Throughout the chapter, $\delta = 2 \mu\text{m}$ is chosen for the calculation of VWF margination, motivated by the range of potential VWF adhesion. Note that this choice only affects the magnitudes of margination probabilities, but their relative importance for different investigated conditions remains unaffected.

Simulations performed for a wide range of H_t and $\dot{\gamma}^*$ values allow the construction of a margination diagram of VWF in blood flow (Figure 3.4(top,left)) which clearly identifies the margination properties of VWF. Margination becomes stronger with increasing H_t because RBCs mediate this process by migrating to the vessel center and expelling VWF toward vessel walls. Interestingly, VWF margination is not enhanced with increasing $\dot{\gamma}^*$ (or flow rate), which is due to the deformation and extension of VWF in flow. At high shear rates, a VWF molecule is subject to significant elongation in flow (i.e., VWF resembles an ellipsoidal shape), which results in a lift force pushing a deformed molecule away from the walls. Indeed, recent works about the lift force on polymers²⁰¹ and vesicles^{1,23,135} near surfaces in simple shear flow suggest that the lift force strongly increases with a polymer or vesicle size. The lift force generally arises from hydrodynamic interactions between deformable objects and a wall in flow^{1,23,135} which is, inter alia, a primary reason for the migration of RBCs toward the vessel center. Thus, the distribution of VWF within a vessel cross-section in microcirculation strongly depends on local blood-flow conditions.

In addition to the margination of VWF, another important aspect for VWF adhesion is its extension in flow, since in a compact configuration internal adhesive sites are shielded and VWF remains non-adhesive. Stretching of large VWFs is shown in Figure 3.4(bottom,left) for various conditions. These data correspond to an average extension $\langle R_S \rangle$ in the flow direction within the RBC-FL, where the shear rate is largest. Clearly, VWF stretches more with increasing non-dimensional shear rate $\dot{\gamma}^*$ or equivalently wall shear rate $\dot{\gamma}_w$. The dependence on H_t also indicates a stronger extension for larger hematocrits. The latter dependence arises from the effect that VWF is effectively confined in the RBC-FL between the wall and the RBC core. The thickness of RBC-FL decreases with increasing H_t as shown in the inset of Figure 3.2(c). This behavior is not entirely surprising and is consistent with the previous results showing a stronger extension of polymers and VWF in close proximity to the wall than in bulk flow^{7,191}. In addition, recent simulations²⁴ suggest that the collision of VWF with colloidal particles can significantly enhance its stretching, which may lead to VWF stretching in the bulk of the flow. In our simulations, we do not observe much stretching of VWF within the RBC-core of the flow, mainly due to the relatively low shear rates in the bulk. The largest wall-shear rates in our simulations are below 700 s^{-1} and shear rates in the bulk are much smaller than this value. Clearly, at much higher flow rates than those investigated here, significant stretching of VWF in the RBC core should be also expected.

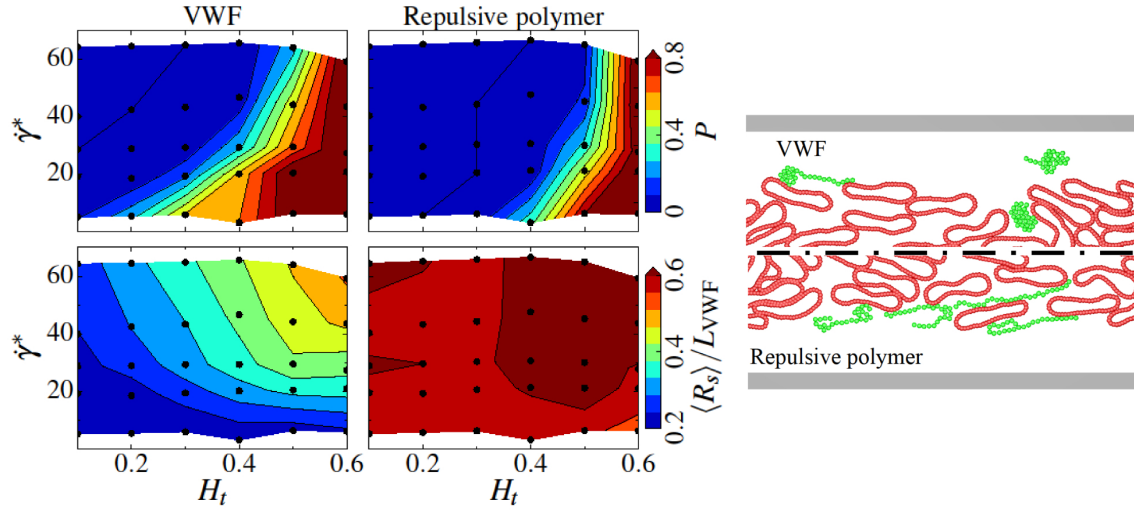


Fig. 3.4 Simulated margination and stretching of VWF and a repulsive polymer. Comparison of margination and stretching of VWF (left column) and a repulsive polymer (right column) in blood flow. In the top row, the simulation snapshots are presented for the conditions $H_t = 0.3$ and $\dot{\gamma}^* \approx 29.7$ ($\dot{\gamma} \approx 31 \text{ s}^{-1}$), where RBCs are colored in red while VWFs and repulsive polymers are in green. Clearly, the repulsive polymer exhibits a much stronger extension in blood flow in comparison to VWF. The middle row shows margination probability P into the near-wall layer with a $2 \mu\text{m}$ thickness for VWF and a repulsive polymer as a function of hematocrit H_t and shear rate $\dot{\gamma}^*$. Both the VWF and repulsive polymer consist of 26 beads corresponding to the contour length of $L_{\text{VWF}} = 15 \mu\text{m}$. The black dots indicate the values of H_t and $\dot{\gamma}^*$ for which simulations have been performed. The color code ranges from blue (low probability) to red (high probability) and is acquired via interpolation. The bottom row compares the normalized average stretching $\langle R_S \rangle / L_{\text{VWF}}$ of VWF and the repulsive polymer within the RBC-FL.

Figure 3.4 also presents analogous results for a repulsive self-avoiding polymer (i.e., a polymer without attractive interactions between monomers). A striking difference is that margination of a repulsive polymer is substantially less pronounced in comparison to VWF. Two mechanisms can be identified, which are both closely related to the higher ease of deformation and stretching of a repulsive polymer in blood flow (see Figure 3.4(bottom,right)). In the vicinity of the wall, the resulting elongated shape implies a larger lift force²⁰¹, which pushes the polymer back into the RBC core. Inside the core, collisions of soft (polymer) and stiff (RBC) objects lead to a displacement of the softer object toward the channel center¹¹²; however, this effect weakens for very soft objects, as they can "sneak" around stiffer cells more easily. In contrast, VWF remains mainly in a compact configuration within the RBC flow core and displays some degree of stretching primarily in the RBC-FL, see the snapshots in Figure 3.4. This means that a compact configuration of VWF does not only prevent undesired adhesion (as adhesive sites remain hidden), but also facilitates an efficient

margination in blood flow. Another striking difference between VWF and the repulsive polymer is that stretching of the repulsive polymer near the wall is much stronger than that of VWF and is nearly independent of the shear rate and hematocrit, as can be seen from the stretching diagram in Figure 3.4(bottom,right).

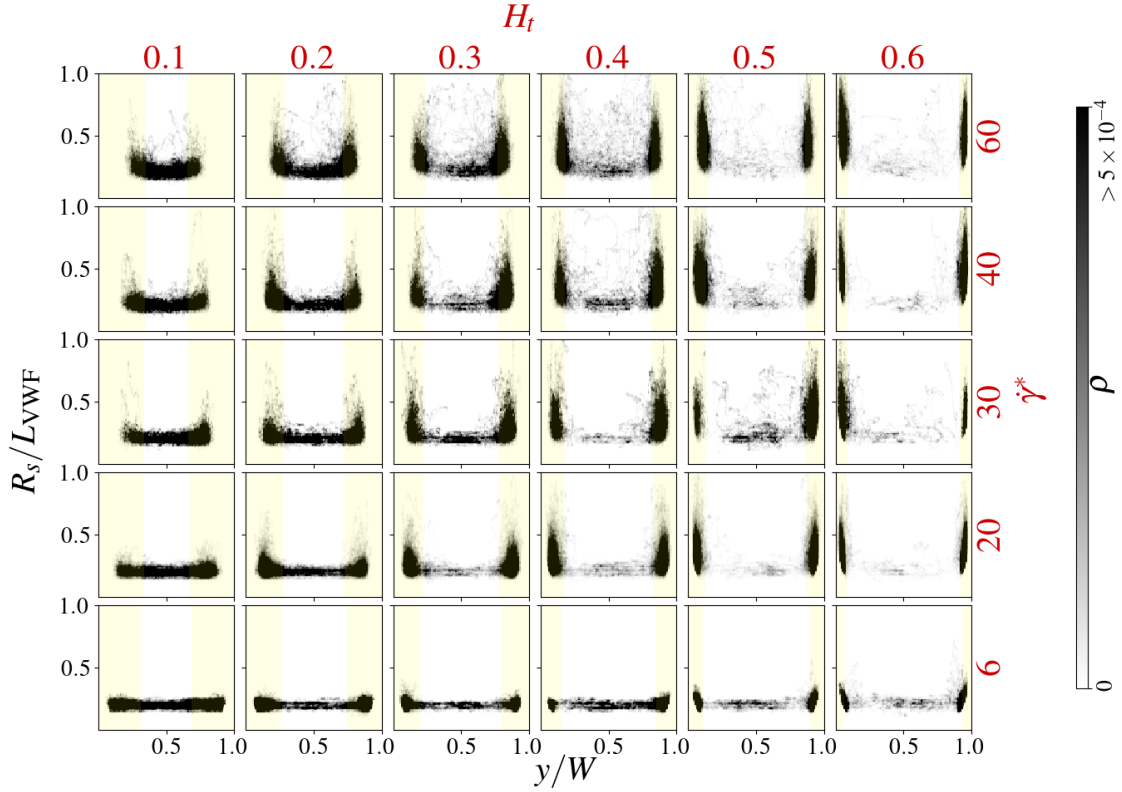


Fig. 3.5 Phase diagrams of VWF polymer location and stretching as a function of hematocrit and shear rate. The yellow-shaded areas represent the RBC-FL for each case. The black shading corresponds to the probability distribution of VWF polymers with a specific extension and cross-sectional location. This diagram shows the margination, stretching, and RBC-FL thickness all at the same time, which could be compared with Figures 3.4 and 3.3.

The RBC-FL thickness, VWF polymer distribution, and their stretching are plotted in the complete phase diagram for all hematocrits and shear rates, as shown in Figure 3.5. The phase diagram shows how well VWFs marginate to the RBC-FL and stretch there. The black shading corresponds to the probability distribution of polymer extension and location.

The experimental margination data are presented in Figure 3.6(a) for different wall shear rates $\dot{\gamma}_w$, which can be compared qualitatively to corresponding simulation results in Figure 3.6(b). Experiments and simulations (remember a shift in H_t in the relation between 2D and 3D) consistently yield an increase of margination with increasing H_t and a decrease in

margination with increasing wall shear rate. A quantitative comparison between experiments and simulations is not possible here, since experimental samples contain a distribution of different VWF lengths and separate VWF molecules cannot be distinguished, as discussed above. However, experimental and simulation results show a good qualitative agreement for the dependence of VWF margination on H_t and shear rate.

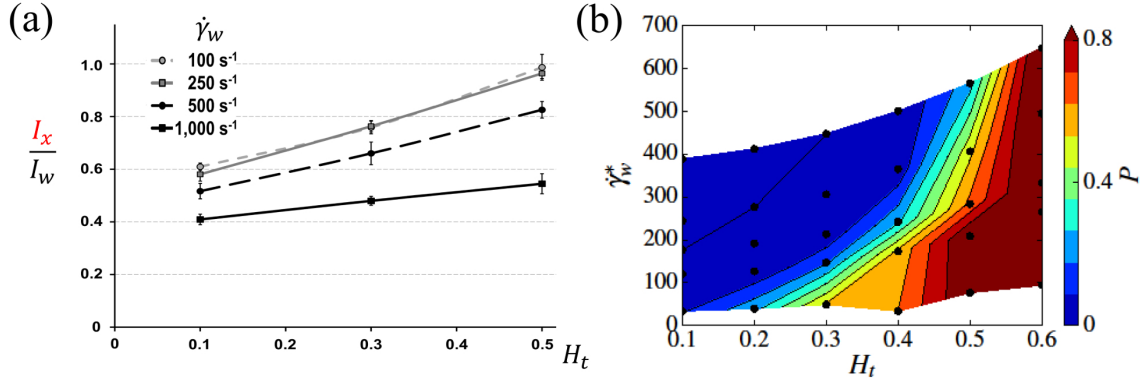


Fig. 3.6 Margination of VWF in microfluidics and simulations. (a) Experimental data of VWF margination as a function of hematocrit and wall shear rate $\dot{\gamma}_w$. For every point, at least four independent experiments were made. (b) Simulation results for VWF margination into a 2 μm layer near the wall as a function of H_t and the normalized wall shear rate. The data in the diagram are same as those in Figure 3.4(top, left), but the VWF margination probability is plotted as a function of $\dot{\gamma}_w^* = \dot{\gamma}_w \tau_{RBC}$ ($\tau_{RBC} \approx 1.1$ s) instead of $\dot{\gamma}^*$ for a better comparison between simulations and experiments. Note that only a qualitative comparison of margination is intended here.

Simulation results for the dependence of VWF margination on its length is presented in Figure 3.7 for VWF models with $N = 17$ and $N = 42$ beads, corresponding to $L_{VWF} = 9.6$ μm and $L_{VWF} = 24.6$ μm , respectively, which should be also compared with Figure 3.4 for $N = 26$ ($L_{VWF} = 15$ μm). The comparison indicates that smaller VWF molecules are margined less efficiently. This observation is consistent with the fact that micron-sized particles possess better margination properties than their sub-micron counterparts¹⁴⁰. The large VWF with $N = 42$ shows similar margination properties as the VWF with $N = 26$ in Figure 3.4. Thus, the most efficient VWF margination is expected to occur for large VWF molecules with a contour length greater than about 12-13 μm .

An interesting observation from Figure 3.7(bottom) is that a shorter VWF stretches generally better than longer chains. A similar behavior has been predicted by the theoretical analysis of shear-induced unfolding of self-attracting polymeric globules⁸, where the critical shear rate for unfolding has been found to depend linearly on the characteristic radius of the globule. Thus, the critical shear rate for VWF stretching is expected to have a weak

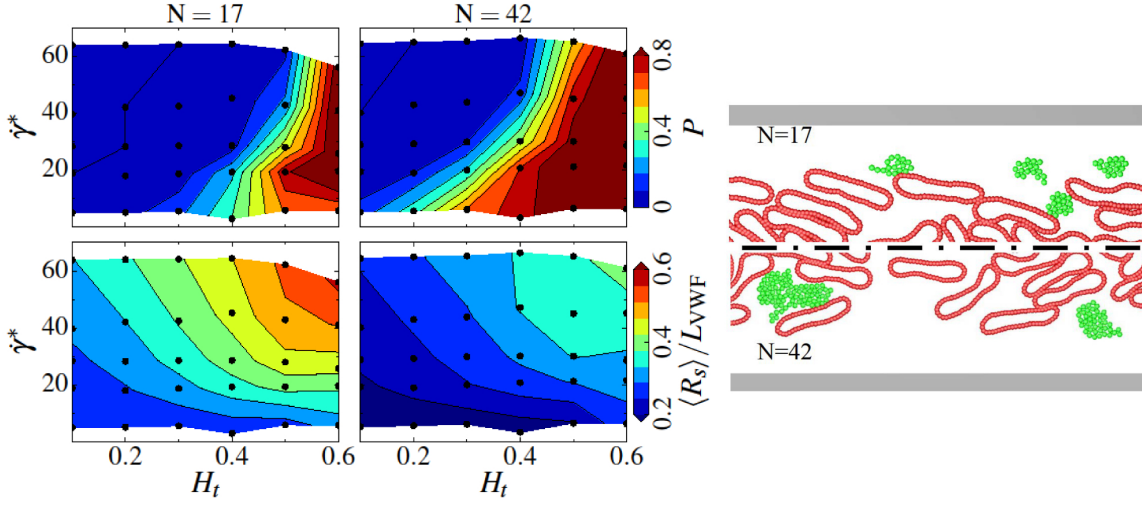


Fig. 3.7 Comparison of margination and stretching of VWFs with a different number of monomers: left column - $N = 17$ ($L_{\text{VWF}} = 9.6 \mu\text{m}$) and right column - $N = 42$ ($L_{\text{VWF}} = 24.6 \mu\text{m}$). The top row presents simulation snapshots for the conditions $H_t = 0.3$ and $\dot{\gamma}^* \approx 29.7$ ($\dot{\gamma} \approx 31 \text{ s}^{-1}$), where RBCs are colored in red while VWFs are in green. The middle row shows margination probability P into the near-wall layer with a $2 \mu\text{m}$ thickness for VWF with a different length as a function of hematocrit H_t and shear rate $\dot{\gamma}^*$. The black dots correspond to the values of H_t and $\dot{\gamma}^*$ for which simulations have been performed. The color code ranges from blue (low probability) to red (high probability) and is acquired via interpolation. The bottom row compares the normalized average stretching $\langle R_s \rangle / L_{\text{VWF}}$ of VWFs within the RBC-FL.

dependence on N ($\approx N^{1/3}$) and shorter VWFs are able to stretch at lower shear rates than longer VWF chains. However, although the relative extension (i.e., normalized by L_{VWF}) of the longer VWF is less compared with the shorter VWF, the physical extension of the longer VWF is larger than that of a shorter VWF.

These results allow us to draw a qualitative picture for VWF behavior in blood flow. VWF remains primarily in a compact configuration within the RBC-flow core, which leads to its efficient margination into RBC-FL. However, VWF is able to stretch near the wall due to high shear rates and the soft confinement between RBCs and the wall. To confirm this proposition, we plot in Figure 3.8 the distributions of VWF extension in the RBC core and RBC-FL. Even though some moderate stretching in the RBC core is possible, the largest VWF extension clearly occurs within the RBC-FL. This indicates that the adhesive interactions of VWF with vessel walls or other blood components should be mainly expected in the RBC-FL.

3.7 VWF adhesion

As already mentioned, VWF margination and stretching are two necessary pre-conditions for adhesion such that their convolution characterizes the potential for VWF adhesion. Even though we do not study VWF adhesion directly in simulations, we have performed data analysis in such a way that we can estimate the potential-adhesion probability Ψ for various conditions. This estimation is based on two conditions: (i) a monomer in VWF chain has to be close enough to the channel wall in order to be able to adhere and (ii) this monomer has to be active for adhesion. The second condition mimics the unfolding of VWF factor

in flow such that hidden adhesive sites become exposed and the VWF adhesion becomes possible^{103,213}. This condition is realized through the degree of local stretching of VWF in flow, see *Methods* for details. Then, the potential-adhesion probability is calculated as $\Psi = \left(\sum_i^{N_{time}} N_{act}^i \right) / (N_{tot} N_{time})$, where N_{act}^i is the number of active VWF beads within the near-wall layer δ_{adhes} at a time instance i , N_{time} is the total number of time instances taken into account, and N_{tot} is the total number of VWF beads in a simulation domain.

Figure 3.9 compares diagrams for the potential-adhesion probabilities of VWF and a repulsive polymer. In both cases, adhesion at low H_t values is extremely limited independently of the shear rate due to poor margination, such that polymers remain far enough from the wall and cannot adhere. However, if H_t becomes high enough ($H_t > 0.4$ in 2D corresponding to $H_t > 0.2$ in 3D) the adhesion becomes possible as the polymers marginate well. In this H_t range, VWF can adhere mainly at large enough shear rates, since at low shear rates VWF does not stretch enough to expose its adhesive sites. In contrast, the adhesion of a repulsive polymer is very much possible at low as well as high shear rates, because it can easily stretch independently of the shear rate, as seen in Figure 3.4. This analysis demonstrates that VWF adhesion in blood flow is the convolution of its margination and stretching, and strongly depends on local blood-flow characteristics within the microcirculation.

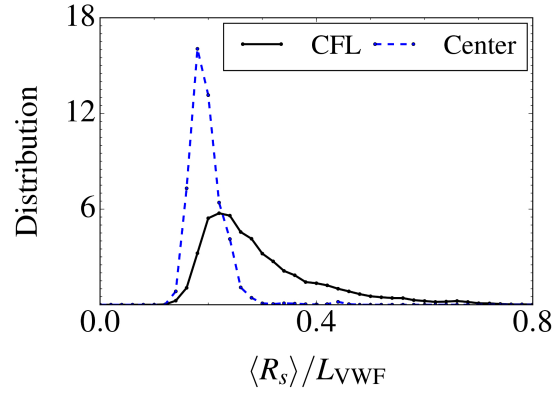


Fig. 3.8 Distributions of VWF extension in the RBC-flow core and RBC-FL, showing that a significant stretching is achieved mainly in the RBC-FL. 2D simulation for the parameters $H_t = 0.3$ and $\dot{\gamma}^* \approx 29.7$ ($\bar{\gamma} \approx 31 \text{ s}^{-1}$).

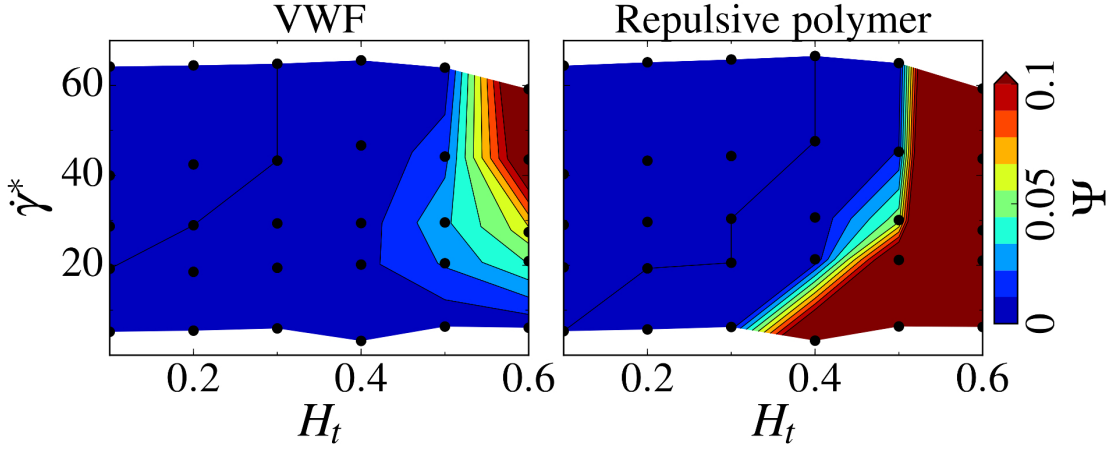


Fig. 3.9 Potential-adhesion probability Ψ of VWF and a repulsive polymer as a function of H_t and shear rate $\dot{\gamma}^*$. The probability of potential adhesion is calculated based on two conditions: (i) a chain monomer has to be close enough to the channel wall ($\delta_{\text{adhes}} < 1 \mu\text{m}$) and (ii) this monomer has to be activated for adhesion which is characterized by the degree of local stretching of the polymer chain (see *Methods* for details). Thus, Ψ is the adhesion probability defined as the average fraction of active polymer beads in close proximity to the walls. Both the VWF and repulsive polymer consist of 26 beads corresponding to the contour length of $L_{\text{VWF}} = 15 \mu\text{m}$. The black dots indicate the values of H_t and $\dot{\gamma}^*$ for which simulations have been performed. The color code ranges from blue (low probability) to red (high probability) and is acquired via interpolation.

Our simulations show that VWF or repulsive polymers can stretch within the RBC-FL and form a contact with the wall, while recent investigations^{173,203} suggest that in order to adhere, a VWF must remain in a compact form, since in a stretched configuration it will immediately be pushed away from the wall by the lift force²⁰¹. The proposed mechanism for adhesion proceeds by first attaching a single monomer to the wall with a subsequent VWF elongation. The main difference between these studies^{173,203} and our simulations is that the previous studies have been performed for a simple shear flow without RBCs. However, the situation in blood flow is strongly affected by the presence of RBCs. In blood flow, VWF marginates and remains quasi-trapped in the RBC-FL between the wall and flowing RBCs. Thus, even in a partially stretched configuration, VWF does not immediately demarginate due to the interactions with flowing RBCs. Then, tumbling dynamics of a partially-stretched VWF within the RBC-FL facilitates a contact with the wall. Even though the adhesion mechanism proposed by Sing et al. 2013²⁰³ and Radtke and Netz 2014¹⁷³ should still be possible in blood flow, our simulations show that the other mechanism described above is dominating in blood flow.

To study VWF adhesion directly, we performed a set of microfluidic experiments, with the results presented in Figure 3.10. VWF adhesion is quantified by measuring in time the intensity $I_{x, \text{particle}}$ of fluorescent spots at the bottom of the channel within an observation area, where the isotropic background intensity related to VWF margination is subtracted, see Figure 3.10(a). For comparison, Figure 3.10(b) presents the potential-adhesion probability of VWF estimated from simulations as a function of H_t and wall shear rate $\dot{\gamma}_w^*$, which can be interpreted as an adhesion rate of a VWF molecule if we multiply it by the rate of forming a bond between VWF monomer and a surface. Thus, the potential-adhesion probability should be proportional to the adhesion rate of a VWF molecule and characterizes qualitatively the degree of accumulation of adhered VWF fluorescent spots followed in time in experiments.

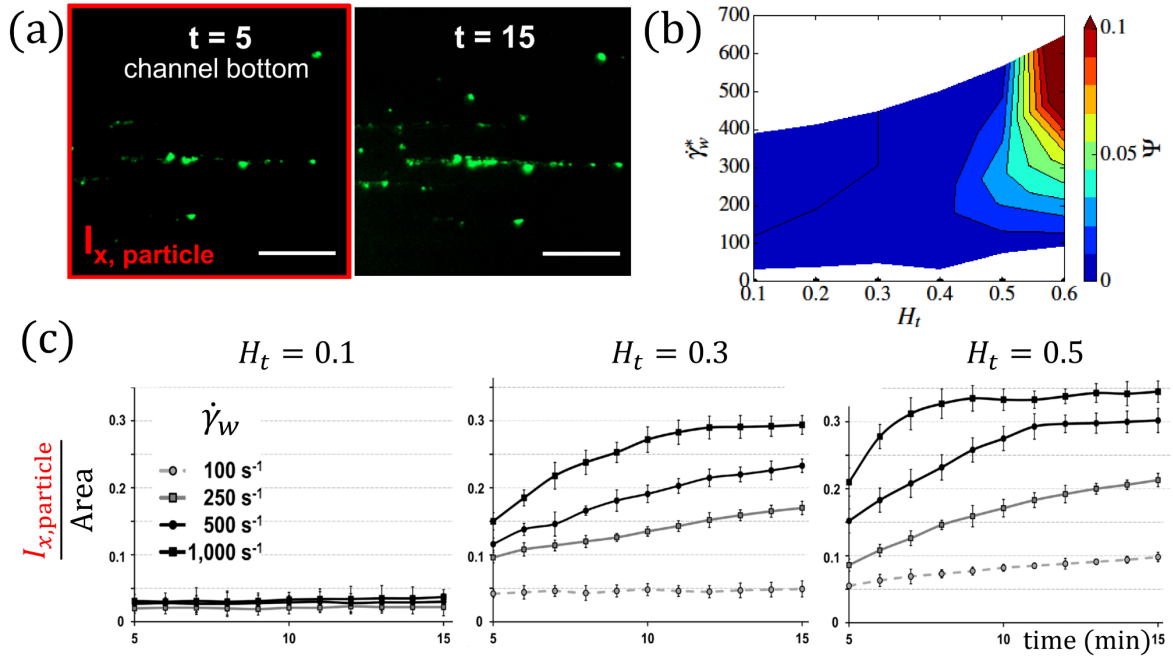


Fig. 3.10 VWF adhesion in experiments. (a) VWF adhesion is monitored over time and represented by the intensity and area of adhered VWF spots at the channel bottom, as shown by the two successive images of the experiment for $H_t = 0.5$ at $\dot{\gamma}_w = 500 \text{ s}^{-1}$. The isotropic background level of intensity, which characterizes VWF margination, is subtracted. (b) Potential-adhesion probability Ψ estimated from simulations as a function of H_t and $\dot{\gamma}_w^*$ for $N = 26$ ($L_{\text{VWF}} = 15 \text{ } \mu\text{m}$). It characterizes the probability of adhesion which is related to the slope of VWF-adhesion curves in experiments at short times before the adhesion saturation has been reached. (c) Adhesion of VWF to collagen in microfluidic channels for various wall shear-rates and hematocrits ($H_t = 0.1$, $H_t = 0.3$, $H_t = 0.5$). VWF adhesion is monitored over time. The error bars in the plots show the deviation of monitored data from four independent experiments.

The experimental results of VWF adhesion, presented in Figure 3.10(c), display three principal behaviors for short times ($\lesssim 10$ min after perfusion with VWF-rich medium): no adhesion, weak adhesion, and strong adhesion. For longer times ($\gtrsim 10$ min), adhesion levels saturate and are no longer indicative of the adhesion probability.

For low hematocrit, $H_t = 0.1$, VWF adhesion remains absent, independent of the applied shear rates, due to weak VWF margination (Figure 3.4). In fact, the two highest shear rates in Figure 3.10(c) should be large enough to achieve the VWF extension needed for adhesion, but VWF chains flow too far away from the wall to bind. For moderate hematocrit, $H_t = 0.3$, VWF adhesion displays a pronounced dependence on shear rate. Here, the volume fraction of RBCs is large enough for pronounced margination, and therefore VWF adhesion becomes possible when VWF chains are able to stretch. For the lowest shear rate, $\dot{\gamma}_w = 100 \text{ s}^{-1}$, no significant adhesion occurs in the experiments, even though the results in Figures 3.4 and 3.6 indicate that there should be considerable VWF margination ($H_t = 0.3$ in 3D corresponds to $H_t \approx 0.5$ in 2D); however, VWF extension is too weak – fully consistent with the potential-adhesion probability in Figure 3.10(b). In contrast, at the highest wall shear rate, $\dot{\gamma}_w = 1000 \text{ s}^{-1}$, a substantial increase in VWF adhesion is observed due to the enhanced VWF ability to stretch. Even though margination decreases with increasing shear rate (see Figures 3.4 and 3.7), VWF stretching over-compensates the reduced margination (see Figure 3.10(b)). Finally, for high hematocrit, $H_t = 0.5$, VWF adhesion is pronounced and a large adhesion rate (i.e., slope of intensity versus time) is observed, again qualitatively consistent with the potential-adhesion probabilities in Figure 3.10(b). Here, both margination and stretching are significant and favor strong adhesion. Interestingly, even for low shear rate, $\dot{\gamma}_w = 100 \text{ s}^{-1}$, some moderate adhesion is detected, indicating that VWF exhibits some stretching due to the confinement effect, since at $H_t = 0.5$ the thickness of RBC-FL is comparable with the VWF size.

3.8 Summary

The results presented above illustrate the behavior of large multimeric VWFs in blood flow. Within the flow core mainly consisting of RBCs, VWF maintains its compact shape and is not subject to significant stretching. This property not only prevents unwanted adhesion of VWF to blood cells, but also facilitates efficient VWF margination. Here, the large size of the VWF protein, which implies a characteristic diameter of a few microns, is also important, since this size seems to be optimal for margination^{117,140,142}, as discussed in more detail below. In contrast, the results for a repulsive polymer without internal attractive interactions clearly show poor margination in comparison to VWF (see Figure 3.4). After margination, VWF

stretches near the wall, which may result in its wall adhesion. Thus, both margination and stretching of VWF need to directly precede adhesion, and VWF behavior strongly depends on hematocrit and shear rate. Adhesion of VWF at a low H_t is limited by margination independent of whether VWF stretches or not (see Figure 3.10). Furthermore, at low wall shear rates, VWF stretching can be a limiting factor for adhesion, even if VWF margination is significant. However, when both conditions are fulfilled, VWF adhesion becomes possible, as seen in Figure 3.10.

The compact shape of VWF allows the comparison of its margination properties with those of rigid nano- and micro-particles. Recent investigations^{117,140,142} have shown that micron-sized particles possess much better margination properties than their sub-micron counterparts. This implies that VWF chains with a relatively short length ($\lesssim 3\text{-}5\text{ }\mu\text{m}$), such that they have a sub-micron diameter, are expected not to marginate as well as larger VWFs. Our results in Figures 3.4 and 3.7 show that VWFs with a length larger than about $12\text{-}13\text{ }\mu\text{m}$ should possess best margination properties in blood flow. Furthermore, the distribution of very short VWF multimers (of only a few dimers) in blood is expected to be similar to the blood-plasma distribution, since very small particles ($\lesssim 200\text{ nm}$) have a nearly homogeneous distribution within the plasma¹⁴⁰.

Another interesting result of our study is that VWF adhesion is possible even for very low shear rates at high H_t . The prediction of critical shear rate required for VWF stretching in free flow in the absence of RBCs corresponds to several thousand s^{-1} ¹⁹¹; however, at $H_t = 0.5$ in Figure 3.10, VWF adhesion was observed at shear rates ten times smaller than this value. This is due to the confinement effect of VWF in the RBC-FL, which leads to an enhanced stretching of VWF and possible adhesion. Such spontaneous adhesion might be of importance in tumor microvasculature, where local hematocrit is often elevated due to plasma leakage through endothelial fenestrations¹⁹⁶. Furthermore, VWF is also able to stretch at relatively low shear rates after a single adhesion point has been formed^{173,203}, facilitating further adhesion interactions.

The comparison between VWF and a repulsive polymer shows that the strength of internal associations (attractive interactions between monomers) within VWF defines not only its margination properties, but also its stretching behavior, where a repulsive polymer is able to stretch at much lower shear rates than VWF. Certain mutations of VWF may affect its physical properties, resulting in the reduction or intensification of the internal associations within VWF. Such changes are expected to strongly affect VWF stretching and margination behavior as was illustrated in Figure 3.4. In addition, stretching of VWF in blood flow is also correlated with the activity of ADAMTS13 protease, which cuts VWF at an open cleavage site within the A2 domain¹⁷⁶. Our results indicate that VWF cleavage should mainly occur

in the RBC-FL in microcirculatory locations with high enough H_t , where the cleavage site of VWF is exposed to ADAMTS13^{213,253}.

In conclusion, VWF exhibits an intricate behavior in blood flow, which depends on a number of conditions including flow rate, hematocrit, VWF length, and intra-protein attraction. The performed simulations provide a theoretical understanding for the complex dynamics of VWF in blood flow, which is entirely consistent with our experimental observations of VWF adhesion in microfluidics. These results are important for the understanding of VWF distribution and adhesion in the microvasculature in health and disease.

Chapter 4

Reverse Fåhræus effect for drug carriers in blood stream

In blood stream, red blood cells (RBCs) migrate to the center of the vessel, leaving a cell free layer close to the walls. Consequently, the volume fraction of RBCs (hematocrit) in microvessels is less than their discharge volume fraction, the well-known Fåhræus effect. However, since RBCs concentrate in the center of the vessel, the other micro-particles in blood such as platelets, drug carriers, large VWF polymers, etc. marginate into the RBC free layer. In contrast to RBCs, margined particles have a higher volume fraction than their discharge volume fraction. Using theoretical analysis and mesoscale simulations, it is shown that this reverse Fåhræus effect for margined particles is rather significant. In contrast to the Fåhræus effect for RBCs, the reverse effect for margined particles is not very sensitive to the vessel size. This phenomenon is beneficial for drug carriers since the effective concentration of drugs in microvasculature would become higher than the total injected concentration. For platelets and von Willebrand factor proteins, this effect facilitates more efficient hemostasis, as well.

4.1 Introduction

A higher concentration of RBCs at the center of the vessels implies that RBC flow rate is larger than the flow rate of blood plasma. This phenomenon is called Fåhræus effect which was first discovered by Robin Fåhræus⁵¹. Similarly, the effective viscosity of blood in microvessels is different from the viscosity of blood in large vessels^{52,168}. Migration and close packing of RBCs in the center of microvessels results in the migration of the other micro-scale blood components such as platelets^{175,256}, ultra-large von Willebrand factor proteins¹⁷²,

micro-scale drug carriers^{140,141}, and even large leukocytes (white blood cells)^{57,58} toward the vessel wall. This margination process depends not only on the geometrical properties of blood vessels, but also on the physiological properties of the blood stream such as hematocrit and pressure gradient or equivalently shear rate^{133,140} of the flow.

According to the Fåhræus effect, the discharge hematocrit is slightly higher than the tube hematocrit. This means that the microcirculation has a fewer number of RBCs locally than the number of RBCs fed into the microvasculature. On the contrary, margined particles must have a larger local volume fraction than the fraction that is fed into the microvasculature. This effect is opposite to the Fåhræus effect, and is beneficial for microcirculation. For instance, a low concentration of platelets and von Willebrand factors in blood is increased in microvasculature, leading to a higher hemostatic efficacy. Similarly, the drug concentration injected into the blood should be elevated in the microvasculature. Here, the discharge and vessel volume fractions of RBCs and margined particles will be quantified for various physiological and geometrical properties of the system.

4.2 Theory

The tube (H_t) and discharge (H_d) hematocrits are defined¹¹⁸, respectively as

$$AH_t = \iint_A H da, \quad (4.1)$$

and

$$AUH_d = \iint_A Hud a, \quad (4.2)$$

where A , U , u , and H stand for the cross sectional area, average blood velocity in the vessel, local velocity, and local volume fraction (hematocrit), respectively. Similarly, the tube and discharge volume fractions of the margined components, such as drug carriers or platelets, are represented here by J_t and J_d , as described in Equations 4.1 and 4.2.

Figure 4.1 shows the volume fractions in blood flow for both 2D and 3D simulations. The margination of platelets and polymers is illustrated by the peak of their density profile in the RBC-FL. 2D simulation results are very similar to 3D simulation results if hematocrit is subtracted by 20% ($H_t^{2D} - 20\% \implies H_t^{3D}$)¹⁷², *i.e.* 2D hematocrit of 70% is equivalent to 3D hematocrit of 50%. This consideration helps us reduce the huge computational cost of large 3D simulations, knowing that 2D results are very reliable.

The velocity profile in the RBC-core is similar to a Newtonian fluid flow with a higher viscosity than that of the plasma. If the RBC-FL is thin compared with the radius of the blood vessel, the velocity profile in the RBC-FL could be approximated as a linear velocity

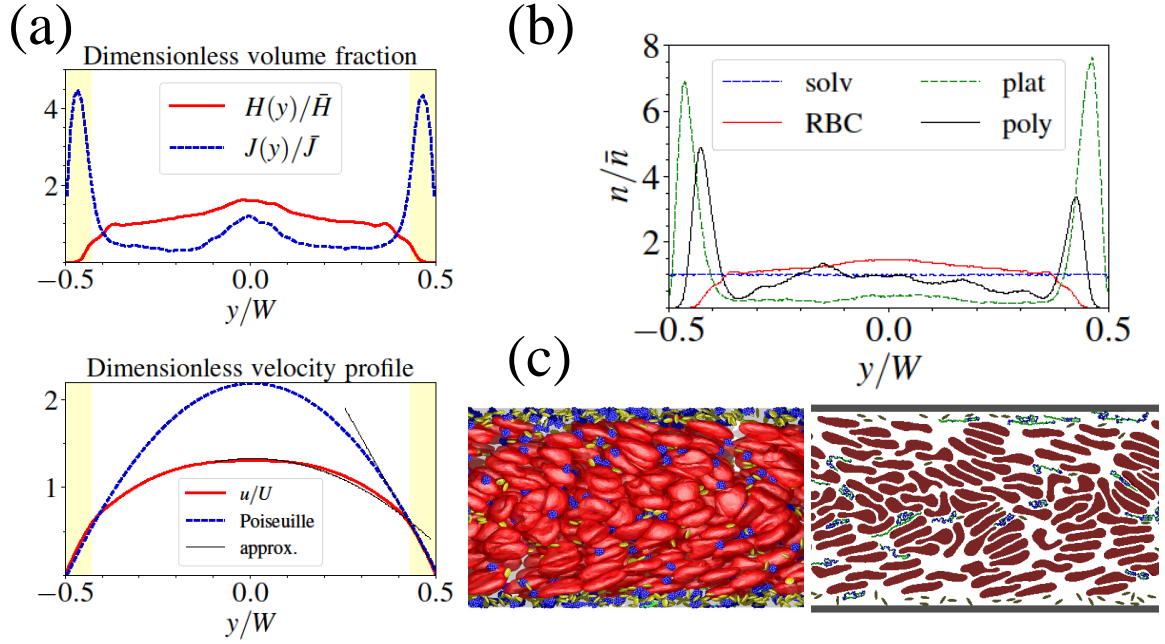


Fig. 4.1 Margination in blood flow. (a) The volume fraction and velocity profile of blood flow in 3D simulations. The yellow strips show the approximate thickness of RBC-FL. The volume fraction of RBCs is almost constant between the RBC-FLs, while the volume fraction of large polymers and platelets is very high in the RBC-FL. The velocity profile can be approximated linearly in the RBC-FL if the layer is thin enough. Between the RBC-FLs, the velocity profile is approximated by Poiseuille flow with slip boundary conditions at the walls. The approximations are represented by black lines. (b) The density profile of all components in a 2D simulation. Platelets and large polymers marginate into the RBC-FL, however, fluid particles have a uniform distribution. 2D and 3D results are equivalent if hematocrit in 2D and 3D are comparable. Simulations show that H_t^{3D} is equivalent to 20% more 2D hematocrit, H_t^{2D} 172. (c) Snapshot of a part of 2D and 3D simulations. RBCs are colored in red, platelets in yellow (dark yellow in 2D), and polymers in blue (for collapsed part) and green (for stretched part).

profile. Then, the RBC-core flow is a Poiseuille flow with slip boundary conditions, whose slip velocity is the velocity at the edge of the RBC-FL, u_δ . Accordingly, the velocity field is approximated as

$$u(r^*) = \begin{cases} \frac{R^2}{4\mu} \frac{dP}{dx} (r^{*2} - (1 - \delta^*)^2) + u_\delta & r^* \leq 1 - \delta^* \\ \frac{u_\delta}{\delta^*} (1 - r^*) & r^* \geq 1 - \delta^* \end{cases}, \quad (4.3)$$

for a tube with radius R , where $r^* = r/R$, $\delta^* = \delta/R$, and μ is the effective viscosity of the fluid in RBC-core flow, which is higher than the plasma viscosity. The average velocity

can be evaluated by integrating this function over the tube section, which yields the average velocity as $U = u_\delta (1 - \delta^* - \delta^{*2}) - \frac{R^2}{8\mu} \frac{dP}{dx} (1 - \delta^*)^4$.

Assuming that the local hematocrit is constant through the RBC-core region and zero in the RBC-FL, and substituting it together with the presumed velocity field in Equation 4.3 into Equations 4.1 and 4.2, the following relation between tube and discharge hematocrits is obtained.

$$\frac{H_d}{H_t} = 1 + 2\delta^* - u_\delta^* \delta^*, \quad (4.4)$$

where $u_\delta^* = u_\delta/U$, neglecting the higher orders of δ^* . In practice, $\delta^* \ll 1$ and $u_\delta^* < 1$, so that the discharge hematocrit is always higher than the tube hematocrit. That means, the microvasculature reduces the RBC concentration which is fed into it. In large vessels, the non-dimensional RBC-FL thickness, δ^* , approaches zero and discharge hematocrit becomes equal to tube hematocrit.

Similar to the hematocrit for RBCs, a tube and discharge volume fraction can be assigned to drug carriers and platelets, which marginate into the RBC-FL^{133,140,141,175,256}. Representing the volume fraction of drug carriers or platelets by J , and integrating Equations 4.1 and 4.2 for J_t and J_d , the discharge volume fraction of margined particles becomes

$$\frac{J_d}{J_t} = \frac{1}{2} \left(u_\delta^* - \frac{1}{6} u_\delta^* \delta^* \right). \quad (4.5)$$

Here, we have assumed that the volume fraction $J(r)$ is zero in the RBC-core and constant in the RBC-FL.

According to the specified conditions, $\delta^* \ll 1$ and $u_\delta^* < 1$, the discharge volume fraction of margined drug carriers is less than half of their tube volume fraction, $J_d < \frac{1}{2} J_t$. It means that drug carriers in the microvasculature have a higher concentration than what is fed into it. Indeed, this phenomenon still occurs for larger vessels since the thickness of the RBC-FL approaches a constant value. However, the assumption of zero volume fraction outside the RBC-FL becomes less and less valid as the size of the vessel increases.

With the linear velocity profile approximation, one can obtain the ratio of discharge and tube volume fractions as $H_d/H_t = 1 + 2\delta^* - \frac{1}{2} C \delta^{*2}$, and $J_d/J_t = \frac{1}{4} C \delta^* (1 - \frac{1}{6} \delta^*)$, where $C = R^2 \nabla P / \mu_\delta U$ and μ_δ is the viscosity of blood plasma. However, the margination of blood components is a function of pressure gradient and tube hematocrit. Also, at low hematocrits, the approximation of thin RBC-FL is not valid anymore.

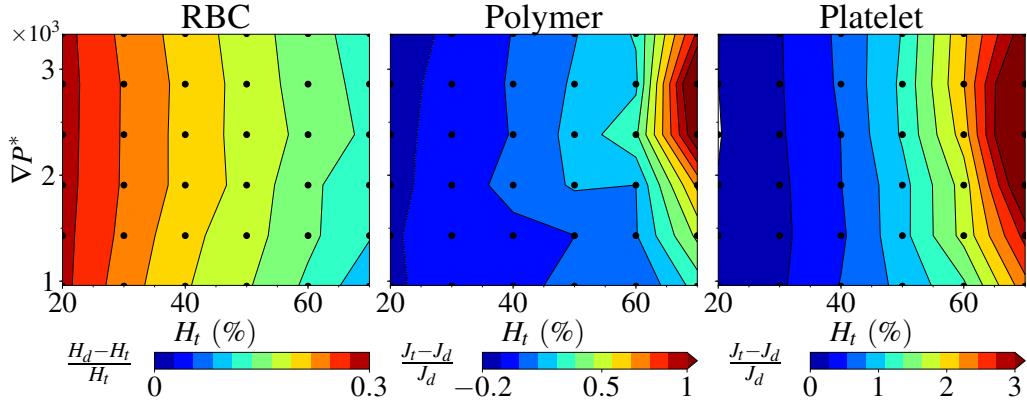


Fig. 4.2 Ratio of tube and discharge volume fractions for RBCs and margined particles, platelets and large polymers. Increasing hematocrit results in a decrease of the RBC-FL thickness and leads to a smaller difference between discharge and tube hematocrits. However, a higher hematocrit results in stronger margination and slower flow rate in a thinner RBC-FL, which causes a greater difference in discharge to tube volume fraction of margined particles.

4.3 Results

In 2D simulations, the tube hematocrit is changed from 20% to 70%, which is equivalent to 3D hematocrit $\sim 0\%$ to 50% . The discharge to tube volume fraction is calculated for each particle and the results are shown in Figure 4.2. The discharge hematocrit is always higher than the tube hematocrit because of RBC migration to the center of the flow. The ratio between discharge and tube hematocrits approaches unity as the tube hematocrit increases, leading to a smaller RBC-FL thickness. In contrast, as the tube hematocrit increases, the margination of platelets and large polymers is elevated such that the tube volume fraction exceeds by far the discharge volume fraction.

Although the Fåhræus effect for RBCs is almost a direct function of the RBC-FL thickness, the reverse Fåhræus effect for margined particles is not only a function of RBC-FL thickness, but also depends on particle margination. Figure 4.3 depicts the RBC-FL thickness at different pressure gradients and hematocrits. Comparing Figure 4.3 to 4.2, a direct relation between the RBC-FL thickness and discharge to tube hematocrit ratio can be observed.

The Fåhræus effect is a result of RBCs migration to the center of the flow. In contrast, the reverse Fåhræus effect for the platelets, polymers, or drug carriers is the result of their margination to the RBC-FL. The margination parameter,

$$M = \frac{4 \int_0^R \rho r dr}{D \int_0^R \rho dr}$$

is assigned to all the particles in order to quantify how much they marginate or migrate to the center. Margination parameter in the range $0 < M < 1$ implies migration to the center of the flow, while $1 < M < 2$ corresponds to the margination of the particles. Figure 4.4 shows how closely the margination parameter is related to the Fåhræus effect depicted in Figure 4.2.

The theoretical predictions for the reverse Fåhræus effect break down if the margination of drug carriers has a non-trivial dependence on shear rate, as we see for the large polymers in Figures 4.2 and 4.4 which mimic von Willebrand factor proteins¹⁷². On the contrary to the Fåhræus effect for RBCs, the reverse Fåhræus effect for platelets, polymers or drug carriers is very prominent at high tube hematocrits.

Accordingly, we observe for RBCs a maximum of 30% increase in the discharge hematocrit in comparison with the tube hematocrit, while the tube volume fraction can become 100% to 300% greater than the discharge volume fraction for polymers and platelets (see Figure 4.2).

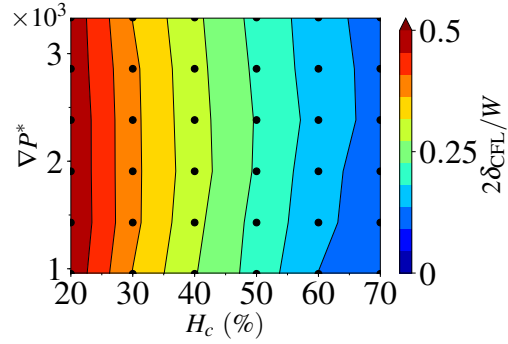


Fig. 4.3 The RBC-FL thickness for different pressure gradients and tube hematocrits. The RBC-FL is mostly sensitive to hematocrit than pressure gradient.

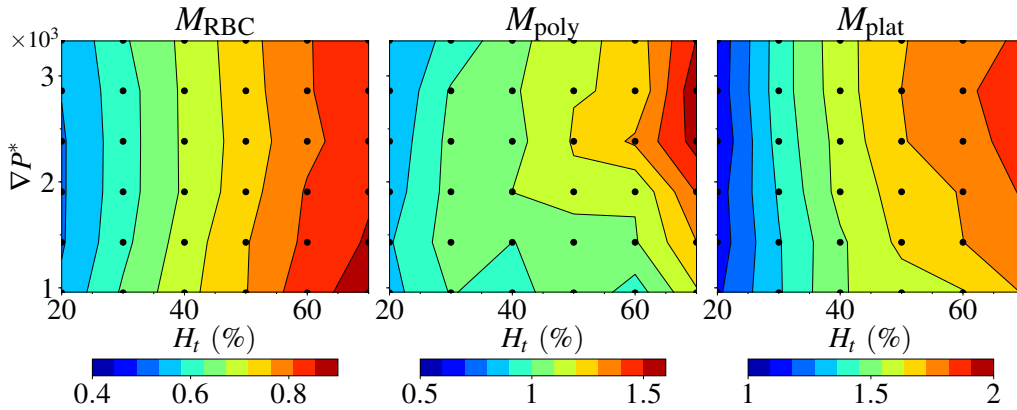


Fig. 4.4 Margination of blood components for different pressure gradients and tube hematocrits. The margination parameter is closely related to the Fåhræus effect plotted in Figure 4.2. Margination parameter in the range $0 < M < 1$ shows migration to the center of the flow, while $1 < M < 2$ implies margination.

4.4 Summary

The reverse Fåhræus effect has been studied for marginated particles in the blood stream, such as platelets, drug carriers, and large polymers or von Willebrand factors. The theoretical analysis and simulation results show that this effect is much stronger than the Fåhræus effect for RBCs. Interestingly, the reverse Fåhræus effect is significantly amplified at high hematocrits, in contrast to the Fåhræus effect which is most pronounced at lower hematocrits. This effect is beneficial for drug delivery such that the concentration of injected drugs would effectively be higher in the microcirculation. This effect is a direct result of the margination process.

Part II

von Willebrand factor adhesion

Chapter 5

Flow-induced adhesion of shear-activated polymers to a substrate

Adhesion of polymers and proteins to substrates plays a crucial role in many technological applications and biological processes. A prominent example is the von Willebrand factor (VWF) protein, which is essential in blood clotting as it mediates adhesion of blood platelets to the site of injury at high shear rates. VWF is activated by flow and is able to bind efficiently to damaged vessel walls even under extreme flow-stress conditions; however, its adhesion is reversible when the flow strength is significantly reduced or the flow is ceased. Motivated by the properties and behavior of VWF in flow, we investigate adhesion of shear-activated polymers to a planar wall in flow and whether the adhesion is reversible under flow stasis. The main ingredients of the polymer model are cohesive inter-monomer interactions, a catch bond with the adhesive surface, and the shear activation/deactivation of polymer adhesion correlated with its stretching in flow. The cohesive interactions within the polymer maintain a globular conformation under low shear stresses and allow polymer stretching if a critical shear rate is exceeded, which is directly associated with its activation for adhesion. Our results show that polymer adhesion at high shear rates is significantly stabilized by catch bonds, while at the same time they also permit polymer dissociation from a surface at low or no flow stresses. In addition, the activation/deactivation mechanism for adhesion plays a crucial role in the reversibility of its adhesion. These observations help us better understand the adhesive behavior of VWF in flow and interpret its adhesion malfunctioning in VWF-related diseases.

5.1 Introduction

Polymer and protein adhesion to substrates is important in many technological and biological systems and processes^{147,179,213,226}. One of the prominent examples of protein-surface interactions under flow is the adhesion of a large blood protein, von Willebrand factor (VWF), which is a key player in primary hemostasis^{36,176,213}. VWF mediates adhesion of blood platelets to a damaged endothelium, and its function is extremely important at high shear rates, when platelets are not able to bind to a surface autonomously^{188,190}. A malfunction in VWF adhesion can result in severe problems ranging from uncontrolled bleeding to thrombus formation^{76,186,192}.

The mesoscopic structure of VWF resembles that of a polymer, as it consists of a number of VWF dimers bound to each other in a chain-like configuration^{71,176,213}. At low shear rates or without flow, VWF exhibits a globular configuration due to its internal associations, while at high shear rates VWF stretches and is able to adhere^{75,191,213}. Therefore, VWF is often referred to as a shear-activated protein^{191,213}. Motivated by the flow properties of VWF, a number of simulation studies about the behavior of a self-attractive^{6–8} and a self-associating^{5,199,200} polymer in flow have been performed. The self-attractive polymer is modeled by an attractive potential between each pair of monomers, while the self-associating model employs inter-monomeric bond-like interactions with prescribed kinetics. Both models were shown to reproduce shear-responsive stretching of a polymer similar to that of VWF^{5,6,8,200}. An interesting result is that unfolding of a globular polymer in shear flow proceeds by pulling one of the polymer ends from the globule by fluid stresses⁶.

The occurrence of interactions between VWF proteins and vascular walls in blood flow is facilitated by red blood cells through a process called margination^{111,140}. Hence, red blood cells migrate to the center of a vessel and aid in the migration (or margination) of VWF toward the walls¹⁷². Near the wall, the shear rate is larger than in the bulk blood flow, promoting extension of VWF. Stretching of VWF in flow leads to an adhesion activation, as the adhesive sites within VWF, which are inactive (or shielded) in a globular configuration, may become exposed^{191,213}. Thus, stretched VWF molecules can adhere to a surface. Also, together with platelets adhesion activation of VWF by shear flow results in the formation of VWF-platelet aggregates, which are actually reversible such that they disappear when the flow strength is significantly reduced or the flow is stopped^{26,40,75,92}. These fascinating properties of VWF are governed by the intra-molecular cohesive interactions and the characteristics of single adhesive bonds, as well as by the collective behavior of multiple bonds formed during adhesion. A recent experimental study with a single adhesive domain of VWF¹⁰³ has demonstrated that single adhesive bonds exhibit two bound states with different dissociation rates, which closely resembles a dual catch-slip bond^{158,167}, whose lifetime first increases

and then decreases as a function of bond extension. Even though the properties of single bond interactions have been measured, the question how their collective behavior governs overall adhesion of VWF multimers remains unanswered.

A recent computational study¹⁷³ has focused on the adsorption of self-attractive polymers to surfaces, with a homogeneous surface potential, under shear flow. A number of interesting adsorption states have been found, from which a rolling globule at moderate adhesion and a slipping disk configuration at high adhesion strength are relevant for the case of a polymer with high cohesive interactions. However, the adhesion of VWF is mediated by specific bond interactions, which may not be properly accounted for by a homogeneous surface potential. Simulation studies with bonded adhesion interactions^{174,203} suggest that a catch-like bond may significantly enhance polymer capture and adsorption at the surface. These studies did not consider the activation of polymer adhesion by shear flow and the reversibility of adhesion under flow stasis, which are the main foci of our study.

We investigate systematically the adhesion of shear-activated polymers. A bead-spring polymer model includes an inter-monomer attractive potential, which promotes a globular configuration of the polymer in equilibrium and defines a critical shear rate for its stretching in flow. Activation of polymer adhesion is directly associated with the degree of local stretching of the polymer. Polymer adhesion starts with a capture of one of its ends by a surface, because its stretching proceeds by a protrusion of one of its ends from a compact globule⁶. This initial tethering has to be strong enough to withstand high shear forces exerted by the flow, which is likely to be mediated by catch-like bonds, consistently with previous studies^{174,203}. Then, a tethered globule is unfolded by the flow, resulting in further polymer activation and complete polymer adhesion. Several different adhesive states are found, including sticking or firm adhesion, slipping along the surface, roll-slipping motion, and rolling at the surface along the flow direction. Transitions between different states are mainly governed by the lifetime of the bonds and the applied shear stress.

Even though the polymer adhesion is mainly influenced by the lifetime of bonds, and not primarily by a bond style, the reversibility of adhesion after flow cessation is strongly affected by a bond type and by the bond activation/deactivation process. For instance, catch bonds mediate stable adhesion of the polymer at high shear stresses, when their lifetime is large, but allow the dissociation of the polymer from a surface when the flow has been stopped, since their lifetime is reduced when the applied stress is turned off. Clearly, the same behavior would not be possible with pure slip-like bonds. Furthermore, we compare the desorption of a shear-activated polymer with a polymer whose beads are always adhesive and conclude the shear activation/deactivation mechanism is crucial for adhesion reversibility. This polymer model motivated by VWF suggests that catch bond interactions and adhesion

activation/deactivation are important components for efficient adhesion of VWF at high shear rates and its desorption after stopping the flow. Our simulation results can be used for the interpretation of changes in VWF adhesion in VWF-related diseases.

5.2 Shear-activated polymer model

Our model for a shear-activated polymer is motivated by VWF, which retains its compact shape at low fluid stresses or in the absence of flow, but is able to stretch at high enough shear rates (or stresses)^{75,176,191}. The model is based on a bead-spring chain with self-avoiding attractive monomers^{6–8}, that has been used for modeling VWF stretching in shear flow. Consecutive polymer beads are connected by springs represented by finite extensible nonlinear elastic (FENE) potential¹⁰⁹,

$$U_{\text{FENE}}(r_{ij}) = -\frac{1}{2}k_s l_{\text{max}}^2 \ln \left(1 - \left(\frac{r_{ij}}{l_{\text{max}}} \right)^2 \right), \quad (5.1)$$

where k_s is the spring stiffness, $l_{\text{max}} = 2d_{\text{pol}}$ is the maximum spring extension, d_{pol} is the

bead diameter, and r_{ij} is the distance between neighboring beads i and j . In all simulations, k_s is set to $25000k_B T d_{\text{pol}}^{-2}$ such that the polymer springs can be considered nearly inextensible. Furthermore, we set the basic units of energy and length to $k_B T = 0.4$ and $d_{\text{pol}} = 0.5$, corresponding to 4.3×10^{-23} J and $0.5 \mu\text{m}$ in physical units, respectively. The polymer model is coupled to a SDPD fluid through a friction force, as described in references^{94,180}.

Self-avoidance and attractive interactions between beads, which lead to a globular configuration, are modeled by the 12-6 Lennard-Jones (LJ) potential as

$$U_{\text{LJ}}(r_{ij}) = 4\epsilon_{\text{LJ}} \left[\left(\frac{d_{\text{pol}}}{r_{ij}} \right)^{12} - \left(\frac{d_{\text{pol}}}{r_{ij}} \right)^6 \right], \quad (5.2)$$

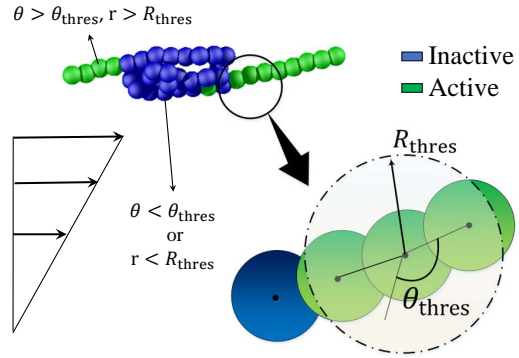


Fig. 5.1 Schematic of an attractive polymer with $N = 30$ beads in shear flow. Different bead colors denote non-activated (blue) or activated (green) polymer beads for adhesion. The colors are assigned using the two criteria from equations (5.3) and (5.4) which determine a conformation-dependent bead activation for adhesion.

where $\epsilon_{LJ} = 4k_B T$ is the depth of the potential well which controls the attraction strength. This self-avoiding attractive polymer model has been shown to exhibit stretching at large enough shear rates^{6–8} which is similar to the behavior of VWF in shear flow^{75,176,191}.

In a globular configuration, the polymer remains non-adhesive, while in a stretched state under flow, adhesive interactions with a surface become possible. This activation mechanism is modeled by tracking the degree of local stretching of the polymer in flow⁹⁴, as illustrated in Figure 5.1. Two geometrical criteria are considered for the bead activation. The first condition corresponds to the angle between two adjacent bonds linking the bead i to its neighboring monomers ($i-1$ and $i+1$) which is directly related to the degree of local stretching of the polymer. Mathematically, it can be expressed as

$$\theta_{i-1,i,i+1} \geq \theta_{\text{thres}} \quad 2 < i < N-1, \quad (5.3)$$

where θ_{thres} is a threshold angle. Note that this condition is always assumed to be true for the first and the last bead in the polymer. The second criterion monitors the proximity of non-direct neighboring beads within a polymer and is expressed as

$$r_{ij} \geq R_{\text{thres}} \quad j \neq i, i \pm 1, \quad (5.4)$$

where R_{thres} is a threshold radius. This condition prohibits activation of a polymer bead for adhesion within a globule, even if the condition (5.3) is satisfied. Thus, an inactive bead becomes activated when the two conditions above are satisfied. Similarly, an active bead will be deactivated when one or both criteria are not met.

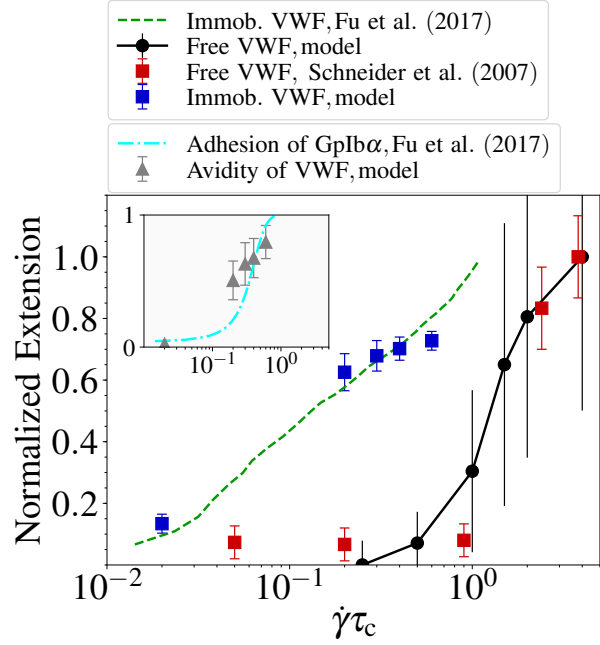


Fig. 5.2 VWF extension and avidity calibrated with the experimental results. The normalization of extension for immobilized polymers is performed with the contour length of the polymer (R_s/L_{VWF}) for both experiments and simulations. For free flowing VWFs, the normalization is based on the maximal stretching because the contour length is not known in experiments. The inset diagram shows the normalized adhesion of platelet receptor GPIb α to immobilized VWFs in experiments, and the avidity of the immobilized VWF in simulations. The experimental results are extracted from the works of Schneider et al. 2007¹⁹¹ and Fu et al. 2017⁷⁵.

In simulations, we set $\theta_{\text{thres}} = 150^\circ$ and $R_{\text{thres}} = 1.5d_{\text{pol}}$. It is important to note that the two criteria are not completely independent. The radial threshold cannot be larger than $\sqrt{2(1 - \cos(\theta_{\text{thres}}))}$, since otherwise it would be already automatically satisfied by the angle criterion. Clearly, different thresholds will result in a weaker or stronger sensitivity of polymer activation to adhesion. Sensitivity tests for a wide range of the thresholds show that a satisfactory correlation between polymer conformation and its activity is achieved within the ranges $\theta_{\text{thres}} \in [120^\circ, 170^\circ]$ and $R_{\text{thres}} \in [1.2d_{\text{pol}}, 1.8d_{\text{pol}}]$. The polymer model with these criteria will be called conformation-dependent (CD) polymer, while a polymer without these criteria is referred to as conformation-independent (CI) polymer. Thus, all CI-polymer beads are always adhesive. Furthermore, active polymer beads and adhesive sites at the wall can form only a single bond, i.e. if a bead (or a site) is already bound to a partner, no further bonds are possible until this bead (or site) becomes free.

Figure 5.2 shows the behavior of the calibrated model in comparison with the experimental results on a free flowing VWF¹⁹¹ and an immobilized VWF⁷⁵. Both model and experiments demonstrate that, (1) the stretching of VWF polymers is critical based on shear rate, (2) the stretching of VWF polymers occurs in order of magnitude smaller shear rates for immobilized polymers than for free flowing ones, and (3) the avidity or adhesiveness of VWF polymers is closely related to their stretching in the flow. The dynamic behavior of our polymer in the flow is quantitatively equivalent to the dynamics of VWF polymers in experiments. The activity and adhesion of the polymer is qualitatively related to the experimental results. It is noted that the size of the VWF in experiments and simulations is in the same order of $10 \mu\text{m}$.

5.3 Adhesive bonds

It is intuitive that bonds should rupture under strong enough stresses. Thus, the slip bond model assumes that the detachment probability of a bond increases as the applied stress (or force) on this bond is elevated. An alternative characteristic to the detachment probability is the lifetime of a bond, which for a slip bond decreases with increasing applied force. However, a number of experiments^{38,108,225} have demonstrated that the lifetime of certain ligand-receptor interactions may increase as the force is elevated. In this case, the bond is referred to as a catch bond³⁸. However, for any physical bond it is clear that when the applied force becomes large enough the bond will eventually rupture. Therefore, the lifetime of an initially catch bond has to start decreasing when a certain value of the applied force is exceeded. As a result, the catch bond behavior should be rather considered as a dual catch-slip behavior. Even though the catch-slip behavior has been found for a limited number

of ligand-receptor cases^{108,225}, it is well accepted that this type of bonds is not special but the rule rather than the exception in biological systems²²⁵. For example, adhesion of VWF to platelet GPIb α receptor exhibits the catch-slip behavior^{40,103,247}.

An adhesive interaction between two available sites can be formulated as a 'chemical' reaction between the unbound and bound states with the rates k_{on} and k_{off} called association and dissociation rates, respectively. The reaction rates determine the frequency of state change, which is modeled by the transition probabilities P_{on} and P_{off} ¹⁸ as

$$\frac{dP_{\text{on}}}{dt} = -k_{\text{on}}P_{\text{on}}, \text{ if } r \leq r_{\text{cut}}^{\text{on}}, \quad (5.5)$$

while $P_{\text{on}} = 0$, if $r > r_{\text{cut}}^{\text{on}}$, and

$$\frac{dP_{\text{off}}}{dt} = -k_{\text{off}}P_{\text{off}}, \quad (5.6)$$

where $r_{\text{cut}}^{\text{on}}$ is the cutoff range for bond association, as shown in Figure 5.3.

In simulations, we assume k_{on} to be constant, while k_{off} follows the aforementioned catch-slip behavior. This can be described by the two-pathway model¹⁵⁸, which assumes two force-dependent barriers for bond dissociation. Thus, the dissociation rate in this model includes both catch-bond and slip-bond dissociation rates,

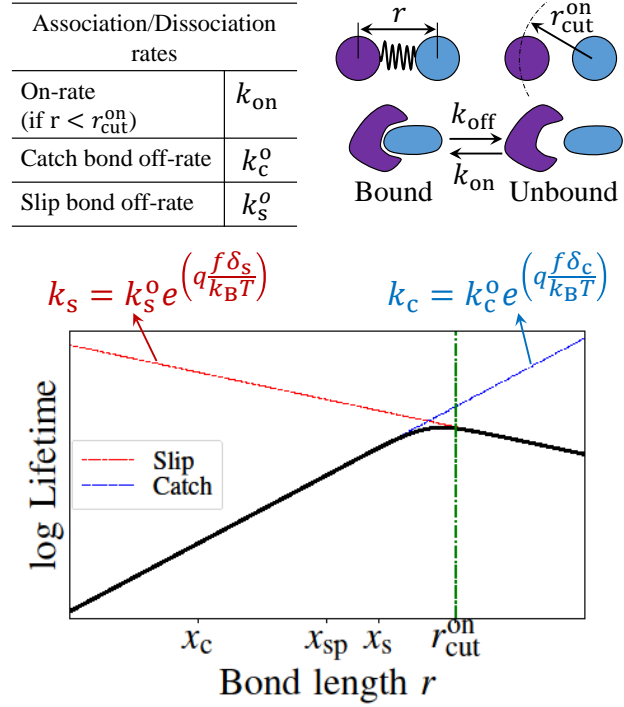


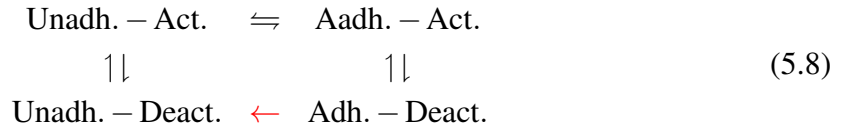
Fig. 5.3 Bond lifetime of the two-pathway model, which first increases and then decreases with an increasing bond length r , imitating the catch-slip behavior. x_c and x_s are the characteristic catch and slip lengths, and x_{sp} is the adhesive bond equilibrium length as specified in Equation (5.7) $r_{\text{cut}}^{\text{on}}$ is the cutoff radius for adhesive bond association as described in Equation (5.5). Correspondence between bond parameters and its lifetime is representing the situation employed in simulations of polymer adhesion.

$$k_{\text{off}} = k_c^o \exp\left(q \frac{f \delta_c}{k_B T}\right) + k_s^o \exp\left(q \frac{f \delta_s}{k_B T}\right), \quad (5.7)$$

where $\delta_c = x_c - x_{\text{sp}}$, $\delta_s = x_s - x_{\text{sp}}$, q is a dimensionless scaling coefficient, and $f = k_b(r - x_{\text{sp}})$ is the harmonic bond force applied to the adhesive bonds with a spring constant k_b and an equilibrium spring length x_{sp} . x_c and x_s are the catch and slip bond characteristic lengths, respectively. Also, k_c^o and k_s^o are the catch and slip off-rates. When $r < x_{\text{sp}}$ the catch bond

dominates, when $r > x_{sp}$ the slip bond dominates. Note that $x_c < x_{sp} < x_s$, in order to have a catch-slip behavior. Figure 5.3 schematically shows the lifetime of such bonds as a function of the bond length r . The lifetime first increases and then decreases with increasing r , mimicking the catch-slip behavior. It is assumed that $x_{sp} = 0.5d_{pol}$, $x_c = 0.8x_{sp}$, $x_s = 1.08x_{sp}$, and $r_{cut}^{on} = 1.2x_{sp}$ as shown in Figure 5.3. The harmonic bond stiffness for adhesive bonds is set to $k_b = 25000k_B T d_{pol}^{-2}$. The dimensionless coefficient q has been added to the expression for k_{off} (equation (5.7)) as a modification of the lifetime of bonds in order to calibrate polymer adhesive behavior with experiments on VWF-platelet adhesion¹⁸⁸. Accordingly, $q = 1/40$ in our simulations, while it is unity in the original two-pathway model¹⁵⁸.

A system of a polymer bead and substrate can be divided into four states, (1) unadhered-activated (U-A), (2) unadhered-deactivated (U-D), (3) adhered-activated (A-A), and (4) adhered-deactivated (A-D). The transition of activated and deactivated states (x-D and x-A) is correlated to the configurations of polymer and satisfy detailed balance by essence because the polymer configurations are directly related to the thermodynamics of the system. The adhesion of the polymer bead is related to the on- and off-rates imposing a detailed balance condition in equilibrium. If an adhered polymer bead gets deactivated, however, the detailed balance condition is not valid anymore. The transitions of the states can be written as,



The probability of the state A-D is close to zero if the activation of the polymer bead correlates with the polymer stretching, which is the case for VWF polymers. Otherwise, the transition from A-A to A-D must be avoided in the model to maintain detailed balance. Thus, the transitions of the states of the the system must be

$$U - D \rightleftharpoons U - A \rightleftharpoons A - A \tag{5.9}$$

eliminating state A-D.

5.4 Setup

A polymer chain is modeled with 30 beads, approximating a VWF polymer with contour length of $L_{VWF} = 15 \mu m$. The basic units used for the normalization of model quantities are length (d_{pol}), thermal energy ($k_B T$), and time (τ_c). The time scale is defined as the inverse of the critical shear rate of globule-stretch transition for a polymer⁹⁴, $\tau_c = \dot{\gamma}_c^{-1}$, where $\dot{\gamma}_c$ is

the critical shear rate above which the polymer globule stretches. $\tau_c = 2$ in simulations and $\tau_c \approx 5 \times 10^{-4}$ s in experiments¹⁹¹, assuming that $\dot{\gamma}_c \approx 2000$ s⁻¹.

The simulation system corresponds to a slit, bound by two walls in y direction, while in the other two directions periodic boundary conditions are applied. The slit size is $60d_{\text{pol}} \times 10d_{\text{pol}} \times 12d_{\text{pol}}$. The walls are modeled by frozen SDPD particles which possess the same structure (characterized by a radial distribution function) as that of the fluid. The wall thickness is equal to r_c . In addition, bounce-back reflection of fluid and polymer particles is imposed at the fluid-solid interfaces. To enforce no-slip boundary conditions at the wall, an adaptive shear force⁵⁹ is applied to fluid particles within a fluid layer with the thickness r_c .

Simple shear flow is imposed by keeping the lower wall (at $y = 0$) stationary and moving the upper wall (at $y = 10d_{\text{pol}}$) with a constant velocity v_x along the x axis. Thus, the imposed shear rate is $\dot{\gamma} = v_x/L_y$, where L_y is the distance between the walls. $L_y = 10d_{\text{pol}}$ has been chosen small enough in order to efficiently initiate the adhesion of a polymer when it becomes activated. Active polymer beads can adhere to adhesive sites at the lower wall, which are homogeneously distributed on a square lattice with a lattice constant $a = 0.5d_{\text{pol}}$. The upper wall does not have any adhesive sites and remains non-adhesive for the polymer. Note that there are no pairwise interactions between the adhesive sites and other particles; thus, the adhesive sites can only form a bond with active polymer beads.

5.5 Initial adhesion

Dynamics of self-avoiding polymer chains in shear flow has been extensively studied^{34,210}. Since the simple shear flow can be decomposed into rotational and elongational fields, a polymer in this flow experiences periodic stretch-tumbling dynamics²¹⁰. The dynamics and stretching behavior of a self-attractive polymer is remarkably different, as high enough shear stresses are needed to initiate unfolding of a globular structure^{6,8}. Interestingly, unfolding of a self-attractive polymer starts by pulling a tether from the globule or equivalently one of the polymer ends⁶. Thus, we expect that the initial adhesion of an attractive polymer is very likely to proceed by binding one of its ends first.

Figure 5.4 illustrates a typical adhesion process of a shear-activated polymer. At first, one end of a partially stretched polymer adheres to the wall (Figure 5.4a) and the polymer becomes tethered. Next, the tethered polymer is subjected to significant shear forces exerted by the fluid flow, leading to a further unfolding of the globule (Figure 5.4b). Note that stretching of an immobilized polymer occurs at much lower shear rates than those required for the stretching of a freely-suspended globule in shear flow²⁰². Thus, after initial tethering, unfolding of a globule proceeds rather rapidly (Figure 5.4c). This behavior is also consistent

with the observation that stretching of a self-attractive polymer in elongational flow occurs at much lower strain rates in comparison to its stretching in shear flow¹⁹⁸. This effect is important at sudden vessel constrictions (e.g., stenosis), where the elongational component of the flow is significantly enhanced. Following a rapid unfolding of the tethered globule (Figure 5.4c), the polymer displays new active (adhesive) sites, which can bind to a surface as the shear flow pushes the free polymer closer to the surface. Finally, the polymer fully adheres (Figure 5.4d).

It is important to emphasize that the formation of an initial adhesion (Figure 5.4a) plays a deciding role for the overall adhesion to a surface. Clearly, this initial interaction has to be strong enough, and the formed bonds need to possess a long enough lifetime in order to sustain large forces exerted by the fluid flow and allow enough time for polymer stretching and further adhesion to occur. Therefore, this process has to be facilitated by a relatively fast association rate and need to involve preferen-

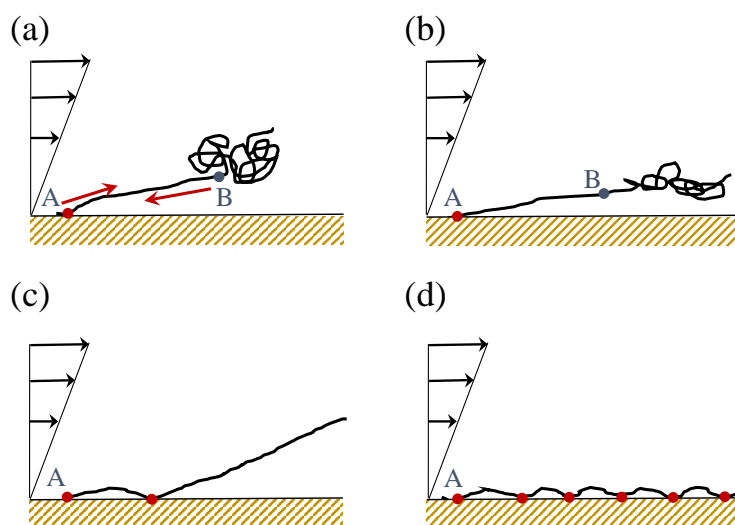


Fig. 5.4 Schematic illustration of polymer adhesion to a substrate. (a) formation of initial adhesion to a surface by one of its ends, (b) stretching of an initially tethered polymer, (c) partially adhered polymer after stretching, and (d) fully adhered polymer.

tially a catch-like bond behavior. In fact, recent simulations²⁰³ suggest that the adhesion of VWF to a surface at high shear rates is controlled by long-lived (catch-like) bonds. Similarly, adsorption of homopolymeric globules to a surface has been found to be enhanced at high shear rates by catch-bond interactions¹⁷⁴.

High enough shear rates are not only required for polymer stretching with a consecutive adhesion activation, but may also lead to the enhancement of polymer adhesion¹⁷⁴. This idea may sound counterintuitive at first glance, because high shear rates obviously result in high shear stresses exerted on an immobilized polymer. Therefore, a necessary precondition here is an efficient initial capture of the polymer at a surface, as discussed above. Nevertheless, after the initial tethering of a shear-activated polymer, high shear rates lead to very rapid

polymer stretching and activation, and push the tethered polymer quickly toward the surface, enabling further contacts with the surface.

5.6 Adhesion states

The behavior of a single bond can be well described, for instance, by the lifetime shown in Figure 5.3, which depends on the bond's kinetic properties. However, the adhesion of shear-activated polymers is governed by a collective behavior of many bonds, whose behavior is much more complex than that of a single bond. Bond cooperativity is facilitated by the elastic backbone of the polymer, making the adhesion dynamics of the whole structure important and limiting a direct association between single bond properties and overall dynamics of the polymer. Therefore, the collective behavior of a number of bonds results in several adhesion regimes of a shear-activated polymer in shear flow. Our simulation results indicate that the adhesion dynamics of a polymer can be divided into five distinct states, including sticking, slipping, roll-stick motion, rolling motion, and complete detachment. The sticking phase corresponds to a firm adhesion and is achieved for highly adhesive interactions between a polymer and substrate. Interestingly, polymers in the sticking state exhibit a high degree of stretching when adhered, such that the maximum extension of an adhered polymer is nearly equal to its contour length. Complete detachment occurs when bonded interactions are not able to withstand shear forces exerted by the flow. Polymer detachment is likely to occur for slip-like bond interactions, as has been shown recently¹⁷⁴.

Our simulation results suggest that the average polymer extension can be used as a marker to separate different states of polymer adhesion into distinct groups. Figure 5.5 illustrates the time evolution of polymer extension, R_s , for the three different states, rolling, roll-stick motion, and slipping. Similar to the sticking state, the extension of an adhered polymer in the slipping state is very close to its contour length L_{VWF} . However, the difference between sticking and slipping states is overall motion of the polymer, such that a slipping polymer slowly slides along the surface, while the motion of a sticking polymer can be practically neglected. The sliding motion of a slipping polymer is facilitated by the continuous breakage of existing bonds and the formation of new ones. Weakening of polymer-substrate adhesion results in intermediate rolling of an adhered polymer. The polymer starts losing some of its adhesive bonds and the freed beads are carried forward by the flow, where they may form new bonds. This motion may persist for a short time and therefore, it resembles rolling. However, in the roll-stick state, the polymer rolling is transient and polymer extension periodically changes from a nearly globular extension ($\sim 0.2L_{VWF}$) to almost fully extended polymer, as shown in Figure 5.5. Hence, in this state, the average polymer extension exhibits significant

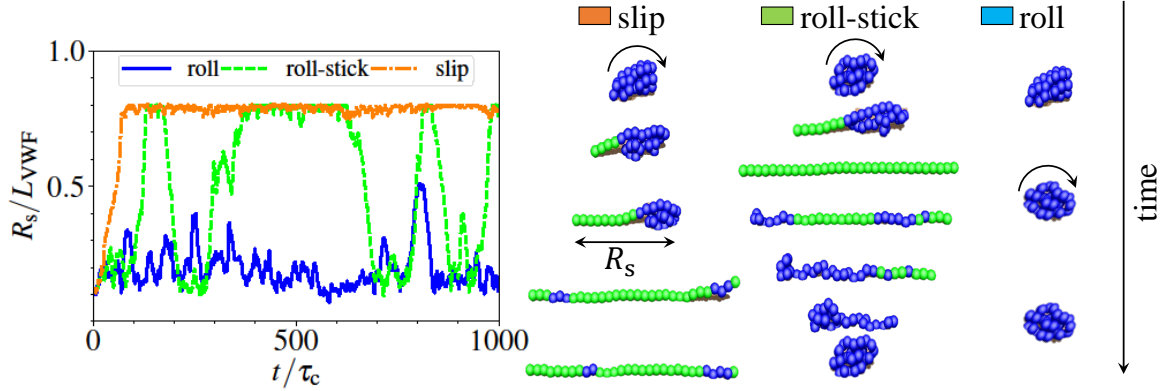


Fig. 5.5 Extension of an adhered polymer followed in time for three different adhesion states: rolling, roll-stick, and slipping. All three simulations are performed with the parameters $k_s^o \tau_c = 2 \times 10^{-2}$ and $k_c^o \tau_c = 2$. Slipping, roll-stick, and rolling states correspond to $k_{on} \tau_c = 2 \times 10^1$, $k_{on} \tau_c = 2$, and $k_{on} \tau_c = 2 \times 10^{-1}$, respectively. On the right, a few successive snapshots of the three phases are shown. The extension R_s in the direction of the flow is also illustrated.

jumps with a large variance of about 50% of its contour length. Finally, a further weakening of adhesive interactions between a polymer and a surface leads to the rolling state, where the polymer experiences nearly constant rolling motion. This state is well characterized by a relatively small polymer extension as shown in Figure 5.5. Note that in the rolling state, the polymer never completely detaches and maintains its contact with the surface.

Based on the observations above, we can define three major adhesion states using the average extension of an adhered polymer. The criteria for different states are given by

$$\frac{\langle R_s \rangle}{L_{VWF}} \begin{cases} \geq 0.7 & \text{sticking/slipping} \\ 0.4 < * < 0.7 & \text{roll - stick} \\ \leq 0.4 & \text{rolling} \end{cases} \quad (5.10)$$

Following this definition, we study the dependence of polymer adhesion on a number of system properties, such as association and dissociation rates and shear rate of the flow. Figure 5.6 presents several adhesion state diagrams of a shear-activated polymer at $\dot{\gamma} \tau_c = 0.4$ with $N = 30$. The orange, green, and blue colored areas correspond to slipping, roll-stick motion, and rolling states, respectively. Figure 5.6a for a fixed $k_c^o \tau_c = 2$ clearly indicates that adhesion of a shear-activated polymer to a surface requires a large enough association rate, which may limit overall polymer adhesion if it is too small in comparison to the shear rate $\dot{\gamma}$. Another interesting observation from Figure 5.6a is that the sticking/slipping state occurs mainly when the slip-rate constant k_s^o of the stick-slip bond model is small enough. Note that a

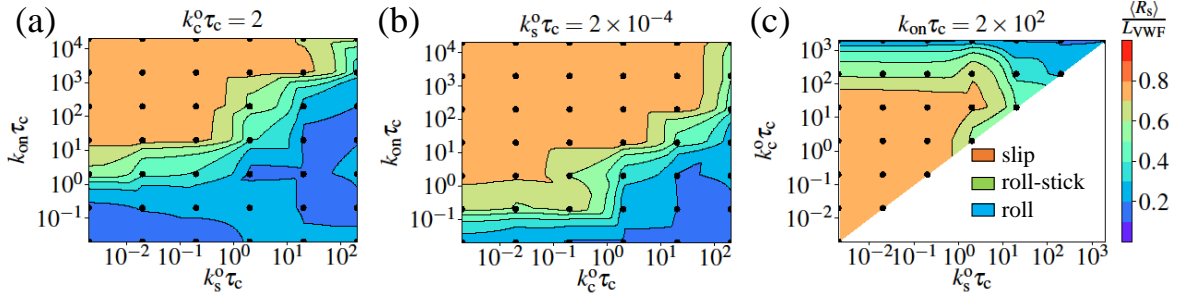


Fig. 5.6 Adhesion state diagrams of a shear-activated polymer at $\dot{\gamma}\tau_c = 0.4$ with $N = 30$. (a) the effect of k_{on} and k_s^0 on adhesion state with fixed k_c^0 ; (b) the effect of k_{on} and k_c^0 on adhesion state with fixed k_s^0 ; (c) the effect of k_c^0 and k_s^0 on adhesion state with fixed k_{on} . The polymer extension is normalized by the polymer contour length, L_{VWF} , and serves as a marker for adhesion states. The color-bars are obtained from the average polymer extension over time.

decrease in both k_c^0 or k_s^0 (see Equation (5.7)) results in a general increase of single bond lifetime. Thus, the bond lifetime is the main determinant of the transition to the rolling state at large enough k_s^0 , because an increase in k_s^0 significantly shortens bond lifetime, making the sticking/slipping state unstable. For even larger k_s^0 values a complete detachment of the polymer occurs.

Figure 5.6b shows polymer adhesion as a function of the normalized on-rate $k_{on}\tau_c$ and catch off-rate $k_c^0\tau_c$ with a fixed slip off-rate $k_s^0\tau_c = 2 \times 10^{-4}$. Similar to the diagram in Figure 5.6a, transition from the sticking/slipping state to the rolling state occurs as k_c^0 is elevated. Again, this transition is governed here by the lifetime of bonds, which is significantly shortened by an increase of k_c^0 . A noticeable difference between the adhesion diagrams in Figure 5.6a and 5.6b is the existence of the slipping state at low association rates k_{on} for small k_c^0 values in Figure 5.6b. This can be explained by the fact that the bond lifetime becomes very large when both k_c^0 and k_s^0 are quite small. Hence, even though bond formation is rather infrequent at low k_{on} , the formed bonds are long lived, allowing enough time for a polymer to stretch and form further bonds with a surface.

Finally, Figure 5.6c presents adhesion diagram as a function of off-rates $k_c^0\tau_c$ and $k_s^0\tau_c$ with a fixed on-rate $k_{on}\tau_c = 2 \times 10^2$. Consistently with the other two diagrams in Figure 5.6a and 5.6b, the transition from the slipping state to the rolling state in Figure 5.6c occurs when both k_c^0 and k_s^0 become large enough or equivalently when the lifetime of bonds becomes small enough. Note that the slipping-to-rolling transition in Figure 5.6 is also qualitatively consistent with that in reference¹⁷³ for highly cohesive polymers, where a decrease in the adhesion strength leads to the slipping-to-rolling transition. A quantitative comparison between our results and this recent simulation study¹⁷³ is not possible, because adhesion

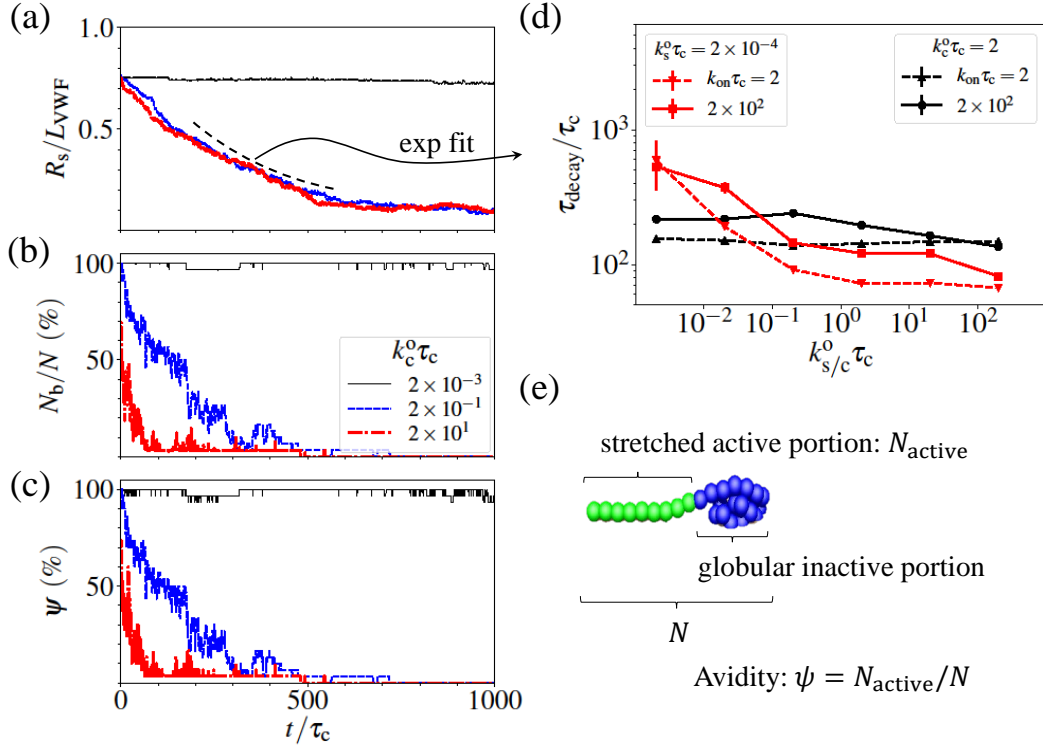


Fig. 5.7 At flow stasis, the adhesion of the polymers to the substrate is characterized by various properties in time. Time evolution of (a) polymer extension R_s , (b) number of adhesive bonds N_b , and (c) polymer avidity ψ for several catch-dissociation rates k_c^0 after the flow has been stopped. (d) The decay time of polymer extension τ_{decay} fitted by an exponential curve. The red curves correspond to a constant slip bond off-rate k_s^0 , while the catch bond off-rate k_c^0 changes, and vice versa for the black curves. The catch bond off-rate clearly affects the detachment time, in contrast to the slip off-rate. (e) The polymer avidity is defined as the ratio between the number of active beads and the total number of monomers. $k_{on} \tau_c = 2 \times 10^2$ and $k_s^0 \tau_c = 2 \times 10^{-4}$ for all diagrams.

is implemented through a homogeneous surface potential, while polymer adhesion here is governed by discrete bond interactions. Another numerical investigation¹⁷⁴ has considered catch bonds for polymer adhesion and shown that catch bonds significantly enhance polymer capture by an adhesive surface. Our work adds the polymer activation/deactivation depending on its conformation, and focuses on the reversible adhesion of a shear-activated polymer to the wall.

Lastly, we would like to mention that the other parameters (e.g., the number of adhesive bonds, the number of active beads or polymer avidity), which can be also used for the characterization of polymer adhesion states, appear to be less robust than the average polymer extension for the identification of different adhesion states. Thus, the average extension of an adhered polymer has been used in all subsequent analyses.

5.7 Reversible shear-dependent polymer adhesion

A very interesting behavior of shear-activated polymers is that their adhesion might be reversible when the flow is stopped or significantly reduced. This behavior is reminiscent of the dissociation of VWF-platelet aggregates, which form at high shear rates, but disaggregate when the flow is stopped^{26,40,182}. Figure 5.7 illustrates time evolution of several characteristics of a fully adhered polymer (in the sticking state) for several values of the catch-dissociation rate k_c^0 after the flow has been stopped. Figure 5.7a shows the polymer extension, which decreases in time if the off-rate k_c^0 is large enough, indicating that the polymer attains a globular configuration from a nearly fully-stretched adhered state. The polymer slowly attains a globular configuration due to its cohesion interactions and a decrease in polymer avidity as it collapses (Figure 5.7c). The avidity (ψ) of a polymer is defined as the active portion of the polymer (Figure 5.7e). Similar to the polymer extension, Figure 5.7b and 5.7c demonstrate that the number of adhesive bonds and the polymer avidity decay in time. Hence, the reversible adhesion process of a shear-activated polymer can be well described. An adhered polymer with catch-slip surface interactions remains stable in shear flow unless the shear stresses become very large or equivalently when formed bonds stretch significantly such that they reach their slip part where the lifetime strongly drops (see Figure 5.3). At an intermediate shear stress, most of the bonds actually have very long lifetime due to the catch part of bond interactions. When the shear stress is removed by stopping the flow, the adhesive bonds return to their nearly unstressed state, and their lifetime significantly drops because of their catch bond characteristic. Hence, the polymer starts losing its bonds to the substrate and forms a globule, mainly due to its internal attractive interactions. Eventually, the globule completely dissociates from the surface, since all polymer beads become inactive.

The decay of the polymer extension at flow stasis is fitted by an exponential curve with a time scale τ_{decay} . The results are shown in Figure 5.7d and indicate that the catch dissociation rate determines reversibility and the detachment of adhered polymers from the wall, when shear flow is turned off. All characteristics in Figure 5.7 corroborate this proposition, because the polymer extension, the number of adhered beads, and polymer avidity decrease in time for the two cases with high k_c^0 . Thus, it is clear that polymer dissociation time scale is governed by the catch-bond dissociation rate k_c^0 .

The third case in Figure 5.7 with $k_c^0 \tau_c = 2 \times 10^{-4}$ exhibits practically no change in all characteristics in time, suggesting that the adhesion remains stable even when the flow is stopped. In this case, the catch-bond dissociation rate k_c^0 is so small that even in a nearly unstressed state, the lifetime of the bonds remains long enough to facilitate stable adhesion. Here, an infrequent bond dissociation is overpowered by the formation of new bonds, maintaining stable polymer adhesion. Thus, reversible adhesion of shear-activated polymers

results from a subtle balance between the catch-bond dissociation rate, bond association rate, and the cohesion strength within the polymer globule. Note that a slip-bond model alone would not result in such behavior of shear-activated polymers. Even though polymer adhesion mediated by slip bonds can be made stable at high shear stresses by having a long enough lifetime for bonds under stress, the lifetime of slip bonds will further increase when the flow is stopped, making polymer adhesion even more stable.

The reversibility of adhesion with catch-slip bonds also nicely illustrates the enhancement of polymer adhesion by shear flow. Thus, the stress applied by the flow on an adhered polymer stabilizes its adhesion, because the lifetime of its bonds under stress can be significantly larger than that when the stress is removed by stopping the flow. This observation is very similar to the behavior of VWF under flow^{26,75,182}.

5.8 Comparison with the adhesion of a conformation-independent polymer

So far we have discussed adhesion of a conformation-dependent (CD) polymer, for which the activation of polymer beads is conformation dependent or the polymer has to stretch enough to be able to adhere. It is also interesting to compare the adhesive behavior of a CD-polymer to that of a conformation-independent (CI) polymer under same flow conditions. In case of the CI-polymer, all beads are always adhesive independently of its conformation in flow and can form bonds with a surface. For comparison we have selected the following adhesion parameters: $k_c^0 \tau_c = 2 \times 10^{-1}$, $k_s^0 \tau_c = 2 \times 10^{-4}$, and $k_{on} \tau_c = 2 \times 10^3$ which lead to a

strong adhesion of a CD-polymer, as shown in Figure 5.6c. Adhesion of the CI-polymer under flow is also stable for these conditions. Figure 5.8 displays snapshots of an adhered polymer under flow, for the two models, where we observe that the CI-polymer is able to

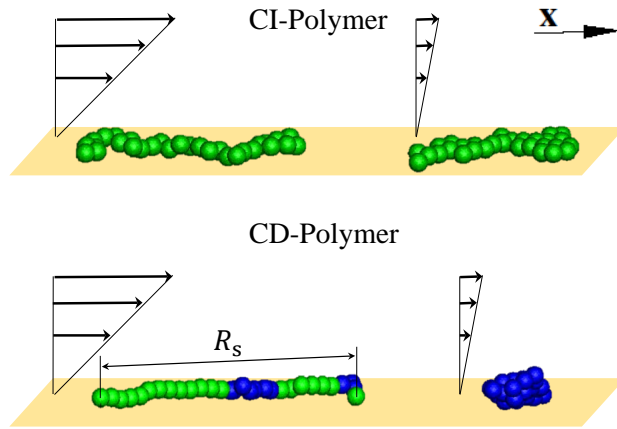


Fig. 5.8 Typical CI- and CD-polymer conformation in shear flow and when the flow is stopped. Blue and green beads represent inactive and active monomers, respectively. CD-polymer dissociates from the surface under no-flow conditions, while the CI-polymer remains adhered.

form more adhesive bonds with the surface in comparison to the CD-polymer. No strong differences in the adhesive behavior between the two models is observed and both polymers show a slow slipping motion at the surface along the flow direction.

The main difference in adhesive behavior of these two polymer models occurs when the flow strength is reduced in a step-wise fashion until the flow is completely stopped, which is presented in Figure 5.9. The number of adhesive bonds, N_b , for the CD-polymer drops to zero in time when the flow is stopped (Figure 5.9a), while N_b of the CI-polymer (Figure 5.9b) does not display any significant changes. This indicates that the CD-polymer dissociates from the surface, while the CI-polymer remains adhesive even after stopping the flow. Extension of the CD-polymer (Figure 5.9a) converges to its globular size. R_s of the CI-polymer (Figure 5.9b) is reduced in time, demonstrating that the CI-polymer attains a more compact form. The typical conformations of both models under no-flow conditions are also illustrated in Figure 5.8, where it is clear that a more compact form of the CI-polymer is still far enough from a globular conformation. Figures 5.9c and 5.9d show the time evolution of the center of mass for both models. The distance y_{cm} between the surface and the center of mass of the CD-polymer increases with time, pointing toward polymer desorption. In contrast, for the CI-polymer, y_{cm} does not display significant changes, indicating that the polymer remains spread and adhered at the surface. Time evolution of the center of mass position along the flow direction x_{cm} in Figure 5.9c and 5.9d demonstrates that both polymers slowly slip along the surface in presence of flow, and finally come to a stationary position after the flow has been stopped.

The drastic difference in reversible adhesion between the CD- and CI-polymers demonstrated above cannot be attributed to the polymer's cohesion strength, polymer-surface bond interactions, or flow conditions, because all these properties were identical in both cases. As the shear flow is decreased to zero, both polymer models tend to attain a globular shape due to the inter-bead cohesive forces, which can be seen from the polymer extension in Figure 5.9a and 5.9b. In case of the CD-polymer, monomers detached from the surface can become deactivated due to a more compact polymer configuration, prohibiting further binding. Gradually, an initially adhered CD-polymer moves toward a globular configuration and finally dissociates from the surface. Even though the initial compression process of the CI-polymer due to the cohesive forces is very similar to that of the CD-polymer, the monomers of CI-polymer are always active for adhesion and able to form new bonds. As a result, the CI-polymer remains bound to the surface irreversibly. Therefore, conformation dependent activation/deactivation of polymer beads plays an important role in reversible adhesion.

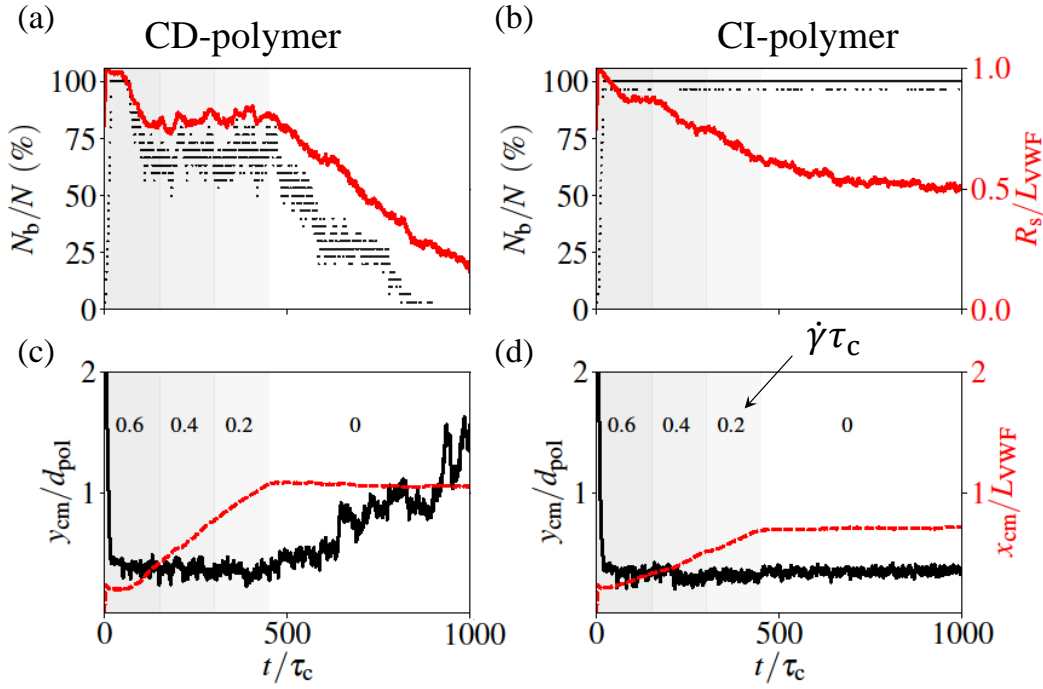


Fig. 5.9 Effect of conformation-dependent activation on the reversibility of polymer adhesion. Number of bonds and polymer extension for (a) a CD-polymer and (b) a CI-polymer with the parameters $k_c^o \tau_c = 2 \times 10^{-1}$, $k_s^o \tau_c = 2 \times 10^{-4}$, and $k_{on} \tau_c = 2 \times 10^3$. As the flow strength is reduced in a step-wise fashion, indicated by different shades of gray and by the corresponding numbers of normalized shear rates, the CD-polymer starts losing its bonds and dissociates from the surface, while the CI-polymer remains bound to the substrate. Time evolution of center of mass positions, including the distance from the surface (y_{cm}) and the position along the flow direction (x_{cm}) is shown for (c) a CD-polymer and (d) a CI-polymer. The evolution of x_{cm} demonstrates that both polymers slowly slip along the surface until the flow is completely stopped, while y_{cm} indicates that the CD-polymer eventually leaves the surface, but the CI-polymer maintains its adhesion.

As already mentioned, VWF is also able to reverse its adhesion when the flow strength is significantly reduced or the flow is stopped^{26,75,182}. In addition, in a globular configuration, VWF remains non-adhesive, because its adhesive sites are shielded^{75,231}. Therefore, it is plausible to suggest that reversible adhesion of VWF proceeds similar to that of the CD-polymer discussed above, and that the deactivation of adhesive sites within VWF molecule due to its partial folding is very important for the reversibility of its adhesion.

5.9 Summary

We have performed a systematic study of adhesion of shear-activated polymers. A polymer is modeled by a bead-spring chain with attractive inter-bead interactions, such that it attains a globular configuration in equilibrium. In shear flow, the polymer is able to stretch if the critical shear rate is exceeded. Polymer stretching in shear flow also governs its activation for adhesion, which is directly associated with the degree of local stretching of the polymer. Adhesive interactions between activated polymer beads and adhesive sites at a surface are mediated by bonds, which are described by the catch-slip adhesion model. Polymer adhesion can be divided into several adhesion states, including sticking or firm adhesion, slipping along the surface, roll-slipping motion, and polymer rolling at the surface along the flow direction. The transition between the sticking/slipping state and the rolling state is mainly governed by the lifetime of bonds and can be triggered when the lifetime is decreased. A further decrease in bond lifetime (or equivalently increase in the bond dissociation rate) leads to a complete detachment of a polymer by the flow or to the inability of a polymer to stably attach to the surface.

Polymer adhesion qualitatively proceeds as follows. At first, strong enough shear stresses result in partial polymer stretching by pulling one of its ends from a compact globular structure, and the activation of the extruded portion of the polymer. Then, the extruded and activated polymer end is able to form initial adhesion (or tethering site) with the surface, which has to be strong enough to withstand high shear forces exerted by the flow on the tethered polymer. After initial tethering, the polymer is rapidly stretched and activated by the flow. Consequently, shear flow pushes the tethered polymer toward the surface, enabling complete polymer adhesion. Note that adhesion stability of the initial tethering site is very important for overall polymer adhesion, which is quickly facilitated by the shear flow.

Even though overall adhesion of shear-activated polymers is mainly governed by the lifetime of bonds, the reversibility of adhesion under a change of flow conditions (e.g., flow cessation) is strongly affected by the type of bonds and by the shear activation/deactivation process. In particular, catch-like bonds facilitate stable adhesion of the polymer at high shear stresses, because their lifetime is large enough under fluid stresses, and permit dissociation of the polymer from a surface when the flow is stopped, since their lifetime significantly drops when shear stress is removed. Given stable adhesion of the polymer at high shear stresses, slip-like bonds would not permit polymer desorption from the surface, because their lifetime increases when shear stresses on them are reduced. Furthermore, a comparison between the conformation-dependent polymer and conformation-independent polymer has shown that the shear activation/deactivation mechanism is important for adhesion reversibility. Adhesion deactivation of non-bound monomers by moving toward a compact globular

structure significantly restricts the renewal of surface bindings and eventually allows polymer dissociation from the surface.

This simulation study has been motivated by the blood protein VWF, which exhibits similar features in flow, including shear activation and the reversibility of adhesion at low or zero shear stresses. The shear-based regulation of VWF adhesion allows efficient blood clotting at high shear rates and leads to the dissolution of VWF-platelet aggregates at low shear rates. Thus, it is plausible to assume that the main results for shear-activated polymers summarized above should be applicable to VWF. These results can also be used for further understanding of changes in VWF adhesion during the course of VWF-related diseases. Since computational methods to study blood flow on the cellular level have made much progress in recent years^{60,74}, a computational study of VWF adhesion under whole blood conditions should be possible in the near future.

Chapter 6

Critical reversible aggregation of platelets and von Willebrand factor

Platelet adhesion to an injured site is important in primary hemostasis. Platelets aggregate at the wounded site in blood vessels by adhering to immobilized stretched von Willebrand factors (VWFs). Counter-intuitively at high shear rates, they aggregate faster than at low shear rates. It has been found in experiments that platelets can adhere to fibrinogen substrates at low shear rates, but they detach from these substrates at shear rates above 900 s^{-1} ¹⁸⁸. Using multi-scale simulations, we show that this critical phenomenon is regulated by VWF avidity - the number of adhesive ligands in VWF concatemer. In addition, platelet-VWF aggregation is reversible when shear rate decreases. This behavior results from the fact that VWF avidity is suppressed at low shear rates by shielding of VWF adhesive domains. Also, considering the strength of the adhesive bonds between VWF and platelet receptors, the reversibility of aggregates is a direct consequence of VWF conformation-dependent avidity. Thus, VWF affinity - the adhesiveness of a single VWF ligand, regulates the dissociation time of aggregates. The simulation results are in excellent qualitative agreement with available experiments.

6.1 Introduction

Many factors synergistically play role in the whole hemostatic process through signalling pathways^{176,187}. But, the molecular structure of VWF polymers plays a key role in this process since a lack of function at any key domain of this protein causes a specific type of von Willebrand Disease (VWD)^{185,213}. The length of VWFs is crucial for the efficiency of primary hemostasis^{36,176,183}, such that overly short VWF concatemers in VWD type 2A

substantially weaken coagulation^{185,213}. It is deduced that the length of VWF polymers is correlated with their avidity or the potential of making bonds with platelet receptors or collagen.

As hypothesized by Springer 2014²¹³, platelet adhesion to VWF is modulated by two mechanisms, avidity and affinity. The avidity of VWF for platelet receptors results from its extension so that more VWF ligands can bind platelet receptors⁸⁹. Moreover, the affinity between VWF A1 domain and platelet receptor GPIb α has two bound-states with different lifetimes¹⁰³ which can be modeled by a catch-slip bond^{89,167}. Both avidity and affinity of VWF concatemers increase when the shear rate is increased.

In this chapter, the platelets are represented by 2 μm -diameter spherical triangulated membranes^{54,55,120,244} with viscoelastic properties at the same order of magnitude of the platelet membrane properties. The vertices on the triangulated platelet membrane are considered as the receptors for VWF ligands. From the simulation results, it is deduced that VWF polymer conformation-dependent avidity is essential in critical adhesion of platelets to VWFs based on shear rate. Moreover, conformation-dependent avidity of VWF is responsible for reversible dissolution of platelet-VWF aggregates at low shear rates which have been formed at high shear rates. In this regard, VWF affinity regulates the dissociation time of the aggregates. The two-state affinity between VWF beads and platelet receptors reduces the lifetime of aggregates substantially at low shear rates.

6.2 Adhesive bonds

Platelet receptors can adhere to different ligands with different bond types. In practice, hemostasis is a synergistic process which includes many ligand-receptor interactions¹⁸⁷; among them, the platelet Glycoprotein complex IIb-IIIa or integrin $\alpha_{\text{IIb}}\beta_3$ for binding to fibrinogen and Glycoprotein Ib α for binding to VWF A1 domain are of most importance in the blood clotting process. The $\alpha_{\text{IIb}}\beta_3$ -fibrinogen bond is irreversible^{188,189}, while GPIb α -VWF A1 domain bond has a very short lifetime¹⁸². However, $\alpha_{\text{IIb}}\beta_3$ -fibrinogen adhesive bond breaks at high shear rates exceeding 600-900 s^{-1} ¹⁸⁸. In contrast, the GPIb α -VWF A1 domain bond is crucial at high shear rates for arresting platelets from the blood stream¹⁸⁸. According to the single molecule measurements of VWF A1 domain and platelet GPIb α receptor interaction¹⁰³, this is a two-state bond depending on the molecular conformation of the VWF A1 domain. This interaction can be modeled by a catch-slip bond formulated by Pereverzev et al. 2005¹⁵⁸. This mechanism is referred to as the VWF two-state affinity which increases at high shear stress. Shear-dependent reversible adhesion of platelets and VWFs

caused by the change of VWF affinity at low shear rates has been verified in experiments using recombinant VWF A1 domain by Doggett et al. 2002⁴⁰.

Since the size of fibrinogen is of the order of nanometers, these ligands are modeled by adhesive points on the surface of the simulation channel. Platelet adhesive interaction with a fibrinogen coated substrate is represented by the Bell model¹⁸. The lifetime of the Bell model is formulated by drawing an analogy between biochemical bond dissociation rates and solid bar fracture rate²⁵⁷ coming from experimental solid mechanics, as

$$\tau = \tau_o \exp\left(\frac{E_o - \gamma f}{k_B T}\right). \quad (6.1)$$

Here, E_o , f , and γ are the bond energy, the bond force, and a characteristic length of the bond, respectively. k_B stands for Boltzmann's constant and T is the temperature. Also, a constant association rate is assigned for bond creation in a short-range distance between a platelet receptor and fibrinogen ligand.

The Bell interaction shows slip-bond characteristics which means that by increasing receptor-ligand distance the bond lifetime decreases as can be seen in Equation (6.1). On the contrary, many biological bonds demonstrate a counter-intuitive catch-slip behavior²²⁶, where the lifetime of a catch-slip bond increases as the force on the bond increases³⁸, and eventually decreases. The catch bond behavior of a receptor-ligand interaction has been measured directly by Kim et al. 2010¹⁰³ for GPIb α -VWF A1 domain bond, and obtained indirectly from the dynamical behavior of a larger system containing one or many receptor-ligand bonds. A very common method is to study shear stress dependent adhesion^{61,225}. For instance, Doggett et al. 2002⁴⁰ and Yago et al. 2008²⁴⁷ have studied the shear-dependent adhesion of GPIb α to VWF, both for the healthy wild-type VWF and the von Willebrand Disease (VWD) mutant type 2B. They found that by applying shear flow on the system, the bond becomes stiffer for the healthy VWF-platelet interaction but not for the mutant type 2B VWF-platelet interaction.

Many models have been proposed to explain the catch-slip behavior of biological bonds¹⁶⁷. Among them, a model introduced by Pereverzev et al. 2005¹⁵⁸ is considered here and explained in [chapter 5](#). Interaction of platelet receptors with substrate ligands is assumed to be slip bonds. Bond parameters are calibrated by the available experimental results. Note that overall qualitative behavior of the system is not very sensitive to the values of the bond parameters, but the model assumed for interactions such as catch-slip or slip bonds.

6.3 Polymer avidity

A conformation change in VWF concatemers alters the number of available ligands for binding^{26,176,212}, referred to as the avidity of VWF²¹³. VWF avidity is correlated with its extension since other domains of VWF polymer shield the adhesive domain (A1 domain) from receptors²³¹. This shielding effect may occur not only at the dimeric level, but also within the whole molecular structure. Therefore, shear stress plays an important role in VWF polymer extension^{191,210} which leads to more platelet-VWF adhesion at high shear rates and less adhesion at low shear rates. Because of high intra-molecular attraction between polymer domains, VWF polymer retains a globular form in equilibrium and stretches at high shear rates, in agreement with simulations^{6,8,191} and experiments¹⁹⁷. Also, since the VWF polymer extension is critically dependent on shear rate^{191,197}, its avidity must be critically dependent on shear rate. For example, the adhesion of blood clot to the vessel wall is reported to be dependent on blood shear rate¹⁴⁶ *in vivo*, and platelet-VWF aggregates reversibly form and dissolve depending on shear rate²⁶ *in vitro*. Moreover, once VWF polymers adhere to an injured site and get immobilized, their extension occurs at shear rates one order of magnitude lower when compared with the free soluble VWF polymers^{7,43}.

In coarse-grained simulations, the VWF avidity, ψ , is defined by the portion of VWF active beads over the total number of VWF beads in the polymer ($\psi = N_{\text{active}}/N_{\text{beads}}$). This quantity shows that how many A1 domains from the VWF polymer are available for GPIb α receptors. It must be noted that each bead of the polymer represents many dimeric VWF subunits containing many A1 domains. As a result, the coarse-grained polymer model mimics the VWF polymer dynamics and adhesion by applying conformation-dependent activity^{89,94}. Thus, the polymer comprises active and inactive beads. Each active bead can adhere to only one receptor within a cutoff distance with a constant association rate, k_{on} .

The model used for VWF adhesive activity is related to two geometrical factors, threshold radius R_{thres} and threshold angle θ_{thres} as follows. The j 'th bead of the polymer is active/adhesive if

$$\begin{cases} r_{ij} \geq R_{\text{thres}} & i \neq j, j \pm 1 \\ \theta_{ijk} \geq \theta_{\text{thres}} & k = j + 1, i = j - 1, \end{cases}$$

where r_{ij} is the distance between the i 'th and j 'th polymer beads and θ_{ijk} is the angle of the bonds shared by the j 'th bead. These criteria supply a conformation-dependent activity for polymers which is similar to VWF behavior. More details of the proposed model can be found in our recent works, Huisman et al. 2017⁹⁴ and Hoore et al. 2018⁸⁹, and in [chapter 5](#). The total avidity of VWF is defined by the dimensionless avidity ψ multiplied by the size of VWF, ψN_{VWF} . This quantity is related to physical conditions such as shear rate and the

size of VWF, and the two imposed criteria. Figure 6.1 shows that the avidity of VWF is not very sensitive to the angle threshold and VWF size if the threshold radius is large enough. Moreover, the change of avidity is critical with respect to shear rate. For instance, at low shear rates, $\dot{\gamma} \leq 2000 \text{ s}^{-1}$, VWF is not avid anymore. The angle and radius thresholds are assumed $\theta_{\text{thres}} = 150^\circ$ and $R_{\text{thres}} = 1.2\sigma$.

For the following, VWF size is kept constant at $N = 30$ which is equivalent to a contour length of $L_{\text{VWF}} = 15 \mu\text{m}$.

6.4 Setup

In simulations, VWF polymers and platelets are positioned on the very proximity of the substrate (lower wall) covered by homogeneously distributed ligands with a high surface density $\sigma_{\text{lig}} = 16 \mu\text{m}^{-2}$ such that all particles (*i.e.* platelets and VWFs) would be able to adhere to the wall. The upper wall is moved with a constant velocity to impose simple shear flow. By applying shear flow, free platelets and VWFs migrate to the center of the channel since a lift force acts on them. Thus, any adhesion with the substrate would happen before they migrate away from the channel wall.

Two different cases are studied. In the first case, one of the ends of VWF polymers is fixed on the substrate, in order to study the critical adhesion of platelets to immobilized VWF polymers. In shear flow, these immobilized VWF polymers stretch and tether a number of freely-flowing platelets depending on shear rate. Because the association-dissociation rates of catch-slip bonds between VWF ligands and platelet receptors are very high, platelets translocate on stretched VWF polymers by losing old bonds and making new ones with a very high frequency (*i.e.* higher than platelet rolling frequency on the substrate). Adhesion of platelets to fibrinogen substrates is also compared with the results of this case. In the second case, VWF polymers are not immobilized so that they can move freely in the channel. The

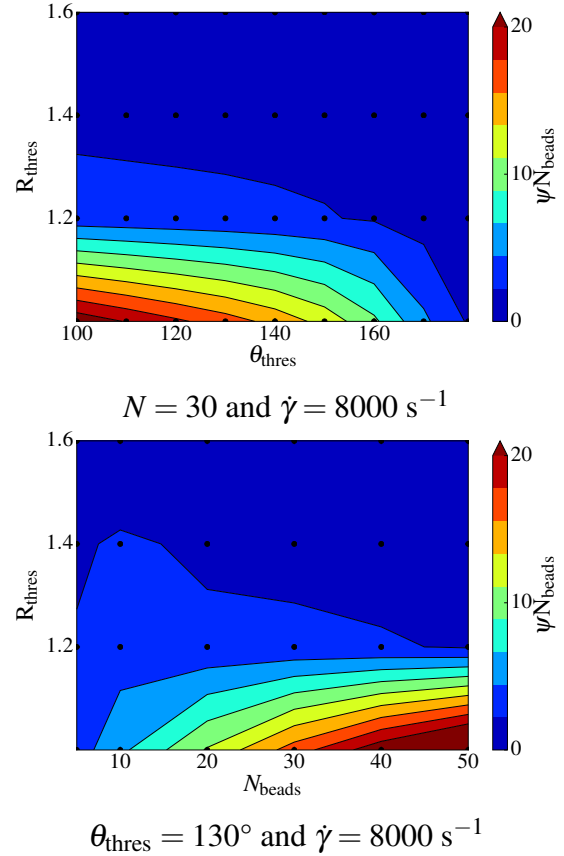


Fig. 6.1 VWF total avidity, ψN_{beads} , as a function of threshold criteria, R_{thres} and θ_{thres} , and VWF polymer size, L_{VWF} . The avidity of VWF increases critically by increasing shear rate (not shown)^{89,94}.

reversibility of the platelet-VWF aggregation in presence and absence of the shear flow is studied in this case.

6.5 Criteria for healthy behavior

VWF affinity and avidity are two crucial properties which determine how hemostasis occurs. These characteristics have to obey certain criteria to bring critical and reversible adhesion. Otherwise, they either do not form stable aggregates with platelets even at high shear rates, or their aggregation is irreversible regardless of shear rate. Figure 6.2 presents a schematic view of VWF stretching and its aggregation with platelets for different shear rates. In the bottom diagram, a critical stretching of a cohesive polymer as a function of shear rate is shown. At low shear rates, VWFs remain globular, while beyond a critical shear rate they start to have coil-stretch dynamics⁸. At even higher shear rates, the rotation of polymer dominates and the polymers perform tumbling dynamics²⁰⁰.

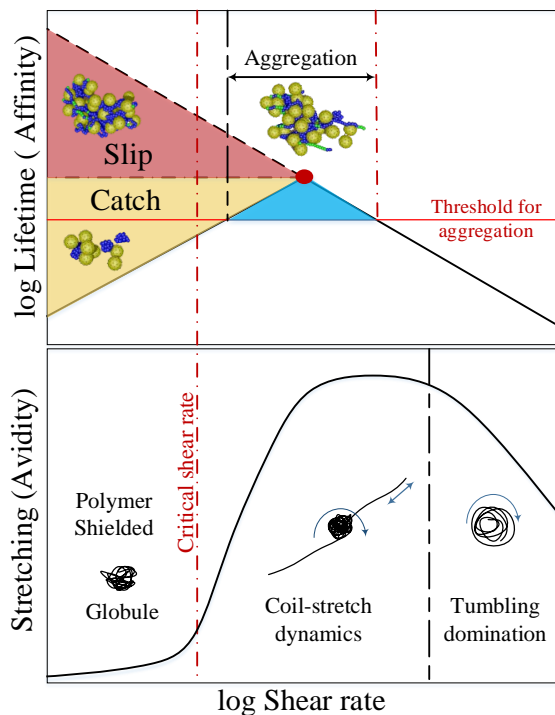


Fig. 6.2 Schematic view of VWF stretching and its aggregation with platelets for different shear rates. Affinity and avidity of VWF polymers are plotted as a function of shear rate. The avidity of the polymer is closely related to its stretching. The affinity between VWF ligands and platelet receptors at a definite high shear rate must be high enough for aggregates to form and remain stable, which is represented by the red circle in the affinity diagram. Therefore, two possibilities remain for the affinity, a slip or catch bond behavior, shown by red and yellow colored areas respectively. Slip-bond behavior leads to no reversibility in the aggregate formation. In catch bond behavior, VWFs and platelets interact and form aggregates only in a specific range of shear rates shown by the blue area.

In the globular state, VWF adhesive sites are shielded so that VWF is not avid for interaction with platelets. Beyond a critical shear rate, VWFs stretch and become avid. There is a range of shear rates where the VWF avidity is high enough for initiating adhesion between platelets and VWFs.

On the other hand, the affinity between single VWF adhesive domains and platelet receptors plays a key role in the stability of aggregates. The affinity can be represented by the lifetime of the bonds between VWF adhesive domains and platelet receptors, as shown in the upper diagram of Figure 6.2. Experiments show that VWFs and platelets form stable aggregates beyond a critical shear rate^{40,188}. It implies that the lifetime of adhesive bonds must be higher than a threshold lifetime for stable aggregation, when the shear rate is larger than the critical shear rate. For this to happen, the affinity of the bonds must be high enough, which is indicated by the red circle in the diagram of Figure 6.2.

Intuitively, an increase in the shear rate or the friction force on the adhesive bond must reduce the lifetime. However, it is known that many biological bonds possess lifetimes that increase with the force against the bond, a so-called catch bond behavior²²⁶. VWF A1 domain affinity to platelet Glycoprotein Ib α shows quite similar behavior¹⁰³. Since the affinity of VWFs at high shear rates is significant, the affinity has to diminish at low shear rates if the aggregates are supposed to be reversible. The red and yellow areas in Figure 6.2 correspond to a slip and catch bond behavior respectively. Accordingly, the bond is most likely a catch bond, in order to make reversibility possible.

The simulation properties are calibrated in such a way that the red circle is located above a threshold lifetime where aggregates can form and grow. The slip and catch bond behaviors are studied afterwards.

6.6 Criticality of VWF-platelet adhesion

Platelets in blood flow are able to adhere to an injured site of the blood vessel at shear rates lower than 900 s^{-1} ¹⁸⁸. Their adhesion is mainly mediated by fibrins or fibrinogens from the sub-endothelial matrix exposed to the blood stream. This behavior can be modeled by assuming slip bonds between platelet receptors and adhesive ligands (fibrinogens) in the simulation. This is done by ignoring the first term in Equation (5.7). The results of simulations with this assumption agrees with experimental results obtained by Savage et al. 1996¹⁸⁸, depicted in Figure 6.3.

The vascular system has another mechanism at high shear rates by using ultra-large VWFs. The adhesion of platelets to VWFs at low shear rates is not necessary because platelets can adhere to injured substrates on their own. Since VWFs are collapsed at low shear rates, their adhesive sites are shielded/inactive, such that they cannot regulate platelets adhesion at low shear rates. However, as they stretch at high shear rates, they become activated and bind platelets. The stretching of VWFs depends critically on shear rate. As a consequence, the

adhesion of platelets to VWFs is dependent on shear rate as well. This result is illustrated in Figure 6.4 in close agreement with the experimental results¹⁸⁸.

In experiments, the adhesion is measured by counting the number of platelets remaining on the substrate after perfusion of platelets for a period of time^{182,187–189}. In simulations, we report the number of adhesive bonds between platelet receptors and the substrate (fibrinogen or VWF). Consequently, adhesion is defined here by the number of total bonds between the platelet receptors and substrate ligands which can be normalized by the total number of platelet receptors. Quantity Φ_i^j is assigned for adhesion as

$$\Phi_i^j = \frac{N_b(i, j)}{N_i} ; i, j \in \{\text{VWF, PL, SUB}\} \quad (6.2)$$

where $N_b(i, j)$ stands for the number of bonds between i and j receptors/ligands, and N_i is the number of i receptors/ligands. VWF, PL, and SUB stand for von Willebrand factor, platelet, and fibrinogen/collagen substrate, respectively. Thus, Φ_i^j provides a measure of how strong the two objects adhere to each other. Of course, the maximum adhesion corresponding to Φ_i^j may not be possible because of geometrical constraints of adhering objects. For example, more than half of the receptors of an adhered platelet at the substrate are located on its opposite side and cannot form a contact with the surface. As a result, the comparison between simulation results and experimental measurements is performed qualitatively.

The total avidity calculated as the mean of individual molecular avidities is represented here by Ψ . Figure 6.5 shows the VWF-platelet adhesion and avidity in time. The shear rate applied in the system increases stepwise each $t^* = 1500\tau^{-1}$ in dimensionless time unit, which is equivalent to $t \approx 0.4$ sec as indicated in the diagram by vertical gray color-bars. The

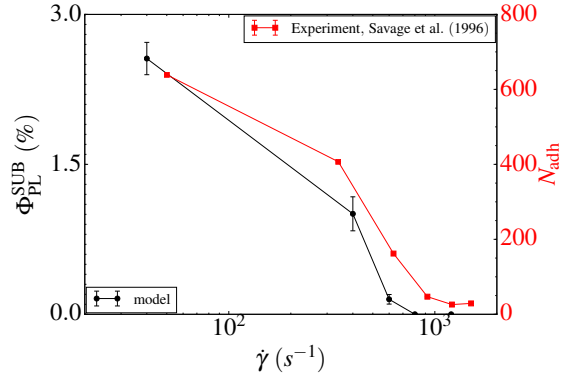


Fig. 6.3 Adhesion of platelets to fibrinogen substrates. Comparison of model and experiment based on the work of Savage et al. 1996¹⁸⁸. The adhesive behavior of platelets on fibrinogen substrate is critically dependent on and inversely proportional to shear rate. Φ_{PL}^{SUB} in simulation is the number of adhesive bonds between platelet receptors and substrate ligands normalized by the total number of platelet receptors. N_{adh} in experiments is the number of platelets remaining on the fibrinogen substrate after perfusion. Simulation and experimental results are depicted respectively in black and red, corresponding to the left and right vertical axes of the diagram. The simulation results agree with experiments for slip-bond interaction between platelet receptors and substrate ligands.

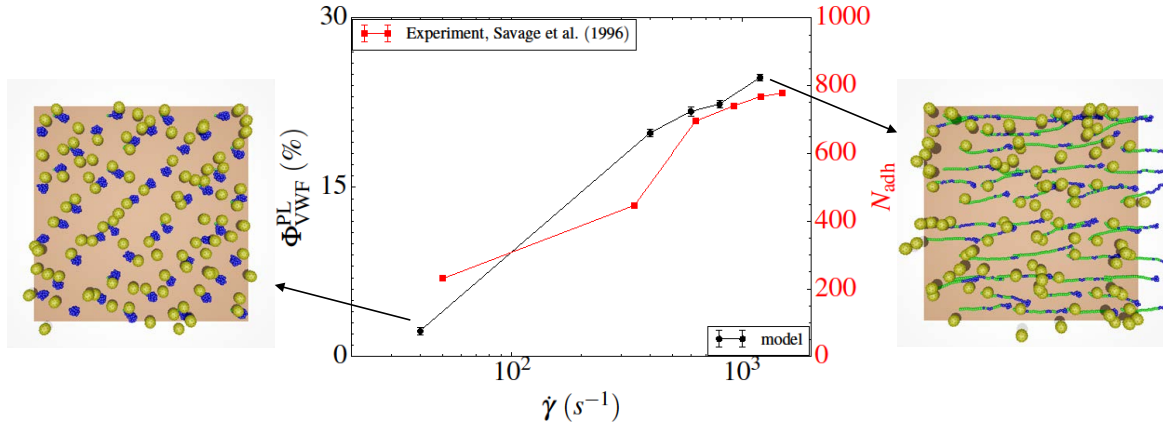


Fig. 6.4 Adhesion of platelets to immobilized VWFs. Comparison of model and experiment based on the work of Savage et al. 1996¹⁸⁸. The adhesion of platelets on VWF coated substrates is critically dependent on shear rate. $\Phi_{\text{VWF}}^{\text{PL}}$ in simulations is the number of adhesive bonds between VWF beads and platelet receptors normalized by the total number of VWF beads (ligands). N_{adh} is the same as explained in the caption of Figure 6.3. Simulation and experimental results are depicted respectively in black and red, corresponding to the left and right vertical axes of the diagram. The top view of the simulation box is shown for high and low shear rates. The active (adhesive) and inactive (non-adhesive) VWF beads are colored in green and blue, respectively. The surface area of the substrate in the simulation is $40 \mu\text{m} \times 40 \mu\text{m}$.

shear rates are written in the diagram in the physical units. To obtain appropriate statistics at each shear rate, separate simulations are performed with different shear rates, rather than subsequent increasing of shear rate shown in the main diagram of Figure 6.5. Hence, the results shown in the inset diagrams of Figure 6.5, are obtained from separate simulations with different shear rates. However, in the main diagram, the subsequent increase of shear rates is illustrated for a better visual presentation. The number of bonds as a measure of adhesion increases as the shear rate increases which correlates with VWF avidity as depicted at the leftmost inset diagram of Figure 6.5. The rightmost inset of Figure 6.5 shows that by increasing shear rate, the avidity of polymers increases depending on the shear rate. As expected, the VWF avidity depends on its extension, $\langle R_s \rangle$, which can be seen in the middle inset of the diagram. L_{VWF} is the contour length of the VWF. This behavior is a direct result of our proposed VWF model⁸⁹.

A question is whether this critical adhesion results from VWF avidity or VWF affinity. In order to answer this question, two simulations are conducted. In the former case, conformation-dependent activity of the polymer is turned off so that the VWF polymer avidity is set to $\psi = 1.0$ regardless of polymer conformation. In the latter case, the catch-bond term

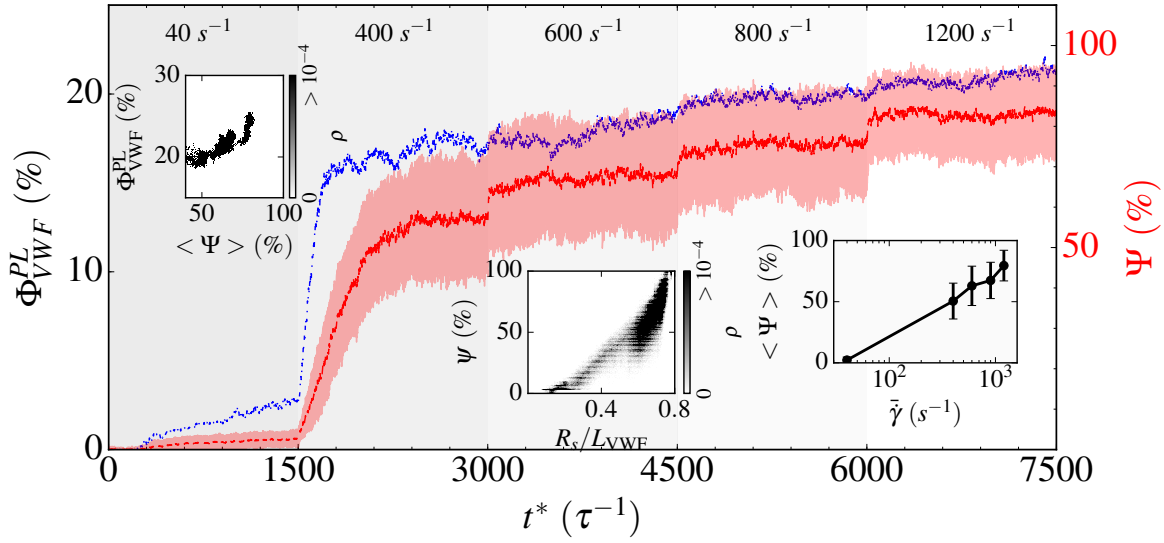


Fig. 6.5 VWF-platelet adhesion and VWF avidity with respect to time and shear rate. The shear rate increases sequentially each $t^* = 1500\tau^{-1}$ as written at the top of the diagram. The mean avidity of the VWFs is shown by the red curve, and the red band represents the variance in avidity. The number of bonds between VWFs and platelets is represented by the blue curve showing that their adhesion increases as shear rate grows. The adhesion is correlated with VWF avidity as shown in the leftmost inset diagram. Here, ρ is the probability density of each point in the cloud point diagrams. The middle inset shows the correlation between avidity and polymer extension which is obtained from the proposed conformation-dependent VWF polymer model⁸⁹. In the rightmost inset, the proportionality of avidity to shear rate is illustrated. The inset diagrams are obtained from the results of separate simulations with different shear rates (*i.e.* not from the single simulation shown in the main diagram).

in Equation (5.7) is omitted from platelet-VWF bond interaction. In consequence, the former simulation does not include the effect of VWF avidity in platelet adhesion on immobilized VWF substrate. On the other hand, the latter simulation does not include the two-state affinity between VWF beads and platelet receptors. The results of the two simulations are compared with the control system, which has both avidity and affinity effects, in Figure 6.6. The results definitely show that the VWF avidity causes the critical shear-dependent platelet adhesion to immobilized VWFs. Thus, the VWF size is crucial in platelet-VWF adhesion. This is indeed the reason why in von Willebrand Disease (VWD) type 2A, platelet adhesion to VWF weakens with absence of long VWF concatemers¹⁸⁵.

Concluding this section, the irreversible platelet adhesion to fibrinogen fails at high shear rates. In contrast, platelets adhere to the immobilized VWF substrate at high shear rates, when VWF concatemers stretch and expose their A1 domain for platelet Glycoprotein Ib α .

Although the VWF A1 domain interaction with GPIIb/IIIa has two bound states¹⁰³, the critical shear-dependent adhesion of platelets on VWF substrates directly results from the VWF polymer conformation which determines the shielding of VWF ligands and their avidity for interaction. This conclusion applies only to the interaction of platelets and wild-type immobilized VWFs, but not to the recombinant VWFs attached to the surface. Here, the main controlling factor for platelet adhesion is the type of adhesive bonds which have a two-state catch-slip behavior.

6.7 Reversibility of aggregate formation

Now, the system is studied when the VWF polymers are not immobilized so that they can move freely in the channel. At high shear rates, the VWF polymers stretch and their avidity for binding platelets increase. Henceforth, platelet receptors and VWF ligands can find each other and form bonds. As depicted in Figure 6.7, the platelet-VWF aggregation in free flow is reversibly dependent on the shear rate. By applying shear flow, the polymers start to stretch and increase their avidity for adhering platelet receptors. Initially, all structures remain close to the lower surface of the channel. Shortly after applying shear stress, all structures tend to move toward the center of the channel because a lift force is acting on them. Each stretched polymer near a platelet adheres to and rolls around it, making more bonds with the platelet if the time scale of polymer rotation is longer than the time scale of adhesion²⁶. Small polymer-platelet aggregates tether to each other by VWF protrusions and form bigger aggregates. Again, Φ_{VWF}^{PL} and Φ_{VWF}^{SUB} are adhesion measures of VWFs to platelets, and VWFs to surface, respectively.

Omitting the influence of RBCs on the aggregate formation, the condition of Figure 6.7 resembles thrombosis. *In vivo*, thrombosis may occur at high shear rates when ultra-large VWFs are present. The results show that thrombi formed at high shear rates dissolve if the

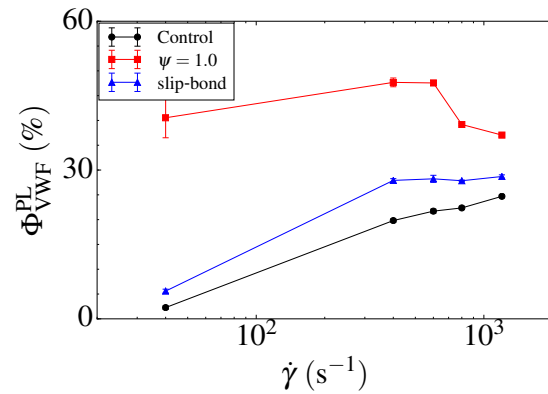


Fig. 6.6 Effect of affinity and avidity on the adhesion of platelets to immobilized VWF substrate. The model excluding two-state affinity effect (the slip-bond curve) shows a similar behavior as the control system. However, the model excluding the avidity effect significantly changes platelet adhesive behavior such that the platelet-VWF adhesion is no longer critically shear-dependent.

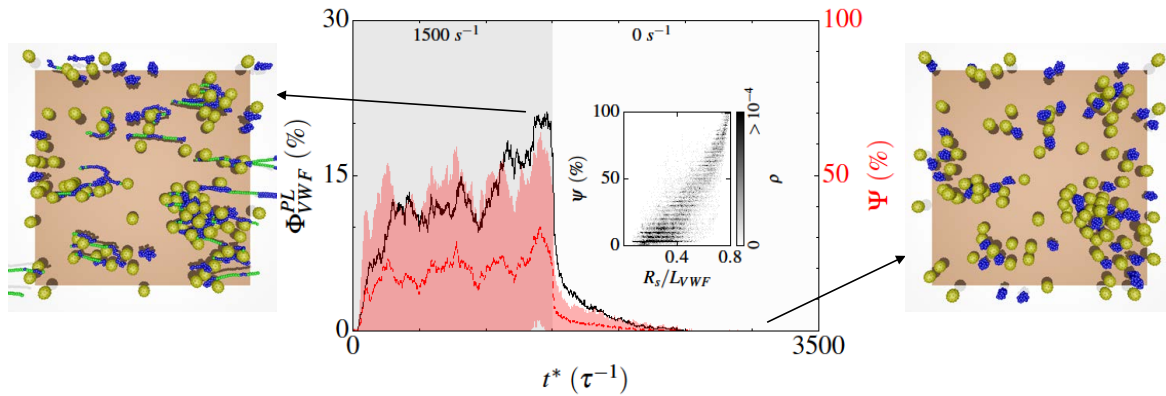


Fig. 6.7 Reversible shear-dependent platelet-VWF aggregation in simple shear flow without interactive substrate. The top view of the simulation box in shear flow and in equilibrium show the reversibility of aggregate formation. The inset diagram depicts the correlation between polymer avidity and its extension. The substrate surface area is $40\ \mu\text{m} \times 40\ \mu\text{m}$ and the channel width is $10\ \mu\text{m}$.

shear rate drops unless the platelets have already become activated and made irreversible bonds to fibrins and other substrates. This mechanism might have evolved for preventing undesired thrombosis which may turn fatal for the organism. The reversible adhesion of polymers results from conformation-dependent VWF avidity and VWF two-state affinity.

Although polymers with simple one-state slip-bonds may also reversibly adhere, as studied by Chen et al. 2013b²⁶, the VWF adhesive bonds with platelets (and also collagen) must be much stronger and remain much longer than to be broken by polymer coiling when the shear flow stops. The reason is that the immobilized VWFs on the surface must be able to arrest freely flowing platelets, as observed in experiments¹⁸⁸; otherwise, VWF polymers would be unable to form a platelet aggregate on the surface at high shear rates. If so, they must be more stable at low shear rates which is against reversibility. This means that the one-state affinity between VWFs and platelets will satisfy only one condition, either high shear rate criticality or fast reversibility, but not both at the same time.

To test this, many adhesive sites are distributed on the lower surface of the channel to represent collagen from an injured subendothelial matrix. The surface density of the adhesive sites is set quite high to insure that VWF polymers encounter many receptors to adhere to the surface if they come close to it. As shown in Figure 6.8, smaller aggregates form and VWF polymers become immobilized on the surface and arrest freely-moving platelets. Note that no firm sticking adhesion is seen neither for VWF polymers nor for platelets. They rather translocate on the surface with much smaller velocities than the bulk of the flow.

Translocation of platelets on immobilized VWFs has been also reported by experiments¹⁸⁸. Smaller aggregates are formed in this case because some of the polymers are immobilized and mixing is limited.

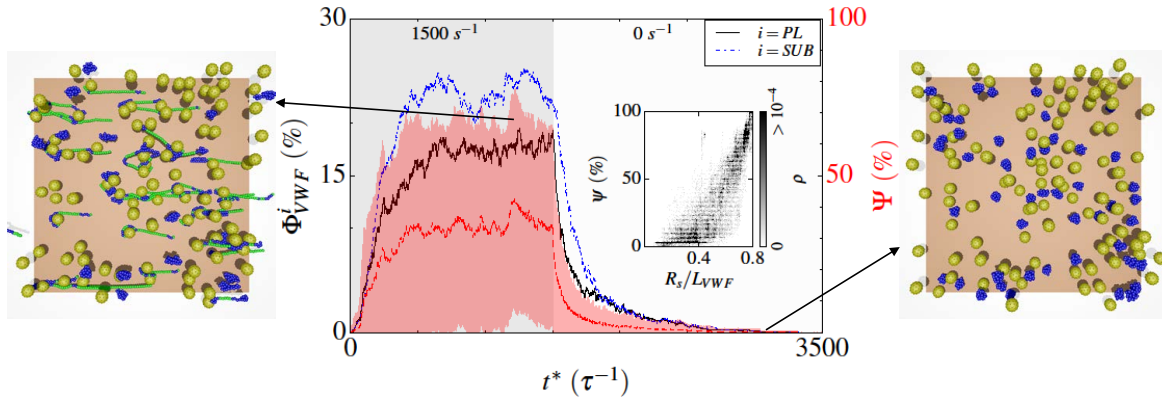


Fig. 6.8 Reversible shear-dependent platelet-VWF aggregation in simple shear flow with interactive substrate. Similar to Figure 6.7, the top view of the simulation box in shear flow and in equilibrium shows the reversibility of aggregate formation. The inset diagram depicts the correlation between polymer avidity and its extension. Here, the soluble VWFs can adhere to the substrate resulting in firm mural aggregates which are smaller in size comparing with the free aggregates in Figure 6.7 since smaller aggregates do not collide with each other to make larger ones.

The case depicted in Figure 6.8 is a representation of primary hemostasis where soluble VWFs can adhere to endothelial collagen and tether platelets. VWF adhesion to platelets is comparable and similar to VWF adhesion to substrates. VWF polymers act as an intermediary between fast moving platelets and stationary substrate. Similar to the free aggregate formation shown in Figure 6.7, the aggregates dissociate shortly after shear flow stops. This shear-activated reversible aggregation-dissociation process is caused by the unique properties of VWF proteins, including their affinity and avidity, as hypothesized by Springer 2014²¹³.

Reversible adhesion is mediated by both VWF A1 domain affinity and shielding of A1 domain affecting total VWF avidity. If either of these mechanisms are prohibited, the reversibility of VWF adhesion disappears. To verify this statement, two different VWF models are used and compared with the control VWF model. In the former model, VWF affinity is modified in such a way that VWF A1 domain interaction with platelet receptors possesses only one bound state. This means that in equilibrium, the affinity of the bonds between polymer beads and receptors remains maximal, lacking the catch-bond dissociation rate. In the latter model, polymer avidity is kept maximal by omitting conformation-dependent activity such that VWF A1 domain shielding is annihilated.

It is noted that polymer cohesive forces from intra-molecular attractions are not able to break strong adhesive forces between VWF and platelets. On the one hand, the cohesive forces are of the order of $f_{\text{coh}} \sim \Delta\epsilon_{\text{coh}}/d_{\text{Kuhn}} \sim 1k_{\text{B}}T/100\text{nm} \sim 0.1\text{pN}$, where $\Delta\epsilon_{\text{coh}}$ is the cohesive energy on the order of hydrogen bonds and d_{Kuhn} is the Kuhn length of the polymer⁶, which is about 100 nm for VWF. On the other hand, the adhesive force must be able to withstand hydrodynamic drag force on a platelet at least, which is on the order of $f_{\text{adh}} \sim 6\pi\eta a_{\text{eff}}^2 \dot{\gamma}$ from the Stokes law, where a_{eff} is the effective radius of a platelet, and η and $\dot{\gamma}$ are viscosity of the fluid and its shear rate, respectively. This yields at least $f_{\text{adh}} \sim 10\text{pN}$ for adhesive force, in agreement with single molecule measurements¹⁰³. This force is much higher than the cohesive force. Thus, the main factors which govern the reversibility of aggregate formation are the lifetime of the adhesive bonds and the time-scale of polymer coiling, since after the breakage of an adhesive bond, the polymer forms a globule where its adhesive sites are shielded.

Figure 6.9 presents the reversible aggregation and dissociation of platelets and VWFs for two-state catch-slip bonds and one-state slip bonds. The dissociation time is quantified by fitting an exponential function to the adhesion measure, $\Phi_{\text{VWF}}^{\text{PL}}$, as depicted in Figure 6.9. The coiling time is simply assumed as the inverse of the critical shear rate above which the polymer stretches. The conversion of simulation time to physical time is also done using polymer coiling timescale. According to the simulation results for the 15 μm VWF polymers, the coiling timescale is $\tau_{\text{sc}}^{\text{model}} = 1/\dot{\gamma}_c \approx 2$. From experimental results, the coiling timescale is evaluated as $\tau_{\text{sc}}^{\text{phys}} = 1/\dot{\gamma}_c \approx 1/2000 \text{ s}$. The dissociation time of the proposed control model is then $\sim 0.01 \text{ s}$, but for the one-state affine model it is around 200 times longer and equal to $\sim 2.2 \text{ s}$. Thus, the VWF-platelet aggregate dissolution with the catch-slip affinity is much

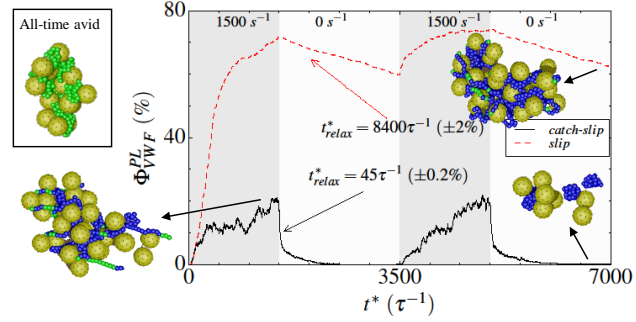


Fig. 6.9 Aggregate dissociation in time for two different affinities. VWF affinity at equilibrium plays a crucial role in the dissociation rate. Dissociation time of the one-state affine VWF model is evaluated as $2.2 \text{ s} \pm (2\%)$ whereas the two-state affinity model dissociates with dissociation time of $0.01 \text{ s} \pm (0.2\%)$. This is resulted from the lifetime of the bonds at equilibrium (zero unbinding force). Images show a few of VWFs and platelets in the simulations for each case. As illustrated, aggregates dissociate much slower if VWF beads make one-state slip-bonds with platelet receptors. An image of an aggregate for the all-time avid polymer with catch-slip bond is illustrated in the box. For all-time avid polymers, aggregation is irreversible.

faster than for the one-state (slip-bond) VWF affinity. The fully avid polymers, on the other hand, aggregate irreversibly, regardless of shear rate.

In conclusion, the cooperation of polymer avidity and affinity leads to shear-induced reversible aggregation. The polymer avidity determines the reversibility of aggregates, and polymer affinity determines the dissociation time of aggregates. Under physiological conditions, the reversible adhesion of VWF polymers is crucial for prohibiting undesired thrombosis. Ignoring the VWF cleavage by ADAMTS13 protease, platelet-VWF aggregates would continuously grow and eventually block the microvessels if their formation was not reversible. Consequently, deviations from healthy VWF properties often result in many types of von Willebrand diseases (VWDs)²¹³.

6.8 Effect of shear rate and polymer cohesion

Physical properties of the system such as shear rate and the properties of polymers such as their cohesion affect the aggregation substantially. In order to elucidate their qualitative effect on the aggregate formation, several 2D simulations of the system are conducted. Since the critical shear rate of each polymer increases by elevating cohesive forces, their avidity for binding platelets is related to their cohesion. The formation of platelet-VWF aggregates has a critical relation with both shear rate and polymer cohesive potential, as plotted in Figure 6.10. In addition, simulation snapshots are shown for different shear rates and constant cohesive potential. The aggregation occurs at high enough shear rates where polymers start to stretch and become avid. The extent of aggregation can be seen by the number of bonds, $\Phi_{\text{VWF}}^{\text{pl}}$, and the size of aggregates is characterized by the radial distribution function, $g(r)$.

By forming aggregates, polymers and platelets attain higher lift forces and migrate toward the center of the channel. A margination parameter is assigned for the system which is defined as

$$M = \frac{4}{W} \frac{\int |y| \rho(y) dy}{\int \rho(y) dy}, \quad (6.3)$$

where $\rho(y)$ is the density profile of a component, W is the width of the channel, and y is the lateral distance to the center of the channel. The value of the margination parameter gives an estimate of how different components are distributed in the channel. If the distribution is homogeneous in the channel, $M = 1$ which is the case for the fluid particles. $M > 1$ shows that the components have margined to the boundaries/walls and $M < 1$ implies that they have migrated to the center of the channel. Because of relatively high lift forces on the aggregates, they migrate to the center of the channel and the margination parameter becomes smaller than one. The contour plot in Figure 6.11 shows the margination parameter for each

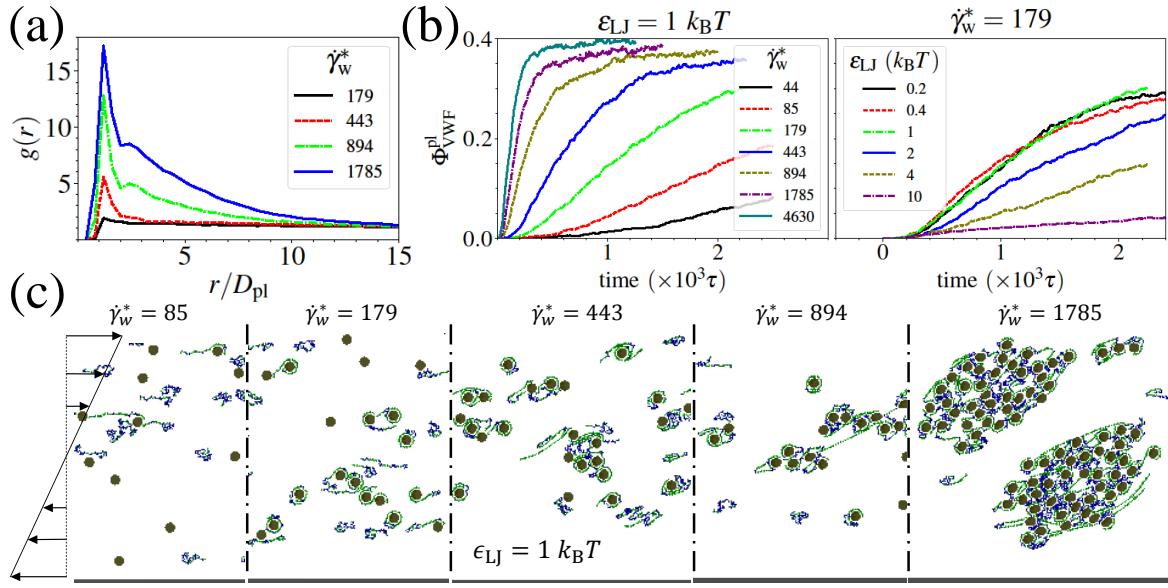


Fig. 6.10 Aggregation in 2D simulations. (a) The normalized radial distribution function, $g(r)$ versus the distance between two platelets. (b) The number of bonds normalized by the number of polymer beads, Φ_{VWF}^{pl} for different shear rates and cohesive potentials. (c) The snapshots of the simulations are illustrated for comparison. The aggregation is critical both with respect to cohesive forces and shear rate.

cohesive potential and shear rate. The density profiles of platelets, VWFs, and solvents are plotted as well for comparison. By increasing shear rate, the aggregates form and grow so that the lift force on them increases. Consequently, they migrate to the center of the channel. However, a further increase of the shear rate affects the margination parameter in an opposite way because the aggregates become more circular due to fast rotation and feel a weaker lift force.

Aggregation is directly related to polymer avidity, but indirectly to their stretching. Figure 6.12 shows that the polymer stretching depends logarithmically on the cohesive potential and shear rate and the avidity is closely related to the stretching. The cohesive potential determines the critical shear rate beyond which the polymer starts to stretch. The molecular properties of VWFs have evolved in such a way that they are globular at low shear rates ($\dot{\gamma} < 1000 \text{ s}^{-1}$) and stretched at high shear rates. This mediates blood coagulation at high shear rates, where platelets cannot adhere to a substrate by themselves.

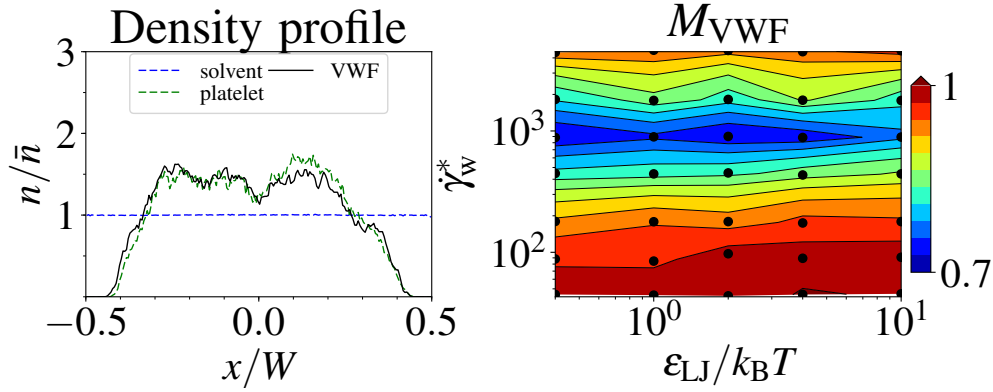


Fig. 6.11 Density profile and margination parameter. Density profile is plotted for the case $\dot{\gamma}_w^* \approx 1000$ and $\epsilon_{LJ} = 4 k_B T$. By increasing shear rate to $\dot{\gamma}_w^* \approx 1000$, migration to the center increases. However, increasing shear rate further leads to a lower migration to the center due to the domination of aggregate tumbling. Tumbling motion changes the elliptical shape of aggregates to circular and reduces the lift force on them.

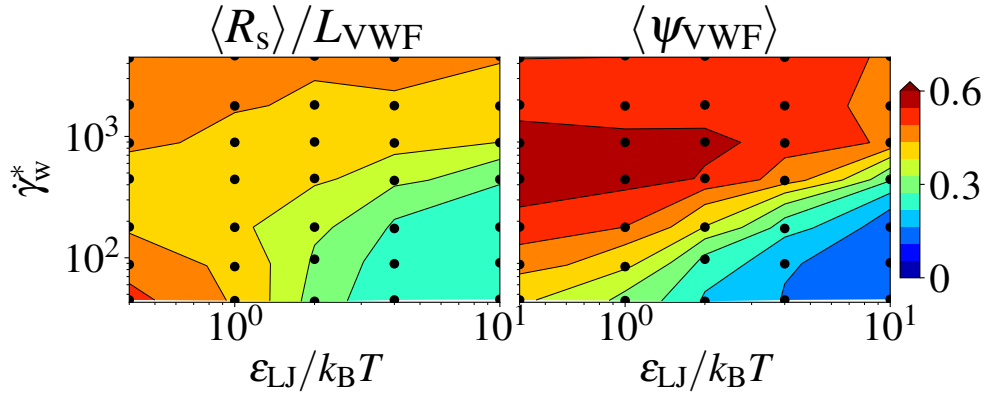


Fig. 6.12 Polymer stretching and avidity with respect to shear rate and cohesive potential. A lower cohesive potential decreases the critical shear rate of polymer stretching such that it stretches at lower shear rates.

6.9 Summary

Platelet and VWF aggregation has been studied using multi-scale hydrodynamic simulations. According to experimental findings, VWF polymers adhere to adhesive substrates and platelets when they are stretched by exposing their adhesive domains. Also, in absence of shear flow, they tend to collapse to a globular form shielding their adhesive sites. This behavior is modeled by a conformation-dependent adhesive polymer comprising self-avoiding polymer beads⁸⁹. In addition, VWF interaction with adhesive substrates has been modeled by catch-slip bonds¹⁵⁸. The adhesion dynamics of platelets on fibrinogen substrates and immobilized VWF substrates has been studied and compared to experiments¹⁸⁸. It has been

deduced that VWF polymer avidity, or the number of exposed adhesive ligands in the VWF polymer, associated with adhesive domain shielding, plays a key role in critical adhesion of platelets on VWF substrates. Thus, shielding of polymer adhesive domains is necessary for critical activity of VWFs and their adhesion to platelets and substrates. This finding is consistent with the problem in von Willebrand disease (VWD) type 2A when short VWF polymers are unable to induce blood clotting.

Another interesting fact about platelet-VWF aggregates is the reversibility of their formation triggered by decreasing shear rate. Again, VWF conformation-dependent avidity is essential for reversible aggregate formation. In addition, force-related two-state affinity between VWF adhesive domains and platelet receptors¹⁰³ modeled by catch-slip bond¹⁵⁸ efficiently regulates the dissociation time of aggregates in absence of high shear rates. This shear-sensitive behavior is beneficial for preventing spontaneous thrombi growth. As a result, mutations in VWF A1 domain can change the affinity of VWFs to platelets leading to an increased platelet-VWF aggregation as in VWD type 2B¹⁸⁵.

As hypothesized by Springer 2014²¹³, the interplay of VWF avidity and affinity determines the behavior of VWF and its adhesion to platelets and substrates. It is important to note that ADAMTS13 protease activity has not been considered in this study. However, its activity is dependent on polymer avidity, since the target domain for ADAMTS13 is close to VWF A1 domain such that it may be shielded similar to VWF A1 domain⁹⁴. Therefore, the activity of ADAMTS13 must be critically dependent on shear rate.

Part III

Aggregates in blood flow

Chapter 7

Platelet-VWF aggregation in blood flow

Platelets form aggregates as they adhere to the stretched von Willebrand factors (VWFs) at high shear rates. Their aggregation is critically dependent on shear rate and the aggregates dissolve reversibly at low shear rates. In blood flow, red blood cells (RBCs) keep away from the vessel walls and leave a RBC free layer (RBC-FL) in which platelets and VWFs are margined and populated. The higher shear rates close to the vessel walls result in VWFs stretching, exposing their interactive sites to platelet receptors, and initiating aggregation regardless of the existence of an injured wall. The formed aggregates in the RBC-FL gain significant hydrodynamic lift force and penetrate the RBC-core flow. The experimental clues on the shear-activated VWF-platelet interaction indicates that these demargined aggregates ought to dissociate in the center of the vessel as the shear rate drops. Mesoscopic hydrodynamic simulations of the blood flow including RBCs, platelets, and VWFs, support these expectations. Such regulation of undesired aggregates is beneficial for the vasculature, prohibiting undesired spontaneous thrombosis and imminent blockage or stroke, and can be altered if the affinity of the platelets to VWFs changes, such as von Willebrand disease type 2B.

7.1 Introduction

Soluble ultra-large VWFs must be present in blood in case of need^{33,176}. VWF adhesion in primary hemostasis takes a few seconds to a few minutes^{176,187,188}, but it takes several minutes for many of them to get cleaved by ADAMTS13^{42,125}. Thus, before VWFs become cleaved, they can play their role in the primary hemostasis until platelets become activated. The role of ADAMTS13 must be the overall regulation of VWF size distribution in the blood stream. The question is why platelet-VWF aggregates are not seen for a long time in blood. In addition to the regulatory activity of ADAMTS13 on aggregates growth, platelets and

VWFs seem to form reversible aggregates²⁵ in the blood flow as far as platelets are still unactivated. The platelet receptors adhere to VWF at high shear rates while VWF is stretched, and dissociate as shear rate drops and VWF coils⁷⁵.

Critical aggregation of platelets at high shear rates and the reversible aggregate dissociation at low shear rates results in a distinct dynamics of platelet aggregates in blood flow. The pressure-driven blood flow generates a range of shear rates at each blood vessel cross section, from a high shear rate at the wall, to zero shear rate at the center of the vessel. Consequently, aggregation may be possible at the wall if the shear rate is high enough, but impossible at the center because the shear rate is very low. Margination of platelets^{140,176} and large VWF polymers¹⁷² to the vessel wall helps their aggregation, too. The many-fold concentration of the platelets and VWFs at the walls compared with the whole blood concentration increases the chance of aggregation at the walls, and decreases it substantially at the center of the vessel.

In this chapter, the dynamics of aggregation is studied based on the known characteristics of VWFs and their aggregates with platelets. Since most VWFs stretch at the walls because of high wall shear rates, aggregation of platelets and VWFs is probable even if there is no injury. The aggregates can grow and obtain hydrodynamic lift force from their highly deformable and porous structure which can tank tread similarly to RBCs. By growing, the aggregates must be able to push into the RBC barrier and penetrate the bulk flow at some point, a process inverse to margination. Their demargination provides the aggregates with lower shear rates at the bulk flow and leads to their dissociation. In a nutshell, VWFs and platelets must continually marginate, aggregate, demarginate, dissolve, and remarginate. This dynamics is thoroughly discussed in the following, and verified by mesoscopic blood flow simulations. An experimental setup for catching this phenomenon is suggested as well.

7.2 Setup

The blood is confined in a channel with 40 μm height, 80 μm length, and 30 μm width. 360 RBCs, 384 VWF polymers, and 768 platelets are located inside the channel. With this, the volume fraction of RBCs (hematocrit), platelets, and VWFs in the channel are $\sim 42\%$, $\sim 1.7\%$, and $\sim 0.8\%$. The volume fractions of VWFs and platelets in blood are taken order of magnitude higher than normal, in order to be able to form large aggregates in a channel with periodic boundary condition. In physiological condition, an aggregate of a few platelets and VWFs would flow and see many other free platelets and VWFs, while in simulations, they cannot meet new platelets downstream because the boundary in the flow direction is periodic. It is to be noted that the increase in concentration of platelets and VWFs does not

change their margination significantly. The simulation setup and the models used in this section are summarized in Figure 7.1.

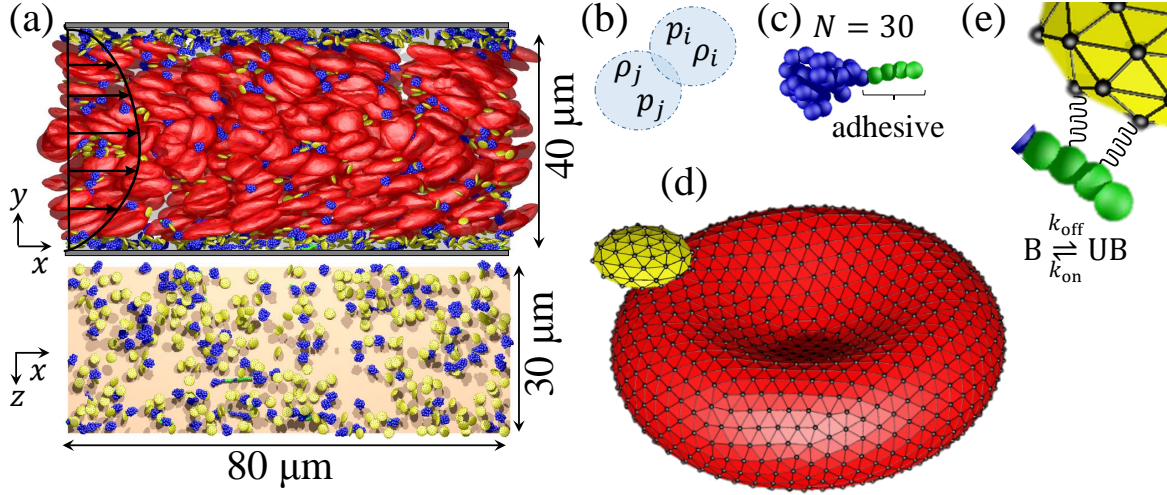


Fig. 7.1 Simulation setup and models. (a) The simulation box contains 360 RBCs, 384 VWF polymers, and 768 platelets immersed in a SDPD fluid with density 3 (288000 solvents.) The snapshot shows margined platelets and VWFs in blood flow, where many margined VWFs are stretched and most of the VWFs in the bulk flow are globular. (b) The schematics of the fluid model, smoothed dissipative particle dynamics (SDPD), where each particle has its own pressure and density and overlaps with other particles. (c) Polymer model shows that the stretched part of the VWF polymer is activated (shown in green) and adhesive to the platelet receptors, and the globular portion (shown in blue) is nonadhesive. The VWF polymers are modelled by 30-bead polymer chains representing 15-μm-long VWFs. (d) Membrane model is composed of triangulated bead-spring network. The membranes keep their volume, global and local surface area. They also have bending rigidity and elasticity. (e) Adhesive bonds between VWF beads and platelet vertices are created and broken with on- and off-rates.

7.3 Results

Characteristics of VWF-platelet aggregates. Both VWF polymer dynamics in shear flow and its adhesive interaction with platelet receptors are important in the spontaneous aggregation of platelets and VWFs. Recent experiments on single VWF A1 domain interaction with platelet receptor Glycoprotein Ib α ¹⁰³ show that their bond has a nontrivial lifetime as a function of the force against it. Accordingly, as the force grows above a threshold, the lifetime of the bond increases orders of magnitude. This behavior is referred to as a catch bond, what is seen for many other biological bonds^{224,226}. The bond between VWF and

platelet may be affected by mutations, destroying the catch-bond behavior of VWF-platelet interaction and causing VWF-related bleeding diseases^{185,247}.

On the other hand, VWF polymers at low shear rates are in a collapsed state, shielding their adhesive domains from interacting with platelet receptors^{71,75,208,231,232}. High shear rates dominate the cohesive forces in the VWF polymer and stretch it^{6,107,191}. Since the polymer is in both elongational and rotational flow field, it shows a coil-stretch dynamics by tumbling and stretching^{34,210}.

At low shear rates, polymer is coiled and inactive (Figure 7.2 - bottom panel). As shear rate passes a critical value $\dot{\gamma}_c$, the coiled polymer changes its phase to coil-stretch dynamics and its avidity toward platelets increases substantially. The avidity of the polymer is a measure of how many active adhesive sites it contains for bonding to receptors. Increasing the shear rate further will lead to another dynamical phase where the rotation of the polymer is fast enough to hinder stretching. VWF shielding in the collapsed state results in the critical shear dependent adhesion of VWFs to platelets or adhesive substrates¹⁸⁸ (see chapter 6).

The affinity of VWF ligand toward platelet receptor is normally based on the force against the ligand-receptor pair (Figure 7.2 - top panel). Here, the schematic diagram is based on the shear rate which is proportional to the tensile force on the VWF polymer chain. The red point demonstrates the working zone of VWF at high shear rates; it must be above a threshold lifetime where the bond lifetime lets the platelets and VWFs to form stable aggregates. The question of interest is what happens to the aggregates if the shear rate decreases below the critical shear rate when stretched bonded polymers tend to recoil and detach from the aggregate, but their bonds with platelets don't let it happen. Note that the adhesive bonds of VWF (both to the injured wall and the platelet receptors) tolerate strong hydrodynamic forces applied on the platelets because the platelets would detach by the flow otherwise. Such forces are order of magnitude larger than the cohesive forces from VWF internal self-associations (see chapter 6). Consequently, the cohesive forces are unable to bring the adhered polymer to the collapsed state and detach it finally from the adhesive substrate. Therefore, the lifetime of the adhesive bonds plays the main role in VWF reversible adhesion⁸⁹ (see chapter 6).

Two scenarios are possible in this regard. The first scenario is when the platelet-VWF affinity is the trivial slip bond. In this case, the lifetime of the bonds remains constant or even increases when the aggregates are back to low shear rates. This causes irreversible aggregation which must not be the case for VWF-platelet interaction since we already know that their aggregates dissolve at low shear rates reversibly^{25,40,75}. Therefore, the second scenario, the catch-bond affinity, ought to be the only possibility. In this case, aggregates dissolve since VWF affinity toward platelet has lower than the threshold lifetime. Although the threshold lifetime for stable aggregates is not constant for all shear rates, it is assumed

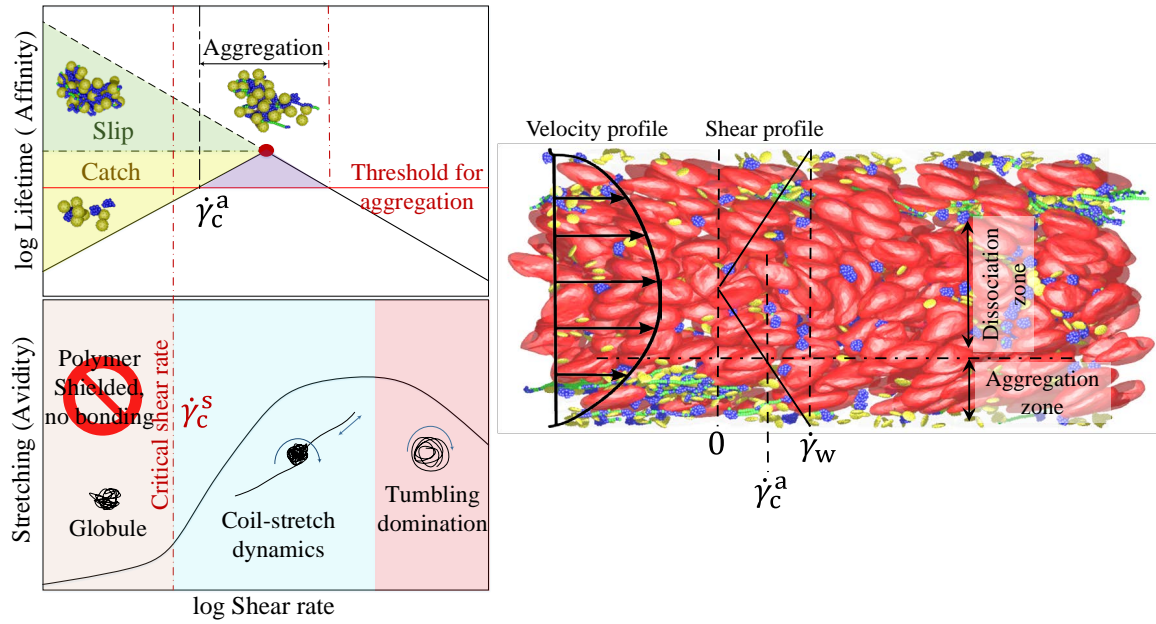


Fig. 7.2 Schematic view on the possibility of VWF-platelet aggregates. The lower panel shows the VWF stretching or equivalently their avidity (number of VWF active sites) with respect to shear rate. The top panel shows different scenarios for the VWF-platelet affinity represented by bond lifetime. The red point in the top panel represents the working zone of VWFs. It must be above a threshold lifetime where stable aggregates can form. In order to get a reversible and critical platelet-VWF aggregation, the only possibility is a catch bond interaction between VWF ligands and platelet receptors. The catch-bond behavior imposes a limiting shear rate for aggregation which is greater than the critical shear rate of VWF polymers stretching ($\dot{\gamma}_c^a \geq \dot{\gamma}_c^s$)⁷⁵. Beyond this shear rate, stable aggregates form. Interestingly in blood flow, this limiting shear rate criterion must be seen somewhere in the vessel, *i.e.* aggregates dissolve at the center of the vessel. In the blood flow snapshot at the right side, RBCs and platelets are shown by red and yellow membranes, respectively. VWF polymers are shown by blue (inactive) and green (active) beads adopted from our recent work, Hoore et al. 2018⁸⁹, and [chapter 6](#).

that it remains in the same order of magnitude for all physiological shear rates. The reversible aggregation of platelets and VWFs has already been seen in experiments^{25,40,75}, and our simulation results show the same behavior, as shown in [Figure 7.3](#).

Accepting that the platelet-VWF interaction is a catch-bond interaction, there must be a limiting shear rate $\dot{\gamma}_c^a$, below which aggregates dissolve. This limiting shear rate can be seen in the blood flow depending on the pressure gradient (bulk shear rate). If the wall shear rate is lower than $\dot{\gamma}_c^a$, all formed aggregates dissolve everywhere in the vessel. If it is higher than $\dot{\gamma}_c^a$, aggregates can form in a layer between the vessel wall and somewhere inside the vessel where shear rate is equal to $\dot{\gamma}_c^a$.

Demargination of aggregates. Before aggregates form, platelets and ultra-large VWFs (UL-VWFs) are pushed to the vessel walls, a phenomenon known as margination^{57,78,140,172,176}. Since RBCs are soft and deformable cells, they acquire hydrodynamic lift force against the vessel wall, lifting them to the center of the vessel and keeping them away from the wall. As a result, they leave a RBC free layer (RBC-FL) on the walls where the other blood components such as platelets and large VWFs are pushed into. The concentration of platelets and VWFs in the RBC-FL increases many-folds and while VWFs stretch at high shear rates close to the walls, they adhere to passing platelets and initiate platelet-VWF aggregation. By forming aggregates in the RBC-FL, they tend to penetrate into the bulk of the blood flow since the aggregates are highly deformable, getting high lift force, to pass the RBC-FL border.

Figure 7.4 shows simulation results for margination and aggregation. At first, the distribution of VWFs and platelets has a substantial peak in the RBC-FL. This in addition to high shear rates in the RBC-FL rise the aggregation probability at the RBC-FL. Then the aggregate forms at RBC-FL, grows and penetrates the bulk flow since the lift force on the aggregate is stronger than the margination force from collisions to the RBC-core flow. It easily passes the flowing RBCs and goes on until it reaches the point that shear rate is lower than $\dot{\gamma}_c^a$. By moving further, the aggregate may dissolve if their aggregation is reversible because of their catch-bond affinity.

Once aggregates reach the point that the shear rate is less than the critical shear rate of aggregation $\dot{\gamma}_c^a$, they must dissolve and marginate back to the RBC free layer (RBC-FL). In

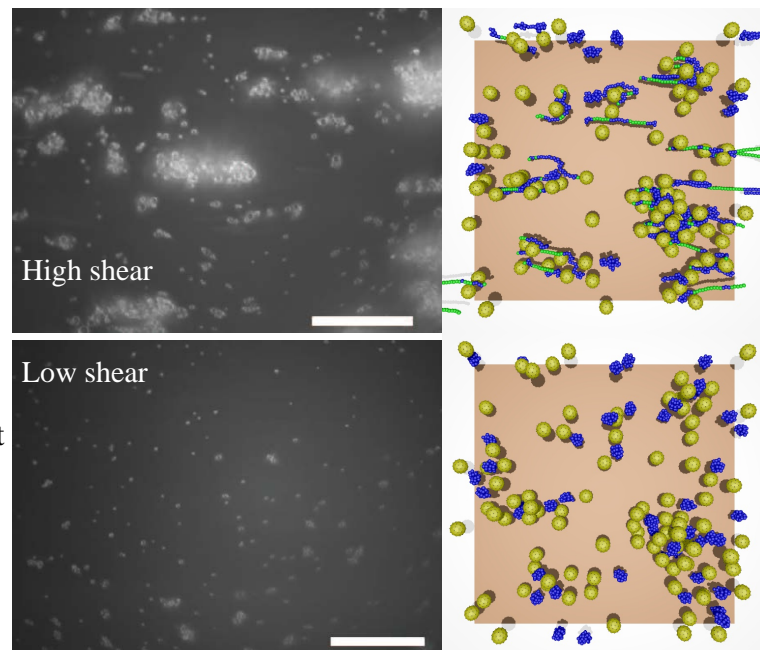


Fig. 7.3 Reversible aggregation of platelets and VWFs in simulations and experiments. For more clarity, platelets are substituted by spherical colloids with the same receptors. The experimental images are reproduced from the work of Chen et al. 2013a²⁵. Note that the aggregates are freely flowing.

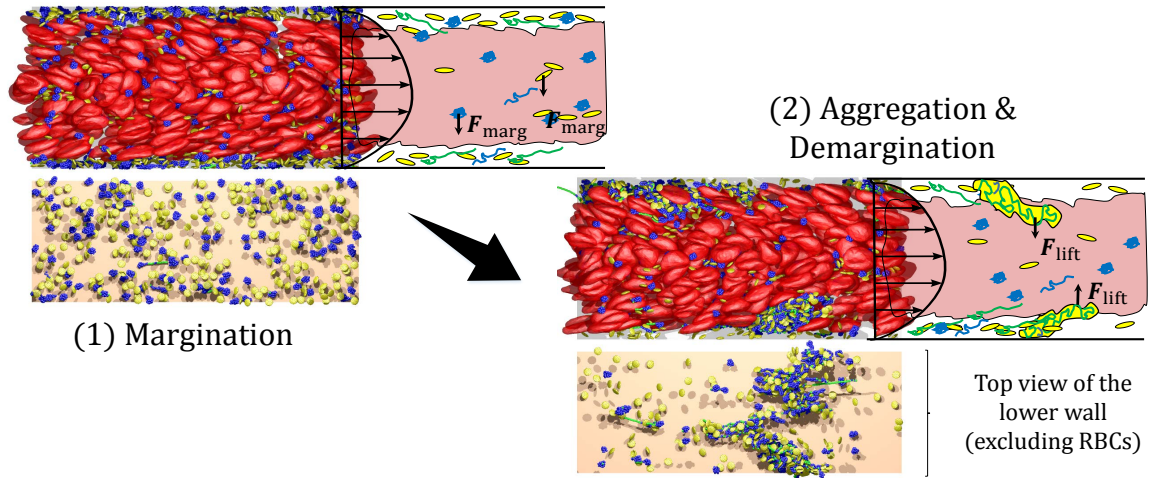


Fig. 7.4 Margination to and aggregation in the RBC-FL. RBCs migrate to the center of the vessel and push other components such as platelets and large VWFs to the walls. Marginated VWFs stretch because of high shear rates close to the walls and initiate aggregation. Formed aggregates in RBC-FL obtain high hydrodynamic force lifting them against the walls. The process is shown schematically along with simulation snapshots.

order to verify this hypothesis, two simulations are conducted with two different affinity scenarios, catch-bond and slip-bond affinities.

Catch-bond scenario: Reversible aggregation. The catch-bond affinity between VWFs and platelets causes reversible aggregation of them. Therefore, demarginated aggregates dissolve when they reach low shear rate regions in the center of the flow. The dissolved VWFs and platelets are pushed back again into the RBC-FL by colliding to RBCs. The dissolved and remarginated platelets and VWFs form new aggregates in RBC-FL initiating the process again. Accordingly, the continual process of margination, aggregation, aggregate demargination, aggregate dissolution, and remargination recurs. The resulting distribution of VWFs (and similarly platelets) is shown in Figure 7.5. There are two peaks in VWF distribution in contrast to normal margination where there is one peak in the RBC-FL. In this case, one peak in the distribution is inside the RBC-FL which corresponds to the single margined VWFs and another peak is somewhere inside the bulk flow depending on the blood pressure (or equivalently shear rate), corresponding to aggregates trapped behind the limiting layer for aggregate dissociation (where shear rate is lower than $\dot{\gamma}_c^a$.)

Slip-bond scenario: Irreversible aggregation. The results for the slip-bond scenario are shown in Figure 7.6. As illustrated, there is no dissociation in this case and aggregates finally reach the center of the channel. The density profile of VWFs in the channel shown in Figure 7.6 brings more insight to what exactly happens. At the first step, we have a normal blood flow with margined platelets and VWFs which do not interact. The peak of their

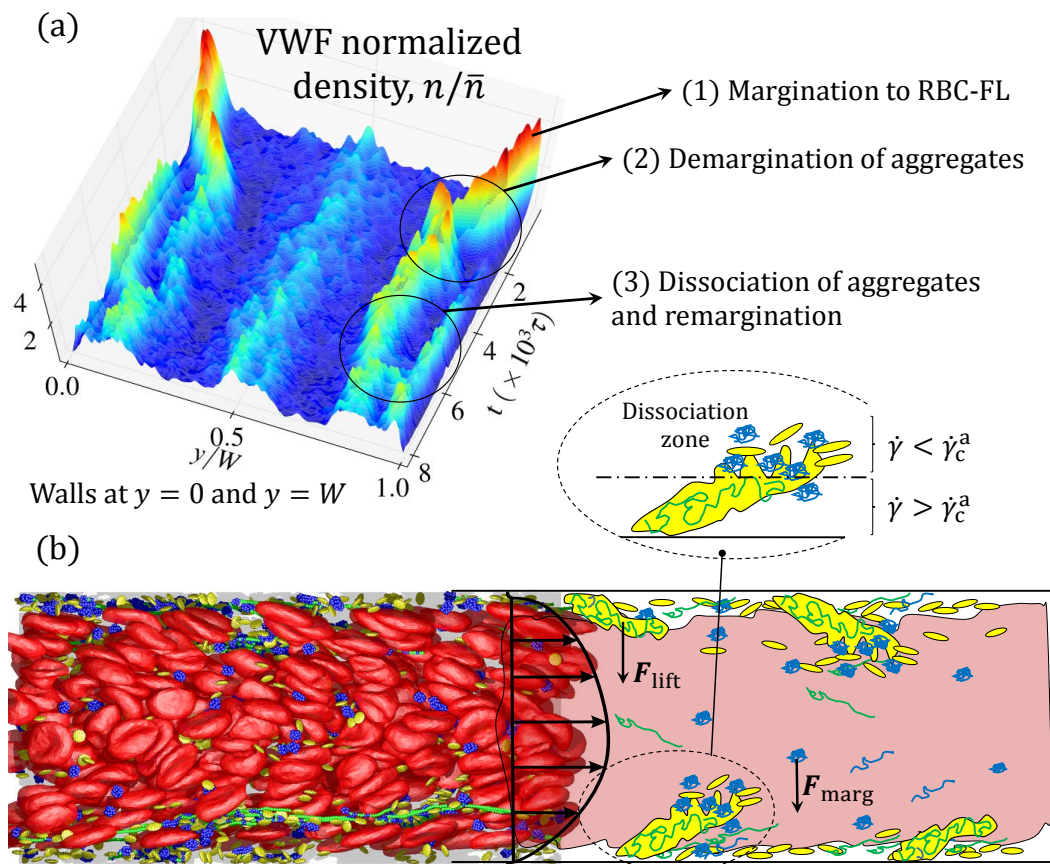


Fig. 7.5 Continual margination, aggregation, demargination, dissociation, and remargination. The catch-bond scenario, which implies reversible aggregation of platelets and VWFs, results in the dissociation of aggregates when they reach the points where shear rate is lower than $\dot{\gamma}_c^a$. Dissolved platelets and VWFs lose their lift force and get back into the RBC-FL forming aggregates again. This continual process happens forever. (a) The density profile normalized by the mean density shows this process. (b) Schematic diagram along with the simulation snapshot shows that the aggregates never reach the center of the flow. The dominant force is shown for each entity, which is the margination force F_{marg} for single platelets and VWFs, and hydrodynamic lift force F_{lift} for aggregates.

distribution lies inside the RBC-FL which is the result of their margination. Afterwards, their interaction is turned on in the simulations and aggregates start to form and grow. Here, there is no limiting shear rate for aggregation so that the aggregates grow and migrate to the center of the blood vessel finally.

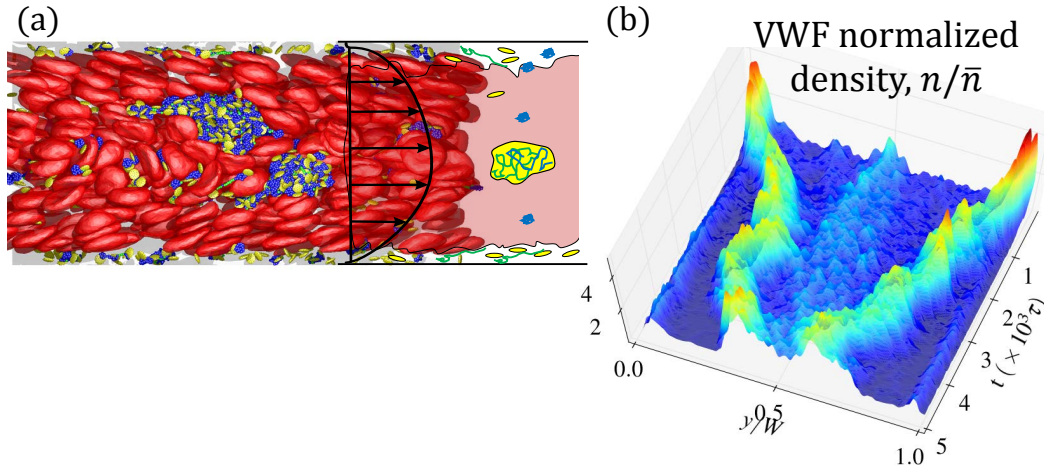


Fig. 7.6 Migration to the center of the vessel (Demargination.) The slip-bond scenario, which implies irreversible aggregation of platelets and VWFs, results in the complete demargination of aggregates. (a) Schematic diagram along with the simulation snapshot shows the condition that aggregates have almost reached the center of the vessel. (b) The density profile normalized by the mean density shows the irreversible process where the aggregates finally reach the center of the vessel.

7.4 Discussion

The system shows completely different behavior based on the affinity of VWFs to platelets. Figure 7.7 compares the density profiles of the two cases with the normal margination without adhesion.

In all cases, the initiation of aggregation occurs in the RBC-FL where the concentration of platelets and VWFs is maximum and VWFs stretch and become avid for platelet receptors. The polymers first stretch in the RBC-FL due to high shear rates they feel close to the wall. Their confinement in such a thin layer helps them to stretch even further⁷. By stretching, they become avid to platelet receptors and bind them. The platelet-VWF aggregates grow and penetrate into the RBC core of the flow. Passing the limiting shear barrier for aggregation where shear rate is equal to $\dot{\gamma}_c^a$, however, VWFs loose their bonds and recoil. The detached platelets and VWFs are pushed back to the RBC-FL. This process happens if the interaction between platelets and VWFs has a catch-bond behavior. Otherwise, the aggregates penetrate to the center of the channel and gather there, although their stretching is much less than their stretching in the RBC-FL. Figure 7.7 shows the distribution of VWFs in the channel for both scenarios and compares them with the normal margination case with no adhesion.

The margination and aggregation-dissociation are two independent processes. In order to see their independence, the aggregation and demargination in pressure-driven quasi-

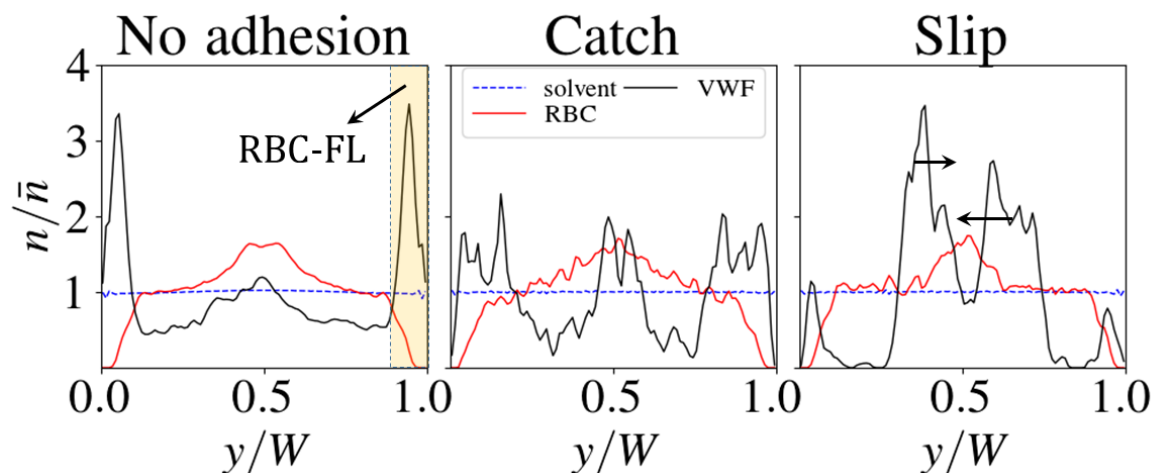


Fig. 7.7 Density profile comparison. From left to right, the density profile of the system is shown in a short period of time for normal margination with no adhesion, catch-bond, and slip-bond scenarios. The steady-state for slip-bond condition is a peak of the density profile at the center of the vessel. The arrows show the direction of the movement of the peaks in the density profile for the slip-bond scenario. The catch-bond scenario has two peaks, one inside the RBC-FL, and the other somewhere between the center and the wall. RBC-FL is highlighted in yellow.

Poiseuille flow can be compared with the simple shear flow (Couette flow.) Demargination of aggregates should occur in Couette flow very similar to Poiseuille flow. However, since shear rate is almost equal everywhere in the cross section for the Couette flow case, the aggregates must remain stable and reach the center of the channel. This behavior is indeed found in simulations, see Figure 7.8.

7.5 Summary

Adhesion of platelets to von Willebrand factor (VWF) proteins is known to have a critical and reversible dependence on shear rate. The criticality of their adhesion is due to the stretching of the VWF polymers at high shear rates and exposure of their ligands to the platelet receptors. The reversibility of their adhesion is caused by both polymer stretching and the shear-sensitive affinity of their ligand-receptor interaction.

The shear rate increases from zero at the center to the highest shear rate at the vessel wall in the pressure-driven blood flow. Aggregation of platelets and VWFs is unstable at the center of the vessel where shear rate is low. Also, platelets and large VWFs are pushed to the vessel walls, to a layer devoid of red blood cells (RBCs), called RBC free layer (RBC-FL), because RBCs keep away from the walls and migrate toward the center of the

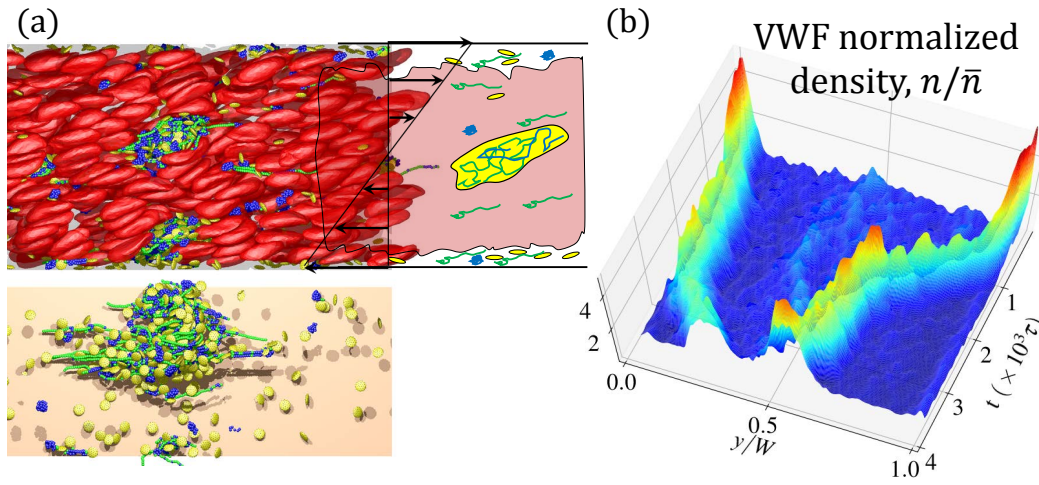


Fig. 7.8 Migration to the center of the vessel (demargination) for blood in a simple shear flow. (a) Schematic diagram together with the simulation snapshot shows the demargination of aggregates. (b) The density profile normalized by the mean density shows the aggregation process where the aggregates reach the center of the vessel, very similar to the slip-bond scenario in Figure 7.6. Here, the shear rate is constant and equal to the wall shear rate, $\dot{\gamma}_w$ all over in the cross section of the channel. Thus, the association of the aggregates never occurs if $\dot{\gamma}_w > \dot{\gamma}_c^a$.

vessel due to a hydrodynamic lift force. The high population of platelets and VWFs in the RBC-FL due to their margination increases the chance for their adhesion. If shear rate at the vessel wall is high enough, even without the existence of an adhesive substrate (a wound), platelets and VWFs are able to adhere and form aggregates. These micro-thrombi obtain significant hydrodynamic lift force and penetrate the bulk RBC flow. However, they migrate to lower-shear-rate regions as they demarginate. This results in their dissociation in the central regions of the vessel. This reasoning is verified by mesoscopic simulations of blood flow in micro-channels. The affinity of the ligand-receptor binding of VWFs to platelets is found to determine whether the aggregates reach the center of the vessel without dissociation or not.

Although, the concentration of VWFs and platelets in simulations are considered much higher than physiological concentrations, the aggregation is independent on concentration and must be present in physiological conditions, too. The rate of aggregation, though, depends on their concentrations.

The whole process can be summarized as follows, shown in Figure 7.9. The existence of RBCs is very beneficial for primary hemostasis, since RBCs migrate to the center of the vessel and lead to the margination of platelets and micro-scale large VWFs. Proximity to the wall helps VWF stretching, activating them for adhesion to platelets or to the wound site

in case of injury. If the affinity of VWFs to platelets is lower than normal, their adhesion is weak and may cause extra bleeding. This condition is observed for von Willebrand disease (VWD) type 2M^{185,213}. Lack of large VWFs has similar symptoms which is related to VWD type 2A^{185,213}. Thus, on the one hand, the high affinity of VWFs to platelets brings efficient hemostasis; on the other hand, it initiates aggregation in red blood cell free layer (RBC-FL), even in absence of injury.

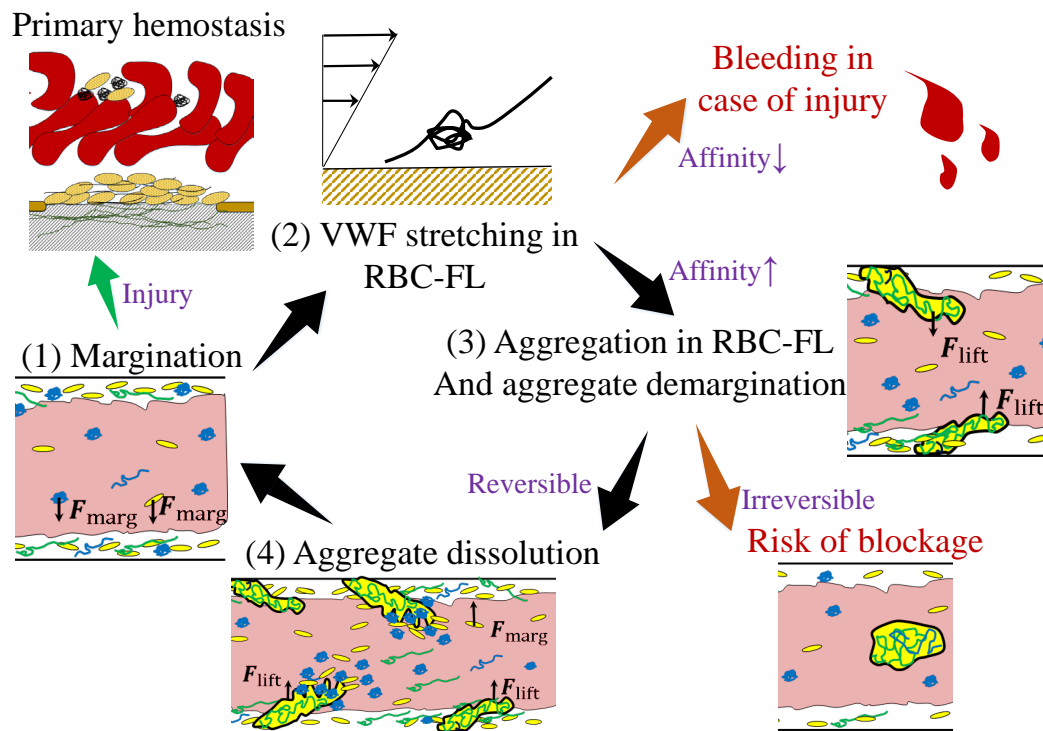


Fig. 7.9 Summary of platelet-polymer aggregation in blood flow. The continual process of margination, VWF stretching in RBC-FL, aggregation, demargination of aggregates, and aggregate dissociation is predicted for healthy physiological conditions in blood. With this, efficient primary hemostasis is possible. Deviations from this process results in bleeding or the risk of blood vessel blockage, which could be related to many pathological conditions.

Aggregates can grow while VWFs are stretched and adhesive to platelets. The formed aggregates are highly deformable and porous so that they can tumble and tank-tread like RBCs and obtain hydrodynamic lift force against the vessel wall. The lift force of the platelet-VWF aggregates dominates the margination force from collisions to RBCs and lifts the aggregates to the bulk flow. As aggregates penetrate to the RBC-core flow, they arrive at lower shear rates. Here two scenarios can occur. If platelets and VWFs form reversible aggregates, which is observed in experiments and calibrated simulations, the aggregates dissolve on their way before reaching the center of the vessel. The dissolved platelets and VWFs marginate back to the RBC-FL and feed new aggregates. The process recurs

continually. This process is predicted for normal physiological conditions. In contrast, if the aggregates are irreversible based on shear rate and remain stable at lower shear rates, they would eventually reach the center of the flow. We relate this to pathological conditions such as VWD type 2B^{185,213}, where the VWFs acquire higher than normal affinities to platelet receptors.

If the concentration of platelets and VWFs is too high, such as the case considered for the simulations, it is possible that platelets become activated on the way of forming large aggregates. In this condition, the aggregates become irreversible and the process of slip scenario takes place. This condition can be related to the fatal disease Thrombotic Thrombocytopenic Purpura (TTP), where VWF protease ADAMTS13 cannot cleave VWFs, causing high concentrations of very large VWFs¹²⁶.

The reason that such a process has not been observed yet in experiments may be that it is very hard to detect. We provide here some suggestions for further experimental studies on this issue. Increasing the concentration of VWFs and platelets will help to see the process on larger length scales and shorter time scales. Then, with a circular flow device, one can get periodicity in the flow so that the aggregate profiles should be measurable. Another way to detect this process is to design a large channel or tube and release large non-activated aggregates in the beginning of the channel and see if they reach the discharge. This could be the easiest way to detect this process.

Last but not least, the biological impact of this process must be also taken into account. The existence of a threshold layer for aggregation in blood vessels is very beneficial for the blood flow to prohibit undesired thrombosis and fatal blood vessel blockage. Physiological conditions such as the volume fraction of red blood cells, and the blood pressure can also affect the position of this threshold layer. Mutations of VWF protein or platelet receptor alters their affinity and deviates this well-tuned process causing bleeding or vessel blockage.

Chapter 8

Aggregate Dynamics in Blood Flow and primary hemostasis

The interaction of platelets and von Willebrand factor (VWF) polymers at high shear rates determine how well hemostasis proceeds. In healthy condition, the platelets and VWFs are able to adhere firmly to the injured wall and plug the wound. For adhesion to occur, it is required that platelets and VWF polymers marginate to the red blood cell free layer (RBC-FL) close to the walls and collide with them every now and then, while VWFs are stretched and active as well. Using mesoscopic simulations of blood flow, it is demonstrated for the first time that these conditions only occur in a specific range of shear rates and hematocrits. The margination and stretching of VWFs in RBC-FL takes place in normal blood flow where platelets and VWFs do not interact or their concentration is dilute enough to suppress microthrombi formation. However, as the concentration of VWFs and platelets increase, they form aggregates in the RBC-FL, even without the presence of an injury. Aggregates acquire different hydrodynamic properties so that they demarginate and penetrate the bulk RBC flow. No matter how an aggregate is first formed, it alters the margination of the other platelets and VWFs if its growth is irreversible. The aggregation is directly affected by shear rate, and indirectly by hematocrit via margination. The roughness of the vessel is found to be unimportant as long as it is not comparable with the vessel diameter. The affinity of VWF and platelets also controls the extent of aggregation.

8.1 Introduction

Platelets aggregation under shear-flow condition directly affects hemostasis and thrombosis. Their aggregation depends on the size distribution of von Willebrand factors (VWF) and

platelet receptor interaction with VWF ligands. The proximity of platelets and VWFs to the blood-vessel wall is a prerequisite for their imminent adhesion to the injured wall. Hopefully, this happens because of the existence of erythrocytes, or red blood cells (RBCs). In blood flow, RBCs with their biconcave elastic membranes transmigrate to the center of the blood vessel away from the vessel walls, known as Fåhræus effect^{51,52}. The centralization of RBCs leaves a thin RBC free layer (RBC-FL) adjacent to the vessel wall. The other micro-scale blood components, whose hydrodynamic lift force is not as large as that of RBCs, are pushed toward this layer, a phenomenon known as margination^{66,133,175,255}. Micro-scale objects have better margination property than nano-scale particles since they must be able to effectively collide with RBCs and get pushed to the RBC-FL^{140,142,144,227}. Even large leukocytes (white blood cells) marginate^{57,58,73,78,145} since their lift force is not high enough to compensate push-back force by RBCs flowing at the center. Accordingly, VWFs marginate if their size is large enough¹⁷². The concentration of large VWFs at the RBC-FL is then higher than their concentration in the bulk of the flow. VWFs stretch and get activated coincidentally with their margination¹⁷² since the shear rate at the vessel wall is order of magnitude higher than the shear rates at the center of the vessel.

The mechanisms of platelet aggregation in blood stream and its dynamics are still open questions. A few approximate methods have been proposed for the problem^{68,69,163,229,246}, but are far from reality by omitting the physical presence of VWF polymers. The difficulty of studying aggregation and aggregate dynamics at the same time is that it is multiscale in many aspects. The initial aggregation process takes place within tens of seconds, while several VWF molecules must adhere to several platelets and form bigger aggregates. The aggregates have a different dynamics than single platelets and VWFs so that their margination properties totally change in blood flow. The items which play an important role in the process are also multiscale. Single VWF domains are sub-micron structures which interact with micron size platelets. They are also affected by a bulk of ten micrometer RBCs. Studying such system needs detailed multiscale modeling of the important objects in the system that is accomplished here. The aggregation on adhesive substrates under the conditions of blood flow as a model of hemostasis is studied. The aggregate dynamics in blood flow is analyzed further and compared with the normal blood flow.

8.2 Setup

The hemostasis process is non-equilibrium and non-steady, where all components flow and aggregates form and grow. The process can be thought of as quasi-steady since the concentration of VWFs is so small and aggregate growth on the injured site takes a long time.

Thus, the concentration of platelets and VWFs is increased to see the aggregation in shorter periods. The setup for 3D simulations is summarized in Table 8.1.

For the adhesive surface, virtual particles are arranged homogeneously on the wall while they have neither hydrodynamic nor LJ interaction with any particle in the box. They can only be seen by platelet receptors and VWF active beads for adhesive bond interaction.

The highly parallel simulation package, LAMMPS, based on short-range interactions of molecular dynamics¹⁶⁴ is used and developed for this work.

In order to study several parameters of the problem, a number of simulations must be run in sufficient period of time. The 3D simulations are extremely large and time consuming. To this end, the simulations are run in 2D to be able to simulate the system with different parameters and study their effect on aggregation. The blood flow in 2D and 3D simulations generate qualitatively similar RBC-FL thickness, similar density profile for all blood components, and similar stretching behavior of VWF polymers^{140,172} (see also chapter 6). It is tried to keep all properties similar to 3D simulation properties to get the most relevant results.

The box size in 2D simulations is $300 \times 40 \mu\text{m}^2$ where 100 VWFs and 200 platelets flow among RBCs with different channel hematocrits H_c .

Table 8.1 Setup for 3D simulations. Effective volume of membranes is computed as the inner volume of their network plus the volume of LJ interaction, $V_{\text{eff}} = V + A\sigma_{\text{LJ}}/2$. For the polymer, it is $\pi N_{\text{bead}}\sigma_{\text{LJ}}^3/6$. Physiological volume fraction of RBCs (hematocrit) is around 30-45% and volume fraction of VWFs and platelets in the blood is less than a percent. However, we presume much more volume fraction of them for our aggregation study.

Type	RBC	plat.	pol.	solvent
Number	360	768	384	288,000
Effec. vol. (μm^3)	112	2.1	2.0	N/A
Vol. frac. (%)	42	1.68	0.84	100
Box size (dir.)	80(flow) \times 40(shear) \times 30 (vort.) μm^3			

8.3 Process of hemostasis

Marginated VWFs stretch at high wall shear rates and adhere to the injured site. The immobilized VWFs make a better substrate for platelets since they make firstly high strength bonds with platelets, and secondly a rough brushy surface for platelets giving them more chance to find a ligand. The adhered platelets make another surface for VWFs to adhere and the process occurs in a cascade until the wall opening gets plugged^{5,176}.

The blood clotting on an adhesive surface is shown in Figure 8.1. The aggregates firmly adhere to the surface thanks to VWF adhesion, whereas the platelets themselves are unable to withstand high shear forces. The phase diagram of such system for VWF stretching vs. its cross-sectional position shows that VWF polymers stretch and adhere firmly to the adhesive surface (injured wall). Most of the platelets and VWF polymers moving in the RBC-FL close to the adhesive surface adhere very quickly. It is seen in the phase diagram as well that most polymers adhere there and get extended from 25% to maximum 75% of the contour length. The VWF polymers in the bulk flow are in collapsed state most of the time. On the other hand, when the vessel wall is not injured, the VWFs do not adhere to the wall, but they still stretch and adhere to platelets. They form moving microthrombi which by growing, penetrate the RBC bulk flow. Those microthrombi which reach the low shear rate regime in the bulk flow dissociate (see chapter 7). This process happens because aggregation of VWFs to platelets is reversible and critical according to shear rate (see chapter 6).

The development of the density profile of the system in time shows how well VWFs adhere to the adhesive surface, as shown in Figure 8.2. The initial state of the simulation is considered as a steady-state blood flow with developed margination. From the very beginning of the simulation, the VWFs close to the adhesive wall adhere to the surface and tether platelets. The process goes on until the RBC-FL lacks extra VWFs and platelets. Although this is an artifact of the simulation with periodic boundary conditions, the initially higher concentration of the platelets and VWFs partially compensates it. Moreover, the aggregation process can be considered as a quasi-steady process as already explained. Thus, Figure 8.2 is only intended to show how fast and firmly the aggregates form on an injured surface. On the other side of the density profile development plot in Figure 8.2, the continual aggregation, demargination, dissociation, and remargination is seen where one peak of the VWF density profile is inside the RBC-FL and the other peak in the bulk flow adjacent to the limiting shear rate for aggregate formation. This process has been studied thoroughly in chapter 7.

Depending on how large the on- and off-rates of the VWF-platelet interaction are, and depending on the polymer cohesive forces, the aggregation of the polymers and platelets is reversible based on the shear rate.

The number of adhesive bonds in time is shown in Figure 8.2 as well. The adhesion parameter is defined as

$$\Phi_i^j = \frac{\text{Number of bonds between } i\text{'s and } j\text{'s}}{\text{Number of } i\text{'s}}, \quad (8.1)$$

where i and j are adhering entities such as VWF beads, platelet receptors, and substrate ligands. The adhesion parameter is between zero and unity, $0 \leq \Phi_i^j \leq 1$.

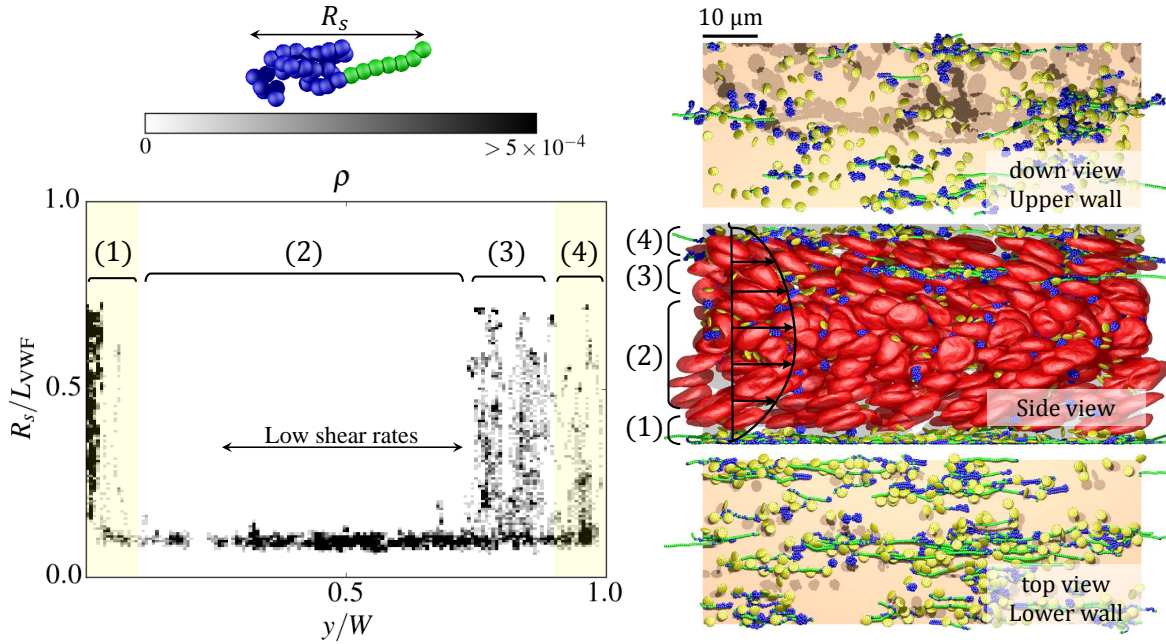


Fig. 8.1 Stretching phase of polymers in blood flow in absence and presence of adhesive wall. In the left panel, the extension of polymer in the flow direction, R_s , normalized by the contour length of the polymer, L_{VWF} , is shown as a function of cross-sectional location in the channel, y . The color bar gives the distribution probability for each point. The extension of the polymer in the flow direction is illustrated at the top with a sample polymer configuration. The stretched parts of the polymer are active and colored in green, while the collapsed inactive parts are colored in blue. The adhesive surface is at $y = 0$, where VWF polymers adhere to. Different layers are specified in the diagram and the simulation snapshot as the following. (1) The adhesion layer inside the RBC-FL adjacent to the adhesive wall. Most VWFs are adhered and stretched substantially from 25% to maximum 75% of the contour length L_{VWF} . (2) The bulk flow with no aggregate where VWFs are collapsed and inactive. The extension in this layer is mostly 10% of the contour length which is roughly the lowest limit for coarse-grain 30-bead polymers. (3) The demargination layer for aggregates where aggregates grow, demarginate and finally hit the low shear rates and become unstable. A mixture of aggregated stretched and free collapsed VWFs are there. (4) the RBC-FL adjacent to a non-adhesive wall where aggregate formation is initiated. The coil-stretch dynamics results in extensions around 10% to 75%. In the snapshot, RBC membranes are shown in red (their vertices are not shown for better representation), platelet membranes are shown in yellow with their vertices shown by black dots, and VWF polymers are represented by blue (inactive) and green (active) beads.

Systematic studies of the problem are very time consuming which makes their simulation inaccessible at this time. In order to investigate all the parameters interfering with the hemostatic process, bunches of 2D simulations are conducted and results are qualitatively

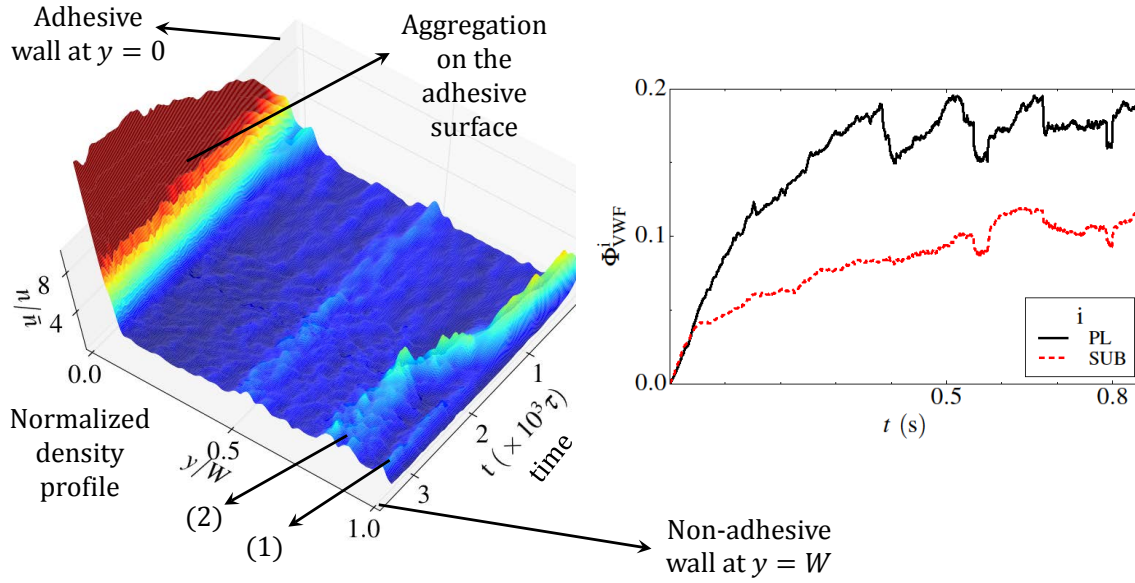


Fig. 8.2 VWF density profile (left) and number of bonds in time (right). Without aggregation, the density profile of VWFs has a peak at each RBC-FL, shown at time $t = 0$. Setting on the adhesive interactions, the aggregates form and adhere to the adhesive wall. On the other side, at $y = W$, aggregates form and penetrate into the bulk flow until they reach low shear rates and dissociate. Dissociated VWFs and platelets remarginate to the RBC-FL. Such continual process causes two peaks of the density profile, one inside the RBC-FL (1) and the other inside the bulk flow (2) right behind the layer where shear rate is low enough to initiate dissociation (see [chapter 7](#)). Φ_{VWF}^{SUB} and Φ_{VWF}^{PL} are adhesion parameter for VWF-substrate and VWF-platelet pair, respectively. The fluctuation in Φ_{VWF}^{PL} shows the aggregation and dissociation of platelets and VWFs which are freely moving; while Φ_{VWF}^{SUB} increases more smoothly showing firm aggregation.

interpreted for the real 3D phenomenon. It is noted that 2D simulations of blood flow are in satisfactory qualitative agreement with 3D simulations and experiments^{140,172}.

8.4 Free aggregate dynamics

Free aggregation of platelets and VWF polymers in blood flow is studied and compared with the normal blood flow without aggregation. Figure 8.3 shows a set of snapshots of the 2D simulations in different flow conditions. The leftmost column of snapshots shows the configuration and positioning of all blood components in the normal margination case for different pressure drops. The margination of polymers and platelets can be easily seen in the images. The middle column shows the same systems, but with adhesive interactions which

make irreversible aggregates. The demargination of aggregates is intensified as pressure drop or equivalently shear rate increases. Thus, when platelets and VWF polymers aggregate, they acquire more hydrodynamic lift force than RBCs such that they can penetrate the bulk RBC flow. Higher shear rates imply larger aggregates. Larger aggregate, larger lift force. And larger lift force, more demargination. The aggregation also depends on hematocrit H_c , the volume fraction of RBCs. The rightmost set of images demonstrate aggregation for different hematocrits.

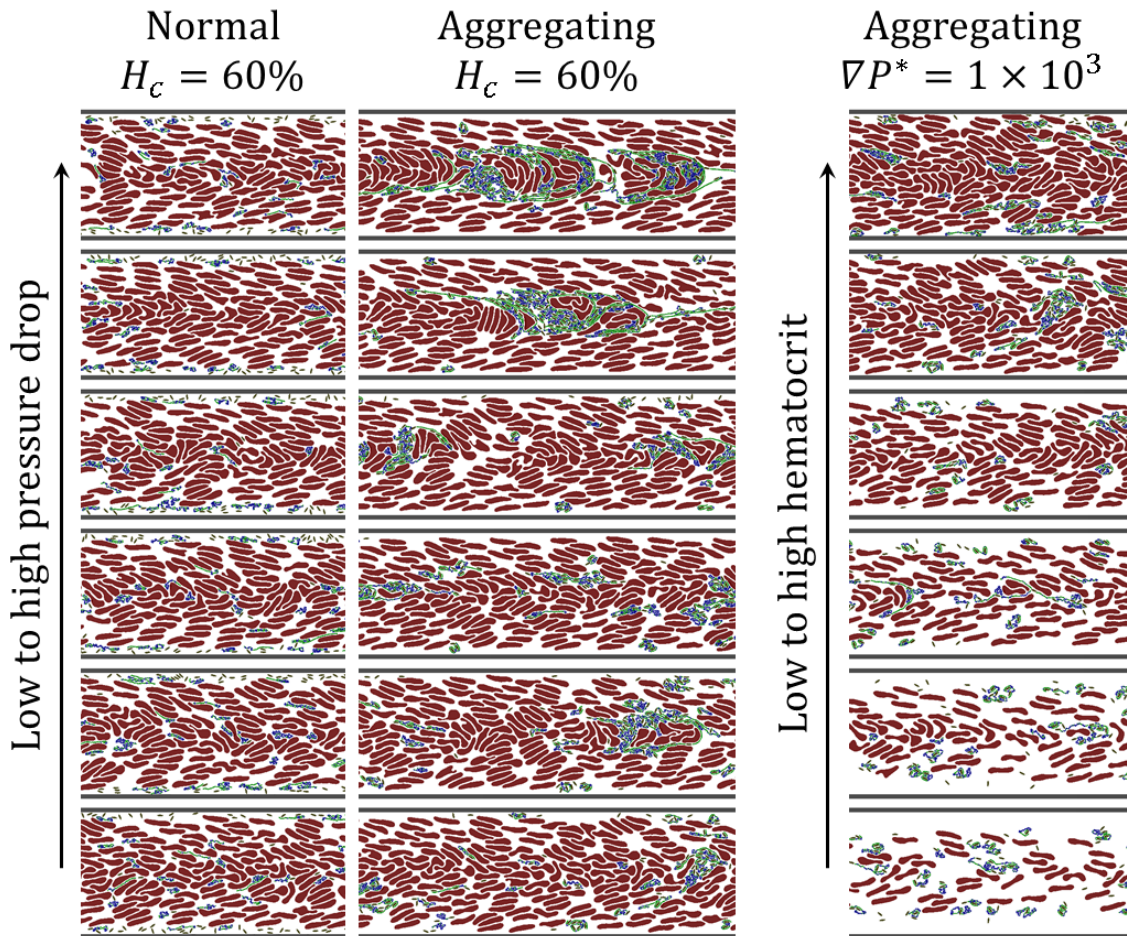


Fig. 8.3 2D simulations of blood flow and aggregation. The leftmost set of images show the blood stream in 2D without adhesive interactions. The middle column shows the aggregation and their demargination for different shear rates. In constant hematocrit, the aggregation and demargination increases by increasing the pressure drop ∇P . The rightmost column shows the same system in different hematocrits and constant shear rate. Here, RBCs and platelets are represented by filled closed areas with dark red and dark yellow colors, respectively. The polymer beads are shown by blue (inactive) and green (active) filled small discs. The whole simulation box for each case is $300\ \mu\text{m}$ long, much longer than what is shown.

It may be questioned that higher than 50% hematocrit is not physiologically possible in microvessels, so why do we study hematocrits up to 70% in 2D simulations? The answer lies in the 2D and 3D comparison of hematocrits. The equivalent 3D hematocrit is 20% less than the 2D hematocrit, as studied recently by comparing the RBC-FL thickness and margination profiles of 2D and 3D simulations¹⁷² (see [chapter 3](#)).

The aggregation and demargination happen successively. If the aggregation is reversible with respect to the shear rate, once aggregates reach low shear rate regime at the central region of the flow, they dissociate and marginate back to the RBC-FL, as explained before and studied in detail in [chapter 7](#). Here, the focus is on aggregate dynamics in the flow so that only the slip-bond irreversible aggregation is studied.

The aggregation process has two main factors, the extent of aggregation, $\langle \Phi_{VWF}^{pl} \rangle$, and the rate of aggregation, τ_{agg} , given by

$$\Phi_{VWF}^{pl}(t) = \langle \Phi_{VWF}^{pl} \rangle \left(1 - e^{-t/\tau_{agg}} \right). \quad (8.2)$$

Figure 8.4 shows both quantities for different hematocrits and pressure drops. The (magnitude of) the pressure drop is normalized such that $\nabla P^* = \nabla PW \tau / \eta$. The pressure drop and wall shear rate are related by

$$\dot{\gamma}_w = \frac{\nabla PW}{2\eta} = \frac{\nabla P^*}{2\tau}. \quad (8.3)$$

The pseudo shear rate $\bar{\gamma} = \bar{u}/W$ is another useful measure which is $\nabla PW/12\eta$ in ideal Poiseuille flow and less in blood flow. The range of wall shear rates studied by 2D simulations is estimated to around 500 s^{-1} to 1500 s^{-1} under physiological conditions.

The aggregation extent is directly proportional to the shear rate (equivalently pressure drop) since the polymer stretching is affected mostly by shear rate. The hematocrit suppresses the aggregation weakly by not letting the aggregates to move and grow freely, whereas it increases the aggregation rate. Nevertheless, both aggregation extent and aggregation rate are more sensitive to shear rate than to hematocrit.

The margination of platelets and VWF polymers changes substantially in case of aggregation. The steady-state density profile of platelets and VWF polymers correlates with their aggregation. In normal case with no adhesive interaction between platelets and VWFs, these microparticles marginate and flow close to the vessel walls, as depicted in Figure 8.5-left. In case of aggregation, the aggregated polymers and platelets demarginate reducing the peak of the density profile in the RBC-FL, as shown in Figure 8.5-right. The remaining platelets and VWF polymers are still marginated, as indicated by a tiny peak in the RBC-FL.

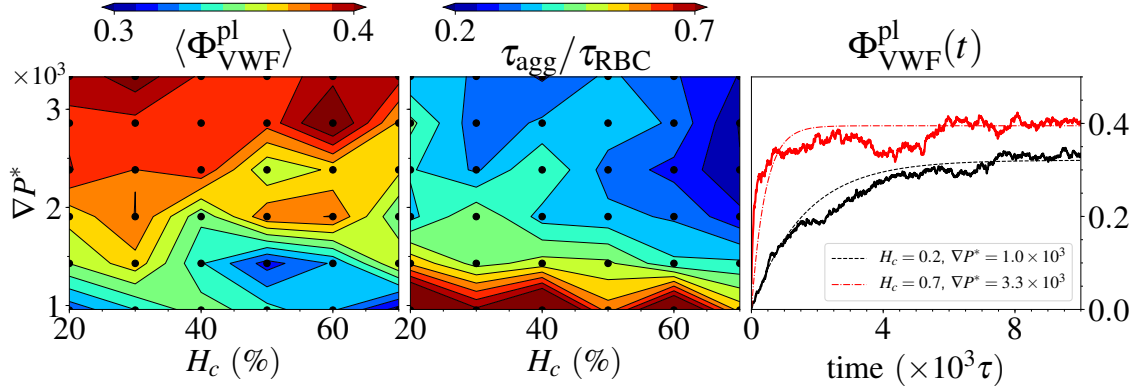


Fig. 8.4 The aggregation process for different pressure drops and hematocrits. The left panel shows the average adhesion in steady state, $\langle \Phi_{VWF}^{pl} \rangle$. The aggregation time, τ_{agg} , normalized by the RBC relaxation time, is depicted in the middle panel. And the right panel gives two examples of how these two factors are fitted to the data. Both the extent of aggregation and aggregation rate (τ_{agg}^{-1}) definitely increase by increasing pressure drop, while it is weakly affected by hematocrit. The black dots in the contour plots are the data points each belonging to an independent simulation.

In order to measure margination, a margination parameter M is defined as

$$M = \frac{4 \int_0^W \rho(y) |y - y_c| dy}{W \int_0^W \rho(y) dy}, \quad (8.4)$$

where y_c is the coordinate of the center of the channel, and $\rho(y)$ is the distribution of the entity. $\rho(y)$ can be considered as the probability distribution such that $\int_0^W \rho(y) dy = 1$. It is computed after the system reaches steady-state (i.e. $t > 5000 \tau$) and is averaged over an adequate period of time ($\Delta t =$

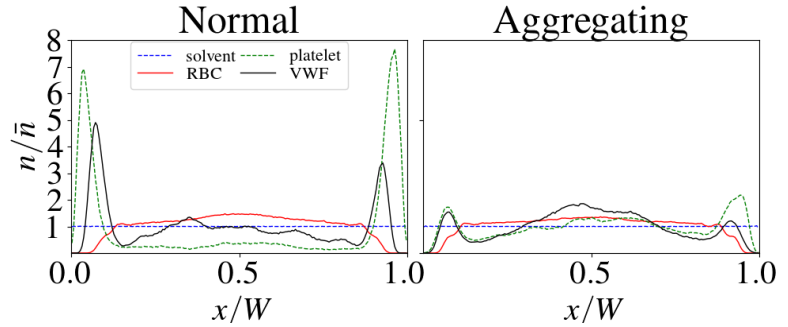


Fig. 8.5 Density profile of blood components in 2D simulations. The left panel shows their distribution in normal flow without adhesive interactions, and the right panel shows the same system but with adhesive interactions. The number density, n , is normalized by the average number density, \bar{n} . In both cases, the solvents fill every space in the channel homogeneously, and the RBCs keep away from the walls and leave a RBC-FL. The platelets and VWF polymers marginate similarly in the normal case, as shown by the peaks of their density profile in the RBC-FL. When they aggregate, they demarginate and flow mostly on the center of the channel. The non-adhered free platelets and VWF polymers still remain margined as shown by tiny peaks in the RBC-FL. Both diagrams are for $H_c = 50\%$ and $\nabla P^* = 10^3$ condition.

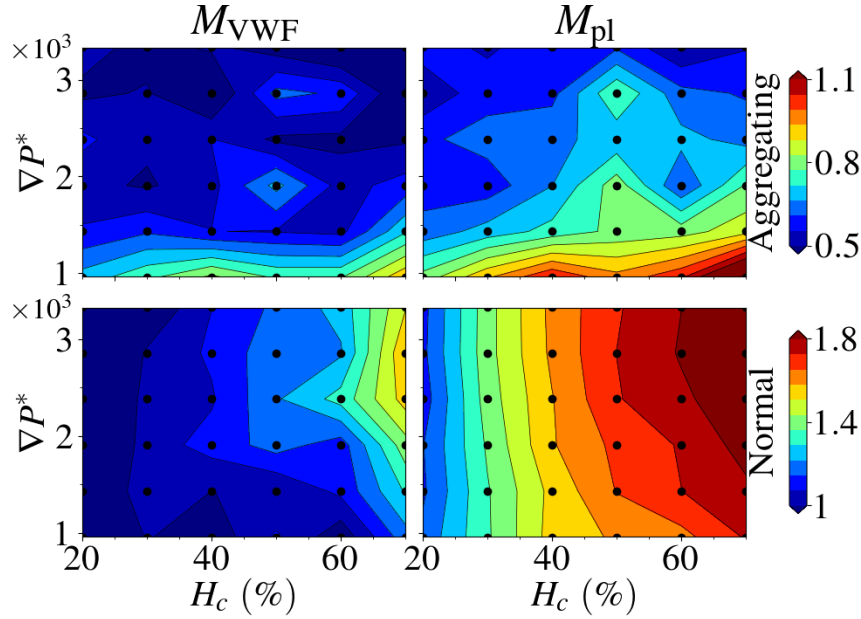


Fig. 8.6 Margination parameter for different hematocrits and pressure drops in normal flow and aggregated flow case. M_{VWF} and M_{pl} refer to the margination parameter of VWF polymers and platelets, respectively. In normal flow, the margination of platelets is mostly related to the hematocrit than the shear rate. The margination of polymers is both affected by shear rate and hematocrit. The margination of polymers is also much weaker than the margination of platelets since they stretch in RBC-FL and can easily penetrate the bulk flow. In case of aggregation, the story is opposite. The margination of both entities becomes almost insensitive to hematocrit, but very sensitive to shear rate. Also, the margination parameter is less than unity meaning that the aggregates are demarginated. Their demargination increases as shear rate increases, which is directly correlated to the increase of aggregation. The black dots represent H_c and ∇P^* for which independent simulations have been performed.

5000 τ). $M > 1$ means the entity gathers mostly close to the walls rather than in the center, that it is margined. $M = 1$ is obtained for a homogeneous distribution in the channel, like solvents or nanoparticles which do not marginate, nor gather at the center. $M < 1$ implies demargination, like for RBCs which keep away from the walls and concentrate mostly on the center of the channel. $M = 0$ as the lowest limit corresponds to full concentration of the entity in the channel center, with $\rho(y)$ being a delta function. On the other hand, $M = 2$ as the upper limit corresponds to full margination. The margination parameter M implies that the whole diagrams in Figure 8.5 can be characterized by only one number in range $[0, 2]$. For instance, $M > 1$ and $M < 1$ for VWFs and platelets in the left and right panel of Figure 8.5, respectively.

Figure 8.6 shows the margination parameter for different hematocrits and pressure drops. The margination of polymers and platelets is mostly determined by hematocrit, and increases

with increasing hematocrit. The margination of polymers is highlighted more at higher shear rates since their dynamics is also dependent on shear rate. When they aggregate, they penetrate the bulk blood flow and demarginate. Their demargination is independent of hematocrit in contrast to the normal margination case. In addition, by increasing the pressure drop, or equivalently shear rate, their demargination increases leading to lower M values.

It is worth to mention another quantity which is very related to the margination parameter; that is the margination probability $p(\delta)$, the probability of finding an entity closer than distance δ to a wall. Setting δ small enough, it gives a measure of how fast polymers or platelets can adhere to an injured wall. Setting δ to the RBC-FL thickness δ_{CFL} , gives a measure of how VWFs and platelets are repelled from the RBC bulk flow. Since RBC-FL thickness varies in different hematocrits¹⁰⁰, $p(\delta_{\text{CFL}})$ takes smaller or larger space into account.

As illustrated in Figure 8.7-a, the RBC-FL

thickness decreases as hematocrit grows and it does not change much whether platelets and polymers aggregate or not. Figure 8.7-b shows the results for margination probability to the RBC-FL. Platelets marginate well to this layer in almost all flow conditions studied. VWFs however, marginate better to this layer as both shear rate (or equivalently pressure drop) and hematocrit increase. When they aggregate, their dynamics changes so that they tend to go to the center of the flow, moving outside of the RBC-FL. As shear rate increases,

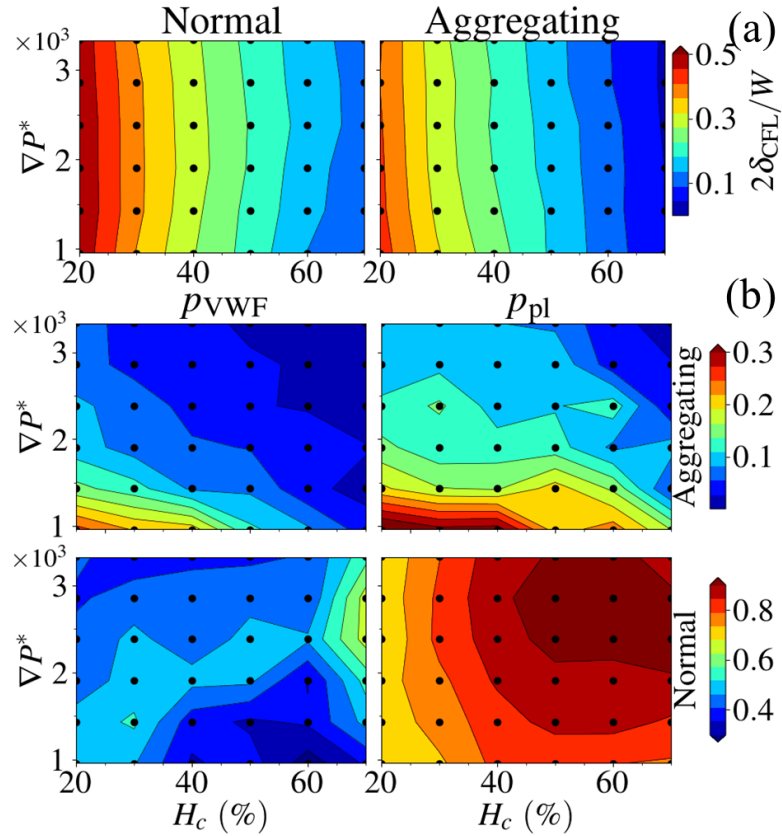


Fig. 8.7 RBC-FL thickness, δ_{CFL} , normalized by the channel width, W (a), and margination probability for platelets and VWF polymers (b) in normal and aggregation condition. RBC-FL thickness is computed as the average distance between the bulk RBC flow and the vessel walls. The black dots represent H_c and ∇P^* for which independent simulations have been performed.

the aggregation increases so that more demargination happens, leading to less probability of margination to the RBC-FL. The hematocrit does not play a crucial role here, but since it defines the RBC-FL thickness, it can affect margination probability to the RBC-FL.

8.5 Aggregation on the wall

The on- and off-rates for the adhesive bonds are also influential in the whole hemostasis process, whose calibrated values in 3D have been already presented. In 2D, there is an opportunity to study their effect on the aggregation.

As explained before in Equations 2.15 and 2.16, the rates k_{on} , k_c , and k_s determine the aggregation process. Figure 8.8 shows a 2D simulation with a 30 μm long adhesive patch at a surface and the immobilized aggregates on it, for two different hematocrits. In addition, the aggregation is plotted as a function of on-rate k_{on} and off-rates k_c , and k_s . The aggregation parameter Φ_{VWF}^{pl} is computed after a 2000 τ time period and averaged over the same period. The adhesive interactions are turned off in the channel for regions 20 μm before and 50 μm after the adhesive surface, in order to avoid free spontaneous aggregation and demargination.

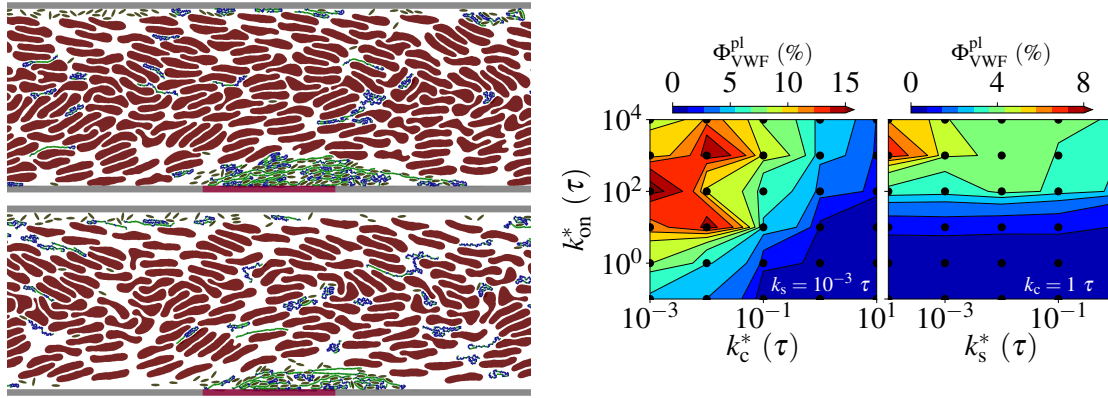


Fig. 8.8 Aggregation as a function of the association and dissociation rates. Two snapshots for two different hematocrits are shown as an example. The adhesive surface represented by red colored walls is 30 μm long, and the whole channel is 300 μm long. The adhesive interactions are set off in the channel for regions 20 μm before and 50 μm after the adhesive surface, in order to avoid free aggregation and demargination. The aggregation extent is averaged over 2000 τ in steady-state. The contour plots show the effect of on-rate k_{on} and off-rates k_s and k_c on the aggregation. The black dots in the contour plots show the data points from independent simulations.

As expected, the bond association rate k_{on} , and dissociation rates k_s and k_c define how fast and firm the aggregation happens in a specific physiological condition, i.e. constant shear rate, hematocrit, platelet and VWF concentration, etc. Increasing on-rate k_{on} increases aggregation, and increasing off-rates k_c , and k_s decreases it. For healthy VWFs, on- and off-rates are finely tuned such that the aggregation takes place and becomes stable at shear rates more than about 1000 s^{-1} at which VWFs stretch^{188,191}. Any deviation, caused by VWF mutations, leads to the lack of aggregation and bleeding disorder or undesired aggregation¹⁸⁵.

Margination of platelets and VWFs in a narrow RBC-FL is required for hemostasis. Since at low hematocrits, the RBC-FL is thick, the polymers never touch the adhesive substrate to be able to adhere, even-though they may have been margined well. No adhesion is found in the 2D simulations of hematocrits less than 50%, equivalent 30% hematocrit in 3D. However, under physiological conditions, blood vessels are not ideally smooth as is assumed in the simulations; the diameter of the vessel varies along the vessel axis. Also, the injured vessel wall presents more additional roughness. To study this, an adhesive surface on a bulge is put inside the channel. Figure 8.9 depicts the streamlines of the flow for a bulged adhesive surface, as well as the relative concentration of platelets and VWF polymers in the channel, and the aggregation extent based on bulge size and hematocrit. As the blood flow is laminar (low Reynolds number), the platelets and polymers keep moving on the streamlines which are deflected because of the presence of the bulge. Thus, they keep their distance to the wall even at the bulge site as long as the flow rate is not increased substantially. The aggregation of platelets and VWFs on the site does not change substantially by increasing the bulge height until it becomes comparable with the vessel size where RBCs change their dynamical phase.

8.6 Summary

The aggregation of platelets and VWF polymers has been studied under different physiological conditions using mesoscopic multiscale hydrodynamic simulation of blood. The thrombus formation on an injured vessel wall has been investigated in detail. It is understood that aggregates can firmly form on the adhesive substrate by stretching of the VWF polymers. The margination of platelets and large VWF polymers is required for their aggregation on the surface. In normal flow, where platelets and VWFs do not form microthrombi, the margination takes place efficiently when they are pushed by RBCs to the RBC-FL close to the vessel walls. However, microthrombi can form in absence of injury in the RBC-FL by the spontaneous adhesion of VWFs to platelets since VWFs are stretched there and get activated. In addition, as thrombi grow on the site of injury, some part of it can detach from the whole

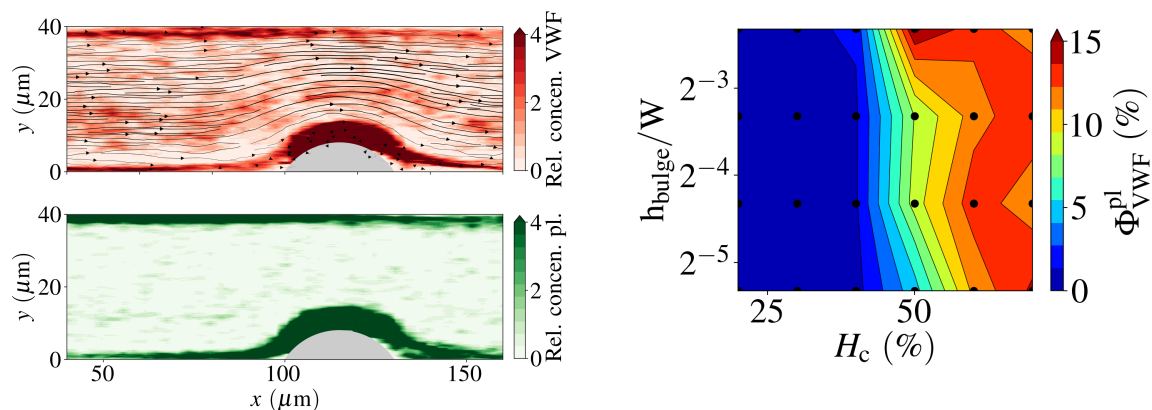


Fig. 8.9 Aggregation of platelets and VWF polymers at the presence of a bulge. The relative concentrations of polymers and platelets are plotted among the streamlines. The aggregation extent as a function of hematocrit and bulge height is depicted at right. The bulge size has a small effect on the aggregation since the polymers and platelets do not hit the bulge by sticking to the streamlines of the laminar flow of the blood. The bulge or the roughness of the vessel must be comparable to the vessel diameter to make a difference in aggregation. The black dots indicate the data points from independent simulations.

aggregate by the shear force and release to the blood flow. Our studies show that the free movement of platelet and polymer aggregates in the blood flow alters the margination of the other platelets and VWF polymers if these aggregates grow spontaneously and irreversibly. It is understood that these aggregates transmigrate to the center of the flow and merge with the bulk flow of RBCs.

The affinity of VWF polymers to platelet receptors plays an important role in their adhesion. Modeling the interaction by two states, with one on-rate and two off-rates, the effect of rates on the interaction has been investigated. The on-rate determines whether aggregation takes place; and the off-rates determine the extent of aggregation and its reversibility. The most important factor for the efficacy of hemostasis is the hematocrit due to its role in promoting VWF and platelet margination. At low hematocrits, the adhesion to the wall never happens since the RBC-FL is too thick to force the margined polymers to contact the walls and adhere. Even the roughness of the vessel cannot compensate for this. Because the blood flow is a low-Reynolds-number laminar flow, the polymers and platelets keep moving along the streamlines so that the roughness of the vessel does not help much in their collision with the wall, as long as the roughness is not in the order of vessel diameter.

Part IV

Regulation of von Willebrand factor by cleavage

Chapter 9

Cleavage of von Willebrand factor by ADAMTS13 protease in flow

Von Willebrand factor (VWF) is a key protein in hemostasis as it mediates adhesion of blood platelets to a site of vascular injury. A proper distribution of VWF lengths is important for normal functioning of hemostatic processes, because a diminished number of long VWF chains may significantly limit blood clotting and lead to bleeding, while an abundant number of long VWFs may result in undesired thrombotic events. VWF size distribution is controlled by ADAMTS13 protease, which can cleave VWF chains beyond a critical shear rate when the chains are stretched enough such that cleavage sites become accessible. To better understand the cleavage process, we model VWF cleavage in shear flow using mesoscopic hydrodynamic simulations. Two cleavage models are proposed, a geometrical model based on the degree of local stretching of VWF, and a tension-force model based on instantaneous tension force within VWF bonds. Both models capture the susceptibility of VWF to cleavage at high shear rates; however, the geometrical model appears to be much more robust than the force model. Our simulations show that VWF susceptibility to cleavage in shear flow becomes a universal function of shear rate, independent of VWF length for long enough chains. Furthermore, VWF is cleaved with a higher probability close to its ends in comparison to cleaving in the middle, which results into longer circulation lifetimes of VWF multimers. Simulations of dynamic cleavage of VWF show an exponential distribution of chain lengths, consistently with available *in vitro* experiments. The proposed cleavage models can be used in realistic simulations of hemostatic processes in blood flow.

9.1 Introduction

In case of a vascular injury, a complex hemostatic process is initiated, where various blood components form a plug (or clot) at the injury site in order to stop bleeding. Von Willebrand factor (VWF) is a key player in the primary hemostatic process and acts as a 'glue', mediating adhesion of blood platelets to the areas of damaged endothelial cells with exposed collagen^{134,213}. In fact, at high enough shear rates VWF function is indispensable, because platelets are not able to bind efficiently to an injury site by themselves^{188,190}. Thus, dysregulation or dysfunction of VWF may lead to severe problems ranging from uncontrolled bleeding to undesired thrombotic formations^{76,186,192}.

VWF is a large, chain-like, multimeric protein made of dimeric subunits⁷¹. It is a shear responsive molecule, because in equilibrium or at low shear rates VWF remains in a globular configuration due to its internal associations^{208,213}, while at high enough shear rates VWF is able to stretch¹⁹¹. In a globular configuration, VWF remains non-adhesive such that its adhesive sites are shielded²³¹, while in a stretched form, the adhesive sites of VWF get exposed and it can adhere to a damaged endothelium and platelets^{103,213}. Also, in a stretched configuration, VWF can be cleaved, which is performed by the ADAMTS13 protease if cleavage sites within VWF become accessible^{42,184,228,252}.

Even though long VWF chains are known to be necessary for efficient blood clotting^{185,212}, size regulation of VWF by ADAMTS13 cleavage plays an important role in hemostasis. Deviations from the normal size distribution of VWFs may cause different types of VWF diseases^{176,213}. The detriment of dysregulation of VWF sizes is evident from two diseases with opposite principle causes: von Willebrand disease (VWD) and thrombotic thrombocytopenic purpura (TTP). VWD is the most common bleeding disorder and is caused by a deficiency in VWF, which results in excessive bleeding. In particular, VWD type 2A results from the shortage in the number of large VWFs in blood caused by a VWF mutation, making VWFs prone to cleavage by ADAMTS13¹⁸⁵. On the other hand, TTP is caused by a VWF mutation, which may inhibit its cleavage, or by defective ADAMTS13, and results in an abundance of large VWFs and therefore excessive undesired clotting¹⁸⁵.

Single molecule studies on VWF cleavage^{252,253} have shown that VWF cleavage sites become accessible beyond a critical tensile force of about 20 pN applied to the protein. This makes a connection between a stretched configuration of VWF in flow and its cleavage by ADAMTS13, since shear flow can exert effective tensile forces above the threshold force for opening cleavage sites. However, it is still not clear how the dynamic cleavage process occurs in flow. Recent *in vitro* experiments on VWF cleavage by ADAMTS13^{124,125} have demonstrated an exponential distribution of VWF sizes with a characteristic chain size gradually decaying in time due to VWF cleavage. These experiments have also shown that a

critical shear rate needs to be exceeded before the cleavage process becomes possible, which is consistent with the existence of a threshold force required for cleavage. Accompanying theoretical analysis¹²⁵ have resulted in the prediction of VWF cleavage kinetics and the threshold force.

In this work, we explicitly model the cleavage of VWF in shear flow and propose two models for VWF cleavage. The first model is based on geometrical conformations of VWF in flow and is associated with the degree of local extension of VWF. The second model utilizes instantaneous tensile forces within a VWF chain, mimicking the force threshold required for cleavage. Both models reproduce VWF susceptibility to cleavage at high enough shear rates. However, the tension-force model appears to be extremely sensitive to the choice of a threshold force due to very large fluctuations of bond tension in flow, making the applicability of this model limited. In contrast, the geometrical model is shown to be very robust. Our simulation results show that VWF susceptibility to cleavage is independent of VWF length for long enough multimers, and is a monotonically increasing function of shear rate. We have also found that VWF is cleaved with a higher probability close to its ends in comparison with its cleavage in the middle. This cleavage pattern implies that long VWF chains are cleaved gradually from their ends, increasing their circulation lifetime. Furthermore, we investigate the dynamics of VWF cleavage and find the evolution of size distribution qualitatively similar to experiments^{124,125}. In the end, the proposed model of cleavage is employed for the investigation of the cleavage scenario in blood flow. The effect of margination and VWF polymer stretching on its cleavage are investigated.

9.2 VWF cleavage model

A VWF chain is cleaved by removing a bond (or spring) which is accessible for cleavage. A geometrical model for the susceptibility of VWF to cleavage is based on the degree of local stretching of a VWF chain, which can be implemented using several criteria. The first criterion is directly related to local stretching of VWF and is defined for a spring $(i, i + 1)$ between beads i and $i + 1$ through the two angles adjacent to this spring as

$$\begin{aligned} \theta_{i-1,i,i+1} &\geq \theta_{\text{thres}} & 2 < i < N - 1, \\ \theta_{i,i+1,i+2} &\geq \theta_{\text{thres}} & 1 < i < N - 2, \end{aligned} \quad (9.1)$$

where $\theta_{i-1,i,i+1}$ is the angle between springs $(i - 1, i)$ and $(i, i + 1)$ and θ_{thres} is a threshold angle. Thus, if both angles hinged to the spring $(i, i + 1)$ are larger than a threshold angle θ_{thres} , the spring $(i, i + 1)$ becomes susceptible to cleavage, see Figure 9.1 for illustration. For the two end-springs of a VWF polymer, this geometrical condition reduces to a single

angle check. We also propose a second criterion, which monitors the proximity of non-direct neighboring beads within VWF to a spring $(i, i + 1)$ as

$$\begin{aligned} r_{i,j} &\geq R_{\text{thres}} & j &\neq i, i \pm 1, \\ r_{i+1,j} &\geq R_{\text{thres}} & j &\neq i, i + 1, i + 2, \end{aligned} \quad (9.2)$$

where $r_{i,j}$ is the distance between beads i and j , and R_{thres} is a threshold radius. This criterion is equivalent to finding only direct bonded neighbors within a threshold radius R_{thres} and no other beads of a VWF chain, see Figure 9.1 for illustration. This condition eliminates undesired cleavage within a VWF globule (or within an intermediate globular structure in flow), as it may contain a straight enough portion (i.e., satisfy the angle condition in Equation (9.1)) which should be inaccessible for cleavage due to the shielding by neighboring beads of a VWF polymer.

Another model for the susceptibility of VWF to cleavage is non-geometric and is based on the local tension within a VWF chain, as suggested by Lippok et al. 2016¹²⁵. This model is defined by

$$f_{(i,i+1)} \geq f_{\text{thres}} \quad 1 < i < N - 1, \quad (9.3)$$

where $f_{(i,i+1)}$ is an instantaneous force on the spring $(i, i + 1)$ and f_{thres} is a threshold force. This condition is rationalized by the existence of a threshold force required for the opening of a VWF cleavage site^{252,253}. As we will demonstrate in detail below, these two models for cleavage are of course not fully independent and have some degree of overlap. We will discuss differences and similarities between the various conditions.

If one or several criteria (depending on the choice made) for cleavage are satisfied for a bond, it can be cut according to a cleavage probability. The cleavage probability per time step Δt is defined as $P = 1 - \exp(-k_c \Delta t)$, corresponding to an ADAMTS13 cleavage rate

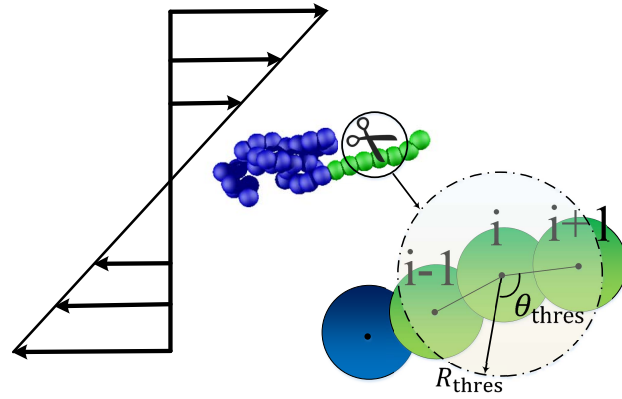


Fig. 9.1 Schematic of a VWF with $N = 40$ in shear flow (shown by a linear velocity profile). Different bead colors correspond to the portions of VWF susceptible or inaccessible for cleavage. Here, springs between two green beads can be readily cleaved (shown by the scissors), while all other bonds are inaccessible for cleavage. The colors are assigned using the two criteria from Equations (9.1) and (9.2) with $\theta_{\text{thres}} = 150^\circ$ and $R_{\text{thres}} = 1.2\sigma_{\text{LJ}}$, respectively. The threshold angle $\theta_{i-1,i,i+1}$ and radius R_{thres} are illustrated schematically in the magnified image.

k_c . Such implicit modeling of ADAMTS13 activity is appropriate, because the size of this protease is only a few nanometers, making the assumption of a homogeneous distribution within the blood plasma at the scale of several micrometers well justified. Nevertheless, the cleavage rate k_c is a function of ADAMTS13 concentration in the plasma¹²⁵, and the effect of ADAMTS13 concentration on VWF cleavage will also be investigated.

9.3 Setup

We model wall-bounded Couette flow in a slit with dimensions $40l \times 20l \times 10l$ (simulations with a single chain) and $40l \times 10l \times 300l$ (simulations with multiple VWFs) corresponding to flow, shear-gradient, and vorticity directions, respectively. Periodic boundary conditions (BCs) are assumed in the flow and vorticity directions. The linear shear flow is generated by moving the walls with the same speed but in opposite directions. Solid walls are modeled by a collection of frozen particles which mimic the fluid structure. No-slip BCs at the walls are implemented through an adaptive shear force^{59,119} and the impenetrability of the walls for solvent and VWF particles is imposed through bounce-back reflections at the fluid-solid interface.

Two scenarios are studied in this work. The first scenario is when a single VWF polymer is immersed at the center of the slit, and the susceptibility of VWF to cleavage, depending on its length and shear rate of the flow, is investigated. Note that in this case, the VWF chain is not explicitly cleaved, but data about the cleavage susceptibility are gathered according to the selected cleavage criteria. The second scenario corresponds to a setup where a number of same-size polymers are immersed into the slit, and these chains are explicitly cleaved (i.e., cut according to the cleavage probability if selected criteria for cleavage are met). In this way, we can follow cleavage dynamics of such a system. The overall concentration of VWF in both cases remains rather dilute, such that interactions between different VWF chains can be neglected. Note that in the case of several suspended VWFs, the attractive part of the LJ potential is present only for monomers within each separate VWF chain. The monomers from different VWFs interact only through the repulsive part of LJ potential (imposed by a cutoff $r_c^{LJ} = 2^{1/6} \sigma_{LJ}$) in order to prevent their overlap.

Relation between simulation and physical units is performed by assuming appropriate length, energy, and time scales. The length scale l in simulations corresponds to two VWF bead diameters ($2\sigma_{LJ}$) and is assumed to be equal to 1 μm . This means that different VWF lengths from $N = 10$ to $N = 50$ considered in simulations correspond to VWF multimers within the length range from $L_{\text{VWF}} = 5\mu\text{m}$ to $L_{\text{VWF}} = 25\mu\text{m}$. The energy unit $k_B T = 0.4$ in simulations corresponds to a thermal energy $k_B T = 4.3 \times 10^{-21}$ J for the physiological

temperature of $T = 37^\circ \text{C}$. Finally, the characteristic time scale is chosen to be $\tau \sim 1/\dot{\gamma}_c$, where the critical shear rate $\dot{\gamma}_c$ for VWF stretching is assumed to be 2000 s^{-1} for all VWF sizes and corresponds approximately to the onset of VWF stretching found experimentally¹⁹¹. In simulations, τ also corresponds to the onset of VWF stretching and is found to be $\tau \approx 2$ for the selected parameters of the VWF model and fluid properties. Note that the critical shear rate might have a slight dependence on VWF length, but we employ the above time scale τ for all cases, independently of the chain length.

For blood flow simulations, the system is put in a channel and under pressure driven flow by applying body forces to the solvents. The channel is bound with walls in the pressure gradient direction, and the periodic boundary condition is assigned for the flow and vorticity directions. For 2D simulations, the simple DPD method is used for hydrodynamics. The polymers remain the same, but the membranes are represented by closed rings of polymers.

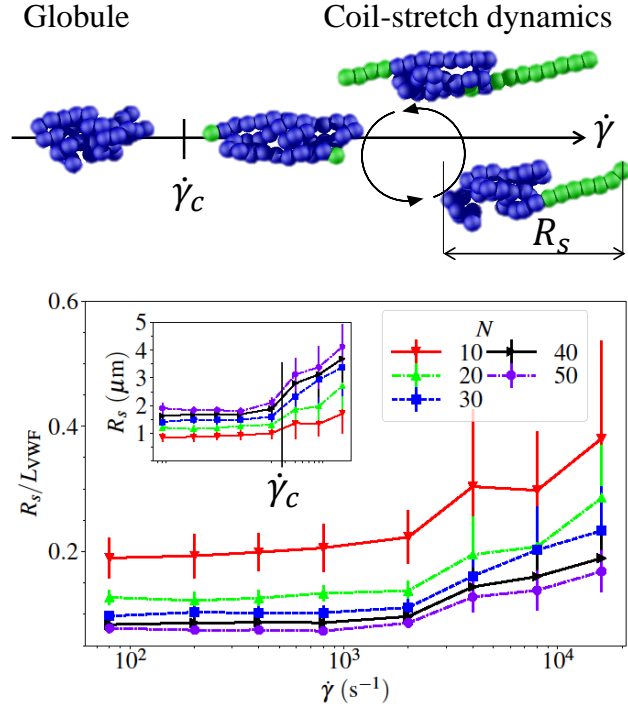
The volume fraction of platelets and VWFs in the system are order of magnitude larger than their physiological volume fraction in the blood in order to get better statistics while their concentration is semi-dilute permitting us to neglect their hydrodynamic interaction. The parameters of the simulation are all taken from our works, Huisman et al. 2017⁹⁴, Rack et al. 2017¹⁷², and Hoore et al. 2018⁸⁹.

9.4 Stretching of VWF in shear flow

The self-avoiding attractive polymer model has been shown to stretch when a critical shear rate $\dot{\gamma}_c$ is reached^{6,8,259}. This behavior closely mimics the stretching of a VWF chain¹⁹¹ and is illustrated in Figure 9.2 by several VWF configurations. Stretching of VWF for $\dot{\gamma} \gtrsim \dot{\gamma}_c$ occurs by drawing one of its ends from a VWF globule by shear-flow forces^{6,8}. Hydrodynamic interactions play an important role in this process, since chain stretching becomes qualitatively different without them⁸. Clearly, the critical shear rate depends on the intra-molecular attraction strength and the length of a VWF polymer^{6,8}. Here, the strength of intra-molecular attraction is calibrated using the experimental results of VWF stretching in shear flow¹⁹¹.

Figure 9.2 shows the average extension of VWF in the flow direction for various VWF lengths N as a function of shear rate, and demonstrates that shorter VWF chains result in a longer relative extension (i.e., normalized by its contour length L_{VWF}). However, the physical (not normalized) extension of VWF is in fact larger for longer chains, which is illustrated in the inset of Figure 9.2. This counter-intuitive dependence of the relative VWF extension on N indicates that R_s increases slower than L_{VWF} with N . In fact, at shear rates lower than $\dot{\gamma}_c$, $R_s \sim N^{1/3}$ corresponding to the size scaling for a collapsed globular conformation (or

Fig. 9.2 Stretching of VWF. At the top, various VWF configurations for $N = 40$ are illustrated, including a globular (unstretched) form for shear rates below a critical shear rate $\dot{\gamma}_c$ and different stretched configurations above $\dot{\gamma}_c$. Different bead colors denote portions of VWF susceptible (green) or inaccessible (blue) for cleavage, as in Figure 9.1. At the bottom, average extension R_s of VWF in the flow direction is shown as a function of $\dot{\gamma}$ for various N . Extension relative to the VWF contour length L_{VWF} appears to be larger for shorter chains, while the physical (not normalized) extension of VWF has an opposite trend, as shown in the inset for the same range of shear rates. The critical shear rate for VWF stretching corresponds to approximately $\dot{\gamma}_c \sim 2000 \text{ s}^{-1}$ for all VWF lengths.



a close-packing limit). By scaling the extension data for shear rates above $\dot{\gamma}_c$, we find that $R_s \sim N^\alpha$ ($\alpha > 1/3$) in the stretched regime, where the exponent α is shear-rate dependent and remains less than unity even at large shear rates. A theoretical analysis⁶ has shown that the critical shear rate for VWF stretching is expected to have a weak dependence on N ($\dot{\gamma}_c \sim N^{1/3}$). This result is based on the fact that the local shear rate at a sphere surface in shear flow is smaller for larger sphere sizes²³⁶. The dependence of $\dot{\gamma}_c \sim N^{1/3}$ would indicate that shorter VWF polymers are expected to stretch at lower shear rates, leading to a larger relative extension of shorter chains at a fixed shear rate. However, the range of polymer lengths in our simulations is too narrow (from $N = 10$ to $N = 50$) to allow a reliable estimate of the dependence of $\dot{\gamma}_c$ on N , and the critical shear rate seems to be nearly independent of N for the range of sizes investigated. Another theoretical model for the extension of immobilized (or tethered) VWF²⁵⁹ predicts that larger VWF globules are expected to stretch at lower shear rates. This results is based on the fact that the drag on an immobilized globule is larger for larger molecule sizes. The situation of a tethered molecule is clearly different from the case of a freely-suspended globule in shear flow, and therefore qualitatively different dependencies of $\dot{\gamma}_c$ on N are expected.

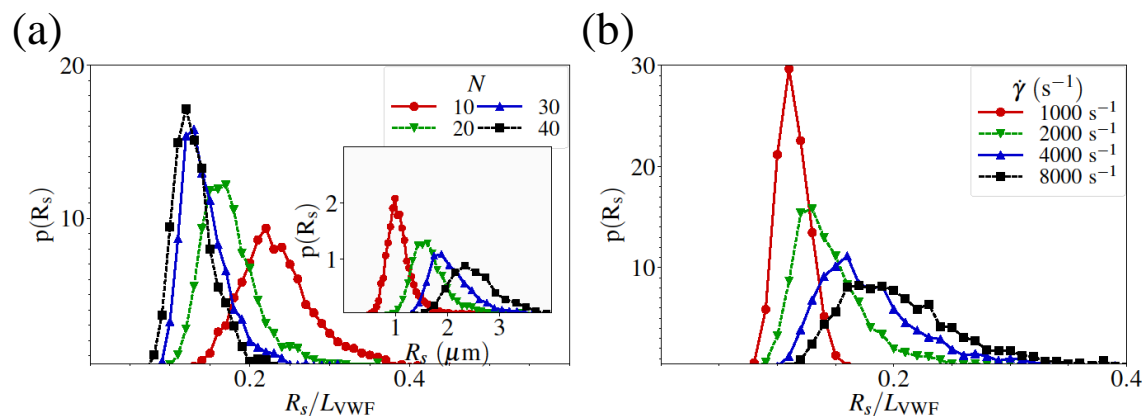


Fig. 9.3 Probability distribution $p(R_s)$ of VWF extension. (a) $p(R_s)$ for different chain lengths as a function of the relative extension at a shear rate of $\dot{\gamma} = 2000 \text{ s}^{-1}$. Inset presents the same data as a function of R_s in micrometers. (b) The distribution of VWF extension for various shear rates with a fixed length of $N = 30$.

Even though the average extension of VWF already conveys general stretching trends, it is interesting to look at the VWF deformation in more detail. Figure 9.3(a) presents the probability distribution of VWF extension in the flow direction for various VWF lengths N at $\dot{\gamma} = 2000 \text{ s}^{-1}$ and confirms that the relative extension of shorter VWFs is larger than that of longer chains. Even though the relative-extension distributions for $N = 30$ and $N = 40$ seem to be very similar, the results in Figure 9.2 indicate that the average extension scales as $R_s \sim N^\alpha$ with $1/3 < \alpha < 1$. However, the physical polymer extension is always larger for longer VWF chains, as seen in the inset of Figure 9.3(a). Figure 9.3(b) shows the relative extension of a VWF with $N = 30$ for different shear rates. As the shear rate is increased, the VWF stretches significantly, which is characterized by an increase of the average chain extension in Figure 9.2 as well as by the broadening of extension distributions in Figure 9.3(b).

It is also interesting to compare the stretching shear rates in Figure 9.2 with shear rates under the physiological conditions. Wall-shear rates in the microvasculature are largest in arterioles and can reach up to about 10000 s^{-1} ¹⁶⁵. Furthermore, VWF multimers in blood flow unavoidably interact with densely-packed blood cells, which effectively impose small quasi-confinements leading to an enhanced VWF stretching. In fact, experimental results^{187,188} show that VWF adhesion becomes possible already at shear rates around 1000 s^{-1} , indicating that VWF stretching does not necessarily require extremely high shear rates.

9.5 Susceptibility of VWF to cleavage

The analysis of VWF stretching in Figures 9.2 and 9.3 shows that VWF is subject to a significant extension for shear rates beyond about 2000 s^{-1} . The cleavage of VWF by ADAMTS13 is associated with its stretching, because cleavage sites are generally hidden in a globular (unstretched) configuration. To test a mesoscopic cleavage model, we investigate the three criteria given in Equations (9.1), (9.2), and (9.3). Figure 9.4(a) shows the relative susceptibility ψ_θ of VWF to cleavage for various N , using only the angle criterion in Equation (9.1). The relative susceptibility is defined as the average number of accessible-to-cleavage sites, normalized by the number $N - 1$ of springs, where the accessibility for cleavage is tested for every spring according to one or several cleavage criteria for a number of VWF configurations under flow. The correlation between VWF relative susceptibility in Figure 9.4(a) and extension in Figure 9.2 is clearly visible, as both increase after a critical shear rate has been exceeded. This indicates that the cleavage model qualitatively captures the activity of ADAMTS13 for VWF. The ψ_θ curves in Figure 9.4(a) also show that susceptibility of VWF to cleavage becomes independent of N for long enough chains, demonstrating a universal cleavage behavior of VWF. However, longer chains are still expected to have a faster cleavage rate than shorter chains, because they expose on average more available-to-cleavage sites, which is shown by $(N - 1)\psi_\theta$ in the inset of Figure 9.4(a).

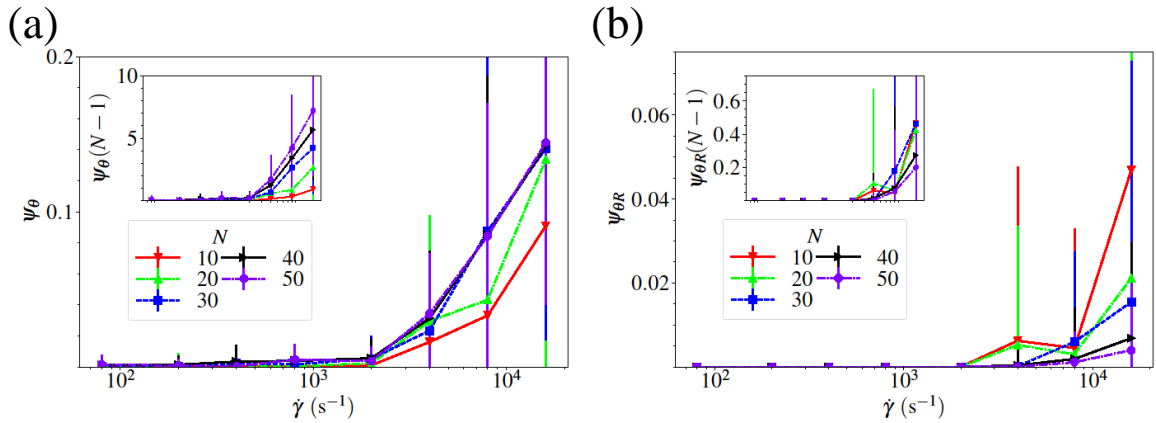


Fig. 9.4 Geometrical model for the susceptibility of VWF to cleavage. Relative susceptibility is defined as the average number of accessible-to-cleavage sites (here springs) per total number of springs ($N - 1$) in the VWF model. (a) ψ_θ computed using only the angle criterion in Equation (9.1) for different VWF sizes N . $\theta_{\text{thres}} = 150^\circ$. For comparison, the inset shows the total susceptibility of VWF for the same range of shear rates. (b) $\psi_{\theta R}$ calculated based on the two conditions from Equations (9.1) and (9.2) with $\theta_{\text{thres}} = 150^\circ$ and $R_{\text{thres}} = 1.2\sigma_{\text{LJ}}$.

Despite a seeming success of the angle criterion, we can see in Figure 9.4(a) that the susceptibility to cleavage can be non-zero even at low shear rates, where no VWF cleavage

by ADAMTS13 is expected^{124,125}. This indicates that a few straight segments (i.e., satisfying the angle criterion) exist within a globular structure of VWF. In general, such situations for VWF cleavage should be avoided, since we expect that ADAMTS13 is unable to cleave VWF in a globular (unstretched) configuration. To alleviate this inconsistency, we apply the criterion for neighboring beads from Equation (9.2) in addition to the angle criterion, which results into VWF relative susceptibility $\psi_{\theta R}$ shown in Figure 9.4(b). The two geometrical criteria lead to a consistent cleavage model, where cleavage is possible only beyond a critical shear rate. Another interesting difference between cases with the two criteria and the angle condition only is that the total cleavage characterized by susceptibility $(N - 1)\psi_{\theta R}$ becomes independent of N for long enough chain lengths (inset in Figure 9.4(b)), and not the relative susceptibility $\psi_{\theta R}$ itself. Thus, the cleavage rate is expected to be nearly independent of N . It is also worthwhile to discuss the choice for the threshold angle $\theta_{\text{thres}} = 150^\circ$ and radius $R_{\text{thres}} = 1.2\sigma_{\text{LJ}}$ employed in Figure 9.4. We have studied sensitivity of the susceptibility results to this choice and found that different values of θ_{thres} and R_{thres} within the ranges $\theta_{\text{thres}} \in (100^\circ, 170^\circ)$ and $R_{\text{thres}} \in [1.0\sigma_{\text{LJ}}, 1.3\sigma_{\text{LJ}}]$ do not significantly modify the presented conclusions. This means that the cleavage model is rather robust and small quantitative differences in VWF susceptibility, resulting from the choice of θ_{thres} and R_{thres} , can easily be absorbed in a concentration-dependent rate for ADAMTS13 activity, if explicit modeling of VWF cleavage is required.

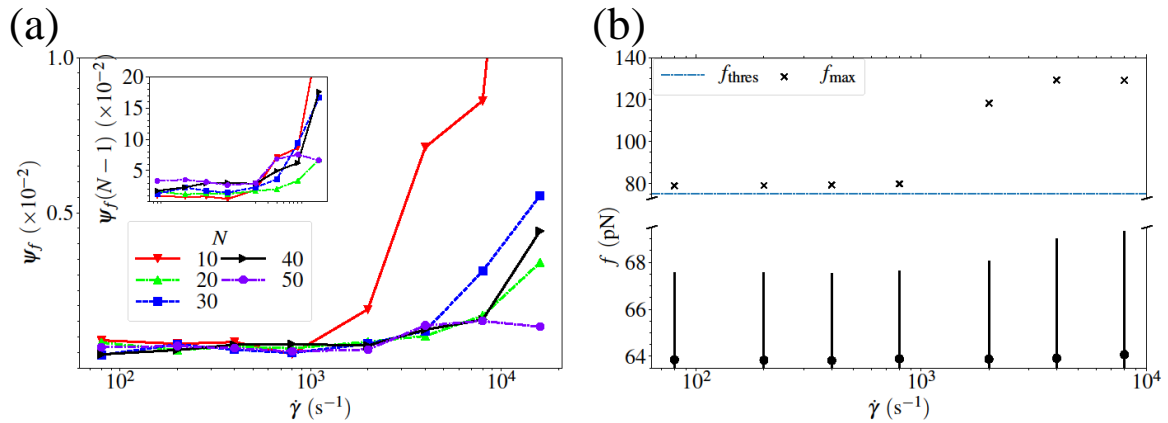


Fig. 9.5 Tension model for the relative susceptibility ψ_f of VWF to cleavage. ψ_f is defined as the average number of accessible-to-cleavage springs per total number of springs $(N - 1)$ in the VWF model. (a) ψ_f is calculated using the force criterion in Equation (9.3) for different VWF lengths N . $f_{\text{thres}} = 75$ pN. Inset shows the total susceptibility of VWF for the same range of shear rates. (b) Average tension within VWF with $N = 50$ characterized by the spring force as a function of shear rate. The bars correspond to one standard deviation around the average tension force, while the 'x' symbols denote maximum forces. The horizontal line denotes $f_{\text{thres}} = 75$ pN.

In addition to the geometrical cleavage model presented above, we examine the tension-force model in Equation (9.3), which has been suggested by Lippok et al. 2016¹²⁵. Figure 9.5(a) presents the relative susceptibility of VWF to cleavage based on the force criterion with the $f_{\text{thres}} = 75$ pN. In general, the force condition does qualitatively reproduce the expected cleavage of VWF at high enough shear rates. The ψ_f values based on the force condition are much smaller than those defined by the geometrical criteria in Figure 9.4; however, these differences can easily be absorbed into the cleavage rate, if explicit VWF cleavage would be of interest. Nevertheless, there is clearly more noise in the force-based ψ_f in comparison with the conformation-based $\psi_{\theta R}$. The main reason is strong fluctuations in instantaneous spring-tension forces, which can be seen in Figure 9.5(b), where the average force along with its deviation is plotted as a function of shear rate. Thus, the maximum force fluctuations appear to be several times larger than the average tension force. This makes the force model for cleavage extremely sensitive to the choice of f_{thres} , leading to very sensitive and inconsistent results. In fact, a selected f_{thres} of 75 pN appears to be rather large, since recent atomic force microscopy experiments with a single VWF domain resulted in a force of about 20 pN needed to open the cleavage site²⁵³. Note that the choice of $f_{\text{thres}} = 75$ pN is made here in order to nearly eliminate cleavage susceptibility at low shear rates, see Figure 9.5(b). If we set f_{thres} to a significantly smaller value, then VWF chain would be highly susceptible to cleavage at low shear rates, which is not desirable. In conclusion, the instantaneous force model for VWF cleavage by ADAMTS13 appears to be not very robust, and therefore the geometrical model is clearly preferable.

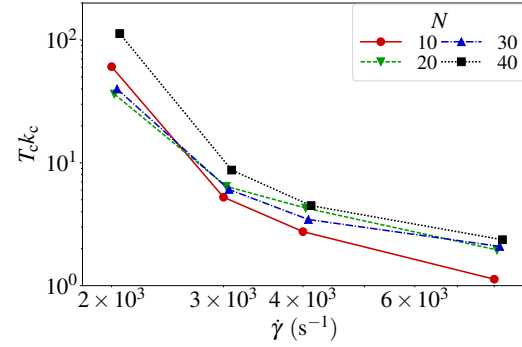


Fig. 9.6 Cleavage period T_c as a function of shear rate. Cleavage period is normalized by the cleavage rate k_c for different VWF lengths N . The cleavage period significantly decreases at high shear rates, which is consistent with the susceptibility of VWF to cleavage. The geometrical model for cleavage with $\theta_{\text{thres}} = 150^\circ$ and $R_{\text{thres}} = 1.2\sigma_{\text{LJ}}$ is employed.

One of the metrics for VWF cleavage is the cleavage period, which is defined as the average time between cleavages of a VWF chain. Here again, we do not explicitly cleave a chain, but just compute average time between two successive cleavages with a cleavage rate k_c . Figure 9.6 presents the cleavage period normalized by k_c for different chain lengths. Clearly, the cleavage period gets tremendously reduced with increasing shear rate, since VWF becomes more and more susceptible to cleavage. So, in comparison to the VWF

susceptibility, the cleavage period shows an inverse dependence on shear rate. Consistently with the VWF relative susceptibility results in Figure 9.4(b), the cleavage period is nearly independent of the VWF length for long enough chains.

9.6 Cleavage pattern

To illustrate cleavage events of VWF, Figure 9.7 presents instantaneous relative extension of a chain with $N = 40$ for two different cleavage rates k_c . Here, the cleavage process is defined by the convolution of cleavage susceptibility and cleavage rate. The geometrical model for cleavage with $\theta_{\text{thres}} = 150^\circ$ and $R_{\text{thres}} = 1.2\sigma_{\text{LJ}}$ is employed and the shear rate is increased from 1000 s^{-1} to 16000 s^{-1} every 5000τ in time. The different cleavage rates mimic different concentrations of ADAMTS13. Obviously, most of the cleavages occur when the chain attains a stretched configuration, which becomes more frequent at high shear rates (see Figures 9.2 and 9.7).

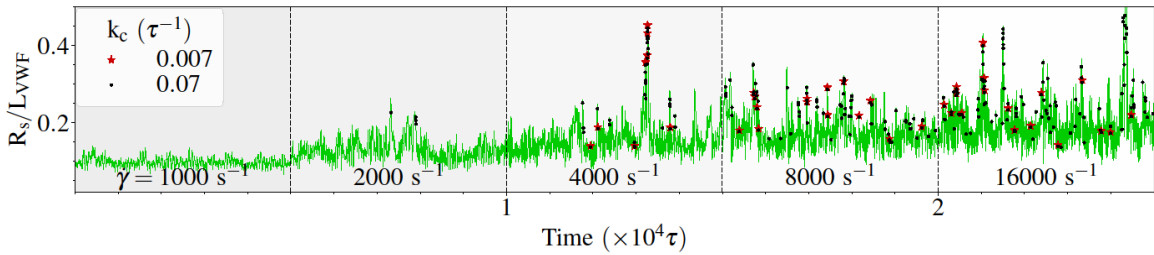


Fig. 9.7 Illustration of cleavage events. Instantaneous relative extension of VWF with $N = 40$ for different shear rates, where the shear rate is increased every 5000τ in time. Cleavage occurrences for two different cleavage rates are depicted along the extension curve by different symbols. Clearly, most cleavage events occur at large enough shear rates and for a stretched VWF configuration. The geometrical model for cleavage with $\theta_{\text{thres}} = 150^\circ$ and $R_{\text{thres}} = 1.2\sigma_{\text{LJ}}$ is employed.

In order to describe cleavage dynamics in more detail, it is interesting to look at the distribution of positions along the chain where VWF is cleaved. Figure 9.8(a) shows the probability distribution of cleavage positions χ_c along the chain for different VWF lengths N . χ_c is defined as the spring number (starting from the chain ends) normalized by the total number of springs $N - 1$ within a VWF. Due to symmetry, χ_c values run up to a maximum of 0.5. The probability curves in Figure 9.8(a) indicate that VWF is much more likely to be cleaved close to its ends than in the middle. These results are fully consistent with the stretching mechanism of VWF for $\dot{\gamma} \gtrsim \dot{\gamma}_c$, such that a thread (one of VWF ends) is initially pulled from a VWF globule by shear-flow forces^{6,8} (see VWF conformations in Figure 9.2).

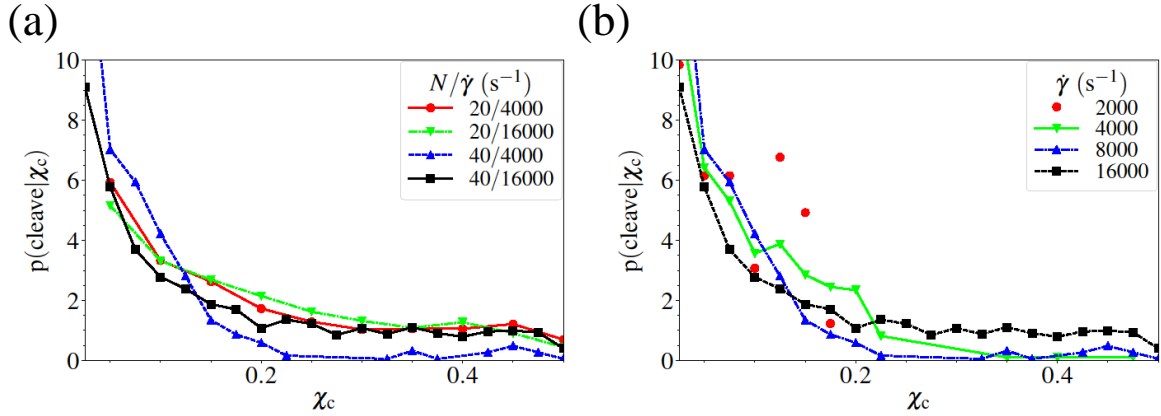


Fig. 9.8 Cleavage pattern of VWF using the geometrical model. (a) Probability distribution of cleavages along VWF chain for different lengths N . Cleavage sites are characterized by χ_c which corresponds to a spring number (starting from the chain ends) normalized by the total number of springs within a VWF. (b) Probability distribution of cleavages as a function of χ_c for various shear rates. $N = 40$. For all cases, the geometrical model for cleavage with $\theta_{\text{thres}} = 150^\circ$ and $R_{\text{thres}} = 1.2\sigma_{\text{LJ}}$ is employed.

Hence, it is expected that VWF chain ends are more susceptible to cleavage by ADAMTS13. This also means that long VWF chains would possess a longer lifetime, since cleavage in the middle is not very probable and VWF chains would be cleaved gradually from their ends to smaller pieces. Another interesting observation from Figure 9.8(a) is that the cleavage distribution is practically independent of VWF length N for long enough chains. This observation is also consistent with a universal susceptibility of VWF to cleavage in Figure 9.4(b) for large enough N .

Figure 9.8(b) shows probability distributions of cleavages along VWF length for various shear rates. The cleavage distribution has a weak dependence on shear rate. However, a slight increase in cleavage probability can be seen in the middle of a VWF chain for very large shear rates such as $\dot{\gamma} = 16000 \text{ s}^{-1}$. The data for $\dot{\gamma} = 2000 \text{ s}^{-1}$ are noisy because cleavage events are very rare near the critical shear rate $\dot{\gamma}_c$. In summary, the probability distributions for cleavage in Figure 9.8 indicate that the cleavage pattern of VWF chains is a

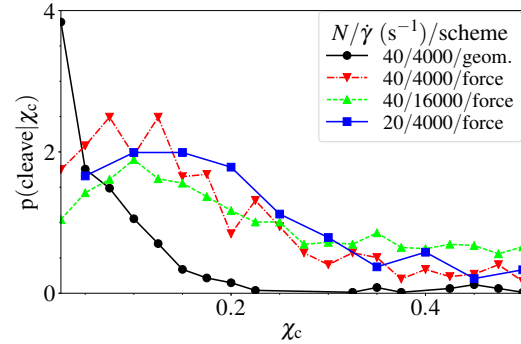
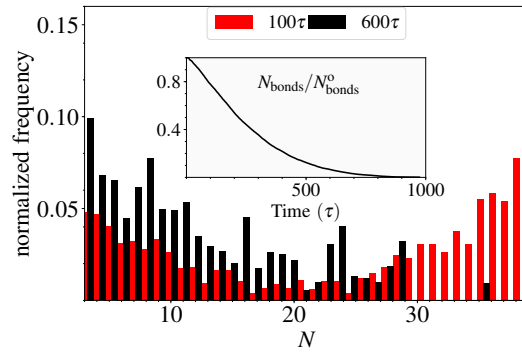


Fig. 9.9 Cleavage pattern of VWF using the tension force model. Probability distribution of cleavages as a function of cleavage site χ_c for different chain lengths N and shear rates. For comparison, a cleavage pattern curve from the geometrical model in Figure 9.8 is also displayed. The force model for cleavage with $f_{\text{thres}} = 75 \text{ pN}$ is employed.

weak function of the chain length and shear rate and they can be approximated well by an average probability-distribution function independent of N and $\dot{\gamma}$.

For comparison, we also present probability distribution of cleavages for the tensile force model in Figure 9.9. Even though the cleavage probability remains larger close to the chain ends than in the middle, the probability function appears to be much flatter in comparison to the geometric model. A flatter distribution of cleavage sites is expected to result in a faster degradation of long VWF chains by ADAMTS13. Consistently with the geometric model, the force model for cleavage leads to a universal cleavage pattern, which is nearly independent of the chain length and shear rate. However, these two models for cleavage will lead to different cleavage dynamics, because of significant differences in the probability distribution of cleavages shown in Figures 9.8 and 9.9.

Fig. 9.10 Temporal evolution of VWF distribution under cleavage. The distribution of VWF lengths at two time points for a system where VWF chains are cleaved explicitly. Initial condition corresponds to 375 chains with $N = 40$. $\dot{\gamma} = 3200 \text{ s}^{-1}$. The geometrical model for cleavage with $\theta_{\text{thres}} = 150^\circ$ and $R_{\text{thres}} = 1.2\sigma_{\text{LJ}}$ is employed. Inset shows an exponential decay of total number of bonds in the system which is qualitatively consistent with experimental measurements^{124,125}. For visual illustration of VWF cleavage.



9.7 Cleavage dynamics

So far we have investigated the susceptibility of VWF to cleavage and the cleavage pattern without explicit cleavage of VWF chains in shear flow. As a next step, we perform a large simulation, where VWF chains are explicitly cleaved. The setup corresponds to a dilute solution of 375 VWF chains with $N = 40$ sheared at $\dot{\gamma} = 3200 \text{ s}^{-1}$. In order to reduce the simulation time, the cleavage rate is set to $k_c = 0.7 \tau^{-1}$. Figure 9.10 presents temporal dynamics of this system as VWFs are being cleaved. As expected, the size distributions shift to smaller VWF lengths in time and the final state of this system corresponds to a state where only single beads remain or analogously all VWF multimers have been cleaved. The cleavage rate k_c has a role of cleavage time scale here and defines the speed of system evolution. The inset in Figure 9.10 plots the evolution of the total number of bonds in the system which

displays an exponential decay. This behavior is qualitatively consistent with the experimental measurements of VWF cleavage^{124,125}.

We also perform a similar analysis of VWF susceptibility to cleavage for this dynamic system shown in Figure 9.11(a). These data demonstrate very similar trends as in Sec. 9.6 that shorter VWF chains are more susceptible to cleavage than longer chains and that cleavage susceptibility becomes independent of N for long enough polymer chains. Figure 9.11(b) presents the average lifetime of VWFs with different lengths. As expected, the lifetime is independent of N for long enough chains, because VWF lifetime is directly associated with the susceptibility to cleavage. Thus, the more VWF is susceptible to cleavage, the shorter is its lifetime. These simulations of dynamic cleavage confirm the potential of the geometrical cleavage model to realistically represent the activity of ADAMTS13 in blood flow simulations.

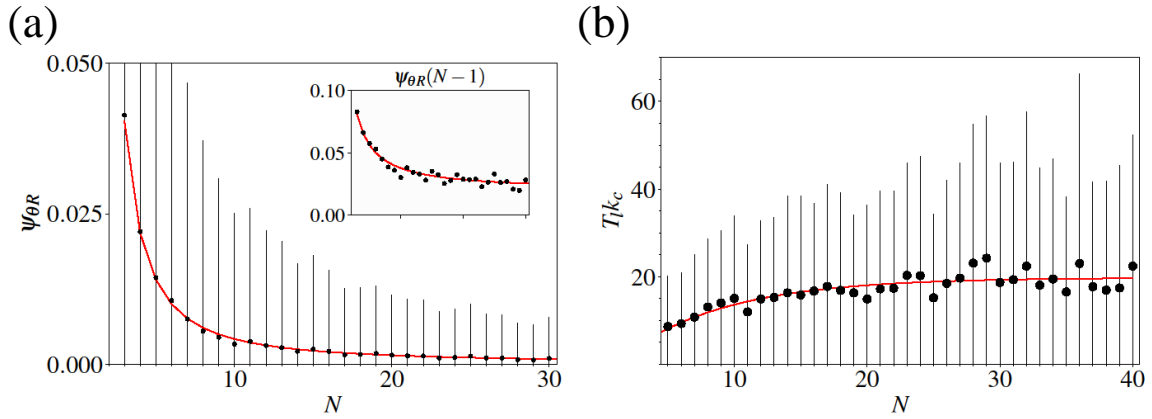


Fig. 9.11 Susceptibility to cleavage and lifetime of VWF. (a) Relative susceptibility $\psi_{\theta R}$ to cleavage of VWF chains with different lengths. The inset also shows total susceptibility $\psi_{\theta R}(N-1)$ as a function of N . The red lines corresponds to a function $\psi_{\theta R}(N-1) = 0.18/N + 0.019$. (b) Lifetime T_l of VWF chains for various lengths N is independent of size for sufficiently large VWFs since the coil-stretch dynamics of VWF adjusts its susceptibility to cleavage. The red line corresponds to a fit with exponential function $T_{lk_c} = 21.9(1 - \exp(-0.127N)) - 2.15$. All data are obtained from dynamic simulations with explicit cleavage.

9.8 Margination of VWFs in blood flow

In blood flow, RBCs concentrate in the center of the channel because a hydrodynamic lift force is applied on them against the boundaries of the flow. The closer to the walls they are, the higher lift forces they experience¹³⁵. Consequently, they leave an RBC free layer (RBC-FL) near the boundaries of the flow¹³³, and other blood components, whose hydrodynamic

lift force is weaker than RBCs', are pushed to that layer instead^{57,140,141}. These objects must be large enough to be pushed away from the central blood flow by mechanical collisions with RBCs¹⁴¹. Ultra-large VWFs in collapsed globular form are large enough to marginate to the boundaries of the flow¹⁷².

Most of the platelets and VWFs are located in the RBC FL. The remaining platelets and VWFs stay in the center of the channel, where the orientation of RBCs creates looser packing and more space compared with the packing in the RBC FL. Additionally, the smaller hydrodynamic lift force applied on the platelets and large VWFs leads to their peak at the center of the channel (vessel). Interestingly, in RBC FL, the shear rate is much higher (almost an order of magnitude) than the other sections so that VWFs stretch there and become hemostatically active. Simul-

taneously, they become susceptible for cleavage by VWF protease ADAMTS13, preventing uncontrolled aggregations. The extension distribution of VWFs in different positions in the channel is shown in Figure 9.12. VWFs in RBC FL extend more than the VWFs at the center.

Marginated VWFs have better chance to bind to the injured site and to the margined platelets for initiating hemostasis because they are both populated and stretched in the RBC FL. However, they are more prone to cleavage by ADAMTS13, prohibiting spontaneous platelet-VWF aggregate formation. So, the interplay between margination and VWF critical stretching at high shear rates determines how VWFs adhere to injured sites and how they are cleaved. These two phenomena depend on the channel size, shear rate, volume fraction of RBCs (known as hematocrit), VWF sizes, and ADAMTS13 concentration in the plasma.

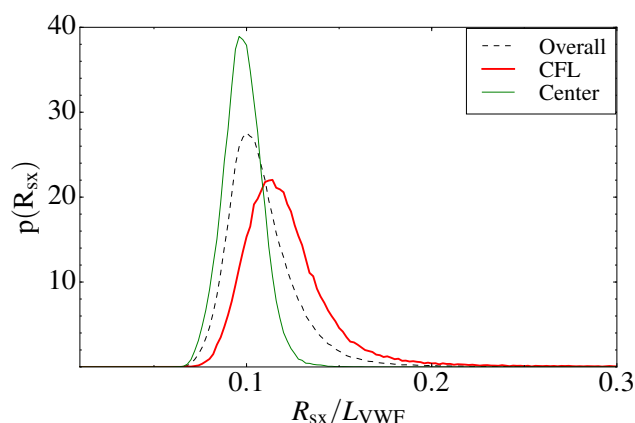


Fig. 9.12 Distribution of polymer extension. The polymers in RBC FL are extended more than the polymers in the central RBC core. R_s and L_{VWF} stand for the extension in the flow direction and the contour length of polymer respectively.

9.9 Cleavage Statistics in blood

Here, the system is kept under steady conditions and the probability of cleavages is obtained based on VWF conformation-dependent susceptibility. Accordingly, in each time step, the cleavage events are reported but the VWFs are not physically cleaved. In this scheme, a large number of cleavage events can be gathered to have accurate statistics of cleavages for a

specified VWF size. In addition, different ADAMTS13 concentrations can be applied to the same simulation saving computation times. It is to be noted that ADAMTS13 proteins are small enough (in nano-scales) to be able to diffuse in the channel like solvents so that they do not marginate, making it possible to model them implicitly by considering cleavage rates. Regardless of ADAMTS13 concentration, the extended polymers are more susceptible for cleavage than globular ones. This fact comes from the shielding of cleavage sites when VWF polymer is collapsed.

Since the marginated VWFs are most probably stretched, they are also more prone to be cleaved. As illustrated in Figure 9.13, VWFs are cleaved most probably in the first 3 micrometers close to the walls and almost never in the blood flow core (RBC FL thickness is around 2 microns). That means, cleavage happens around RBC FL where shear rate is much higher than the bulk flow. In the inset of Figure 9.13, the distribution of cleavage events in the channel is shown. Although the VWF cleavage probability is higher closer to the walls, the distribution of cleavages is affected by the distribution of VWFs in the channel as well. It means, the presence of VWFs is also important for cleavage to happen. In effect, the cleavage distribution is the multiplication of VWF distribution function and cleavage probability based on cross-sectional location, $p(\text{cleave}) = P(\text{cleave}|y)p(y)$. In the long term, this results in lowering the distribution of ultra-large VWFs in the RBC FL while leaving the central flow VWFs untouched as a reserve for hemostasis.

Although the concentration of ADAMTS13 changes the cleavage probability at all locations, it does not play a role in the cleavage distribution, as seen that all curves collapse into one universal distribution curve in inset of Figure 9.13.

The cleavage pattern of VWFs in blood flow is very different than their cleavage pattern in simple shear flow. In the latter case, VWFs coil and stretch frequently and successively

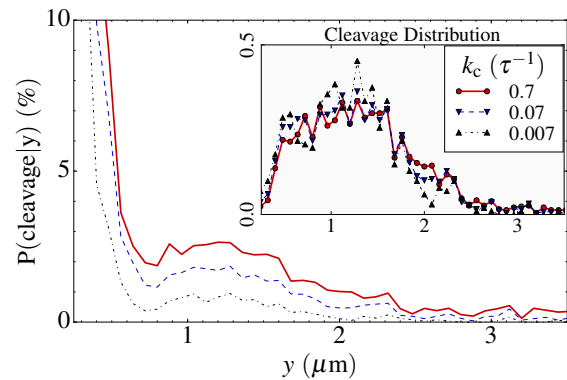


Fig. 9.13 Cleavage probability in the blood flow during simulation period. Probability of cleavage near the boundaries of the blood stream in RBC FL is much higher than the other locations. As VWF polymers approach the walls, the probability increases almost exponentially. But, as illustrated in the inset diagram, the distribution of cleavages obeys the density profile of VWFs in the flow, too. The total distribution of cleavages is dependent on the interplay between the density profile of the VWFs in the blood stream and the extension of VWFs in the channel resulting in different cleavage probabilities, $P(\text{cleave}|y)$, in different locations.

which affects their cleavage pattern. The cleavage sites of globular VWFs are shielded against ADAMTS13 and resistant for cleavage. By stretching, they become exposed to their protease enzyme and get cleaved. Since the polymer stretches and coils successively, the amount of time that a cleavage site is exposed to ADAMTS13 strongly correlates with its distance to the nearest end of the VWF polymer chain. In consequence, the cleavage pattern shows high frequency of cleavages at the VWF polymer ends and very low frequency as the cleavage site approaches the middle of the polymer⁹⁴. However, in the blood stream, VWF conformations and dynamics are affected by the collisions with RBCs and by their interaction with the walls. Then, the resulting cleavage pattern in the blood flow becomes uniform as shown in Figure 9.14 compared with the cleavage pattern in simple shear flow with no RBCs.

In order to understand the effect of RBC volume fraction (hematocrit), and the blood pressure on the cleavage rate of VWFs, many large scale simulations with different hematocrits and different shear rates must be conducted to get the whole view on the problem. 2D simulations come useful for drawing a qualitative picture of the problem. The setup of 2D simulations is similar to chapter 8. 2D simulations catch approximately the same phenomena as 3D simulations and experimental results^{57,140,172}. The most important phenomenon in the current case is margination and the thickness of the RBC-FL. 2D simulations of blood flow give similar cross-sectional distribution of large polymers and almost equal RBC-FL thickness for hematocrits 20% higher than the 3D hematocrit¹⁷². It means, the 2D simulation results of hematocrit $H_c = 70\%$ corresponds to 3D hematocrit $H_c = 50\%$. The 2D simulation results of the cleavage problem are depicted in Figure 9.15. The effective cleavage rate normalized by the cleavage rate of a completely susceptible polymer is drawn besides the extension of polymers both with respect to blood pressure and hematocrit.

Hematocrit and pressure gradient influence the effective cleavage rate of the polymers almost equally. However, the VWF polymer extension is mostly affected by hematocrit than pressure gradient.

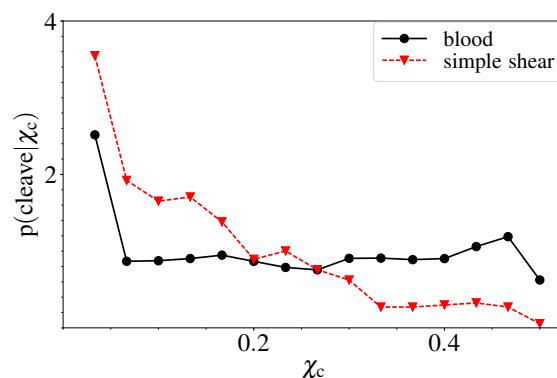


Fig. 9.14 Cleavage pattern of VWF in pressure driven blood flow and in simple shear flow. The distribution of cleavages is plotted as a function of the cleavage site distance to the VWF polymer ends, χ_c , which is already normalized by the contour length of VWF polymer. Presence of RBCs and the closeness to the walls affect the cleavage pattern of VWFs substantially so that almost all loci in the polymer chain have the same probability of being cleaved by ADAMTS13.

9.10 Summary

We have performed a systematic analysis of VWF cleavage in shear flow. Two cleavage models have been proposed. The first model is based on two geometrical criteria in Equations (9.1) and (9.2), which identify the degree of local stretching of VWF. The second model is based on the instantaneous spring tension (Equation (9.3)), which mimics a force-responsive opening of VWF cleavage sites. Both models qualitatively reproduce the cleavage of VWF by ADAMTS13 in shear flow, such that chain cleavage becomes possible beyond a critical shear rate or when the VWF chain is significantly stretched. The geometrical model appears to be very robust, such that the results for VWF cleavage only weakly depend on the choice of two necessary model parameters: the angle threshold θ_{thres} and the cutoff for neighboring beads R_{thres} . However, the force model is very sensitive to the choice of a critical force for cleavage f_{thres} , which limits the application of this model in practice. Thus, the geometrical model for VWF cleavage is clearly preferable over the force model.

Our simulation results show some universal features of VWF cleavage by ADAMTS13 in shear flow. VWF susceptibility to cleavage appears to be independent of chain length N for long enough chains, see Figure 9.4. Thus, the VWF susceptibility is a monotonically increasing function of only shear rate and it becomes non-zero beyond a critical shear rate. This also implies that the average period between cleavages and VWF lifetime are independent of N and depend only on the shear rate.

Probability distributions of cleavages along VWF (Figures 9.8 and 9.9) also show a universal behavior for the cleavage pattern. These distributions are independent of VWF length for long enough chains and they show only a weak dependence on the shear rate. As a result, we obtain a qualitative picture for the cleavage progression. VWF chains appear to be cleaved much more often close to their ends than in the middle. This result is consistent with the stretching mechanism of VWF in shear flow such that the stretching is initiated by

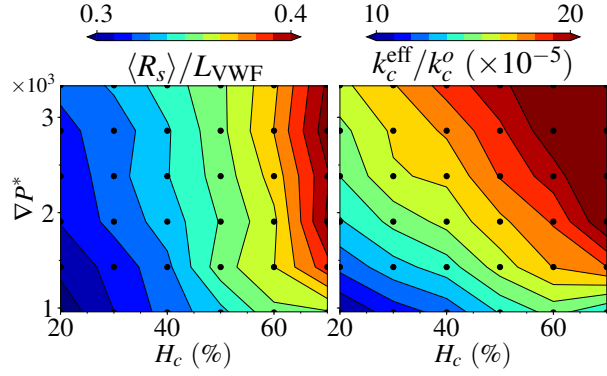


Fig. 9.15 Effective cleavage rate and VWF extension in flow direction of blood stream with respect to blood pressure and hematocrit, for 2D simulations. Referring to¹⁷², 2D hematocrit corresponds to 20% less 3D hematocrit. $\nabla P^* = \nabla P \tau W / \eta$ is the normalized pressure gradient. $W = 40 \mu\text{m}$. Although the blood pressure has a weaker effect on polymer extension, it affects the effective cleavage rate of polymers almost equally as hematocrit affects it.

pulling polymer ends out of the globule due to shear forces^{6,8}. In fact, this cleavage pattern is advantageous for the lifetime of long VWFs, because their cleavage will proceed gradually from the chain ends (and less often in the middle), increasing the circulation time of long VWF multimers.

The cleavage pattern of the VWFs in the blood stream is almost uniform meaning that every dimer of the long VWF concatemer has the same probability of being cleaved as the others. This is in contrast to the cleavage of VWFs in absence of RBCs. In such cases, since polymers coil and stretch successively, the amount of time that the extruded parts of polymer are exposed to the ADAMTS13s is more than the middle part. Thus, the dimers located at the ends of the VWF concatemer are most probably cleaved before the dimers at the middle of the polymer.

Chapter 10

Size distribution of degrading polymers

The size distribution of von Willebrand factor (VWF) polymers in the blood stream is maintained in the vasculature, although VWFs are cleaved continually in the flow. In general, all polymeric systems have a size distribution which depends on the degradation pattern and on the production rate of various sizes. The current theoretical study shows that the steady state size distribution of continually degrading polymers is directly related to their degradation/cleavage pattern, *i.e.* how often the cleavage takes place at each site along the polymer chain. The energetically beneficial case for the system to maintain its size distribution is when the polymers are cleaved from their tips than in the middle. It is predicted that the size distribution of degrading polymers, such as VWFs in blood, obeys an approximate power-law. The time-dependent decay of the system keeps the distribution shape if the degradation is not dependent on polymer size.

10.1 Introduction

The size regulation of the components of a polymeric system is necessary for its optimal performance. The size regulation of VWF is a profound example. VWFs are large concatemers of protein units whose lengths can reach several micrometers^{33,42,71}. The ultra-large VWFs which are multimers of tens of dimeric VWF units are crucial in hemostasis, especially at high shear rates^{176,212}. A dysregulation of the size distribution of VWFs by ADAMTS13 in vascular system results in either bleeding disease, or in undesired spontaneous platelet aggregations. A lack of large VWFs in the blood stream causes von Willebrand disease (VWD) type 2A, and an excess of large VWFs leads to the fatal disease Thrombotic Thrombocytopenic Purpura (TTP)¹⁸⁵. The VWF example motivates the current work, though other degrading polymer systems should obey the same principles^{77,83}. VWF cleavage, accomplished by its protease ADAMTS13, occurs only at high shear rates where VWF polymers

unfold and expose their cleavage sites^{42,252}. At low shear rates, the polymers are collapsed because of intra-molecular attractions and their interactive sites are shielded^{208,231}. The way such polymers are cleaved, referred here as the cleavage pattern, depends mostly on physiological conditions. Degradation or cleavage pattern of polymers together with their secretion or production rate determine their overall size distribution. The process can be investigated analytically to see how cleavage or degradation pattern of the polymers affects their size distribution.

10.2 Results

Under constant physical conditions, the cleavage probability of each site of the multimer is a function of the position of the site in the multimer, and the length of the polymer. The probability distribution function for cleavage is represented by $p(i, n)$ where i denotes the site position in the chain, and n denotes the multimer size in the sense that it is the number of bonds linking all monomers. Hence, $\sum_{i=1}^n p(i, n) \frac{1}{n} = P(n)$ where $P(n)$ is the probability of a polymer with size n to be cleaved. The probability of cleavage can also be defined as the cleavage rate. The cleavage probability itself is a function of physical conditions such as shear rate, temperature, pH, etc. We can find the rate of change of the population of any length using the master equation

$$\dot{f}_n = -P(n)f_n + g_n, \quad (10.1)$$

where g_n is the rate of generation of the polymer size n , and f_n stands for the frequency/population of polymers with size n . In steady state, $\frac{\partial}{\partial t} \equiv 0$ and

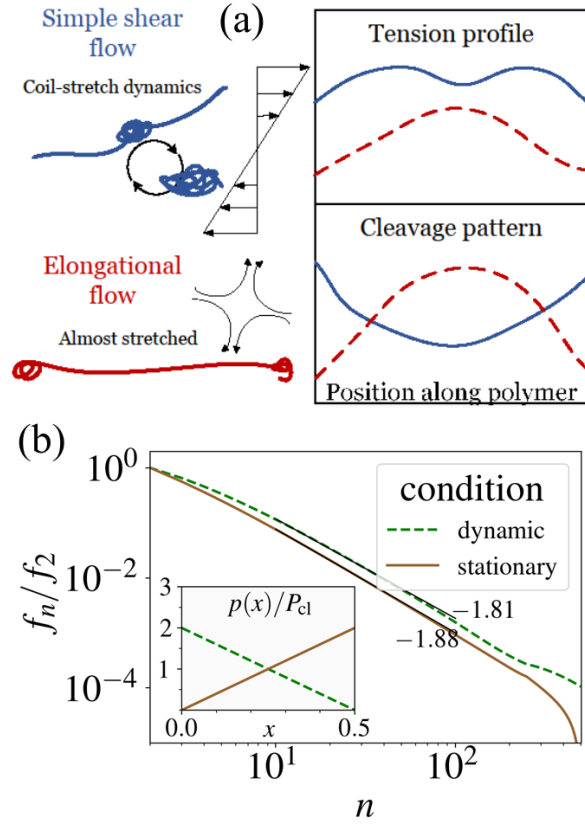
$$f_n = \frac{g_n}{P(n)}, \quad (10.2)$$

where g_n is the superposition of the actual production rate of polymers with that length in the system and the remnants of the longer cleaved polymers. For VWF, the production rate is the secretion rate of the polymer from endothelial cells in the blood stream. Mathematically, it can be written in the form

$$g_n = s_n + 2 \sum_{m=n+1}^{\infty} p(n+1, m) \frac{1}{m} f_m. \quad (10.3)$$

Here, s_n is the secretion rate of the polymer of size n and the second term corresponds to the remnants of the longer polymers cleavages. The factor 2 represents the symmetry in polymer

Fig. 10.1 Size distribution of polymers is dependent on the physical condition of the system. (a) Cleavage pattern is directly related to the tension along the polymer and the extent of exposure of the polymer cleavage sites to their proteases. Accordingly, the coil-stretch dynamics of the polymer causes a completely different cleavage pattern as depicted in the schematic diagrams. (b) The simulation results show that the size distribution follows a higher power-law exponent when the middle parts of the polymer become less prone to cleavage. The fitted power-law exponents are shown in the plot. The inset shows the linear approximation of the related cleavage patterns.



cleavage pattern, *i.e.* there are two ways for a polymer to be cleaved to give a shorter polymer with a specific size. The steady-state solution (10.2) for the frequency of the polymers with any size can then be written as

$$f_n P(n) = s_n + 2 \sum_{m=n+1}^{\infty} p(n+1, m) \frac{1}{m} f_m. \quad (10.4)$$

In practice, there is a size limit for the production/secretion of polymers so that the sum in Equation (10.4) must not be taken up to infinity but to a maximum polymer size n_{\max} . If one knows the secretion rate of the polymers in each length and the cleavage pattern of the polymers given by $p(i, n)$, the distribution of the polymer sizes can be easily obtained by induction starting from the longest polymer. If the polymer sizes are large, the discrete version of Equation (10.4) can be converted to a continuum version,

$$f_n P(n) = s_n + 2 \int_n^{n_{\max}} p(n, x) \frac{1}{x} f_x dx. \quad (10.5)$$

From a recent study, the cleavage probability of VWFs is found to be almost independent of their size for large enough polymers⁹⁴. Also, the frequency normally has a power-law relation with the polymer size, *i.e.* $f_n = f_0 n^{-\beta}$. Therefore, any cleavage pattern results in a different power-law exponent β . The cleavage pattern depends on the physical conditions of the system. For instance, if cleavage is proportional to the tension on the polymer, the cleavage pattern takes a different form depending on how the external forces are applied on the polymer. This implies that the size distribution of the polymers in the solution also depends on the physical conditions. Thus, if the polymers are in simple shear flow where they dynamically coil and stretch, or in pure elongational flow, where they are stationary and stretched, their force pattern over the chain and their configuration in the solvent differ a lot, affecting the cleavage pattern as well. Figure 10.1 shows these two different conditions and their resulting size distributions. The inset of Figure 10.1 shows the linear approximation of cleavage patterns as a function of cleavage site along the polymer from the polymer ends to its middle point. Since the cleavage depends on the tensile force exerted on the polymer chain, the cleavage pattern should depend on the tension profile. For example, cleavage pattern of VWFs in simple shear flow has been calculated from the simulations in chapter 9.

The exponent of the size distributions under dynamical conditions (*i.e.* coil-stretch dynamics) is higher than the exponent in the stationary condition of elongational flow, since the polymers are cleaved from their ends more often than in the middle part, keeping larger polymers for longer times in the system. This statement is a direct result of the physics of the VWF polymer cleavage as agreed by the simulations in chapter 9.

The cleavage pattern of VWFs in shear flow is important since they are exposed to blood flow continuously. From the dynamical models of VWF, it is deduced that the cleavage pattern is almost exponential where its minimum probability occurs in the middle of the polymer⁹⁴. Figure 10.2 shows the difference among three different assumed cleavage patterns. The exponential cleavage pattern has a higher exponent than the other two patterns. The higher the exponent is, the longer the larger polymers remain in

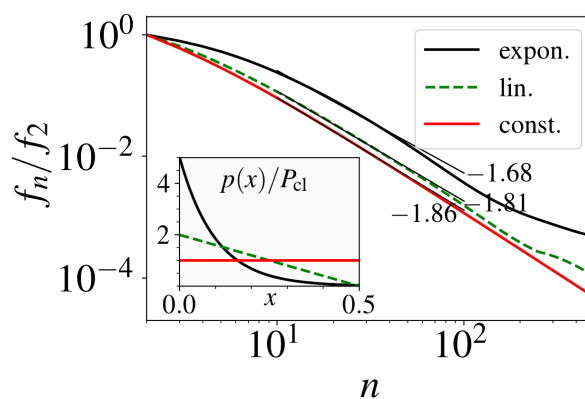


Fig. 10.2 Frequency vs. size. The size distribution of polymers depends on their cleavage pattern, shown in the inset diagram. As the cleavage increases at the polymer ends, the power-law exponent of the size distribution increases.

the system. This means ultra-large VWFs which are hemostatically efficient have a higher population if their cleavage occurs at their ends.

Usually in experiments, a sample of polymers is taken and their size distribution in the presence of their protease is studied. The experiments on the ADAMTS13 activity on cleaving VWFs¹²⁴ is one example. The predicted cleavage pattern from simulations of the VWF model⁹⁴ can be compared to the experimental size distribution. Equation (10.1) is easily solvable if the production/secretion rate of polymers is zero for all lengths, *i.e.* $s_n = 0$, and $P(n) = P_{cl} = \text{cte}$. The time evolution of the longest polymer is given by $f_{n_{\max}}(t) = f_{n_{\max}}^o \exp(-P_{cl}t)$. Recursively, the time derivative of any polymer is linearly proportional to the sum of the longer polymers if $s_n = 0$. That means, the particular solution of differential Equation (10.1) is the same as the homogeneous solution. Therefore, all polymers exponentially lose their population with the same rate,

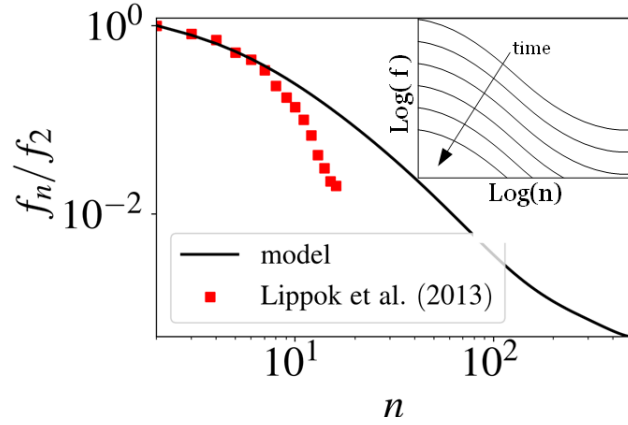


Fig. 10.3 Size distribution in experiments and the model. It is assured by the theoretical analysis that the distribution does not change shape in time if the system is left to decay without input. The inset diagram shows this fact. The size distribution keeps its shape if $P(n) = \text{cte}$ since all polymers decay with the same equation $f_n(t) = f_n^o \exp(-P_{cl}t)$. The simulation results of a decaying system has a fixed normalized distribution as a verification (not shown).

$$\dot{f}_n = -P_{cl}f_n + 2 \sum_{m=n+1}^{\infty} p(n+1, m) \frac{1}{m} f_m^o e^{-P_{cl}t}. \quad (10.6)$$

Hence, the decay equation for all polymer lengths is similar and has equal time scale $\tau = 1/P_{cl}$. This result is schematically sketched in the inset of Figure 10.3. The stationary distribution of polymers remains similar in time. The comparison between the predicted model and experiments is depicted in Figure 10.3. Although model and experiment do not lie on the same curve, they show almost the same pattern. The problem in experiments is that it is difficult to track the population of longer than 16-dimer polymers with appropriate accuracy. Not enough experimental data are available to validate if the distribution of VWFs in reality obeys a power law. In an experimental work done by Lippok et al. 2013¹²⁴, an exponential distribution is suggested which fits well with the 16 points they have from the gel-chromatography experiments.

It's very important for a degrading system to maintain its steady state. A higher power-law exponent (*i.e.* lower β) helps the system in this regard by reducing the necessity for a large polymer input to the system, saving energy loss for the polymer production. As a rule of thumb, the input rate of the largest polymer to the system must be

$$s_{n_{\max}} = f_0 n_{\max}^{-\beta} P(n_{\max}). \quad (10.7)$$

Although a lower power-law exponent demands less energy input to the system, for some systems like VWFs in vasculature, the most important part of the distribution belongs to the large polymers. Consequently, greater power-law exponent (smaller β) brings higher numbers of larger polymers and makes the system energetically more efficient. The system must maintain the concentration of large enough polymers, *i.e.* $\sum_{n=n_o}^{n_{\max}} f_n n = \text{cte}$ with n_o being the minimum polymer size for sufficient performance. In integral form, the system must satisfy

$$f_0 n_{\max}^{-\beta} \int_{\alpha_0}^1 x^{1-\beta} dx = c_0 = \text{cte}. \quad (10.8)$$

Figure 10.4 shows the results for different α_0 values, which define the minimum size for efficient activity of the polymers, n_o , normalized by the maximum polymer size n_{\max} . Note that the power-law exponent $-\beta$ should be between -2 and zero to have a stable system (the integral must converge for α_0 approaching zero.) Power-law exponents greater than zero do not make much sense in degrading systems, since the population of smaller polymers must be more than larger ones. As shown in Figure 10.4, smaller β helps in decreasing the energy cost for the system to filter monomers and insert large polymers. Fewer monomers mean less filtration and less need for large polymers production. The minimum size for polymer efficiency, shown in normalized form by α_0 , is also important.

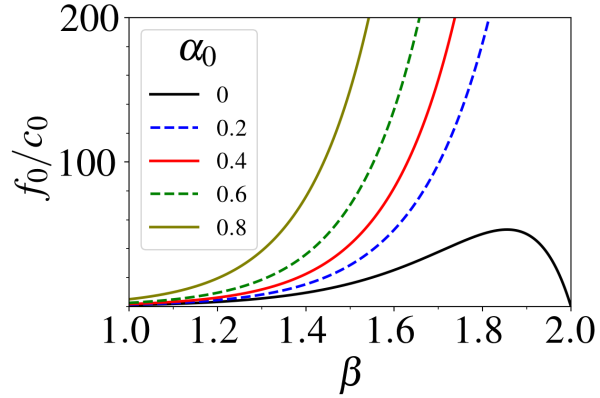


Fig. 10.4 The monomer frequency as a function of power-law exponent $-\beta$ and α_0 . $n_{\max} = 1000$. Lower β is better for the system to reduce the number of waste monomers.

10.3 Summary

In conclusion, the theoretical analysis of polymer production and cleavage predicts a power-law steady-state distribution for the system of VWFs in blood stream rather than an exponential distribution. It is energetically better for the system to cleave the polymers from the end points than in the middle part. Also, the time-dependent solution for a decaying system, when no new polymer is secreted or produced, obeys a similar exponential decay if the cleavage rate of polymers is not a function of polymer size. Consequently, the normalized size distribution of the polymers remains constant in time. Such analysis is not only valid for VWFs, but also can be used for studying other degrading polymer systems.

Part V

Red blood cell aggregates

Chapter 11

Mapping the erythrocyte doublet forms

Red blood cell (RBC) aggregates play an important role in determining blood rheology. RBCs in solution interact attractively to form various shapes of RBC doublets. Here, the attractive interactions can be varied by changing the solution conditions. A systematic numerical study on RBC doublet formation is performed, which takes into account the shear elasticity of the RBC membrane due to the spectrin cytoskeleton, in addition to the bending rigidity. The results are obtained from simulations of triangulated surfaces considering thermal fluctuations. The phase space of RBC doublet shapes in a wide range of adhesion strengths, reduced volumes, and shear elasticities is obtained. The shear elasticity of the RBC membrane changes the doublet phases significantly. Experimental images of RBC doublets in different solutions show similar configurations. Furthermore, it is shown that rouleau formation is affected by the doublet structure.

11.1 Introduction

In whole blood, RBCs experience a pronounced attractive interaction, which is mediated by bridging proteins, such as fibrinogen, or by depletion interactions due to dextran^{17,148,149} or other macromolecules. This attraction leads to the formation of RBC aggregates, in particular large rouleaux, which play an essential role in the strong shear-thinning behavior of blood at low and moderate shear rates²⁰. Thus, the interaction of RBCs with each other and with the adhesive surfaces is of high interest to understand the rheology of blood and rouleau formation. The first step for studying RBC assemblies into rouleaux is an aggregate of two RBCs, called doublet. The formation and shape of RBC doublets is determined by the competition between bending and shear elasticity, and the adhesion energy.

The characteristic biconcave shape of RBCs is very well described by the Helfrich bending elasticity⁸⁵. Bending free energy and volume and area conservation of a closed

membrane define the shape of fluid vesicles^{123,193}. Red blood cell membranes respect the same bending energy^{39,122}, but in addition possess a shear elasticity due to their spectrin cytoskeleton network.

The first theoretical studies^{28,205,206} of RBC doublets considered a flat shape for the contact surface between RBCs to simplify the analysis. Later, numerical studies have shown that two fluid vesicles with bending rigidity and constant volumes form a curved contact surface^{220,258}. Different shapes of vesicle doublets as a function of their adhesion strength and bending rigidity were predicted. A recent work by Flormann et al. 2017⁶⁷ has explored different RBC doublet phases based on the dextran and fibrinogen concentration. Although their experiments are conducted systematically over a wide range of dextran and fibrinogen concentration, which modifies the attractive interaction⁶⁷, their numerical investigation lacks systematic 3D simulations to clarify the whole phase space of the system. Moreover, there is still lack of knowledge about which RBC doublet phases exist in practice, in particular when thermal fluctuations are present.

Here, we study the complete phase space of the RBC doublets using simulations with high resolution triangulated membranes having correct bending, shear elasticity, and thermal fluctuations. The various phases of RBC doublets, predicted theoretically, are compared with experimental results.

11.2 Membrane model

The RBC membrane is represented by a triangular mesh, as described in detail by Li et al. 2005¹²⁰, Fedosov et al. 2010b⁵⁵, Fedosov et al. 2010a⁵⁴, and Wu et al. 2014²⁴⁴ (see [chapter 2](#)).

The most important energies in RBC doublets are the bending energy from lipid bilayer elasticity, shear elasticity of the spectrin network, and the adhesive energy between the two RBCs. The bending energy for fluid membranes, which do not possess a preferred radius of curvature, reads^{48,80,81,85,97}

$$U_b = \frac{1}{2} \kappa_c \oint_{\partial V} da (c_1 + c_2)^2 + \kappa_g \oint_{\partial V} da c_1 c_2, \quad (11.1)$$

where κ_c , κ_g , c_1 , and c_2 are the bending rigidity, Gaussian bending modulus, and principal curvatures of the membrane, respectively. The energy is integrated over the whole membrane enclosing the volume V with total area $A = \partial V$. The integral over the Gaussian curvature $K = c_1 c_2$ is constant for a fixed topology, due to the Gauss-Bonnet theorem^{80,81}.

The simplest discretized bending model has been proposed by Kantor and Nelson 1987⁹⁸ for every pair of adjacent triangles,

$$U_{\text{KN}} = \sum_{i,j} \kappa_b (1 - \mathbf{n}_{ijk} \cdot \mathbf{n}_{ijk'}), \quad (11.2)$$

where κ_b is the bending constant, and \mathbf{n}_{ijk} is the unit normal vector of the triangle with vertices i , j , and k (see Figure 11.1). The quantity κ_b is related to the bending rigidity κ_c by $\kappa_c = \kappa_b \sqrt{3}/2$ for a sphere in continuum limit^{19,55,80,121}. Even though such discretized bending model for RBCs has been quite successful in predicting RBC behavior including its fluctuations²³⁰, mechanical properties^{54,55,120}, and flow dynamics^{57,114}, it is not accurate enough if the bending energy of the membrane dominates.

A more accurate discretization for bending has been proposed by Gompper and Kroll 1996⁸⁰, as

$$U_{\text{GK}} = \frac{1}{2} \kappa_c \sum_i \frac{1}{\sigma_i} \left(\sum_{j(i)} \sigma_{ij} \hat{r}_{ij} \right)^2, \quad (11.3)$$

where $\sigma_i = \frac{1}{4} \sum_{j(i)} \sigma_{ij} r_{ij}$, $\sigma_{ij} = r_{ij} (\cot \theta_k + \cot \theta_{k'})/2$, r_{ij} is the distance from vertex i to j , \hat{r}_{ij} is the unit vector pointing to vertex i from j , $j(i)$ are the vertices connected to vertex i by bonds, and θ_k and $\theta_{k'}$ are the angles opposite to the bond between vertex i and j in triangles ikj and $ik'j$. σ_i and σ_{ij} are the area of each cell and the length of each bond, respectively, in the dual lattice of the triangulated lattice of the membrane⁸⁰, as shown in Figure 11.1. Different discretization models have been explained in more detail by Gompper and Kroll 2004⁸².

The network model of the membrane conserves its global surface area and volume by a harmonic constrain potentials. The local area of each triangle is also kept constant by a harmonic potential.

The worm-like chain (WLC) model is employed to represent the membrane elasticity due to the spectrin bonds^{54,55}. Because the WLC potential is purely attractive, the repulsive part

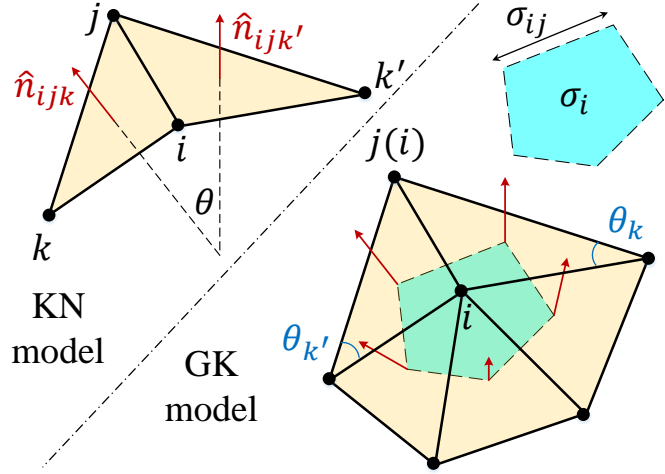


Fig. 11.1 Schematic of the two discretization models for the bending energy. The KN discretization (11.2) considers the bending between each two triangles, while the GK discretization (11.3) considers the bending of each vertex with respect to all of its linked vertices.

of the Lennard-Jones (LJ) potential is added to the pairwise interactions of the vertices, in order to capture the volume exclusion of membrane patches. The Young and shear moduli are derived from the WLC potential and the area and volume conservation potentials, as described by Seung and Nelson 1988¹⁹⁵, Dao et al. 2006³², Fedosov et al. 2010a⁵⁴, and Fedosov 2010⁵³.

The equilibrium shape of a fluid vesicle with reduced volume $v = 3V/4\pi R_s^3 = 0.64$, where $4\pi R_s^2 = A$, is a biconcave shape¹⁹⁴, which is also the equilibrium shape of RBCs²². Here, A and V correspond to the membrane area and volume, respectively. For fluid vesicles, the shape is determined by the bending energy and reduced volume^{123,193,194}. Removing shear elasticity from our model (by omitting the bond potential) with discretization (11.2) does not preserve the biconcave shape of the membrane, indicating that this state does not remain the equilibrium point for the membrane. In contrast, the discretized bending energy (11.3) successfully keeps the biconcave shape without the spec-

trin network elasticity, as shown in Figure 11.2. The shear elasticity of the RBC membrane from spectrin network partially compensates the inaccuracy of the KN model, however, for more accuracy, the GK model is considered in this work.

The membrane properties are tabulated in Table 11.1.

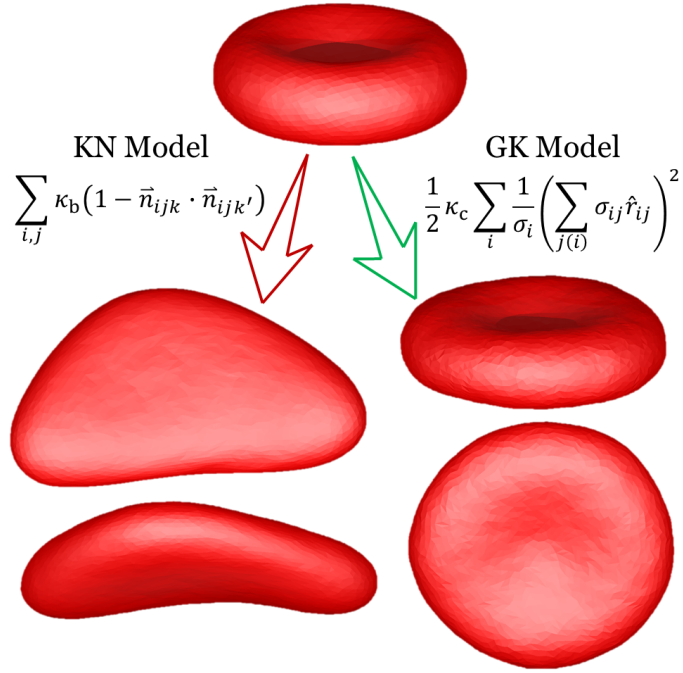


Fig. 11.2 Result of bending model discretization scheme. The bond potential is set to zero so that no shear elasticity is present. The standard biconcave shape of RBC is maintained if the discretization is based on GK scheme. The KN scheme fails to keep the RBC biconcave shape.

Table 11.1 Membrane properties in simulations and related references.

Item	Value	References
number of vertices, N_v	3000	
equilibrium surface area, A_0 (μm^2)	134	22,50,54,55
equilibrium volume, V_0 (μm^3)	94	22,50,54,55
effective diameter, $D_{\text{eff}}^2 = \frac{A_0}{\pi}$ (μm)	6.5	
bending rigidity, $\kappa_c/k_B T$	70	20-170 $k_B T$ ^{49,55,209,216}
Shear modulus, $\mu_0 D_{\text{eff}}^2/\kappa_c$	640	2-10 ($\mu\text{N}/\text{m}$) ^{54,86,169,216,218,241}
global area rigidity, $k_a D_{\text{eff}}^2/\kappa_c$	29,600	55
local area rigidity, $k_l D_{\text{eff}}^2/\kappa_c$	603	55
global volume rigidity, $k_v D_{\text{eff}}^3/\kappa_c$	19,620	55

11.3 Adhesion model

The adhesive interaction between the adjacent vertices of membranes in contact is modeled by the Lennard-Jones (LJ) potential

$$U_{\text{LJ}}(r) = 4\epsilon_{\text{LJ}} \left[\left(\frac{\sigma_{\text{LJ}}}{r} \right)^{12} - \left(\frac{\sigma_{\text{LJ}}}{r} \right)^6 \right], \quad (11.4)$$

where ϵ_{LJ} and σ_{LJ} are the energy and characteristic length of the LJ interaction. The LJ potential is cut off at $r_{\text{cut}} = 2.5\sigma_{\text{LJ}}$.

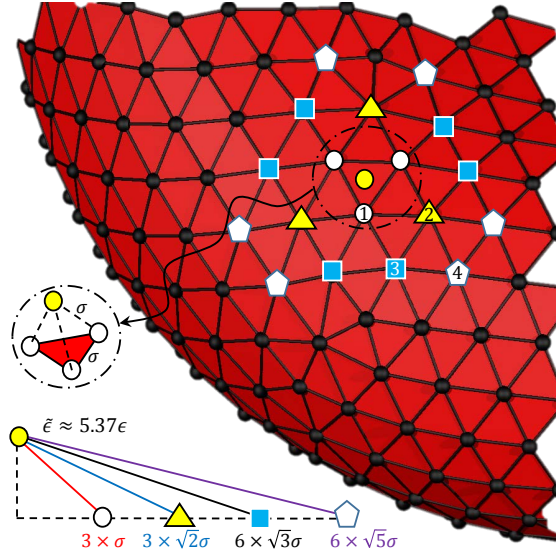
The RBC contact interaction can be represented by the adhesion free energy^{220,258}

$$E_{\text{adh}} = -\Gamma A_c, \quad (11.5)$$

where Γ is called the adhesion strength and A_c is the contact area. Providing that the adhesion energy is modeled by a pairwise interaction, such as the LJ potential (11.4), between membrane vertices, the adhesion strength Γ can be directly related to the potential strength ϵ . If N_c vertices from one RBC interact with the vertices from another RBC, the total adhesion energy is $-N_c \tilde{\epsilon}$, where $\tilde{\epsilon}$ is the effective adhesion energy of one RBC vertex with the other RBC vertices. $\tilde{\epsilon}$ can be calculated approximately by considering the closest vertices to a vertex from another membrane, as illustrated in Figure 11.3. In a minimal energy state, a vertex sits on top of three vertices with equal distance σ to all of them. The adhesion energy of this vertex with the other closest neighbors sums up to about -5.37ϵ . Consequently, the total adhesive energy, when N_c vertices participate in the adhesion, is about $-5.4N_c\epsilon$. However, this high symmetry situation of course does not occur for all of the vertices, resulting in a somewhat smaller adhesion energy.

As vertices of a membrane are homogeneously distributed on the membrane, $N_c/A_c = N/A$, in which N and A are total number of vertices and total area of the RBC membrane.

Fig. 11.3 Analysis of the contact area and the approximation of effective adhesion energy. The minimum adhesion energy for a vertex is obtained when it is located at the head of an equilateral tetrahedron, one of whose faces is the triangle of the other membrane vertices. The four closest neighbors to this vertex are shown by different symbols with assigned numbers 1-4. The closest neighbors are 3 vertices with distance σ , the second closest neighbors are again 3 vertices with approximately $\sqrt{2}\sigma$ away from this vertex. Also 6 neighbors with $\sqrt{3}\sigma$ and 6 other with $\sqrt{5}\sigma$ distance are the farthest neighbors which affect the adhesion potential energy. The farther neighbors have minuscule effect on the energy and are ignored. Thus, the effective potential energy of one interacting vertex is $\approx 5.37\epsilon$. In another configuration where a vertex sits close to only one vertex from the other membrane, the effective adhesion energy would be $\approx 4.1\epsilon$.



Thus, the adhesion strength is directly proportional to the LJ adhesion energy ϵ , *i.e.* $\Gamma = N_c \tilde{\epsilon} / A_c = N \tilde{\epsilon} / A$.

The effective reduced adhesion energy, $\tilde{\gamma}$, is defined as the ratio of the total effective adhesion energy (*i.e.* when $A_c = A$) to the bending energy of a sphere,

$$\tilde{\gamma} = \frac{\Gamma A}{8\pi\kappa_c} = \frac{N\tilde{\epsilon}}{8\pi\kappa_c}. \quad (11.6)$$

This implies that the adhesion strength is proportional to the LJ parameter ϵ . Similarly, γ is defined as the reduced adhesion energy, $\gamma = N\epsilon / 8\pi\kappa_c$. The ratio $\tilde{\gamma}/\gamma$, as a function of γ and reduced volumes v_1 and v_2 ($v_1 = v_2 = v$) is depicted in Figure 11.4.

Since $\tilde{\gamma}/\gamma = \tilde{\epsilon}/\epsilon$, the diagram shows how the effective potential energy is related to the

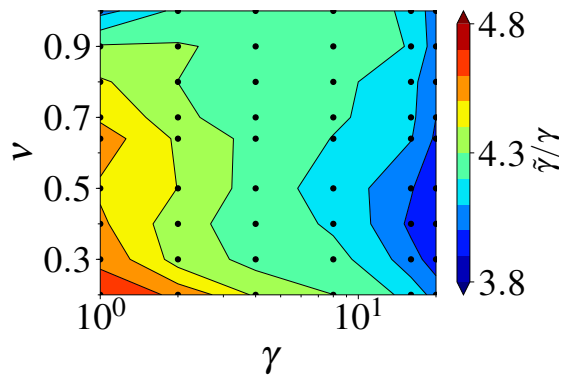


Fig. 11.4 The ratio of the reduced adhesion energy to the reduced pairwise energy. $\tilde{\gamma}/\gamma$ is equal to $\tilde{\epsilon}/\epsilon$.

pairwise LJ energy. Generally, as γ decreases, the effective potential energy increases. On average, $\tilde{\epsilon}/\epsilon = 4.23 \pm 0.03$.

Simulations are conducted for the system until it reaches equilibrium. The reported data are averaged over 250 uncorrelated points in simulations from the equilibrium states.

11.4 Experiment

RBCs were taken by finger prick, from a healthy donor, and washed twice with Phosphate Buffered Saline (PBS, 290 mOsm) following the standard procedure. RBCs were resuspended in several solutions to obtain several doublet configurations. In order to have various adhesion energies¹⁴⁸, we prepared dextran solutions with different molecular weights:

- 40 kDa at a concentration of 10 mg/ml with an adhesion energy close to $-1 \mu\text{Jm}^{-2}$;
- 70 kDa at a concentration of 20 mg/ml with an adhesion energy close to $-4 \mu\text{Jm}^{-2}$;
- 500 kDa at a concentration of 10 mg/ml with an adhesion energy close to $-6 \mu\text{Jm}^{-2}$.

Fibrinogens were added with a concentration of 6 mg/ml to autologous plasma as they don't induce spontaneous aggregation on their own. A hypotonic solution of NaCl at 0.6% was also prepared to increase RBC volume. To induce aggregation, dextran 70 kDa was added with a concentration of 50 mg/ml into this solution. The hematocrit level was kept at 0.5% for every sample. Such low concentration of RBCs allows us to manipulate cells freely with holographic optical tweezers. Then, cells were held at their extremity with four optical traps. RBCs were brought together and the traps were released, so that they can spontaneously aggregate. As dextran is known to induce spontaneous aggregation²¹⁴, we observe the formation of rouleaux over time. RBCs were let to sediment for 30 mins and micro-photographs were taken. Morphologies of these aggregates were characterized similarly as in the simulations.

11.5 Doublet shapes

The theoretical adhesion strength Γ is related to dextran and fibrinogen concentrations in experiments^{20,214}. RBC doublet shapes are determined by the adhesion strength (Γ , or equivalently $\tilde{\gamma}$ or γ), the reduced volumes v_1 and v_2 , and the elastic parameters such as bending rigidity κ_c and shear elasticity μ_0 . The adhesion strength of the RBC membranes is about $1\mu\text{J}/\text{m}^2$ in plasma and about $10\mu\text{J}/\text{m}^2$ in dextran solutions²¹, corresponding to $\gamma \approx 4$

in plasma and $\gamma \approx 40$ in dextran. The RBC volume is also subject to change in different solutions, and also varies from one cell to the other.

Figure 11.5 shows doublet conformations, contact area and bending energy, for various $v_1 = v_2 = v$ and γ . The configurations are depicted both for the initially aligned and for offset doublets. For both cases, the contact area is more sensitive to the reduced adhesion strength and bending energy is more sensitive to the reduced volume (see Figure 11.5-a). Overall, as the reduced volumes decrease and the adhesion strength increases, both contact area and membrane bending energy increase.

The phases of RBC doublets for the initially aligned and offset doublets match at high adhesion strengths or high reduced volumes. However, a mismatch of doublet phases is seen for low adhesion strengths and low reduced volumes (see Figure 11.5-d, -e, and -f).

The contact area A_c is normalized by the RBC area A . The effective bending energy \tilde{E}_b is normalized by the bending energy $8\pi\kappa_c$ of a sphere,

$$\tilde{E}_b = \frac{\tilde{E}_b}{8\pi\kappa_c}, \quad (11.7)$$

where \tilde{E}_b is called the reduced effective bending energy.

Various phases can be distinguished, as specified in Figure 11.5-e, and -f. All possible shapes are categorized based on their contact surface and their non-adhered free surfaces, as follows:

- **Male-Female (M-F) phase:** Both RBCs take a cup shape and plug each other like male and female terminals of a socket. The M-F shape provides the highest contact surface while minimizing the bending energy so that both bending and adhesion free energies are at their local minima.

- **Sigmoid-Concave (Yin-Yang) phase:** The RBCs make a sigmoid contact area which is different than the native sigmoid (concave) shape of RBC membrane. This condition occurs at high adhesion strengths since the bending free energy of the RBCs increases substantially, but is compensated by the decrease in the adhesion energy. Since the section view of the Sigmoid-Concave shape looks like the Yin-Yang symbol, we also call it Yin-Yang phase.

- **Sigmoid-Biconcave (S-B) phase:** This phase is between Yin-Yang and M-F. The RBCs are attached to each other such that the concave part of one RBC fills the convex part of the other. In other words, the contact surface is sigmoid and the free surface is biconcave.

- **Flat-Concave (F-C) phase:** If both RBCs are swollen, the M-F phase becomes unstable and both RBCs reconcile by making a flat contact surface, keeping their swollen free surface. This phase usually appears at high reduced volumes.

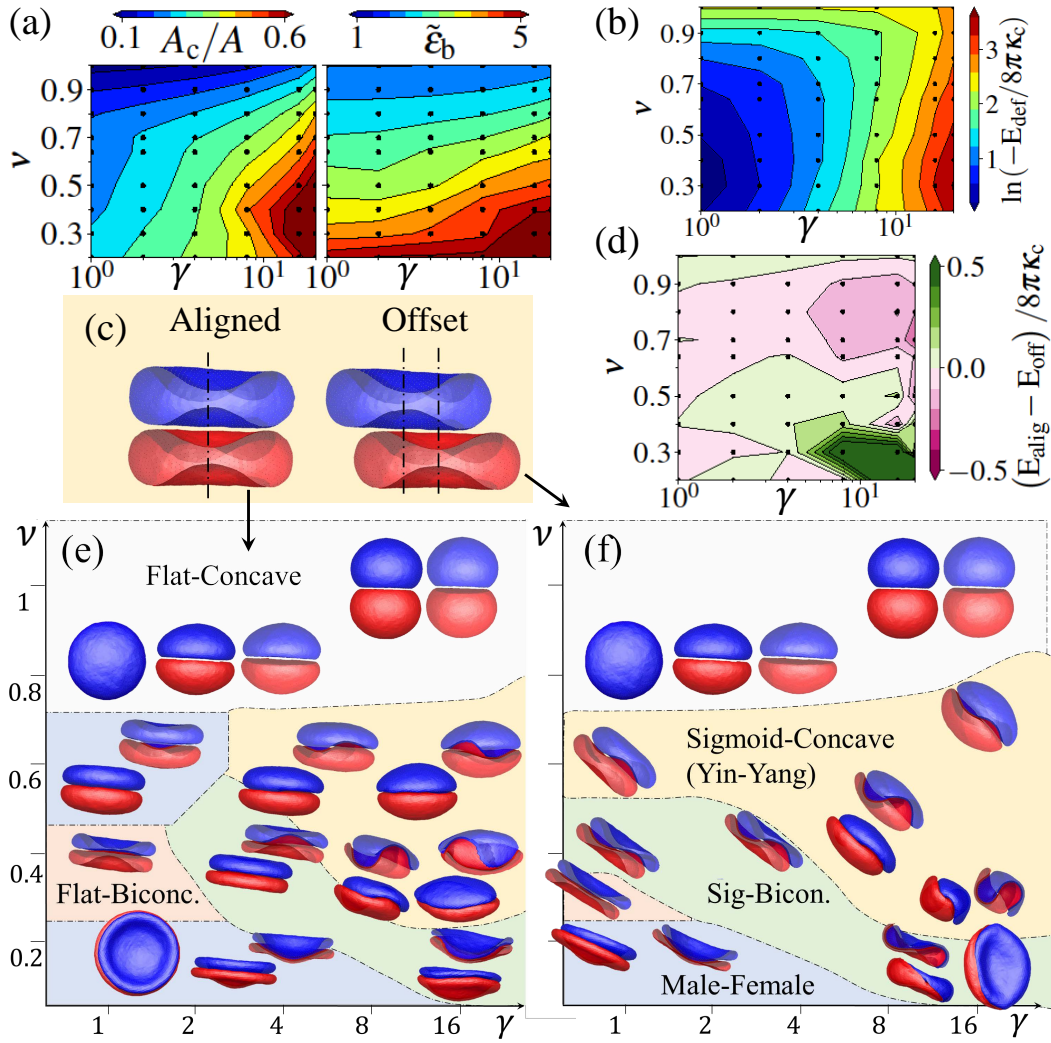


Fig. 11.5 RBC doublet configurations as a function of $v_1 = v_2 = v$ and γ with aligned and offset first point of contact. (a) Contour plots for the contact area and the effective bending rigidity for the aligned RBCs. (b) Contour plot for the difference between the free energy of the doublet and the free RBCs. The change in free energy is normalized by the bending energy of a vesicle with bending modulus κ_c , $8\pi\kappa_c$, and the colorbar shows its logarithm. The black dots (\bullet) in contour plots represent the values for which simulations have been conducted. The configuration of a doublet depends on the way the RBCs make their first contact. (c) RBCs can contact while they have an offset or while they are aligned. (d) The difference between the free energy of the doublets in the aligned and offset case is shown. If $E_{\text{alig}} - E_{\text{off}}$ is positive, it means the offset doublet has less free energy so that it is a more favorable configuration. The phase diagrams of the aligned (e) and offset (f) cases are different in the region where $E_{\text{alig}} - E_{\text{off}}$ is positive. Various phases are distinguished based on their cross-sectional views.

• **Flat-Biconcave (F-B) phase:**

This phase with a flat contact area and biconcave intact areas, is obtained at $v_1 = v_2 \approx 0.3-0.4$ and $\gamma \approx 1-2$ when the RBCs align with no offset. According to Figure 11.5, the F-B phase shrinks to a very small region if the RBCs are initially in contact with an offset. This explains why the F-B phase is less probable to be seen in physiological cases where the offset contact is far more probable than the aligned contact.

Although the F-B phase is the stable doublet configuration for the aligned doublets, the bending energy at this state is not at a global minimum. It is seen from the free energy difference between the aligned and offset configurations in Figure 11.5-d. If the RBCs reach each other with an offset, they tend to form M-F or S-B phase configurations (compare left and right phase diagrams in Figure 11.5-e and -f). Under physiological conditions, RBCs rarely make an aligned contact to each other so that the F-B phase is not observed in experiments.

Figure 11.6 illustrates various doublet shapes of two RBCs with different reduced volumes, for fixed reduced adhesion energy $\gamma = 8$. Another phase, the sheath phase, appears here.

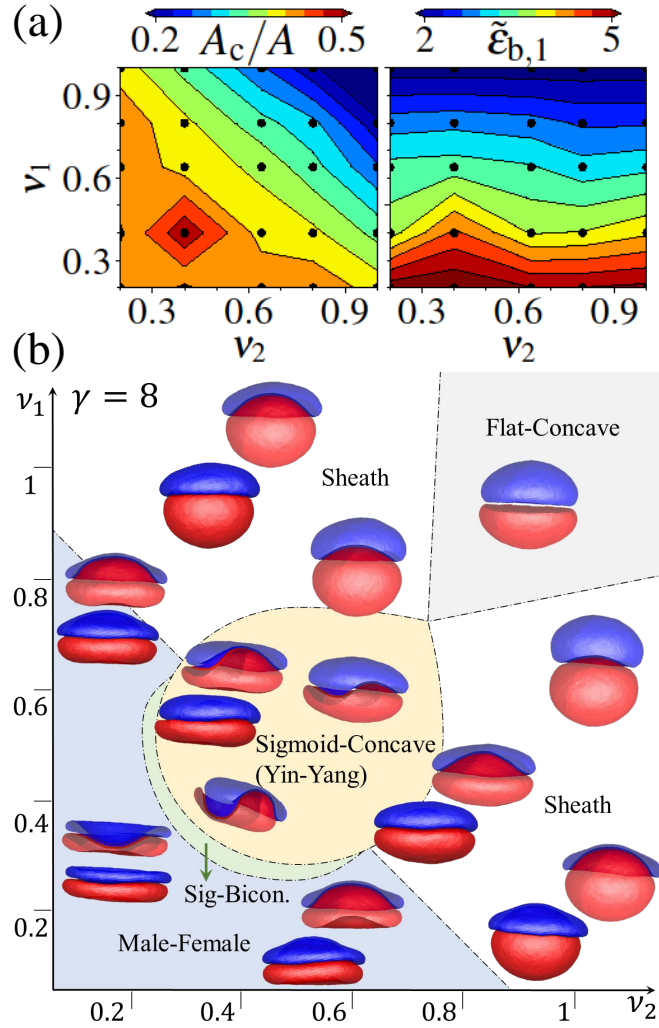
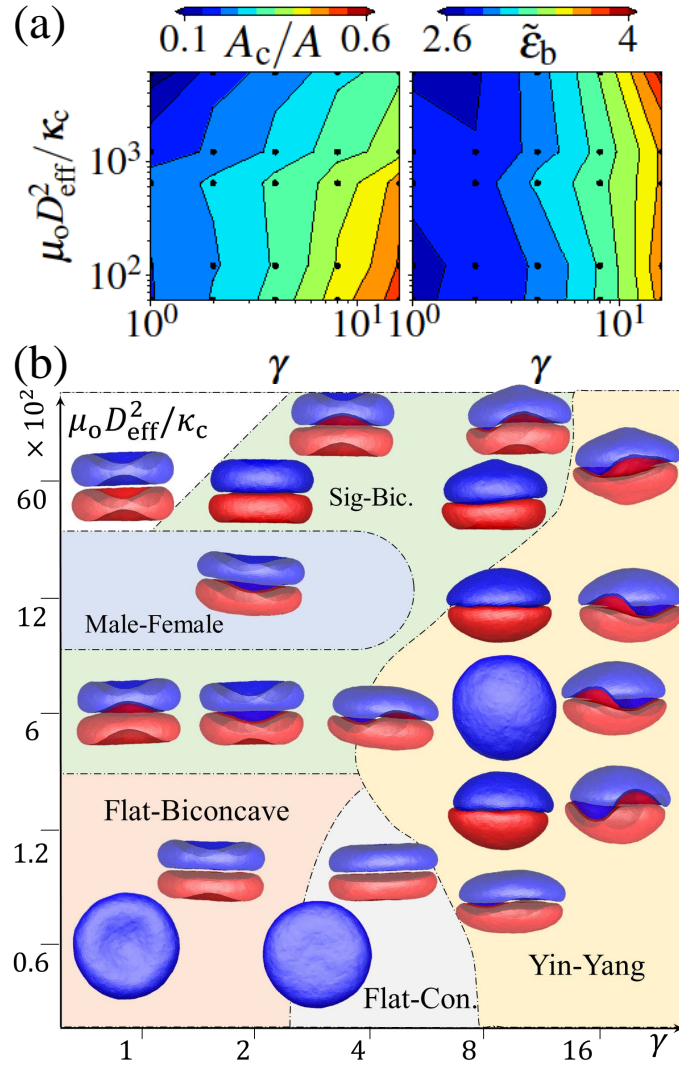


Fig. 11.6 RBC doublet configurations as a function of v_1 and v_2 at a constant adhesion strength $\gamma = 8$. (a) The contour plots show the contact area and the reduced effective bending energy as a function of v_1 and v_2 . The black dots (•) in contour plots represent the values for which simulations have been performed. (b) The side and section views of some configurations are shown in the phase diagram, omitting some shapes for more clarity. The different phases are separated by different colors. The S-B phase occurs in a narrow region between Yin-Yang and M-F phases, which has not been detected in the simulation points (specified by black dots •.)

Fig. 11.7 RBC doublet configurations as a function of spectrin network's shear modulus μ_o , and reduced adhesion strength γ at constant reduced volume $v = 0.64$. (a) The contour plots show the contact area and the effective bending rigidity. The black dots (\bullet) represent the values for which simulations have been conducted. (b) The side and section views of some configurations are shown, omitting some shapes for more clarity. The different phases are separated by different colors. The physiological shear modulus is in the range 2-12 ($\mu\text{N}/\text{m}$) corresponding to $\mu_o D_{\text{eff}}^2 / \kappa_c = 300$ -1500. The low shear moduli correspond to vesicle doublets. The membrane is assumed to be stress-free at its biconcave shape.



• **Sheath phase:** If the reduced volume of one RBC is large, and of the other is small, the former would swell to an elliptical shape and the latter would bend to a cup shape. Therefore, the best configuration for their adhesion occurs when the inner cup of the latter RBC matches the swollen belly of the former RBC. This configuration remains the minimal free energy condition for almost all adhesion strengths. Since most RBCs have reduced volumes in range 0.4 to 0.8, such a phase is not detected under physiological conditions.

In the case of unequal reduced volumes (see Figure 11.6), the contact area is roughly proportional to the inverse of the average of the reduced volumes ($A_c \propto (v_1 + v_2)^{-1}$) and varies from about 0 to 0.7. The reduced effective bending energy $\tilde{\epsilon}_b$ is roughly proportional to the inverse of the average of reduced volume squares ($\tilde{\epsilon}_b \propto (v_1^2 + v_2^2)^{-1}$). It is obviously unity for $v_1 = v_2 = 1$ and increases as the reduced volumes decrease.

In order to study the effect of the spectrin network's shear elasticity on the doublet phases, the membrane shear modulus μ_0 is varied. Figure 11.7 shows the phase diagram together with the contact area and reduced effective bending energy as a function of shear modulus and adhesion strength, with constant reduced volume of healthy RBCs $v \approx 0.64$. The shear modulus of healthy RBCs lies in the range $2\text{--}10 \mu\text{N}/\text{m}^{54,86,169,216,218,241}$ which corresponds to the dimensionless normalized shear modulus $\mu_0 D_{\text{eff}}^2 / \kappa_c$ of $300\text{--}1500$, provided that the bending rigidity is $70 k_B T$. The phases obtained for very low shear moduli agree well with the numerical energy-minimization study by Ziherl and Svetina 2007²⁵⁸, where the contact area is flat for low adhesion strengths and it buckles as adhesion strength increases. The F-B phase appears in a broader range of adhesion strengths when the shear modulus is much lower than the healthy RBC shear moduli. Also, the F-C phase which has never been detected for normal RBC reduced volumes of $v \approx 0.64$, appears at very low shear moduli. On the other hand, at shear moduli of healthy RBCs, the M-F and S-B phases are detected at low adhesion strengths. If the shear modulus is very high, the RBCs do not tend to form contact area from their center. This condition could be relevant for diseased RBCs, such as in malaria.

The doublet phases are determined by the balance of deformation energies and adhesion energy. The shear elasticity of the membrane attributed to the spectrin network has a strong effect on the doublet phases. For vesicle doublets, the effect of shear elasticity is absent since vesicles are made of fluid membrane. Accordingly, the lower region of the phase diagram ($\mu_0 \approx 0$) in Figure 11.7 corresponds to the previous works on vesicle doublets, with the three phases, F-C, F-B, and Sigmoid-Concave (Yin-Yang)^{67,220,258}, categorized based on the contact surface only. A distinct difference between the results of ours and previous studies on vesicle and RBC doublets is seen here. As shown in Figure 11.7, the F-B phase only appears if the shear elasticity of the RBC spectrin network is neglected. It is seen here that such phase cannot be seen in RBC doublets because they have significant shear elasticity.

Since shear elasticity of membranes has a significant effect on the doublet configurations, the stress-free shape of RBC might also play an important role in determining the shape of the RBC membrane and their doublet phases. Whether the spectrin network of RBC is stress-free in the biconcave or spherical shape, or something in between, is still under debate^{30,31,63,219}. So far in this work, the RBCs were stress-free at their biconcave shape. In order to study the effect of the stress-free state of RBCs on doublet phases, the stress-free biconcave shape is compared with the cases where the network is stress-free at a deflated sphere shape with eccentricity 0.94 and 0.96. The change in the configuration of the doublets is not very significant, as shown in Figure 11.8. The most important difference between the two cases is the change of F-B phase to the M-F phase at small adhesion strengths. If the stress-free shape of RBC is a sphere, the change between the M-F and the Yin-Yang phase

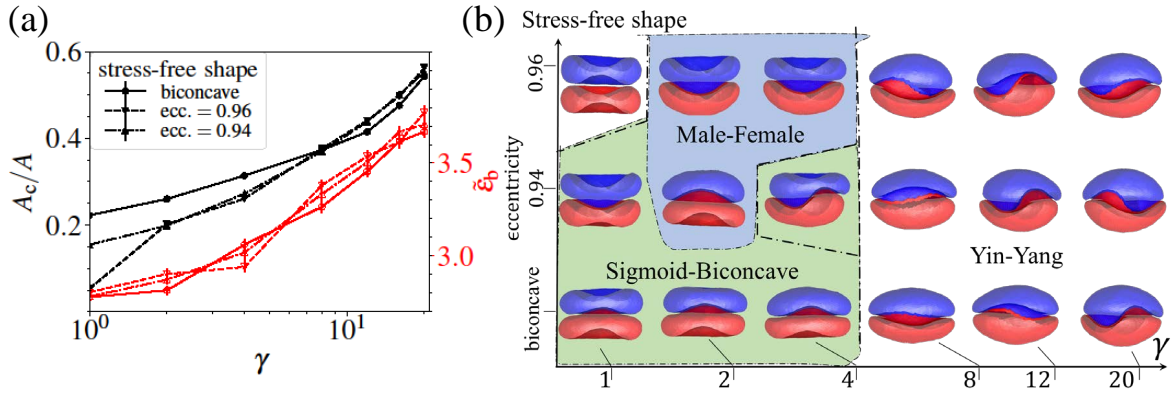


Fig. 11.8 Stress-free shape of RBC affects the doublet phases at low adhesion strengths and low reduced volumes ($v \approx 0.4$). (a) The stress-free shape has minuscule effect on the reduced effective bending energy, while the contact area changes slightly with respect to the stress-free shape. (b) Also, the phase change between M-F and Yin-Yang occurs at higher adhesion strengths. However, this tiny change is faded by the natural variance of the RBC mechanical properties and reduced volumes.

happens at slightly higher adhesion strengths, as shown in Figure 11.8. This slight change is seen from the contact area between the two RBCs in a doublet. In practice, this small change cannot be detected in experiments, not only because of the lack of the imaging precision, but also because of the natural variance of the mechanical properties of RBC membranes and their reduced volumes.

11.6 Comparison with experiments

The experimental images of the different phases are compared to the simulation results in Figure 11.9. The F-B phase is not seen in experiments and not predicted by simulations for the physiological reduced volumes of RBCs.

Both in simulations and experiments, the M-F doublets form when the adhesion strength is intermediate, and the reduced volume is small. The Yin-Yang phase appears when the adhesion strength is strong. The S-B phase is seen as a transition state between these two phases. The flat biconcave phase has not been observed in experiments. The F-C phase occurs when both RBCs are swollen and the Sheath phase happens when there is significant difference in the reduced volumes of the two RBCs. To see the F-C phase in experiments, the osmolality of the solution needs to increase about two-fold. For increasing reduced volume of RBCs in experiments, they are immersed in hypotonic solution of NaCl.

At low shear rates, RBCs aggregate in stacks, known as rouleaux. The rouleaux increase the viscosity of the blood at low shear rates. The nucleation of rouleaux starts from RBC

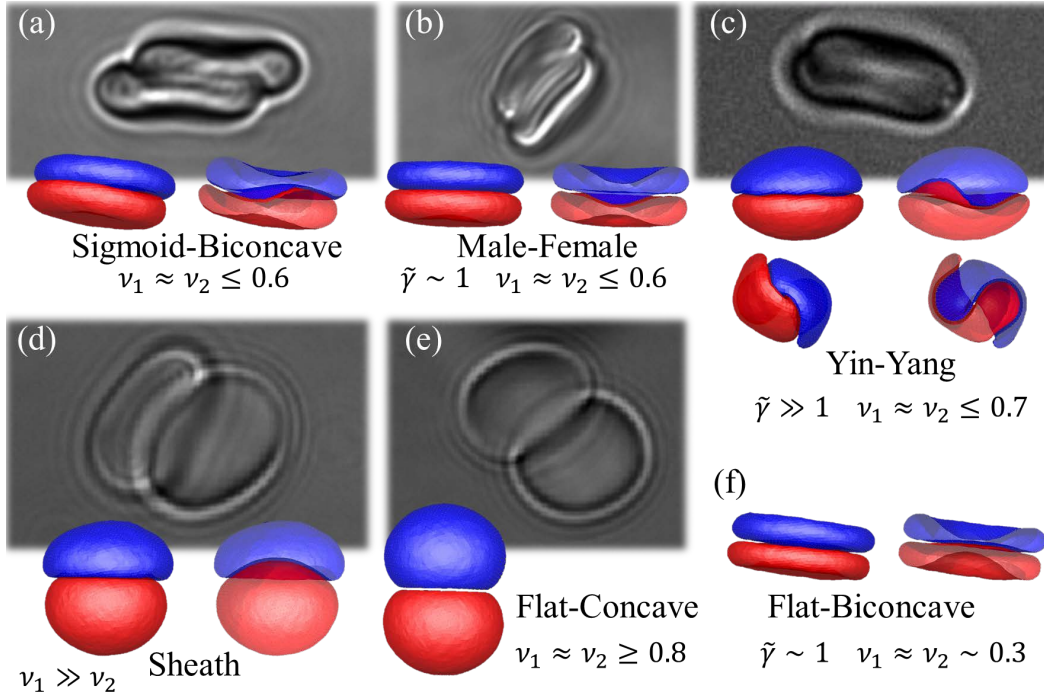


Fig. 11.9 RBC doublet shapes. Determined by the adhesion strength and bending modulus via the reduced adhesion energy $\tilde{\gamma}$, and the reduced volume of RBCs, 6 distinct doublet phases appear. The shapes from experiments together with their similar configurations from simulations are shown. For simulations, the side view and the section views are presented for each case. The phase names Sigmoid-Biconcave (a), M-F (b), Sigmoid-Concave (Yin-Yang) (c), Sheath (d), Flat-Concave (e), and Flat-Biconcave (f) denote to each configuration. The Sheath, Flat-Concave, and Flat-Biconcave phases are not probable for RBC doublets under physiological conditions.

doublets. While some doublet structures allow for large rouleaux formation, some prevent formation of large rouleaux. Among all the doublet phases, the M-F and S-B phases let the RBCs to form large rouleaux. The Yin-Yang phase however, prevents large rouleau structures to appear. Thus, the size of rouleaux in a solution of RBCs depends on their adhesion strength as well which is defined by the concentration of different adhesive factors in the solution (dextran, fibrinogen, etc.) Figure 11.10 shows some experimental and simulation results of different rouleau structures. The shapes of rouleaux for high adhesive strengths are very different depending on the reduced volumes of the RBCs, and the number of RBCs in the rouleau. In contrast, the M-F and S-B phases should allow the rouleau size to increase with no limit.

The limit for the nucleation of rouleaux can be explained by the free energy of the whole system. Doublet formation changes the free energy of the system by $2E_{\text{def}} - \Gamma A_c$. E_{def} is the deformation energy of a RBC, mostly due to bending rigidity and shear elasticity. In

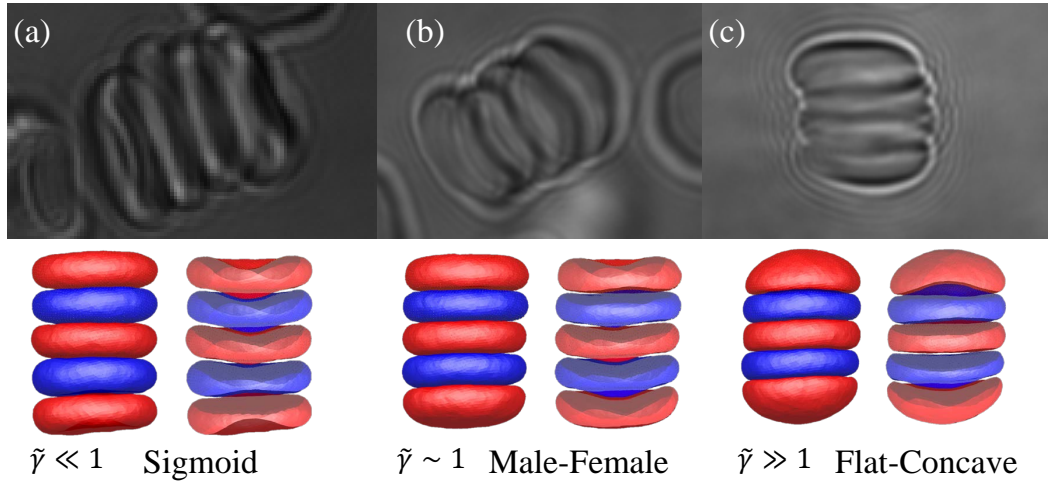


Fig. 11.10 Various rouleau phases in experiments and simulations. The doublet S-B and M-F phases impose no limit on the size of the rouleau. However, the Flat-Concave rouleaux are strongly dependent on the number of interacting RBCs, and their reduced volumes. The nucleation point of a Flat-Concave rouleau is a Yin-Yang doublet.

principle, it is always positive since any deviation from the equilibrium biconcave shape of RBC must have a higher energy. Therefore, the adhesion energy ΓA_c must be larger than $2E_{\text{def}}$ for doublet formation to be favorable. Adding one more RBC to the doublet to make a triplet aggregate of RBCs, adds $\Delta E_+ = E_{\text{def}} - \Gamma A_c + E_{\text{def}}^0$ to the total free energy, where E_{def}^0 is the additional deformation energy of the original aggregate, E_{def} is the deformation energy of the newly added RBC to the original aggregate and $-\Gamma A_c$ is the adhesion energy due to it. Assuming the other RBCs in the aggregate do not deform substantially, $E_{\text{def}}^0 \approx 0$; otherwise, the deformation and adhesion energy of all RBCs must be considered in the rearranged configuration. This rearranged configuration has definitely higher energy for the RBCs already in the aggregate, since they get away from their equilibrium configuration. For S-B and M-F phases, addition of an RBC to the aggregate adds a constant negative ΔE_+ to the free energy so that the growth of the rouleau is energetically favorable. ΔE_+ is constant since the contact area and curvature of the newly added RBC is similar to the other RBCs in the aggregate. On the contrary, ΔE_+ grows as a new RBC is added to a Yin-Yang doublet, because the contact area for the new RBC is less than the contact area of a doublet, and the new RBC deforms much more to be able to fit to the concave shape of a rouleau. As a result, ΔE_+ becomes positive at some point preventing more RBCs to adhere to the aggregate. This limiting point happens for larger cluster sizes as the adhesion strength Γ increases.

11.7 Summary

A systematic study of red blood cell (RBC) doublet formation has been performed. The analytical model employs a triangulated membrane with a polymerized mesh as representation of the spectrin network. It also takes thermal fluctuations into account. The simulation results demonstrate various doublet phases, namely, the Male-Female, Sigmoid-Biconcave, Yin-Yang, Sheath, Flat-Concave, and Flat-Biconcave phase, with their stability determined by the adhesion strength between two membranes and the reduced volume of each RBC. The Male-Female phase implies a curved contact area of two RBCs, like a female-male socket connection. The Sigmoid-Biconcave phase refers to the condition that two RBCs make a sigmoid S-shape contact while they keep their biconcave curvature. The Yin-Yang phase, then, refers to the same condition, but when the intact membranes of RBCs swell or bend to a concave form. The section view of the doublets in this phase looks like Yin-Yang symbol. The sheath phase occurs when one RBC is swollen so that the other RBC makes a sheath by contacting it. The Flat-Concave phase is referred to the flat contact area case. It occurs mostly when both RBCs are swollen. The predicted phases are compared with the experimental images obtained from optical imaging of RBCs in different solutions.

The RBC doublet phases are mainly defined by the interplay of bending energy and adhesion energy, and are closely related to the reduced volume of RBCs, which is a dimensionless ratio between the volume and area of RBCs. However, the shear elasticity of the RBC membrane, due to the spectrin network beneath their lipid bilayers, affects their doublet phases. At very low shear moduli, the Flat-Biconcave shape appears at low adhesion strengths while this phase is never stable for healthy RBCs with normal shear moduli. The very peculiar Flat-Concave phase at the normal reduced volumes of RBCs is also reported for very low shear moduli. This proves that the spectrin network's shear elasticity is a key player in defining the RBC doublet phases, differentiating them from previously studied fluid vesicle doublets.

Rouleau nucleation depends on how RBCs make doublets first. Aggregation of RBCs always brings a rise in the bending free energy and a decrease in the adhesive energy. Depending on the doublet shape, this pair of energy-changes determines whether rouleau formation is allowed. As a result, at high adhesion strengths, the doublets tend to prevent large stacks, since the Yin-Yang phase makes the positive change of the bending energy so large that it cannot be compensated by the adhesion energy related to the contact area of the membranes. At low and moderate adhesion strengths, the Sigmoid-Biconcave and Male-Female phases allow the growth of the rouleaux since the addition of RBC to the aggregate does not change the shapes of the other RBCs which have been already adhered to

the aggregate. These results are useful for determining the adhesion strength and membrane properties of healthy and diseased RBCs.

Chapter 12

Conclusion & future perspective

Most of the work in this thesis was about the behavior of the plasma protein von Willebrand factor (VWF) in the flow and its interaction with red blood cells (RBCs), platelets, and vessel walls. The most important addressed issues, include:

- **The dynamics and activity of VWFs in shear flow.** It is known that only large VWFs play an important role in the process of primary hemostasis^{33,176}. Also, VWFs are collapsed into globules at low shear rates, whereas they stretch at high shear rates^{75,191,212}. The stretching behavior of VWFs can be modeled well by mesoscale simulations, assuming VWF as a self-attractive⁶⁻⁸ or a self-associating polymer chain^{5,199,200}. The self-attractive polymer is the simplest model which captures a stretching behavior similar to the experimental results⁸⁹. It considers attractive pairwise Lennard-Jones interactions between all polymer beads. A more sophisticated model, the self-associating polymer model, employs inter-monomeric bond-like interactions with prescribed kinetics while the polymer beads have volume exclusion. It also shows similar results^{5,6,8,200}, but is more complicated to implement and unnecessarily detailed for coarse-grained mesoscopic simulations. Therefore, the self-attractive polymer model has been used for simulating VWF polymer dynamics in flow.

Not only the dynamics of VWF in flow, but also its adhesive behavior is important for primary hemostasis. Experiments have shown that VWFs are non-adhesive in the collapsed state at low shear rates where their adhesive ligands are shielded^{75,231}. VWFs become adhesive at high shear rates, where they stretch⁷⁵. Two mechanisms are important for the reversibility of VWF adhesion, the avidity and affinity²¹³. The avidity of a polymer is the number of adhesive ligands exposed to receptors, which is related to the polymer size and its shielding effect. The affinity is the likelihood and lifetime of single bonds between VWF ligands and a substrate.

A coarse-grained model has been proposed in this thesis, which mimics VWFs adhesive behavior. The dynamics of the polymer in shear flow and its avidity have been calibrated with experiments^{75,89,191}. Affinity of VWF polymers to adhesive substrate, such as vessel wall collagens or platelet receptors, has also been modeled with respect to the actual affinity of single VWF ligands to the platelet receptors¹⁰³. A catch-slip bond model^{158,167}, whose lifetime first increases and then decreases with increasing force, results in a similar bond affinity compared to experiments¹⁰³ ([chapter 5](#)).

The aggregation of platelets and VWFs has been studied by simulating mixtures of many VWF polymers and platelets. The calibrated polymer model shows a very good agreement with macroscopic experimental results on platelet adhesion to VWFs^{40,188}. Platelets are considered here as spherical rigid membranes whose vertices represent platelet receptors.

The results show that platelets and VWFs aggregate at high shear rates, and dissolve at low shear rates. The presence of VWFs helps platelets adhere to the adhesive substrate at high shear rates, when platelets are unable to adhere on their own. The simulations demonstrate that an increase in the affinity of VWFs to platelets leads to a slower dissolution time of aggregates, while a decrease in their affinity results in the lack of aggregation ([chapter 6](#)).

- **The contribution of RBCs to platelet-VWF aggregation.** The migration of RBCs to the center of the blood flow induces a high concentration of platelets and VWFs close to the vessel walls. This process, known as margination, helps in increasing the probability of platelets and VWFs adhesion to injured vessel walls. Using the mesoscopic models of blood flow^{53,54,60}, it has been shown that not only platelets marginate in blood flow, but also large VWFs do^{140,172}. In consequence, the cross-sectional distribution of VWFs in microvessels is such that most of large VWFs gather close to the vessel walls, where they stretch under a high shear stress. VWFs that are at the center of the vessel remain collapsed and non-adhesive ([chapter 3](#)). Similar to the Fåhræus effect due to the migration of RBCs to the center of the blood stream, the margination of microscale particles leads to their increased concentration at the walls, which can be interpreted as a reverse Fåhræus effect. The Fåhræus effect results from the formation of a RBC free layer near the vessel walls, and is referred to a lower effective hematocrit than the discharge hematocrit. Accordingly, the effective volume fraction of margined particles in blood vessels is larger than their discharge/injection volume fraction ([chapter 4](#)).

Freely flowing platelet-VWF aggregates feel a strong hydrodynamic lift force, due to their high porosity and deformability, leading to their demargination. In pressure-driven flow, the shear stress applied on demarginated aggregates drops at the center of the vessel so that they dissolve. Although the demargination of aggregates is correlated with their dissolution in blood flow, it is not a cause of it. The pressure-driven flow in the blood vessels helps in keeping platelet-VWF aggregates close to the vessel walls and letting the blood cells flow beside them ([chapter 7](#)).

In case the platelets are activated, or VWFs have a high affinity to platelets, the demarginated aggregates do not dissolve and eventually end up at the center of the vessel, increasing the risk of vessel blockage. Both aggregate formation and demargination depend on flow rate and volume fraction of RBCs in blood stream. Also, the presence of plasma VWFs helps in stable aggregation on the injured/adhesive surface ([chapter 8](#)).

- **VWF length regulation in flow.** The VWFs size distribution is regulated by enzymatic activity. Similar to VWF adhesiveness, the cleavage of VWF by its protease, ADAMTS13, is correlated with its stretching, induced by shear stress^{42,184,228,252}. A realistic model of VWF cleavage, calibrated with experimental results, shows that VWF cleavage in shear flow occurs at the extruded ends of the polymer when it starts stretching, provided that shear rate is beyond a critical value. The cleavage of VWFs in blood flow shows that the margined VWFs are more prone to cleavage ([chapter 9](#)). The size distribution of VWFs due to their cleavage has been theoretically analyzed, and the results show that their size distribution obeys a power law ([chapter 10](#)).
- **RBCs aggregation.** Because RBC aggregation is suppressed by high shear rates, it has been neglected in the study of the platelet-VWF aggregation in the blood flow. The formation of RBC doublets is important as a nucleation step for larger RBC aggregates. Various RBC doublet phases have been determined as a function of the reduced volume of RBCs, the adhesion strength of RBCs (due to both depletion and bridging), the shear elasticity of RBCs, and the bending rigidity of RBC membranes. Some doublets allow large stacks of RBCs, or rouleaux, to form, but some other doublets are stable only in their doublet form ([chapter 11](#)).

The proposed models are considered as building blocks for further research on primary hemostasis with more complexity, especially in mesoscales for the first time. In particular, important issues to be addressed are:

- **Study of the whole process of primary hemostasis.** Current simulations use periodic boundary conditions. It limits the growth of thrombi on the adhesive injured surface.

Addition of inflow and outflow boundary conditions to the system, with the correct concentration of VWF polymers and platelets in blood flow, will make it possible to simulate the whole primary hemostasis process.

- **VWF and platelet margination in more complex vascular geometries.** In vivo, the blood flow passes through complex microvessel networks with numerous bifurcations. Larger simulations are needed to study a more physiologically relevant case. The distribution of blood components may be different from the simple case of a straight tube or channel.
- **Primary hemostasis in more complex vasculature.** Once the margination of platelets and VWFs in microvasculature is known, the discharge of the blood from an injured vessel and the process of primary hemostasis can be studied.
- **Formation of RBC rouleaux and their dynamics in flow.** Formation of large RBC aggregates can be studied. The dynamics of RBC aggregates in flow would provide a better understanding of the viscous properties of blood.

Bibliography

References

- [1] Abkarian, M., Lartigue, C., and Viallat, A. (2002). Tank treading and unbinding of deformable vesicles in shear flow: determination of the lift force. *Phys Rev Lett*, 88(6):068103.
- [2] Abkarian, M. and Viallat, A. (2008). Vesicles and red blood cells in shear flow. *Soft Matter*, 4(4):653–657.
- [3] Agarwal, U. S., Dutta, A., and Mashelkar, R. A. (1994). Migration of macromolecules under flow: the physical origin and engineering implications. *Chem Eng Sci*, 49:1693–1717.
- [4] Alexander, B. and Goldstein, R. (1953). Dual hemostatic defect in pseudohemophilia. *J Clin Invest*, 32(6):551–551.
- [5] Alexander-Katz, A. (2014). Toward novel polymer-based materials inspired in blood clotting. *Macromolecules*, 47:1503–1513.
- [6] Alexander-Katz, A. and Netz, R. (2008). Dynamics and instabilities of collapsed polymers in shear flow. *Macromolecules*, 41(9):3363–3374.
- [7] Alexander-Katz, A. and Netz, R. R. (2007). Surface-enhanced unfolding of collapsed polymers in shear flow. *Europhys Lett*, 80(1):18001.
- [8] Alexander-Katz, A., Schneider, M. F., Schneider, S. W., Wixforth, A., and Netz, R. R. (2006). Shear-flow-induced unfolding of polymeric globules. *Phys Rev Lett*, 97:138101.
- [9] Alexander-Katz, A., Wada, H., and Netz, R. R. (2009). Internal friction and nonequilibrium unfolding of polymeric globules. *Phys Rev Lett*, 103(2):028102.
- [10] Allahyarov, E. and Gompper, G. (2002). Mesoscopic solvent simulations: Multiparticle-collision dynamics of three-dimensional flows. *Phys Rev E*, 66(3):036702.
- [11] Auton, M., Sowa, K. E., Smith, S. M., Sedláč, E., Vijayan, K. V., and Cruz, M. A. (2010). Destabilization of the a1 domain in von willebrand factor dissociates the a1a2a3 tri-domain and provokes spontaneous binding to glycoprotein $\text{ib}\alpha$ and platelet activation under shear stress. *J Biol Chem*, 285(30):22831–22839.
- [12] Bagge, U. and Karlsson, R. (1980). Maintenance of white blood cell margination at the passage through small venular junctions. *Microvasc Res*, 20:92–95.

- [13] Barg, A., Ossig, R., Goerge, T., Schneider, M. F., Schillers, H., Oberleithner, H., and Schneider, S. W. (2007). Soluble plasma-derived von Willebrand factor assembles to a haemostatically active filamentous network. *Thromb Haemost*, 97:514–526.
- [14] Basu, H., Dharmadhikari, A. K., Dharmadhikari, J. A., Sharma, S., and Mathur, D. (2011). Tank treading of optically trapped red blood cells in shear flow. *Biophys J*, 101(7):1604–1612.
- [15] Bathe, K.-J. and Wilson, E. L. (1976). *Numerical methods in finite element analysis*. Prentice-Hall, NJ.
- [16] Bauer, A. T., Suckau, J., Frank, K., Desch, A., Goertz, L., Wagner, A. H., Hecker, M., Goerge, T., Umansky, L., Beckhove, P., Utikal, J., Gorzelanny, C., Diaz-Valdes, N., Umansky, V., and Schneider, S. W. (2015). von Willebrand factor fibers promote cancer-associated platelet aggregation in malignant melanoma of mice and humans. *Blood*, 125:3153–3163.
- [17] Bäumler, H., Neu, B., Donath, E., and Kiewewetter, H. (1999). Basic phenomena of red blood cell rouleaux formation. *Biorheology*, 36(5, 6):439–442.
- [18] Bell, G. I. (1978). Models for the specific adhesion of cells to cells. *Science*, 200(4342):618–627.
- [19] Boal, D. H. and Rao, M. (1992). Topology changes in fluid membranes. *Phys Rev A*, 46(6):3037.
- [20] Brust, M., Aouane, O., Thiébaud, M., Flormann, D., Verdier, C., Kaestner, L., Laschke, M., Selmi, H., Benyoussef, A., Podgorski, T., et al. (2014). The plasma protein fibrinogen stabilizes clusters of red blood cells in microcapillary flows. *Sci Rep*, 4:4348.
- [21] Buxbaum, K., Evans, E., and Brooks, D. (1982). Quantitation of surface affinities of red blood cells in dextran solutions and plasma. *Biochemistry*, 21(13):3235–3239.
- [22] Canham, P. B. (1970). The minimum energy of bending as a possible explanation of the biconcave shape of the human red blood cell. *J Theor Biol*, 26(1):61–77.
- [23] Cantat, I. and Misbah, C. (1999). Lift force and dynamical unbinding of adhering vesicles under shear flow. *Phys Rev Lett*, 83:880–883.
- [24] Chen, H. and Alexander-Katz, A. (2011). Dynamics of polymers in flowing colloidal suspensions. *Phys Rev Lett*, 107:128301.
- [25] Chen, H., Angerer, J. I., Napoleone, M., Reininger, A. J., Schneider, S. W., Wixforth, A., Schneider, M. F., and Alexander-Katz, A. (2013a). Hematocrit and flow rate regulate the adhesion of platelets to von willebrand factor. *Biomicrofluidics*, 7(6):064113.
- [26] Chen, H., Fallah, M. A., Huck, V., Angerer, J. I., Reininger, A. J., Schneider, S. W., Schneider, M. F., and Alexander-Katz, A. (2013b). Blood-clotting-inspired reversible polymer–colloid composite assembly in flow. *Nat Commun*, 4:1333.
- [27] Chen, S. and Doolen, G. D. (1998). Lattice boltzmann method for fluid flows. *Annu Rev Fluid Mech*, 30(1):329–364.

- [28] Chien, S., Sung, L. A., Simchon, S., Lee, M. M., Jan, K.-m., and Skalak, R. (1983). Energy balance in red cell interactions. *Ann NY Acad Sci*, 416(1):190–206.
- [29] Cines, D. B., Konkle, B. A., and Furlan, M. (2000). Thrombotic thrombocytopenic purpura: a paradigm shift? *Thromb Haemostasis*, 84(4):528–535.
- [30] Cordasco, D., Yazdani, A., and Bagchi, P. (2014). Comparison of erythrocyte dynamics in shear flow under different stress-free configurations. *Phys Fluids*, 26(4):041902.
- [31] Daily, B., Elson, E. L., and Zahalak, G. I. (1984). Cell poking. determination of the elastic area compressibility modulus of the erythrocyte membrane. *Biophys J*, 45(4):671–682.
- [32] Dao, M., Li, J., and Suresh, S. (2006). Molecularly based analysis of deformation of spectrin network and human erythrocyte. *Mater Sci Eng C*, 26:1232–1244.
- [33] De Ceunynck, K., De Meyer, S. F., and Vanhoorelbeke, K. (2013). Unwinding the von willebrand factor strings puzzle. *Blood*, 121(2):270–277.
- [34] De Gennes, P. (1974). Coil-stretch transition of dilute flexible polymers under ultrahigh velocity gradients. *J Chem Phys*, 60(12):5030–5042.
- [35] De Gennes, P.-G. (1990). *Introduction to polymer dynamics*. Cambridge University Press, Cambridge.
- [36] De Meyer, S. F., Deckmyn, H., and Vanhoorelbeke, K. (2009). von willebrand factor to the rescue. *Blood*, 113(21):5049–5057.
- [37] Decuzzi, P., Lee, S., Bhushan, B., and Ferrari, M. (2005). A theoretical model for the margination of particles within blood vessels. *Ann Biomed Eng*, 33(2):179–190.
- [38] Dembo, M., Torney, D., Saxman, K., and Hammer, D. (1988). The reaction-limited kinetics of membrane-to-surface adhesion and detachment. *P Roy Soc Lond B Bio*, 234(1274):55–83.
- [39] Deuling, H. and Helfrich, W. (1976). Red blood cell shapes as explained on the basis of curvature elasticity. *Biophys J*, 16(8):861–868.
- [40] Doggett, T. A., Girdhar, G., Lawshé, A., Schmidtke, D. W., Laurenzi, I. J., Diamond, S. L., and Diacovo, T. G. (2002). Selectin-like kinetics and biomechanics promote rapid platelet adhesion in flow: the gpib α -vWF tether bond. *Biophys J*, 83(1):194–205.
- [41] Dong, J.-F. (2005). Cleavage of ultra-large von Willebrand factor by ADAMTS-13 under flow conditions. *J Thromb Haemost*, 3:1710–1716.
- [42] Dong, J.-f., Moake, J. L., Nolasco, L., Bernardo, A., Arceneaux, W., Shrimpton, C. N., Schade, A. J., McIntire, L. V., Fujikawa, K., and López, J. A. (2002). Adamts-13 rapidly cleaves newly secreted ultralarge von willebrand factor multimers on the endothelial surface under flowing conditions. *Blood*, 100(12):4033–4039.
- [43] Doyle, P. S., Ladoux, B., and Viovy, J.-L. (2000). Dynamics of a tethered polymer in shear flow. *Phys Rev Lett*, 84(20):4769–4772.

- [44] Ellero, M. and Español, P. (2018). Everything you always wanted to know about sdpd(but were afraid to ask). *Adv Appl Math Mech*, 39(1):103–124.
- [45] Español, P. and Revenga, M. (2003). Smoothed dissipative particle dynamics. *Phys Rev E*, 67(2):026705.
- [46] Español, P. and Warren, P. (1995). Statistical mechanics of dissipative particle dynamics. *Europhys Lett*, 30(4):191.
- [47] Estren, S., Médal, L. S., and Dameshek, W. (1946). Pseudohemophilia. *Blood*, 1(6):504–533.
- [48] Evans, E. A. (1974). Bending resistance and chemically induced moments in membrane bilayers. *Biophys J*, 14(12):923–931.
- [49] Evans, E. A. (1983). Bending elastic modulus of red blood cell membrane derived from buckling instability in micropipet aspiration tests. *Biophys J*, 43:27–30.
- [50] Evans, E. A. and Skalak, R. (1980). *Mechanics and thermodynamics of biomembranes*. CRC Press, Inc.
- [51] Fåhræus, R. (1929). The suspension stability of the blood. *Physiol Rev*, 9(2):241–274.
- [52] Fåhræus, R. and Lindqvist, T. (1931). The viscosity of the blood in narrow capillary tubes. *Am J Physiol*, 96(3):562–568.
- [53] Fedosov, D. A. (2010). *Multiscale modeling of blood flow and soft matter*. PhD thesis, Brown University, USA.
- [54] Fedosov, D. A., Caswell, B., and Karniadakis, G. E. (2010a). A multiscale red blood cell model with accurate mechanics, rheology, and dynamics. *Biophys J*, 98(10):2215–2225.
- [55] Fedosov, D. A., Caswell, B., and Karniadakis, G. E. (2010b). Systematic coarse-graining of spectrin-level red blood cell models. *Comput Method Appl M*, 199(29):1937–1948.
- [56] Fedosov, D. A., Caswell, B., Popel, A. S., and Karniadakis, G. E. (2010c). Blood flow and cell-free layer in microvessels. *Microcirculation*, 17:615–628.
- [57] Fedosov, D. A., Fornleitner, J., and Gompper, G. (2012). Margination of white blood cells in microcapillary flow. *Phys Rev Lett*, 108(2):028104.
- [58] Fedosov, D. A. and Gompper, G. (2014). White blood cell margination in microcirculation. *Soft matter*, 10(17):2961–2970.
- [59] Fedosov, D. A. and Karniadakis, G. E. (2009). Triple-decker: interfacing atomistic–mesoscopic–continuum flow regimes. *J Comp Phys*, 228(4):1157–1171.
- [60] Fedosov, D. A., Noguchi, H., and Gompper, G. (2014). Multiscale modeling of blood flow: from single cells to blood rheology. *Biomech Model Mechan*, 13(2):239–258.

- [61] Finger, E. B., Puri, K. D., Alón, R., Lawrence, M. , von Andrian, U. H., and Springer, T. A. (1996). Adhesion through I-selectin requires a threshold hydrodynamic shear. *Nature*, 379:18.
- [62] Firrell, J. C. and Lipowsky, H. H. (1989). Leukocyte margination and deformation in mesenteric venules of rat. *Am J Physiol*, 256:H1667–H1674.
- [63] Fischer, T., Haest, C., Stöhr-Liesen, M., Schmid-Schönbein, H., and Skalak, R. (1981). The stress-free shape of the red blood cell membrane. *Biophys J*, 34(3):409–422.
- [64] Fischer, T. M. (2004). Shape memory of human red blood cells. *Biophys J*, 86:3304–3313.
- [65] Fischer, T. M. (2007). Tank-tread frequency of the red cell membrane: dependence on the viscosity of the suspending medium. *Biophys J*, 93:2553–2561.
- [66] Fitzgibbon, S., Spann, A. P., Qi, Q. M., and Shaqfeh, E. S. G. (2015). In vitro measurement of particle margination in the microchannel flow: effect of varying hematocrit. *Biophys J*, 108:2601–2608.
- [67] Flormann, D., Aouane, O., Kaestner, L., Ruloff, C., Misbah, C., Podgorski, T., and Wagner, C. (2017). The buckling instability of aggregating red blood cells. *Sci Rep*, 7(1):7928.
- [68] Fogelson, A. L. and Guy, R. D. (2004). Platelet–wall interactions in continuum models of platelet thrombosis: formulation and numerical solution. *Math Med Biol*, 21(4):293–334.
- [69] Fogelson, A. L. and Guy, R. D. (2008). Immersed-boundary-type models of intravascular platelet aggregation. *Comput Method Appl M*, 197(25):2087–2104.
- [70] Fogelson, A. L. and Neeves, K. B. (2015). Fluid mechanics of blood clot formation. *Annu Rev Fluid Mech*, 47:377.
- [71] Fowler, W. E., Fretto, L. J., Hamilton, K. K., Erickson, H. P., and McKee, P. A. (1985). Substructure of human von willebrand factor. *J Clin Invest*, 76(4):1491.
- [72] Franchini, M., Frattini, F., Crestani, S., Bonfanti, C., and Lippi, G. (2013). von Willebrand factor and cancer: a renewed interest. *Thromb Res*, 131:290–292.
- [73] Freund, J. B. (2007). Leukocyte margination in a model microvessel. *Phys Fluids*, 19:023301.
- [74] Freund, J. B. (2014). Numerical simulation of flowing blood cells. *Annu Rev Fluid Mech*, 46:67–95.
- [75] Fu, H., Jiang, Y., Yang, D., Scheifflinger, F., Wong, W. P., and Springer, T. A. (2017). Flow-induced elongation of von Willebrand factor precedes tension-dependent activation. *Nat Comm*, 8:324.
- [76] Furlan, M. (1996). Von Willebrand factor: molecular size and functional activity. *Ann Hematol*, 72:341–348.

- [77] Gold, L. (1958). Statistics of polymer molecular size distribution for an invariant number of propagating chains. *J Chem Phys*, 28(1):91–99.
- [78] Goldsmith, H. L. and Spain, S. (1984). Margination of leukocytes in blood flow through small tubes. *Microvasc Res*, 27:204–222.
- [79] Gompper, G., Ihle, T., Kroll, D. M., and Winkler, R. G. (2009). Multi-particle collision dynamics: a particle-based mesoscale simulation approach to the hydrodynamics of complex fluids. *Adv Polym Sci*, 221:1–87.
- [80] Gompper, G. and Kroll, D. (1996). Random surface discretizations and the renormalization of the bending rigidity. *J Phys I*, 6(10):1305–1320.
- [81] Gompper, G. and Kroll, D. (1997). Network models of fluid, hexatic and polymerized membranes. *J Phys Condens Mat*, 9(42):8795.
- [82] Gompper, G. and Kroll, D. M. (2004). Triangulated-surface models of fluctuating membranes. In Nelson, D. R., Piran, T., and Weinberg, S., editors, *Statistical mechanics of membranes and surfaces*, pages 359–426. World Scientific, Singapore, 2nd edition.
- [83] Göpferich, A. (1996). Mechanisms of polymer degradation and erosion. *Biomaterials*, 17(2):103–114.
- [84] Groot, R. D. and Warren, P. B. (1997). Dissipative particle dynamics: Bridging the gap between atomistic and mesoscopic simulation. *J Chem Phys*, 107(11):4423.
- [85] Helfrich, W. (1973). Elastic properties of lipid bilayers: theory and possible experiments. *Z Naturforsch C*, 28(11-12):693–703.
- [86] Henon, S., Lenormand, G., Richert, A., and Gallet, F. (1999). A new determination of the shear modulus of the human erythrocyte membrane using optical tweezers. *Biophys J*, 76:1145–1151.
- [87] Henriquez-Rivera, R. G., Zhang, X., and Graham, M. D. (2016). Mechanistic theory of margination and flow-induced segregation in confined multicomponent suspensions: simple shear and Poiseuille flows. *Phys Rev Fluids*, 1:060501.
- [88] Hoogerbrugge, P. and Koelman, J. (1992). Simulating microscopic hydrodynamic phenomena with dissipative particle dynamics. *Europhys Lett*, 19(3):155.
- [89] Hoore, M., Rack, K., Fedosov, D., and Gompper, G. (2018). Flow-induced adhesion of shear-activated polymers to a substrate. *J Phys Condens Mat*, 30(6):064001.
- [90] Hosseinzadegan, H. and Tafti, D. K. (2017). Modeling thrombus formation and growth. *Biotechnol Bioeng*, 114(10):2154–2172.
- [91] Huang, R.-H., Wang, Y., Roth, R., Yu, X., Purvis, A. R., Heuser, J. E., Egelman, E. H., and Sadler, J. E. (2008). Assembly of weibel–palade body-like tubules from n-terminal domains of von willebrand factor. *Proc Natl Acad Sci USA*, 105(2):482–487.
- [92] Huck, V., Schneider, M. F., Gorzelanny, C., and Schneider, S. W. (2014). The various states of von Willebrand factor and their function in physiology and pathophysiology. *J Thromb Haemost*, 111:598–609.

- [93] Huebner, K. H. (2001). *The finite element method for engineers*. John Wiley & Sons.
- [94] Huisman, B., Hoore, M., Gompper, G., and Fedosov, D. A. (2017). Modeling the cleavage of von willebrand factor by adamts13 protease in shear flow. *Med Eng Phys*, 48:14–22.
- [95] Jackson, S., Nesbitt, W., and Westein, E. (2009). Dynamics of platelet thrombus formation. *J Thromb Haemost*, 7(s1):17–20.
- [96] Jeffery, G. B. (1922). The motion of ellipsoidal particles immersed in a viscous fluid. *Proc Roy Soc A*, 102:161–179.
- [97] Jülicher, F. (1996). The morphology of vesicles of higher topological genus: conformal degeneracy and conformal modes. *J Phys II*, 6(12):1797–1824.
- [98] Kantor, Y. and Nelson, D. R. (1987). Phase transitions in flexible polymeric surfaces. *Phys Rev A*, 36(8):4020.
- [99] Karnis, A., Goldsmith, H., and Mason, S. (1963). Axial migration of particles in poiseuille flow. *Nature*, 200(4902):159.
- [100] Katanov, D., Gompper, G., and Fedosov, D. A. (2015). Microvascular blood flow resistance: role of red blood cell migration and dispersion. *Microvasc Res*, 99:57–66.
- [101] Keller, S. R. and Skalak, R. (1982). Motion of a tank-treading ellipsoidal particle in a shear flow. *J Fluid Mech*, 120:27–47.
- [102] Khare, R., Graham, M. D., and de Pablo, J. J. (2006). Cross-stream migration of flexible molecules in a nanochannel. *Phys Rev Lett*, 96:224505.
- [103] Kim, J., Zhang, C.-Z., Zhang, X., and Springer, T. A. (2010). A mechanically stabilized receptor-ligand flex-bond important in the vasculature. *Nature*, 466(7309):992–995.
- [104] Kim, S., Kong, R. L., Popel, A. S., Intaglietta, M., and Johnson, P. C. (2006). A computer-based method for determination of the cell-free layer width in microcirculation. *Microcirculation*, 13(3):199–207.
- [105] Kim, S., Kong, R. L., Popel, A. S., Intaglietta, M., and Johnson, P. C. (2007). Temporal and spatial variations of cell-free layer width in arterioles. *Am J Physiol*, 293:H1526–H1535.
- [106] Kim, S., Ong, P. K., Yalcin, O., Intaglietta, M., and Johnson, P. C. (2009). The cell-free layer in microvascular blood flow. *Biorheology*, 46(3):181–189.
- [107] Knoch, F. and Speck, T. (2017). Nonequilibrium markov state modeling of the globule-stretch transition. *Phys Rev E*, 95(1):012503.
- [108] Kong, F., García, A. J., Mould, A. P., Humphries, M. J., and Zhu, C. (2009). Demonstration of catch bonds between an integrin and its ligand. *J Cell Biol*, 185(7):1275–1284.
- [109] Kremer, K. and Grest, G. S. (1990). Dynamics of entangled linear polymer melts: A molecular-dynamics simulation. *J Chem Phys*, 92(8):5057–5086.

- [110] Krüger, T., Gross, M., Raabe, D., and Varnik, F. (2013). Crossover from tumbling to tank-treading-like motion in dense simulated suspensions of red blood cells. *Soft Matter*, 9(37):9008–9015.
- [111] Kumar, A. and Graham, M. D. (2012a). Margination and segregation in confined flows of blood and other multicomponent suspensions. *Soft Matter*, 8:10536–10548.
- [112] Kumar, A. and Graham, M. D. (2012b). Mechanism of margination in confined flows of blood and other multicomponent suspensions. *Phys Rev Lett*, 109:108102.
- [113] Lai, W. M., Rubin, D. H., Rubin, D., and Krempf, E. (2009). *Introduction to continuum mechanics*. Butterworth-Heinemann.
- [114] Lanotte, L., Mauer, J., Mendez, S., Fedosov, D. A., Fromental, J.-M., Claveria, V., Nicoud, F., Gompper, G., and Abkarian, M. (2016). Red cells' dynamic morphologies govern blood shear thinning under microcirculatory flow conditions. *Proc Natl Acad Sci USA*, 113(47):13289–13294.
- [115] Larrieu, M. and Soulier, J. (1953). Déficit en facteur antihémophilique a chez une fille, associé a un trouble du saignement. *Rev Hematol*, 8(3):361–370.
- [116] LeDuc, P., Haber, C., Bao, G., and Wirtz, D. (1999). Dynamics of individual flexible polymers in a shear flow. *Nature*, 399(6736):564.
- [117] Lee, T.-R., Choi, M., Kopacz, A. M., Yun, S.-H., Liu, W. K., and Decuzzi, P. (2013). On the near-wall accumulation of injectable particles in the microcirculation: smaller is not better. *Sci Rep*, 3:2079.
- [118] Lei, H., Fedosov, D. A., Caswell, B., and Karniadakis, G. E. (2013). Blood flow in small tubes: quantifying the transition to the non-continuum regime. *J Fluid Mech*, 722:214–239.
- [119] Lei, H., Fedosov, D. A., and Karniadakis, G. E. (2011). Time-dependent and outflow boundary conditions for dissipative particle dynamics. *J Comput Phys*, 230(10):3765–3779.
- [120] Li, J., Dao, M., Lim, C., and Suresh, S. (2005). Spectrin-level modeling of the cytoskeleton and optical tweezers stretching of the erythrocyte. *Biophys J*, 88(5):3707–3719.
- [121] Lidmar, J., Mirny, L., and Nelson, D. R. (2003). Virus shapes and buckling transitions in spherical shells. *Phys Rev E*, 68(5):051910.
- [122] Lim H. W., G., Wortis, M., and Mukhopadhyay, R. (2002). Stomatocyte-discocyte-echinocyte sequence of the human red blood cell: Evidence for the bilayer-couple hypothesis from membrane mechanics. *Proc Natl Acad Sci USA*, 99:16766–16769.
- [123] Lipowsky, R. (1991). The conformation of membranes. *Nature*, 349(6309):475.
- [124] Lippok, S., Obser, T., Müller, J. P., Stierle, V. K., Benoit, M., Budde, U., Schneppenheim, R., and Rädler, J. O. (2013). Exponential size distribution of von willebrand factor. *Biophys J*, 105(5):1208–1216.

- [125] Lippok, S., Radtke, M., Obser, T., Kleemeier, L., Schneppenheim, R., Budde, U., Netz, R. R., and Rädler, J. O. (2016). Shear-induced unfolding and enzymatic cleavage of full-length vwf multimers. *Biophys J*, 110(3):545–554.
- [126] Lowe, E. J. and Werner, E. J. (2005). Thrombotic thrombocytopenic purpura and hemolytic uremic syndrome in children and adolescents. *Semin Thromb Hemost*, 31(06):717–730.
- [127] Lucy, L. B. (1977). A numerical approach to the testing of the fission hypothesis. *Astron J*, 82:1013–1024.
- [128] Madabhushi, S. R., Zhang, C., Kelkar, A., Dayananda, K. M., and Neelamegham, S. (2014). Platelet gpib α binding to von willebrand factor under fluid shear: Contributions of the d9d3-domain, a1-domain flanking peptide and o-linked glycans. *J Am Heart Assoc*, 3(5):e001420.
- [129] Malevanets, A. and Kapral, R. (1999). Mesoscopic model for solvent dynamics. *J Chem Phys*, 110(17):8605–8613.
- [130] Martin, C., Morales, L., and Cruz, M. (2007). Purified a2 domain of von willebrand factor binds to the active conformation of von willebrand factor and blocks the interaction with platelet glycoprotein ib α . *J Thromb Haemost*, 5(7):1363–1370.
- [131] Maxey, M. and Patel, B. (2001). Localized force representations for particles sedimenting in stokes flow. *Int J Multiphas Flow*, 27(9):1603–1626.
- [132] Mehrabadi, M., Casa, L. D., Aidun, C. K., and Ku, D. N. (2016a). A predictive model of high shear thrombus growth. *Ann Biomed Eng*, 44(8):2339–2350.
- [133] Mehrabadi, M., Ku, D. N., and Aidun, C. K. (2016b). Effects of shear rate, confinement, and particle parameters on margination in blood flow. *Phys Rev E*, 93(2):023109.
- [134] Mendolicchio, G. L. and Ruggeri, Z. M. (2005). New perspectives on von Willebrand factor functions in hemostasis and thrombosis. *Semin Hematol*, 42:5–14.
- [135] Meßlinger, S., Schmidt, B., Noguchi, H., and Gompper, G. (2009). Dynamical regimes and hydrodynamic lift of viscous vesicles under shear. *Phys Rev E*, 80(1):011901.
- [136] Misbah, C. (2006). Vacillating breathing and tumbling of vesicles under shear flow. *Phys Rev Lett*, 96:028104.
- [137] Moake, J. L., Turner, N. A., Stathopoulos, N. A., Nolasco, L. H., and Hellums, J. D. (1986). Involvement of large plasma von Willebrand factor (vWF) multimers and unusually large vWF forms derived from endothelial cells in shear stress-induced platelet aggregation. *J Clin Invest*, 78:1456–1461.
- [138] Monaghan, J. J. (1992). Smoothed particle hydrodynamics. *Annu Rev Astron Astr*, 30:543–574.
- [139] Monaghan, J. J. (2005). Smoothed particle hydrodynamics. *Rep Prog Phys*, 68:1703–1759.

- [140] Müller, K., Fedosov, D. A., and Gompper, G. (2014). Margination of micro-and nano-particles in blood flow and its effect on drug delivery. *Sci Rep*, 4:4871.
- [141] Müller, K., Fedosov, D. A., and Gompper, G. (2015). Smoothed dissipative particle dynamics with angular momentum conservation. *J Comput Phys*, 281:301–315.
- [142] Müller, K., Fedosov, D. A., and Gompper, G. (2016). Understanding particle margination in blood flow—a step toward optimized drug delivery systems. *Med Eng Phys*, 38(1):2–10.
- [143] Naghdi, P. M. (1973). The theory of shells and plates. In *Linear Theories of Elasticity and Thermoelasticity: Linear and Nonlinear Theories of Rods, Plates, and Shells*, pages 425–640. Springer.
- [144] Namdee, K., Thompson, A. J., Charoenphol, P., and Eniola-Adefeso, O. (2013). Margination propensity of vascular-targeted spheres from blood flow in a microfluidic model of human microvessels. *Langmuir*, 29:2530–2535.
- [145] Nash, G. B., Watts, T., Thornton, C., and Barigou, M. (2008). Red cell aggregation as a factor influencing margination and adhesion of leukocytes and platelets. *Clin Hemorheol Microcirc*, 39:303–310.
- [146] Nesbitt, W. S., Westein, E., Tovar-Lopez, F. J., Tolouei, E., Mitchell, A., Fu, J., Carberry, J., Fouras, A., and Jackson, S. P. (2009). A shear gradient-dependent platelet aggregation mechanism drives thrombus formation. *Nat Med*, 15(6):665–673.
- [147] Netz, R. R. and Andelman, D. (2003). Neutral and charged polymers at interfaces. *Phys Rep*, 380:1–95.
- [148] Neu, B. and Meiselman, H. J. (2002). Depletion-mediated red blood cell aggregation in polymer solutions. *Biophys J*, 83(5):2482–2490.
- [149] Neu, B., Wenby, R., and Meiselman, H. J. (2008). Effects of dextran molecular weight on red blood cell aggregation. *Biophys J*, 95(6):3059–3065.
- [150] Nilsson, I., Blombäck, M., and Francken, I. (1957a). On an inherited autosomal hemorrhagic diathesis with antihemophilic globulin (ahg) deficiency and prolonged bleeding times. *J Intern Med*, 159(1):35–58.
- [151] Nilsson, I., Blombäck, M., Jorpes, E., Blombäck, B., and Johansson, S.-a. (1957b). v. Willebrand’s disease and its correction with human plasma fraction 1-0. *J Intern Med*, 159(3):179–188.
- [152] Nobis, U., Pries, A. R., Cokelet, G. R., and Gaehtgens, P. (1985). Radial distribution of white cells during blood flow in small tubes. *Microvasc Res*, 29:295–304.
- [153] Noguchi, H. and Gompper, G. (2004). Fluid vesicles with viscous membranes in shear flow. *Phys Rev Lett*, 93:258102.
- [154] Noguchi, H. and Gompper, G. (2007). Swinging and tumbling of fluid vesicles in shear flow. *Phys Rev Lett*, 98:128103.

- [155] Olla, P. (1997a). The lift on a tank-treading ellipsoidal cell in a shear flow. *J Phys II*, 7(10):1533–1540.
- [156] Olla, P. (1997b). The role of tank-treading motions in the transverse migration of a spheroidal vesicle in a shear flow. *J Phys A Math Gen*, 30:317–329.
- [157] Pereverzev, Y. V. and Prezhd, O. V. (2007). Universal laws in the force-induced unraveling of biological bonds. *Phys Rev E*, 75(1):011905.
- [158] Pereverzev, Y. V., Prezhd, O. V., Forero, M., Sokurenko, E. V., and Thomas, W. E. (2005). The two-pathway model for the catch-slip transition in biological adhesion. *Biophys J*, 89(3):1446–1454.
- [159] Perkins, T. T., Smith, D. E., and Chu, S. (1997). Single polymer dynamics in an elongational flow. *Science*, 276(5321):2016–2021.
- [160] Perkins, W. (1946). Pseudohemophilia. *Blood*, 1(6):497–503.
- [161] Peskin, C. S. (2002). The immersed boundary method. *Acta numerica*, 11:479–517.
- [162] Phillips, R., Kondev, J., Theriot, J., and Garcia, H. (2012). *Physical biology of the cell*. Garland Science.
- [163] Pivkin, I. V., Richardson, P. D., and Karniadakis, G. (2006). Blood flow velocity effects and role of activation delay time on growth and form of platelet thrombi. *Proc Natl Acad Sci USA*, 103(46):17164–17169.
- [164] Plimpton, S. (1995). Fast parallel algorithms for short-range molecular dynamics. *J Chem Phys*, 117:1–19.
- [165] Popel, A. S. and Johnson, P. C. (2005). Microcirculation and hemorheology. *Annu Rev Fluid Mech*, 37:43–69.
- [166] Pozrikidis, C. (1992). *Boundary integral and singularity methods for linearized viscous flow*. Cambridge University Press.
- [167] Prezhd, O. V. and Pereverzev, Y. V. (2009). Theoretical aspects of the biological catch bond. *Accounts Chem Res*, 42(6):693–703.
- [168] Pries, A., Neuhaus, D., and Gaehtgens, P. (1992). Blood viscosity in tube flow: dependence on diameter and hematocrit. *Am J Physiol-Heart C*, 263(6):H1770–H1778.
- [169] Puig-de Morales-Marinkovic, M., Turner, K. T., Butler, J. P., Fredberg, J. J., and Suresh, S. (2007). Viscoelasticity of the human red blood cell. *Am J Physiol*, 293:C597–C605.
- [170] Qi, Q. M. and Shaqfeh, E. S. (2017). Theory to predict particle migration and margination in the pressure-driven channel flow of blood. *Phys Rev Fluids*, 2(9):093102.
- [171] Quick, A. and Hussey, C. (1953). Hemophilic condition in the female. *J Lab Clin Med*, 42(6):929–930.

- [172] Rack, K., Huck, V., Hoore, M., Fedosov, D. A., Schneider, S. W., and Gompper, G. (2017). Margination and stretching of von Willebrand factor in the blood stream enable adhesion. *Sci Rep*, 7:14278.
- [173] Radtke, M. and Netz, R. (2014). Shear-induced dynamics of polymeric globules at adsorbing homogeneous and inhomogeneous surfaces. *Eur Phys J E*, 37(3):1–11.
- [174] Radtke, M. and Netz, R. R. (2015). Shear-enhanced adsorption of a homopolymeric globule mediated by surface catch bonds. *Eur Phys J E*, 38(6):1–11.
- [175] Reasor Jr, D. A., Mehrabadi, M., Ku, D. N., and Aidun, C. K. (2013). Determination of critical parameters in platelet margination. *Ann Biomed Eng*, 41(2):238–249.
- [176] Reininger, A. (2008). Function of von willebrand factor in haemostasis and thrombosis. *Haemophilia*, 14(s5):11–26.
- [177] Reininger, A. J., Heijnen, H. F. G., Schumann, H., Specht, H. M., Schramm, W., and Ruggeri, Z. M. (2006). Mechanism of platelet adhesion to von Willebrand factor and microparticle formation under high shear stress. *Blood*, 107:3537–3545.
- [178] Richardson, J. L., Shivdasani, R. A., Boers, C., Hartwig, J. H., and Italiano, J. E. (2005). Mechanisms of organelle transport and capture along proplatelets during platelet production. *Blood*, 106(13):4066–4075.
- [179] Roach, P., Farrar, D., and Perry, C. C. (2005). Interpretation of protein adsorption: surface-induced conformational changes. *J Am Chem Soc*, 127:8168–8173.
- [180] Römer, F. and Fedosov, D. A. (2015). Dense brushes of stiff polymers or filaments in fluid flow. *Europhys Lett*, 109:68001.
- [181] Ruggeri, Z. M. (2003). Von Willebrand factor, platelets and endothelial cell interactions. *J Thromb Haemost*, 1:1335–1342.
- [182] Ruggeri, Z. M., Orje, J. N., Habermann, R., Federici, A. B., and Reininger, A. J. (2006). Activation-independent platelet adhesion and aggregation under elevated shear stress. *Blood*, 108(6):1903–1910.
- [183] Sadler, J. E. (1998). Biochemistry and genetics of von willebrand factor. *Annu Rev Biochem*, 67(1):395–424.
- [184] Sadler, J. E. (2002). A new name in thrombosis, ADAMTS13. *Proc Natl Acad Sci USA*, 99:11552–11554.
- [185] Sadler, J. E. (2005). New concepts in von willebrand disease. *Annu Rev Med*, 56:173–191.
- [186] Sadler, J. E., Budde, U., Eikenboom, J. C. J., Favaloro, E. J., Hill, F. G. H., Holmberg, L., Ingerslev, J., Lee, C. A., Lillicrap, D., Mannucci, P. M., Mazurier, C., Meyer, D., Nichols, W. L., Nishino, M., Peake, I. R., Rodeghiero, F., Schneppenheim, R., Ruggeri, Z. M., Srivastava, A., Montgomery, R. R., and Federici, A. B. (2006). Update on the pathophysiology and classification of von Willebrand disease: a report of the subcommittee on von Willebrand factor. *J Thromb Haemost*, 4:2103–2114.

- [187] Savage, B., Almus-Jacobs, F., and Ruggeri, Z. M. (1998). Specific synergy of multiple substrate–receptor interactions in platelet thrombus formation under flow. *Cell*, 94(5):657–666.
- [188] Savage, B., Saldívar, E., and Ruggeri, Z. M. (1996). Initiation of platelet adhesion by arrest onto fibrinogen or translocation on von willebrand factor. *Cell*, 84(2):289–297.
- [189] Savage, B., Shattil, S., and Ruggeri, Z. (1992). Modulation of platelet function through adhesion receptors. a dual role for glycoprotein iib-iiia (integrin alpha iib beta 3) mediated by fibrinogen and glycoprotein ib-von willebrand factor. *J Biol Chem*, 267(16):11300–11306.
- [190] Savage, B., Sixma, J. J., and Ruggeri, Z. M. (2002). Functional self-association of von willebrand factor during platelet adhesion under flow. *Proc Natl Acad Sci USA*, 99(1):425–430.
- [191] Schneider, S., Nuschele, S., Wixforth, A., Gorzelanny, C., Alexander-Katz, A., Netz, R., and Schneider, M. (2007). Shear-induced unfolding triggers adhesion of von willebrand factor fibers. *Proc Natl Acad Sci USA*, 104(19):7899–7903.
- [192] Schneppenheim, R., Budde, U., Oyen, F., Angerhaus, D., Aumann, V., Drewke, E., Hassenpflug, W., Häberle, J., Kentouche, K., Kohne, E., Kurnik, K., Mueller-Wiefel, D., Obser, T., Santer, R., and Sykora, K.-W. (2003). von Willebrand factor cleaving protease and ADAMTS13 mutations in childhood TTP. *Blood*, 101:1845–1850.
- [193] Seifert, U. (1997). Configurations of fluid membranes and vesicles. *Adv Phys*, 46(1):13–137.
- [194] Seifert, U., Berndl, K., and Lipowsky, R. (1991). Shape transformations of vesicles: Phase diagram for spontaneous-curvature and bilayer-coupling models. *Phys Rev A*, 44(2):1182.
- [195] Seung, H. S. and Nelson, D. R. (1988). Defects in flexible membranes with crystalline order. *Phys Rev A*, 38:1005–1018.
- [196] Sevvick, E. M. and Jain, R. K. (1988). Blood flow and venous pH of tissue-isolated Walker 256 carcinoma during hyperglycemia. *Cancer Res*, 48:1201–1207.
- [197] Siedlecki, C., Lestini, B., Kottke-Marchant, K., Eppell, S., Wilson, D., and Marchant, R. (1996). Shear-dependent changes in the three-dimensional structure of human von willebrand factor. *Blood*, 88(8):2939–2950.
- [198] Sing, C. E. and Alexander-Katz, A. (2010). Elongational flow induces the unfolding of von willebrand factor at physiological flow rates. *Biophys J*, 98(9):L35–L37.
- [199] Sing, C. E. and Alexander-Katz, A. (2011a). Equilibrium structure and dynamics of self-associating single polymers. *Macromolecules*, 44:6962–6971.
- [200] Sing, C. E. and Alexander-Katz, A. (2011b). Giant nonmonotonic stretching response of a self-associating polymer in shear flow. *Phys Rev Lett*, 107(19):198302.

- [201] Sing, C. E. and Alexander-Katz, A. (2011c). Non-monotonic hydrodynamic lift force on highly extended polymers near surfaces. *Europhys Lett*, 95:48001.
- [202] Sing, C. E. and Alexander-Katz, A. (2011d). Theory of tethered polymers in shear flow: the strong stretching limit. *Macromolecules*, 44:9020–9028.
- [203] Sing, C. E., Selvidge, J. G., and Alexander-Katz, A. (2013). Von willebrand adhesion to surfaces at high shear rates is controlled by long-lived bonds. *Biophys J*, 105(6):1475–1481.
- [204] Singer, K. and Ramot, B. (1956). Pseudohemophilia type b: hereditary hemorrhagic diathesis characterized by prolonged bleeding time and decrease in antihemophilic factor. *Arch Intern Med*, 97(6):715–725.
- [205] Skalak, R. and Chien, S. (1983). Theoretical models of rouleau formation and disaggregation. *Ann NY Acad Sci*, 416(1):138–148.
- [206] Skalak, R., Zarda, P., Jan, K., and Chien, S. (1981). Mechanics of rouleau formation. *Biophys J*, 35(3):771–781.
- [207] Skotheim, J. M. and Secomb, T. W. (2007). Red blood cells and other nonspherical capsules in shear flow: oscillatory dynamics and the tank-treading-to-tumbling transition. *Phys Rev Lett*, 98:078301.
- [208] Slayter, H., Loscalzo, J., Bockenstedt, P., and Handin, R. (1985). Native conformation of human von willebrand protein. analysis by electron microscopy and quasi-elastic light scattering. *J Biol Chem*, 260(14):8559–8563.
- [209] Sleep, J., Wilson, D., Simmons, R., and Gratzer, W. (1999). Elasticity of the red cell membrane and its relation to hemolytic disorders: an optical tweezers study. *Biophys J*, 77(6):3085–3095.
- [210] Smith, D. E., Babcock, H. P., and Chu, S. (1999). Single-polymer dynamics in steady shear flow. *Science*, 283(5408):1724–1727.
- [211] Smith, D. E. and Chu, S. (1998). Response of flexible polymers to a sudden elongational flow. *Science*, 281(5381):1335–1340.
- [212] Springer, T. A. (2011). Biology and physics of von willebrand factor concatamers. *J Thromb Haemost*, 9(s1):130–143.
- [213] Springer, T. A. (2014). von willebrand factor, jedi knight of the bloodstream. *Blood*, 124(9):1412–1425.
- [214] Steffen, P., Verdier, C., and Wagner, C. (2013). Quantification of depletion-induced adhesion of red blood cells. *Phys Rev Lett*, 110:018102.
- [215] Stein, D., van der Heyden, F. H. J., Koopmans, W. J. A., and Dekker, C. (2006). Pressure-driven transport of confined DNA polymers in fluidic channels. *Proc Natl Acad Sci USA*, 103:15853–15858.
- [216] Strey, H., Peterson, M., and Sackmann, E. (1995). Measurement of erythrocyte membrane elasticity by flicker eigenmode decomposition. *Biophys J*, 69:478–488.

- [217] Succi, S. (2001). *The Lattice Boltzmann equation for fluid dynamics and beyond*. Oxford University Press, Oxford.
- [218] Suresh, S., Spatz, J., Mills, J. P., Micoulet, A., Dao, M., Lim, C. T., Beil, M., and Seufferlein, T. (2005). Connections between single-cell biomechanics and human disease states: gastrointestinal cancer and malaria. *Acta Biomater*, 1:15–30.
- [219] Švelc, T. and Svetina, S. (2012). Stress-free state of the red blood cell membrane and the deformation of its skeleton. *Cell Mol Biol Lett*, 17(2):217.
- [220] Svetina, S. and Ziherl, P. (2008). Morphology of small aggregates of red blood cells. *Bioelectrochemistry*, 73(2):84–91.
- [221] Tangelder, G., Teirlinck, H. C., Slaaf, D. W., and Reneman, R. S. (1985). Distribution of blood platelets flowing in arterioles. *Am J Physiol-Heart C*, 248(3):H318–H323.
- [222] Tangelder, G. J., Slaaf, D. W., Teirlinck, H. C., Alewijnse, R., and Reneman, R. S. (1982). Localization within a thin optical section of fluorescent blood platelets flowing in a microvessel. *Microvasc Res*, 23(2):214–230.
- [223] Tateishi, N., Suzuki, Y., Soutani, M., and Maeda, N. (1994). Flow dynamics of erythrocytes in microvessels of isolated rabbit mesentery: cell-free layer and flow resistance. *J Biomech*, 27(9):1119–1125.
- [224] Thomas, W., Forero, M., Yakovenko, O., Nilsson, L., Vicini, P., Sokurenko, E., and Vogel, V. (2006). Catch-bond model derived from allostery explains force-activated bacterial adhesion. *Biophys J*, 90(3):753–764.
- [225] Thomas, W. E., Trintchina, E., Forero, M., Vogel, V., and Sokurenko, E. V. (2002). Bacterial adhesion to target cells enhanced by shear force. *Cell*, 109(7):913–923.
- [226] Thomas, W. E., Vogel, V., and Sokurenko, E. (2008). Biophysics of catch bonds. *Ann Rev Biophys*, 37(1):399–416.
- [227] Thompson, A. J., Mastria, E. M., and Eniola-Adefeso, O. (2013). The margination propensity of ellipsoidal micro/nanoparticles to the endothelium in human blood flow. *Biomaterials*, 34:5863–5871.
- [228] Tsai, H.-M. (1996). Physiologic cleavage of von willebrand factor by a plasma protease is dependent on its conformation and requires calcium ion. *Blood*, 87(10):4235–4244.
- [229] Tsubota, K.-i., Wada, S., and Yamaguchi, T. (2006). Particle method for computer simulation of red blood cell motion in blood flow. *Comput Meth Prog Bio*, 83(2):139–146.
- [230] Turlier, H., Fedosov, D. A., Audoly, B. A., Auth, T., Gov, N. S., Sykes, C., Joanny, J.-F., Gompper, G., and Betz, T. (2016). Equilibrium physics breakdown reveals the active nature of red blood cell membrane fluctuations. *Nat Phys*, 12:513–519.
- [231] Ulrichs, H., Udvardy, M., Lenting, P. J., Pareyn, I., Vandeputte, N., Vanhoorelbeke, K., and Deckmyn, H. (2006). Shielding of the a1 domain by the d d3 domains of von willebrand factor modulates its interaction with platelet glycoprotein ib-ix-v. *J Biol Chem*, 281(8):4699–4707.

- [232] Ulrichts, H., Vanhoorelbeke, K., Girma, J., Lenting, P., Vauterin, S., and Deckmyn, H. (2005). The von willebrand factor self-association is modulated by a multiple domain interaction. *J Thromb Haemost*, 3(3):552–561.
- [233] Usta, O. B., Butler, J. E., and Ladd, A. J. C. (2006). Flow-induced migration of polymers in dilute solution. *Phys Fluids*, 18:031703.
- [234] Vahidkhah, K., Diamond, S. L., and Bagchi, P. (2014). Platelet dynamics in three-dimensional simulation of whole blood. *Biophys J*, 106:2529–2540.
- [235] Valentijn, K. M., Sadler, J. E., Valentijn, J. A., Voorberg, J., and Eikenboom, J. (2011). Functional architecture of weibel-palade bodies. *Blood*, 117(19):5033–5043.
- [236] Van De Ven, T. G. M. (1989). *Colloidal hydrodynamics*. Academic Press, London.
- [237] Vázquez-Quesada, A., Ellero, M., and Español, P. (2009). Consistent scaling of thermal fluctuations in smoothed dissipative particle dynamics. *J Chem Phys*, 130:034901.
- [238] Versteeg, H. K. and Malalasekera, W. (2007). *An introduction to computational fluid dynamics: the finite volume method*. Pearson Education.
- [239] Von Willebrand, E. (1999). Hereditary pseudohaemophilia. *Haemophilia*, 5(3):223–231.
- [240] Von Willebrand, E. A. (1926). Hereditäre pseudohemofili. *Fink Lak Handl*, 68:87–112.
- [241] Waugh, R. and Evans, E. A. (1979). Thermoelasticity of red blood cell membrane. *Biophys J*, 26:115–131.
- [242] Weibel, E. R. and Palade, G. E. (1964). New cytoplasmic components in arterial endothelia. *J Cell Biol*, 23(1):101–112.
- [243] Woldhuis, B., Tangelder, G., Slaaf, D. W., and Reneman, R. S. (1992). Concentration profile of blood platelets differs in arterioles and venules. *Am J Physiol-Heart C*, 262(4):H1217–H1223.
- [244] Wu, Z., Xu, Z., Kim, O., and Alber, M. (2014). Three-dimensional multi-scale model of deformable platelets adhesion to vessel wall in blood flow. *Philos Tr R Soc S-A*, 372(2021):20130380.
- [245] Xu, Z., Chen, N., Kamocka, M. M., Rosen, E. D., and Alber, M. (2008). A multiscale model of thrombus development. *Journal of the Royal Society Interface*, 5(24):705–722.
- [246] Xu, Z., Chen, N., Shadden, S. C., Marsden, J. E., Kamocka, M. M., Rosen, E. D., and Alber, M. (2009). Study of blood flow impact on growth of thrombi using a multiscale model. *Soft Matter*, 5(4):769–779.
- [247] Yago, T., Lou, J., Wu, T., Yang, J., Miner, J. J., Coburn, L., López, J. A., Cruz, M. A., Dong, J.-F., McIntire, L. V., et al. (2008). Platelet glycoprotein $\text{Ib}\alpha$ forms catch bonds with human wt vwf but not with type 2b von willebrand disease vwf. *J Clin Invest*, 118(9):3195.

- [248] Yamaguchi, S., Yamakawa, T., and Niimi, H. (1992). Cell-free plasma layer in cerebral microvessels. *Biorheology*, 29:251–260.
- [249] Yazdani, A., Li, H., Humphrey, J. D., and Karniadakis, G. E. (2017). A general shear-dependent model for thrombus formation. *PLOS Comput Biol*, 13(1):e1005291.
- [250] Yazdani, A. Z., Kalluri, R. M., and Bagchi, P. (2011). Tank-treading and tumbling frequencies of capsules and red blood cells. *Phys Rev E*, 83(4):046305.
- [251] Zhang, J., Johnson, P. C., and Popel, A. S. (2009a). Effects of erythrocyte deformability and aggregation on the cell free layer and apparent viscosity of microscopic blood flows. *Microvasc Res*, 77:265–272.
- [252] Zhang, Q., Zhou, Y.-F., Zhang, C.-Z., Zhang, X., Lu, C., and Springer, T. A. (2009b). Structural specializations of $\alpha 2$, a force-sensing domain in the ultralarge vascular protein von willebrand factor. *Proc Natl Acad Sci USA*, 106(23):9226–9231.
- [253] Zhang, X., Halvorsen, K., Zhang, C.-Z., Wong, W. P., and Springer, T. A. (2009c). Mechanoenzymatic cleavage of the ultralarge vascular protein von willebrand factor. *Science*, 324(5932):1330–1334.
- [254] Zhao, H. and Shaqfeh, E. S. (2011). Shear-induced platelet margination in a microchannel. *Phys Rev E*, 83(6):061924.
- [255] Zhao, H., Shaqfeh, E. S., and Narsimhan, V. (2012). Shear-induced particle migration and margination in a cellular suspension. *Phys Fluids*, 24(1):011902.
- [256] Zhao, R., Kameneva, M. V., and Antaki, J. F. (2007). Investigation of platelet margination phenomena at elevated shear stress. *Biorheology*, 44(3):161–177.
- [257] Zhurkov, S. (1984). Kinetic concept of the strength of solids. *Int J Fracture*, 26(4):295–307.
- [258] Zihlerl, P. and Svetina, S. (2007). Flat and sigmoidally curved contact zones in vesicle–vesicle adhesion. *Proc Natl Acad Sci USA*, 104(3):761–765.
- [259] Zlobina, K. E. and Guria, G. T. (2016). Platelet activation risk index as a prognostic thrombosis indicator. *Sci Rep*, 6:30508.

Declaration

I hereby declare that the contents of this dissertation are original and have not been submitted in whole or in part for consideration for any other degree or qualification in this, or any other university. This dissertation is my own work in addition to the outcome of my collaboration with others, provided that I have contributed equal or more than 50% of the whole work. Excluding the contribution of my PhD supervisors, Dr. Dmitry Fedosov, and Prof. Dr. Gerhard Gompper, my contribution for the chapters of this thesis are as below;

- **chapter 9: Cleavage of von Willebrand factor by ADAMTS13 protease in flow** is the results of the collaboration with my summer student, Ms. Brooke Huisman, from the University of Michigan. I designed the research and supervised her in doing simulations and analyzing the results. I declare that I contributed more than 75% in this research. This chapter is directly related to the publication

B. Huisman, M. Hoore, G. Gompper, and D.A. Fedosov. *Modeling the cleavage of von Willebrand factor by ADAMTS13 protease in shear flow*. Medical Engineering & Physics, 2017

- **chapter 3: Margination of von Willebrand factor in the blood stream** is the results of the collaboration with my predecessor PhD student, Dr. Kathrin Rack (Müller), and with experimental collaborators Dr. med. Volker Huck, and Prof. Dr. Stefan W. Schneider. The raw simulations have been conducted by Dr. Kathrin Rack. I declare that I contributed more than 50% in this research, by doing further simulations, analysis, interpretations, and writing of the article. This chapter is directly related to the publication

K. Rack, V. Huck, M. Hoore, D.A. Fedosov, S.W. Schneider, and G. Gompper. *Margination and stretching of von Willebrand factor in the blood stream enable adhesion*. Scientific Reports, 2017

- **chapter 5: Flow-induced adhesion of shear-activated polymers to a substrate** is the results of my own research with the help and basic idea of my predecessor PhD student, Dr. Kathrin Rack (Müller). I declare that I contributed around 100% in this research. This chapter is directly related to the publication

M. Hoore, K. Rack, D.A. Fedosov, and G. Gompper. *Flow-induced adhesion of shear-activated polymers to a substrate*. Journal of Physics: Condensed Matter, 2018

Masoud Hoore
Jülich 2018

Erklärung

Ich versichere, dass ich die von mir vorgelegte Dissertation selbständig angefertigt, die benutzten Quellen und Hilfsmittel vollständig angegeben und die Stellen der Arbeit einschließlich Tabellen, Karten und Abbildungen, die anderen Werken im Wortlaut oder dem Sinn nach entnommen sind, in jedem Einzelfall als Entlehnung kenntlich gemacht habe; dass diese Dissertation noch keiner anderen Fakultät oder Universität zur Prüfung vorgelegen hat; daß sie abgesehen von unten angegebenen Teilpublikationen noch nicht veröffentlicht worden ist sowie, dass ich eine solche Veröffentlichung vor Abschluss des Promotionsverfahrens nicht vornehmen werde.

Die Bestimmungen dieser Promotionsordnung sind mir bekannt. Die von mir vorgelegte Dissertation ist von Prof. Dr. Gerhard Gompper betreut worden.

.....
Ort, Datum

.....
Unterschrift

Teilpublikationen

- B. Huisman, M. Hoore, G. Gompper, and D.A. Fedosov. *Modeling the cleavage of von Willebrand factor by ADAMTS13 protease in shear flow*. Medical Engineering & Physics, 2017
- K. Rack, V. Huck, M. Hoore, D.A. Fedosov, S.W. Schneider, and G. Gompper. *Margination and stretching of von Willebrand factor in the blood stream enable adhesion*. Scientific Reports, 2017
- M. Hoore, K. Rack, D.A. Fedosov, and G. Gompper. *Flow-induced adhesion of shear-activated polymers to a substrate*. Journal of Physics: Condensed Matter, 2018

Curriculum Vitae

EDUCATION

Forschungszentrum Jülich GmbH, Germany

- **PhD Physics** 05.2015 - 05.2018
Advisors: Dmitry Fedosov, Gerhard Gompper

Sharif University of Technology, Tehran, Iran

- **MSc. Mechanical Engineering** 09.2012 - 08.2014
Thesis: Deformation of protein embedded vesicles in shear flow
Advisor: Mir Abbas Jalali
- **BSc. Mechanical Engineering** 09.2007 - 08.2012
Thesis: Bending of microbeams based on the modified couple stress theory
Advisor: Mohsen Asghari
- **BSc. Physics** (Dual Major) 02.2009 - 08.2012
Thesis: Critical behavior of small-world Abelian sand-pile model
Advisor: Saman Moghimi-Araghi

PUBLICATIONS

- M. Hoore, K. Rack, D.A. Fedosov, G. Gompper, *Flow-induced adhesion of shear-activated polymers to a substrate*, J Phys Cond Mat (2017)
- K. Rack, V. Huck, M. Hoore, D.A. Fedosov, S. Schneider, G. Gompper, *Margination and stretching of von Willebrand factor in the blood stream enable adhesion*, Sci Rep (2017)
- B. Huisman, M. Hoore, G. Gompper, D.A. Fedosov, *Modeling the cleavage of von Willebrand factor by ADAMTS13 protease in shear flow*, Med Eng Phys **48** (2017)
- M. Hoore and S. Moghimi-Araghi, *Critical behavior of a small-world sandpile model*, J Phys A Math Theor **46** (2013)
- M.H. Kahrobaian, M. Asghari, M. Hoore and M.T. Ahmadian, *Nonlinear size-dependent forced vibrational behavior of microbeams based on a non-classical continuum theory*, J Vib Control **18** (2012)

